Panagiotis Kyratsis
J. Paulo Davim   *Editors*

Experiments and Simulations in Advanced Manufacturing

Springer

Materials Forming, Machining and Tribology

Series Editor

J. Paulo Davim, Department of Mechanical Engineering, University of Aveiro, Aveiro, Portugal

This series fosters information exchange and discussion on all aspects of materials forming, machining and tribology. This series focuses on materials forming and machining processes, namely, metal casting, rolling, forging, extrusion, drawing, sheet metal forming, microforming, hydroforming, thermoforming, incremental forming, joining, powder metallurgy and ceramics processing, shaping processes for plastics/composites, traditional machining (turning, drilling, miling, broaching, etc.), non-traditional machining (EDM, ECM, USM, LAM, etc.), grinding and others abrasive processes, hard part machining, high speed machining, high efficiency machining, micro and nanomachining, among others. The formability and machinability of all materials will be considered, including metals, polymers, ceramics, composites, biomaterials, nanomaterials, special materials, etc. The series covers the full range of tribological aspects such as surface integrity, friction and wear, lubrication and multiscale tribology including biomedical systems and manufacturing processes. It also covers modelling and optimization techniques applied in materials forming, machining and tribology. Contributions to this book series are welcome on all subjects of "green" materials forming, machining and tribology. To submit a proposal or request further information, please contact Dr. Mayra Castro, Publishing Editor Applied Sciences, via mayra.castro@springer.com or Professor J. Paulo Davim, Book Series Editor, via pdavim@ua.pt.

More information about this series at http://www.springer.com/series/11181

Panagiotis Kyratsis · J. Paulo Davim
Editors

Experiments and Simulations in Advanced Manufacturing

🐎 Springer

Editors
Panagiotis Kyratsis 🆔
Department of Product and Systems Design
Engineering
University of Western Macedonia
Kila Kozani, Greece

J. Paulo Davim 🆔
Department of Mechanical Engineering
University of Aveiro
Aveiro, Portugal

Dedicated to our families and associates

Preface

The present book aims in concentrating the latest advances in manufacturing from both the experimental and simulation point of view. It aims to cover all aspects of manufacturing engineering, i.e., theoretical, analytical, computational, and experimental studies. Experimental studies on manufacturing processes require funds, time, and expensive facilities, while numerical simulations and mathematical models can improve the efficiency of using the research results. They also provide high level of prediction accuracy and the basis for novel research directions.

A number of high-quality works has been incorporated within the following chapters. The initial chapter "Energy Efficient Machining Through Evolutionary Real–Time Optimization of Cutting Conditions on CNC-Milling Controllers" presents a novel approach of applying on-line on-board multi-objective optimization techniques for adaptive improvement of CNC-milling processes through IEC 61499 standardized Function Blocks running on an industrial CNC machine controller. The chapter "Modeling and Experimental Work on Electrical Discharge Machining" covers the electrical discharge machining, which is one of the most extensively used non-conventional machining processes, with many applications in the modern industrial environment. Chapter "Simulations and Experiments in Single Point Incremental Forming Process" pertains the entire flow of a single point incremental forming process starting from simulations to experiments. Chapter "Designing Novel Synthetic Grafts for Large Bone Defects: Experimental and Numerical Studies" describes the main steps associated to the design and fabrication of biodegradable bone bricks. Chapter "CAD Software Integration with Programming Tools for Modelling, Measurement and Verification of Surfaces" presents methodologies and procedures to automate the modeling of parts, the assembly of mechanical sets, the processing of these parts via milling, turning, and Wire Electrical Discharge Machining (WEDM) and finally the verification of the measures of the simulated parts. The chapter "Experimental Investigation of Process Parameters Effect on Laser Engraving Process Quality" incorporates an experimental investigation of stainless steel SAE304, aluminum 7075, pressure vessel steel P355GH, and yellow brass C26000 nanosecond pulsed Q-switched Nd:YAG 1064 nm laser engraving process. Chapter "The Effects of 3D Printing Structural Modelling on Compression Properties for Material Jetting and FDM Process" determines the effects of

structure's design and applied technology of 3D printing with relation to strength of the designed structure. Chapter "Atomistic Modelling of Nanocutting Processes" presents some of the state-of-the-art investigations on Molecular Dynamics simulations of Nanocutting processes. Chapter "Advanced Manufacturing of the Holes by Controlled Texture" aims to establish the optimal texture area, when four areas are analyzed depending on the stroke of the lubrication segment. The final chapter "Parametric Study of Electro Discharge Boring of Inconel 718 with Radial Tool Movement Using Taguchi Method" is dedicated on EDM that has been used for carrying out boring operation of Ni-based superalloy (Inconel 718), by guiding and controlling the movement of tool electrode on radial orbital tool path.

The editors acknowledge the aid of Springer Publications and express their gratitude for this opportunity and for their professional support. The editors also express their gratitude to all the chapter authors for their availability and for delivering their high-quality research work.

Kila Kozani, Greece   Panagiotis Kyratsis
Aveiro, Portugal   J. Paulo Davim
April 2021

Contents

Editors and Contributors

About the Editors

Dr. Panagiotis Kyratsis (www.kyratsis.com) is Associate Professor in the Department of Product and Systems Design Engineering, University of Western Macedonia, Greece. He is the Director of the Institute of Traditional Architecture and Cultural Heritage, University Research Center "TEMENUS" (urc.uowm.gr). Dr. Panagiotis Kyratsis received his Ph.D. in the area of CAD-based manufacturing process simulations from the Department of Production Engineering and Management, Technical University of Crete, Greece. He holds a diploma in Mechanical Engineering from the Aristotle's University of Thessaloniki—Greece, and he received his M.Sc. in Automotive Product Engineering and M.Sc. in CAD/CAM from Cranfield University—UK, in 1997 and 1999, respectively. He has been involved in a number of industrial projects and he has a great deal of expertise in both the design and the manufacturing aspects of product development. His main research interests include manufacturing, machining, CAD/CAM/CAE systems, product design, reverse engineering, and prototyping. He has published 18 books and more than 120 papers in Scientific Journals and International Conferences. He acts as member of the editorial board and reviewer to numerous scientific journals and holds 12 industrial designs and one patent registered within the Greek Patent Office.

Prof. J. Paulo Davim is a Full Professor at the University of Aveiro, Portugal. He is also distinguished as honorary professor in several universities/colleges/institutes in China, India and Spain. He received his Ph.D. degree in Mechanical Engineering in 1997, M.Sc. degree in Mechanical Engineering (materials and manufacturing processes) in 1991, Mechanical Engineering degree (5 years) in 1986, from the University of Porto (FEUP), the Aggregate title (Full Habilitation) from the University of Coimbra in 2005 and the D.Sc. (Higher Doctorate) from London Metropolitan University in 2013. He is Senior Chartered Engineer by the Portuguese Institution of Engineers with an MBA and Specialist titles in Engineering and Industrial Management as well as in Metrology. He is also Eur Ing by FEANI-Brussels and Fellow (FIET) of IET-London. He has more than 30 years of teaching

and research experience in Manufacturing, Materials, Mechanical and Industrial Engineering, with special emphasis in Machining & Tribology. He has also interest in Management, Engineering Education and Higher Education for Sustainability. He has guided large numbers of postdoc, Ph.D. and master's students as well as has coordinated and participated in several financed research projects. He has received several scientific awards and honors. He has worked as evaluator of projects for ERC-European Research Council and other international research agencies as well as examiner of Ph.D. thesis for many universities in different countries. He is the Editor in Chief of several international journals, Guest Editor of journals, books Editor, book Series Editor and Scientific Advisory for many international journals and conferences. Presently, he is an Editorial Board member of 30 international journals and acts as reviewer for more than 100 prestigious Web of Science journals. In addition, he has also published as editor (and co-editor) more than 200 books and as author (and co-author) more than 15 books, 100 book chapters and 500 articles in journals and conferences (more than 280 articles in journals indexed in Web of Science core collection/h-index 59+/11000+ citations, SCOPUS/h-index 63+/14000+ citations, Google Scholar/h-index 81+/23000+ citations). He has listed in World's Top 2% Scientists by Stanford University study.

Contributors

Anil A. Acar Faculty of Engineering and Natural Sciences, Sabanci University, Orhanli-Tuzla, Istanbul, Turkey

Aristomenis Antoniadis Micromachining & Manufacturing Modeling Laboratory, School of Production Engineering & Management, Technical University of Crete, Chania, Greece

M. K. A. Ariffin Department of Mechanical and Manufacturing Engineering, Universiti Putra Malaysia, Serdang, Seri Kembagan, Selangor, Malaysia

B. T. H. T. Baharudin Department of Mechanical and Manufacturing Engineering, Universiti Putra Malaysia, Serdang, Seri Kembagan, Selangor, Malaysia

Paulo Bartolo School of Mechanical, Aerospace and Civil Engineering, University of Manchester, Manchester, UK

Gordon Blunn School of Pharmacy and Biomedical Sciences, University of Portsmouth, Portsmouth, UK

Jevgenijs Butans Cranfield University, Cranfield, UK

Daniel Chiriţa Gheorghe Asachi Technical University of Iasi, Iasi, Romania

Glen Cooper School of Mechanical, Aerospace and Civil Engineering, University of Manchester, Manchester, UK

Evangelos Daskalakis School of Mechanical, Aerospace and Civil Engineering, University of Manchester, Manchester, UK

Harshit K. Dave Department of Mechanical Engineering, S. V. National Institute of Technology, Surat, Gujarat, India

Keyur P. Desai Department of Mechanical Engineering, S. V. National Institute of Technology, Surat, Gujarat, India

Mohammadreza Lalegani Dezaki Department of Mechanical and Manufacturing Engineering, Universiti Putra Malaysia, Serdang, Seri Kembagan, Selangor, Malaysia

Ali Fallah Faculty of Engineering and Natural Sciences, Sabanci University, Orhanli-Tuzla, Istanbul, Turkey

César García-Hernández Department of Design and Manufacturing Engineering, University of Zaragoza, Zaragoza, Spain

Rafael Gella-Marín Department of Design and Manufacturing Engineering, University of Zaragoza, Zaragoza, Spain

Francisco Rodriguez-Hernandez Manufacturing Theme, Cranfield University, Cranfield, UK

José-Luis Huertas-Talón Department of Design and Manufacturing Engineering, University of Zaragoza, Zaragoza, Spain

Panagiotis Karmiris-Obratański School of Mechanical Engineering - Laboratory of Manufacturing Technology, National Technical University of Athens, Athens, Greece;
Faculty of Mechanical Engineering and Robotics - Department of Manufacturing Systems, AGH University of Science and Technology, Cracow, Poland

Bahattin Koç Faculty of Engineering and Natural Sciences, Sabanci University, Orhanli-Tuzla, Istanbul, Turkey

Sudhanshu Kumar Department of Mechanical Engineering, M. A. National Institute of Technology, Bhopal, Madhya Pradesh, India

Panagiotis Kyratsis Department of Product and Systems Design Engineering, University of Western Macedonia, Kila Kozani, Greece

Fengyuan Liu School of Mechanical, Aerospace and Civil Engineering, University of Manchester, Manchester, UK

Angelos P. Markopoulos School of Mechanical Engineering - Laboratory of Manufacturing Technology, National Technical University of Athens, Athens, Greece

Jörn Mehnen University of Strathclyde, Glasgow, UK

D. Nasulea Department of Manufacturing Engineering, Transilvania University of Brasov, Brasov, Romania

Dumitru Nedelcu Gheorghe Asachi Technical University of Iasi, Iasi, Romania

Evangelos Nikolidakis Micromachining & Manufacturing Modeling Laboratory, School of Production Engineering & Management, Technical University of Crete, Chania, Greece

G. Oancea Department of Manufacturing Engineering, Transilvania University of Brasov, Brasov, Romania

Abdalla M. Omar School of Mechanical, Aerospace and Civil Engineering, University of Manchester, Manchester, UK

Michail Papanikolaou Manufacturing Theme, Cranfield University, Cranfield, UK

Emmanouil L. Papazoglou School of Mechanical Engineering - Laboratory of Manufacturing Technology, National Technical University of Athens, Athens, Greece

Marek Płaczek Department of Engineering Processes Automation and Integrated Manufacturing Systems, Silesian University of Technology, Gliwice, Poland

Konstantinos Salonitis Manufacturing Theme, Cranfield University, Cranfield, UK

Nikolaos Tapoglou University of Sheffield, Sheffield, UK

Anastasios Tzotzis Department of Design and Manufacturing Engineering, University of Zaragoza, Zaragoza, Spain

Andrew Weightman School of Mechanical, Aerospace and Civil Engineering, University of Manchester, Manchester, UK

Zhanyan Xu School of Mechanical, Aerospace and Civil Engineering, University of Manchester, Manchester, UK

Energy Efficient Machining Through Evolutionary Real-Time Optimization of Cutting Conditions on CNC-Milling Controllers

Nikolaos Tapoglou, Jörn Mehnen, and Jevgenijs Butans

Abstract Optimizing the use of manufacturing resources is vital for any engineering enterprise. Modern responsible industry is also taking increasingly the environmental impact into account. In milling the correct selection of cutting conditions can help minimizing the energy consumption, thus achieving a more sustainable operation. This paper presents a novel approach of applying on-line on-board multi-objective optimization techniques for adaptive improvement of CNC milling processes through IEC 61499 standardized Function Blocks running on an industrial CNC machine controller. The results show that it is possible to run even complex advanced evolutionary optimization algorithms on modern CNC machines in real-time. The case study also demonstrates that this approach can reduce up to 25% of the peak energy demand and 12% of cutting time when compared to conventional non optimized solutions.

1 Introduction

Manufacturing constitutes one of the most energy demanding sectors accounting for 36% of the total energy consumption in Europe according to the European Environment agency [1]. In the current environment, the use of sustainable techniques is paramount and must consider energy, material and component efficiency [2, 3]. It is therefore essential to optimize the use of manufacturing equipment since this leads to improved energy efficiency while simultaneously shortening the production

N. Tapoglou (✉)
University of Sheffield, Sheffield S60 5TZ, UK
e-mail: n.tapoglou@sheffield.ac.uk

J. Mehnen
University of Strathclyde, Glasgow G1 1XJ, UK
e-mail: jorn.mehnen@strath.ac.uk

J. Butans
Cranfield University, Cranfield MK43 0AL, UK
e-mail: eugene.butans@cranfield.ac.uk

time and time to market of manufactured products. Machine tools are an essential piece of equipment in every manufacturing workshop and the optimization of cutting conditions of machine tools can lead to cost savings during production and to greater resource efficiency.

In recent years, many methods have been proposed for both on-line and offline optimization of the cutting conditions with respect to maximizing production, minimizing tool wear and stabilizing cutting forces. In parallel, the advances in information technology have enabled machine tool controllers to execute more complex calculations and perform a series of supporting tasks in parallel, such as collision checking and chatter suppression [4].

The recent concept of Cloud Manufacturing [5, 6] is being adopted by industry along with the emerging technology of Internet of Things [7]. These concepts have been changing the way modern manufacturing is realized, creating a new and more efficient way of manufacturing goods.

In the modern environment, robust algorithms are needed to balance several contradicting objectives, such as machining time, power consumption and vibrations in parallel. Moreover, in order to allow for maximum flexibility, the optimization must run in the control loop to adapt the cutting conditions without the need to redo the conventional CAD/CAM chain. This paper presents a framework for on-line on-board multi-objective optimization of cutting parameters in milling. The novelty of the proposed system is based on the use of an optimization algorithm on-board an industrial CNC controller. The optimization algorithm is running in tandem with the controller loop adjusting the cutting parameters based on environmental criteria. A novel simulation model, validated through experimental data, is used as part of the optimization process to assist the optimization algorithm during execution. The system incorporates interconnectivity modules so that it can be part of a broader Cloud based manufacturing system.

The remainder of the paper is organized as follows: Sect. 2 presents the state-of-the-art on the relevant subjects of optimization and energy efficient machining. The optimization framework is presented in Sect. 3 while Sect. 4 details the novel optimization method. Section 5 describes the mathematical models used in the optimization process, followed by a case study in Sect. 6. Finally, Sect. 7 finishes with concluding remarks.

2   State of the Art

The proposed system optimizes cutting conditions with respect to energy consumption while minimizing the time needed for machining the part. Smart multi-objective optimization algorithms are used on-board the machine tool controller to adjust the cutting parameters. The on-line optimization module also communicates with a Cloud Manufacturing environment for receiving necessary toolpath information and updating the worker about work progress and its efficiency. Optimization of cutting conditions of machine tools is usually realized either in an on-line or offline mode.

Offline optimization occurs prior to the actual machining of the workpiece. Herein, empirical data from test runs or simulation models that predict the cutting process variables and optimize the cutting parameters accordingly are used to determine optimal processing parameters [4].

2.1 Offline Optimization

This approach allows the manipulation of the parameters of a cutting process; time limitations are usually not considered as critical and hence, the results can be very accurate and close to optimal. The models used in the offline approach are able to calculate the cutting forces, chatter lobes, energy consumption and surface quality [4, 8, 9].

D'Addona and Teti [10] presented a cutting parameter optimization framework based on Genetic Algorithms. The objective of their framework was the minimization of the production time of turned parts. In the framework a series of mathematical models were used to predict the production time, cutting forces and tool wear during the cutting process. Guo et al. [11] studied the same subject focusing on finish turning, optimizing the cutting conditions for achieving a given surface roughness with the minimum energy consumption. A Genetic Algorithm framework for minimizing the surface roughness in end milling by selecting the optimal cutting conditions was presented by Zain et al. [12]. Hanafi et al. [13] studied the optimal cutting conditions in turning of PEEK-CF30 focusing on surface roughness and energy consumption by using grey relational theory and Taguchi optimization method. The same method was used by Sivasakthivel et al. [14] for calculating the optimal parameters in milling. The main goal of that optimization was the reduction of the amplitude of the vibrations in order to reduce tool wear and surface roughness.

Campatelli et al. [15] studied the effect of cutting conditions on the energy consumption during milling of carbon steel, producing maps for the selection of cutting conditions that minimize the specific energy during milling. In their research Rajemi et al. [16] and Mativenga and Rajemi [17] studied the optimization of cutting conditions while taking into consideration the energy consumption in turning. The optimization was based on a series of mathematical relations describing the energy consumption and tool wear.

Reduction of the impact of machining on the environment was the main subject of many of the optimization papers presented above. In addition to the optimization of the cutting parameters to reduce the energy consumption, researchers have studied the use of vegetable oil based coolant for milling [18].

A series of researchers have also studied the modelling of the energy consumption during the cutting process in order to predict cutting characteristics. Lee et al. [19] presented a model for milling machines that is able to predict the surface quality as well as the cutting forces during the cutting process taking into consideration the dynamics of the process. Their system was based on a state-space model that was able to simulate the feed drive, spindle as well as the cutter dynamics and was

verified using three case studies of peripheral 2D milling. Effective strategies for reducing energy consumption in milling and drilling were presented by Mori et al. [20]. The recommendations included proposals on the cutting conditions, adaptive peck drilling cycles and the synchronization of spindle acceleration/deceleration with the feed system. Modelling of the energy required for machining was studied by Balogun and Mativenga [21] who classified the energy consumption into three categories: the start-up, the cutting energy and the ready state, which is the energy required to bring the cutting tool and workpiece to an about to cut state. In following research Balogun and Mativenga [22] investigated the effect of un-deformed chip thickness in the specific energy coefficient for three materials. Aramcharoen and Mativenga [23] presented a model for the energy consumption of milling machines which was used in the evaluation of the energy demand of different toolpath strategies.

2.2   On-Line Optimization

In contrast to offline optimization, on-line optimization determines the optimal processing parameters during the machining of the workpiece. The cutting process is monitored using sensors measuring e.g. cutting forces, vibration, acoustic emissions and power consumption. The cutting parameters are adjusted during the cutting process in order to reach predefined targets. The objective functions considered during the optimization included the maximization of production rate, elimination of chatter vibrations and surface roughness control. One of the first to achieve this was Altintas [24] who designed an adaptive controller for end milling. This approach was followed by Denkena and Floter [25] and Kakinuma et al. [26]. Soft computing approaches were also proposed using Neural Networks [27, 30] and Fuzzy Logic [28, 29]. Ko and Kim [31] presented an on-line optimization framework based on a Genetic Algorithm and Neural Networks for turning. Their framework optimized the process by adapting the cutting feed and speed and included a series of constraints for limiting the cutting force, spindle motor current, and acceleration. In industrial environments the application of online strategies has found limited adoption. The reluctance of adopters in these technologies can be attributed to many reasons. The limited IT infrastructure on smaller workshops, the variability in input conditions as well as the cost and reliability of the sensor systems and controllers are amongst some of the reasons limiting the wider spread adoption of online optimization solutions [32, 33]. Smart manufacturing initiatives across the world are actively trying to overcome these hurdles and establish improved sensing and control capabilities on production equipment.

2.3   *Multi-objective Optimization*

The problem of optimizing machining parameters is inherently multi-objective. Multi-objective optimization procedures typically develop a set of trade-off solutions between several objectives. A popular approach to solving multi-objective optimization problems are Evolutionary Algorithms (EAs). Multi-Objective Evolutionary Algorithms (MOEAs) are general-purpose optimization algorithms capable of producing the entire set of solutions to the problem (the Pareto front) simultaneously and in a single optimization run. They are based on Darwin's hypothesis that life forms adapt to their environment by a process known as natural selection [34]. MOEAs evolve a set of alternative solutions to a problem, termed as population. Because the solutions themselves are stochastically distributed, the algorithm is inherently robust to noise. Likewise, the population concept allows the algorithm to be scaled up or down for tasks of different complexity and improve its performance by means of parallel execution [35, 36].

MOEAs are problem-agnostic, i.e., they can be applied to a wide range of optimization problems including problems that are difficult to understand and fully formalize. Because the algorithm develops a Pareto-optimal front instead of a single solution, a practitioner is not required to rank or compare different objectives prior to the optimization run [37].

Evolutionary approaches contain a number of properties that are especially useful in optimization of dynamic problems. Intermediate solutions can be obtained from the population at any stage of the optimization run, therefore enabling continuous process control. With slight modifications to existing state-of-the-art evolutionary algorithms, they can adapt to changes in the environment, continuously tracking moving optima [38]. One particularly interesting feature is that an unfeasible solution can potentially be evolved into a good one after a number of generations. Storing previously fit solutions often leads to an increase in performance for problems with cyclic optima transitions, whereby the position of the moving optimum repeatedly visits previous locations [39]. Dynamic multi-objective optimization is still a new and relatively undeveloped research area. Some early works include formulation of test problems in [40], swarm guidance using multi-objective co-evolutionary on-line algorithm [41] and another set of optimization test problems and a study of dynamic multi-objective optimal control problem, in which a PID controller is being optimized on-line [42]. Following these studies, a number of better performing algorithms, which included elitism and clustering were proposed, such as D-QMOO [43] and DNSGA-II [38]. A dynamic multi-objective evolutionary algorithm based on decomposition and focused on improved tracking of changes in environment and guiding parts of population to evolve in different directions was presented in [44]. A comprehensive review of the related work in the area is outlined in [45]. Examples of the most recent publications show a diverse range of research interests. A number of studies improve an algorithm's response to change, e.g., by adaptive diversity introduction [46] or by storing fit solutions from previously visited states and reusing them when necessary [47]. Zhang et al. have developed a co-evolutionary algorithm based on ecological

strategy [48]. The research also continues on more challenging test problems [49], where the authors additionally presented a multi-objective EA which was based on decomposition (MOEA/D).

The numerous advantages of evolutionary algorithms and their relative ease of implementation make MOEA a dominant approach in the field of multi-objective optimization, with a multitude of published research works, algorithms and wide range of applications [50].

Dynamic MOEA (DMOEA) has been used in on-line control of dynamic systems. Deb et al. [51] use a Non-dominated Sorting Genetic Algorithm II (NSGA-II) algorithm to control a hydro-thermal power plant. Hughes et al. [52] use Differential Evolution (DE) to control a swarm of cooperating missiles against multiple targets [53]. In manufacturing, MOEA were used mostly for offline optimization [54–56] owing to perceived performance and implementation complexity issues of DMOEAs. A rare example of DMOEA applied for on-line optimization for machining of gradient materials is presented in [57].

In the field of Cloud technologies a series of papers have been presented describing the benefits of using such technologies. Wang et al. [58] presented a system for process planning, operation planning and control of manufacturing equipment based on IEC 61499 standard Function Blocks [59]. The main structure of Function Blocks consists of a set of input events, data variables as well as a set of outputs. The internal structure of the Function Blocks consists of a set of algorithms that are triggered through an execution control chart according to the events inputs. This technology can be used in order to bypass the G-code generation and communicate directly with the CNC controller on-board of the CNC machine. The inherent networking capabilities of Function Blocks make them ideal for the use in a web based manufacturing environment.

This research presents a framework for on-line on-board optimization of cutting parameters in milling, using multiple optimization criteria based on Function Blocks. In order to realize the above, the proposed framework uses an Evolutionary Multi-Objective Model Predictive Control (EMO MPC) approach, which consists of an on-line multi-objective evolutionary optimization algorithm (MOEA) and a dynamic multi-criteria decision maker (MCDM). EMO MPC is capable of continuously tracking the trade-off surface between multiple objectives while continuously producing a control action from a set of optimal solutions following a supplied preference vector. While the MPC-based algorithms are commonly associated with slow-paced processes, this approach has been shown to work successfully when applied to problems that require a fast decision making algorithm to respond and adequately control the dynamic process, such as an inverted pendulum [60, 61].

The originality of the proposed system lies in the fact that EMO MPC runs in tandem with the controller software and uses multiple objectives to plan the control strategy. The system is also supported by mathematical simulation models that are used to provide feedback regarding the cutting process for the case these inputs are not available.

3   On-Board Optimization Framework

The proposed system uses an on-board optimization algorithm to select the optimal cutting conditions during machining. The architecture of the system is shown in Fig. 1. A commercial industrial CNC controller Beckhoff TwinCAT® V3.1 [62] has been employed as a base for the development. Beckhoff CNC controllers are Windows based platforms and provide a corresponding software development platform which is integrated into Microsoft Visual Studio 2012. The Beckhoff platform is ready-to-run and applicable to a vast variety of machine tools. This platform is also able to emulate industrial CNC machines which can be tuned to the exact specifications of the machine tool and thus provide a platform for very close-to-real software development. The proposed system was developed using the Beckhoff TwinCAT® platform as an integral basis, i.e. all modules were embedded in the controller core or Function Blocks. All components are connected via an Ethernet bus embedded in the controller. Utilizing these advantages of TwinCAT®, the proposed system can run both, in simulation mode as well as on milling machines—in the following called "real mode".

In the simulation mode the input needed for the on-board optimization module are calculated from a simulation model, which is presented later in this paper. This model is based on mathematical relations and can provide high accuracy parameter estimations in high sampling rates. In real mode, the required values are collected from embedded and external sensors and processed on-line, i.e. without any significant time delay.
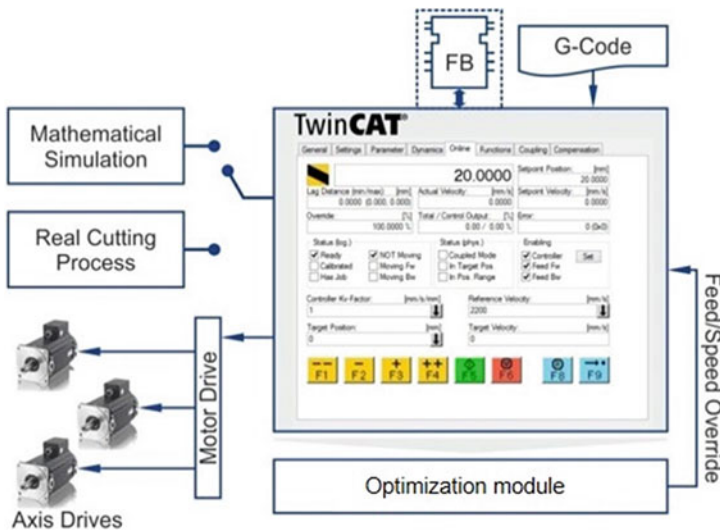

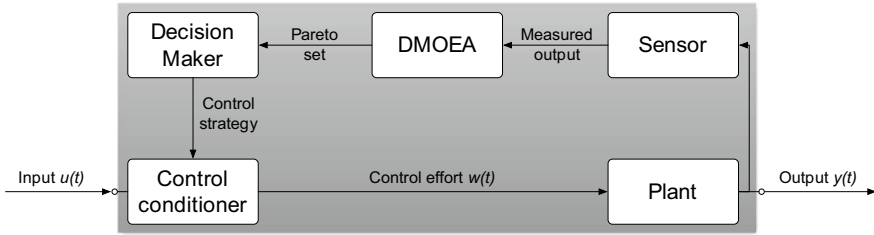**Fig. 1** On-board optimization scheme

Fig. 2 Evolutionary multi-objective model predictive control

The overall system is composed of the CNC controller which is connected to a series of modules including the optimization module, the motor drives and the mathematical simulation or the real cutting data. The process starts with the execution of the machining commands orchestrated by the TwinCAT® environment. These commands can come from either plain G-code or from Function Blocks running on-line directly on CNC machine controllers. The proposed implementation of IEC Function Blocks running on machine controllers is a practical extension of any Cloud Manufacturing platform.

The controller parameters affecting the cutting process such as position of the axes, the current feed and speed override as well as the sensory input regarding the power consumption are read by the EMO MPC algorithm and are used to provide the optimized cutting feed and speed to the controller. The EMO MPC has to operate in real time mode, i.e., it has to provide the next control action within a fixed period of time. This is achieved by measuring the time that is required for a single generation of the optimizer (DMOEA in Fig. 2) and budgeting the remaining time before the next deadline making allowance for the time required by the decision maker. In the simulation mode the optimized results are returned back into the emulator while in real mode it is fed back into the on-board controller hardware. As the proposed system uses an industrial CNC controller, it can be installed and operated through the Machine-User Interface of CNC machines—a fact that makes it ideal for real-world industrial applications. The system does not require an external PC connection, which minimizes the disturbance in the shop floor. This helps with the long-term utilization of the system.

4   Evolutionary Multi-objective Model Predictive Control

In on-line systems optimization one of the main challenges is to avoid areas in the control space that have undesired properties, such as chatter or excessive tool wear, while trying to move towards areas with more preferable properties, such as low cutting forces, high production rates and large material removal rates. In the proposed system the objective is the minimization of cutting forces and time which in nature are conflicting objectives while altering the feed override value.

The proposed optimization approach presents an extension to classic Model Predictive Control by replacing MPC cost functions with a dynamic multi-objective evolutionary optimization algorithm and an a posteriori decision maker to select a Pareto-optimal control action. In contrast to traditional controllers such as PID or H∞, a MOEA-based controller produces optimal solutions even for nonlinear, uncertain and varying problems, while its population-based nature offers a level of tolerance against measurement and process noise [39, 52]. MOEA use an internal plant model to predict plant changes over a fixed prediction horizon. As the choice between optimal solutions is made a posteriori, a more informed decision can be made, unlike a priori decision making, whereby only a narrow portion of the search space is considered.

The MOEA has an internal plant model to evaluate the solution fitness by examining a series of technological constraints such as the maximum permissible force on the system and the acceleration. Referring to Fig. 2, the measured output from the sensor is used by the dynamic MOEA to continuously track the optimal control surface for the plant. A dynamic decision maker is used at regular intervals to select a control strategy from the set of Pareto-optimal solutions. The Pareto-optimal control strategy is used by the control conditioner to generate the control effort w(t).

The control conditioner is designed to address the mismatch between relatively long MOEA iteration times and fast response required by the plant, herein the CNC machine, which is typically faster that 10 ms. Referring to Fig. 3, the DMOEA continuously tracks moving optima and selects a control strategy at δC intervals. The control conditioner decodes the control strategy at interval δA, δA ≤ δC, which matches the requirements of the plant. In the present study, a constant control conditioner is used that keeps its output constant throughout the control interval. Other control conditioning strategies such as linear and B-spline [63] are further options but were not implemented in the current solution. Having a control conditioner allows
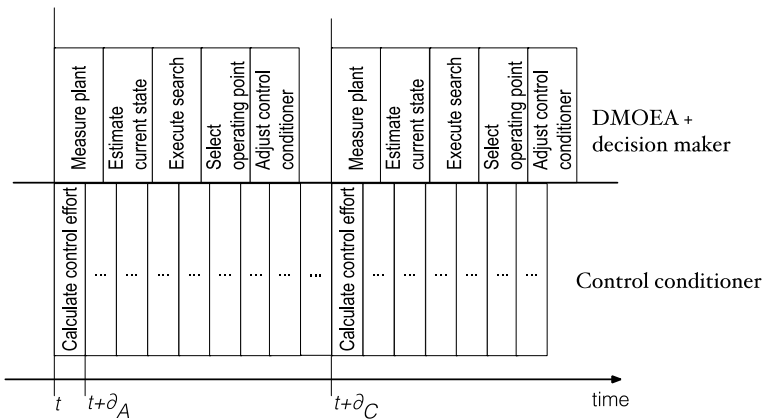

Fig. 3 Timing diagram of EMO MPC. Main loop (sensing, DMOEA and decision maker) at the top, control conditioner at the bottom

creating control intervals that are long enough for dynamic MOEA to maintain high convergence and at the same time outputting control actions at high frequencies.

Typical off-the-shelf MOEA, such as the well-known and well-tested NSGA-II [51], which was used as a basis in this study, require modification to handle dynamic problems. In particular, the fitness of elite individuals becomes more uncertain over time. To address this, a test of a random sample from the solution space is performed before every generation. If any of the objective values or the constraints changed, a change in the problem is assumed and all parent solutions are re-evaluated before the next selection proceeds. This approach allows generating offspring solutions from the population according to the current state of the problem and updating the Pareto-solutions simultaneously.

To select a control action (P) on-line from the Pareto-optimal set, in this study a weighted sum model (Eq. 2) decision maker is used, which aggregates a number of objectives into a scalar value using a weight vector. This model is the most widely used aggregation technique owing to its intuitive interpretation and low computational overhead.

$$P(\alpha_1, \alpha_2, \omega_1, \omega_2) = \alpha_1 \omega_1 + \alpha_2 \omega_2 \tag{1}$$

where ω_1 and ω_2 are weights from the interval [0,1] and α_1 and α_2 are real values from the MOEA—in Eq. 1 these are values from a two-dimensional objective space as used in this study (feedrate and cutting power).

5 Milling Model

Cutting process simulation and cutting force prediction has been a subject of numerous studies in literature [4]. The kinematics of milling are well known and consist of one rotation which is the primary cutting motion and one translation parallel to the surface being machined which is the primary feed motion. In order to evaluate and support the optimization algorithm, a model of the physical system had to be constructed. For this model, only inserted cutters were considered but the model can be extended to solid cutting tools as well. Figure 4 presents the cutting force calculation outline.

The developed model is based on the well-known equations of Kienzle and Victor [64] (Eq. 2) for predicting the cutting forces according to the non-deformed chip area.

$$F_i(\varphi) = K_i \cdot b \cdot h^{1-m} \forall i \in \{r, s, v\} \tag{2}$$

where Kr, Ks, Kv and m are the specific cutting resistances of the material, b is the width and h is thickness of the non-deformed chip.

For estimating the cutting forces on every cutting edge, the above-mentioned values must be calculated. The estimation of the cutting force for a given angular
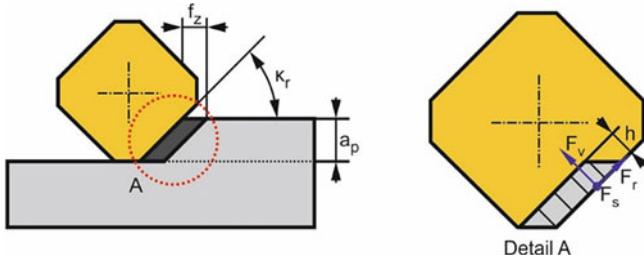
Fig. 4 Cutting force calculation outline

position (φ) of the cutter begins with the discretization of the cutting edge into segments, as presented in Fig. 4, in order to increase the accuracy of the model.

This process is repeated for every cutting edge of the cutter. Cutting forces for each individual cutting edge are summed up and transformed into the global coordinate system. The cutting force model was validated (Fig. 5) with the aid of experimental data from the literature [65].

The cutting force model was used to calculate the power required for the process using (Eq. 3) following Altintas et al. [4],

$$\text{Power}(\varphi) = F_t(\varphi) \cdot D \cdot \pi \cdot n \big/ 60 \cdot 10^{-3} \text{in [W]}, \tag{3}$$

where $F_t(\varphi)$ is the tangential component of the cutting force, D the cutter diameter and n is the programmed spindle speed.

The milling model—called plant module in Fig. 2– serves the calculations of the power as one of the objectives in the EMO MPC. The second objective considered is the machining time. The model, the optimizer and the sensor module are all running on-board the TwinCAT® controller.

Fig. 5 Cutting force validation

6 Application Scenario

The system was deployed on a PC workstation with a three-axis milling machine configuration running the TwinCAT® controller environment. The controller was setup to a cycle time of 2 ms, while the sampling of the physical system wa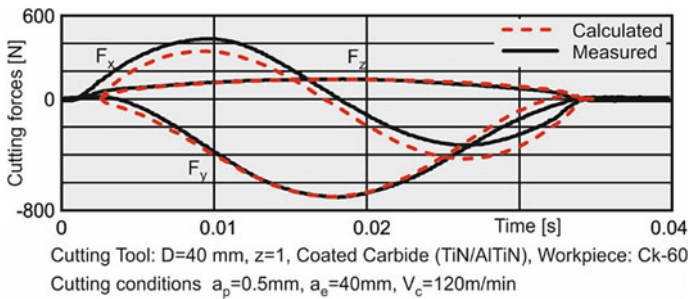s executed every millisecond. The dynamic characteristics of the axes such as the acceleration, deceleration and jerk were also set in the controller to values that are found in modern CNC machines [66] thus replicating a realistic application scenario.

In order to examine the robustness and stability of the proposed approach, a case study has been constructed with a part geometry highlighting the characteristics of the approach. The case study combines sudden as well as smooth changes in the shape of the cut surface. The stock geometry as well as the process parameters are presented in Fig. 6.

The system was run in simulation mode for a Ck-60 carbon steel workpiece using an inserted cutting tool. The TwinCAT® controller environment was used to realistically emulate the machining process. The results regarding the response of the system are shown in Fig. 7.

The EMO MPC optimizer, which is implemented in Java with parts from the jMetal library [67], adapts the cutting feed (velocity) according to the changes in the geometry of the part in a smooth way without creating large values of acceleration and deceleration (see Fig. 7). After the initial start of the drive, the algorithm speeds up the drive during the first part of the toolpath where no material is machined (area 1 on Fig. 7). When the tool enters the cut (area 2), the drive decelerates to a lower speed level to prevent damage of the cutting tool. There it remains steady until the start of the ramp in the geometry is reached (area 3). There the drive gradually gains speed due to the reduction of the depth of cut thus minimizing cutting time. The speed of the drive during this stage reaches the maximum permissible value. When the tool reaches the upward ramp, the tool is again gradually decelerated. The machining of

Workpiece: Ck-60
Cutting Tool :D=40 mm, z=3, Coated Carbide (TiN/AlTiN)
Cutting conditions : a_p=1-3mm, a_e=30mm, V_c=120m/min, f_z=0.1mm/rev tooth
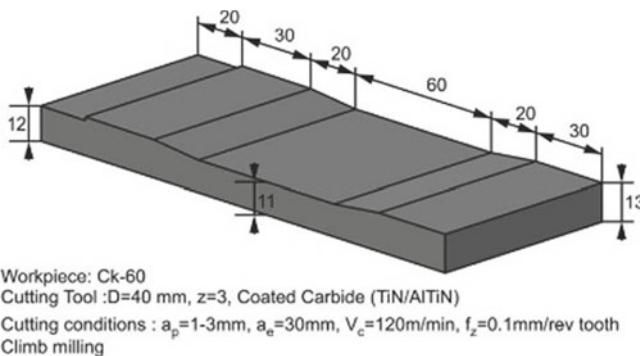Climb milling

Fig. 6 Case study showing stock geometry and process parameters; the cut was performed along the length of the material (front right to left back in this figure) with a constant depth of cut
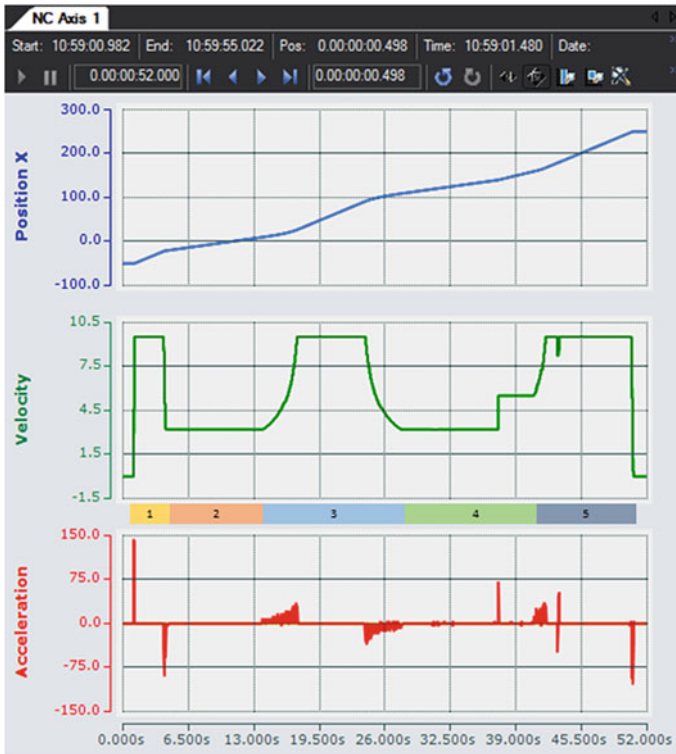
Fig. 7 Optimal control strategy (screenshot from the TwinCAT® control process environment; position x of the cutting head in [mm], velocity in [mm/s] and acceleration in [mm/s^2])

the part finishes with the step in the geometry (area 4) followed by the exit of the cutting tool from the part (area 5).

Figure 8 shows the required power consumed by the main spindle for constant feed and optimized feed. The proposed strategy minimizes the air-cut time as well as the overall machining time, while, in the same time it reduces the maximum required energy consumed by the main spindle.

The EMO MPC optimizer achieves a significant reduction in cutting time compared to the constant feed rate solution. In this case, study the cutting time is reduced by 7% whereas the overall machining time is reduced by 12% and the peak energy required is reduced up to 25%. By reducing the overall time of machining, a reduction of the overall power required by the machine is achieved since all the subsystems of the machine have to operate for a reduced amount of time. As Rajemi et al. [16] presented, the machining power only accounts for a third of the overall power consumption of the machine, so the reduction of the operational time of the peripheral systems, by reducing the machining time, could lead to substantial energy savings and promote a more sustainable solution in manufacturing. The employed EMO MPC optimizer offers by design solutions for a wide range of cutting conditions
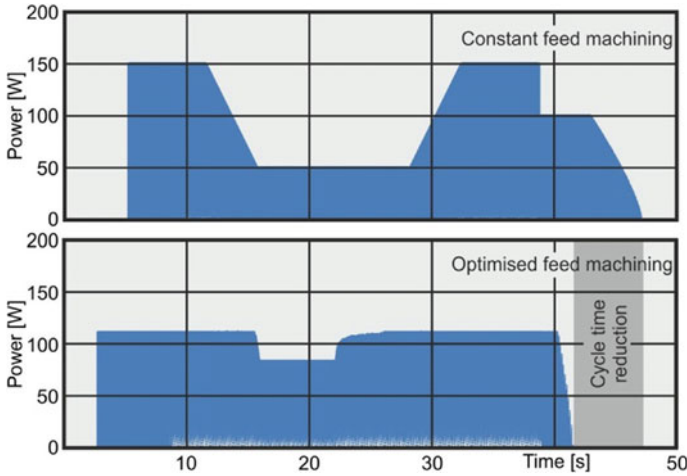
Fig. 8 Initial (top) and optimized required power (bottom)

without requiring any changes to the optimizer and thus being widely and robustly applicable.

7 Conclusions

This research introduces an on-board optimization system using a dynamic multi-objective optimization framework for on-line use in CNC machine tools. The proposed solution was embedded in a real industrial controller TwinCAT® and tested through a case study. The bi-objective problem, which considers time and power as most important factors, was determined in collaboration with industry. The developed system was embedded in a real controller and tested with realistic CNC parameter settings. The results show that the proposed framework can cope with the challenging tight real-time constraints of real-world controllers while providing constantly adapting optimal results. The proposed strategy minimizes the cutting time while—at the same time—being able of keeping the power required by the main spindle at a minimum. The proposed evolutionary on-line EMO MPC solution excels existing deterministic controller solutions in several aspects:

- It adapts automatically to dynamically changing environments that do not need to be programmed explicitly into a deterministic controller, hence being much easier to implement.
- Multiple new fitness functions can be adopted by the system without the need of changing the core optimization strategy.
- It adapts on-line and on-board the CNC machine controller hence not requiring complex wiring to external PCs.

- It uses latest state-of-the-art Function Block technology which allows adopting new Industry 4.0 standards that make CNC machines more intelligent and agile than before.

The system uses a multi-objective optimization algorithm which was embedded in the machine tool controller. Existing literature uses single objective approaches that are optimized in an on-line manner with devices outside the machine tool controller. The proposed system can optimize the process parameters for achieving sustainability at factory level. The system proposed in this research could be extended to gather information from other subsystems of the machine tool such as the drives of the axes, the coolant motors and the machine tool cabinet and use the information in order to make a well informed decision. Additional external sensors could also be considered as an addition to the system that could offer better insight on the machining process.

References

1. European Environment Agency (EEA), Final energy consumption by sector and fuel (CSI 027/ENER 016) 01 Jan 2015
2. Sharif Ullah AMM, Fuji A, Kubo A, Tamaki J (2014) Analyzing the sustainability of bimetallic components. Int J Autom Technol 8(5):745–753
3. Sharif Ullah AMM, Akamatsu T, Furuno M, Chowdhury MAK, Kubo A (2016) Strategies for developing milling tools from the viewpoint of sustainable manufacturing. Int J Autom Technol, 727–736
4. Altintas Y, Kersting P, Biermann D, Budak E, Denkena B, Lazoglu I (2014) Virtual process systems for part machining operations. Annals CIRP 63(2):585–605. https://doi.org/10.1016/j.cirp.2014.05.007
5. Wang L, Adamson G, Holm M, Moore P (2012) A review of function blocks for process planning and control of manufacturing equipment. J Manufact Syst 31(3):269–279. https://doi.org/10.1016/j.jmsy.2012.02.004
6. Li W, Mehnen J (2013) Cloud manufacturing: distributed computing technologies for global and sustainable manufacturing. Springer, UK
7. Follett J (2014) Designing for emerging technologies: UX for genomics, robotics, and the internet of things. O'Reilly Media
8. Erkorkmaz K, Layegh S, Lazoglu I, Erdim H (2013) Feedrate optimization for freeform milling considering constraints from the feed drive system and process mechanics. Annals CIRP 62(1):395–398. https://doi.org/10.1016/j.cirp.2013.03.084
9. Shamoto E, Fujimaki S, Sencer B, Suzuki N, Kato T, Hino R (2012) A novel tool path/posture optimization concept to avoid chatter vibration in machining—proposed concept and its verification in turning. Annals CIRP 61(1):331–334. https://doi.org/10.1016/j.cirp.2012.03.133
10. D'Addona DM, Teti R (2013) Genetic algorithm-based optimization of cutting parameters in turning processes. Procedia CIRP 7:323–328. https://doi.org/10.1016/j.procir.2013.05.055
11. Guo Y, Loenders J, Duflou J, Lauwers B (2012) Optimization of energy consumption and surface quality in finish turning. Procedia CIRP 1:512–517. https://doi.org/10.1016/j.procir.2012.04.091
12. Zain AM, Haron H, Sharif S (2010) Application of GA to optimize cutting conditions for minimizing surface roughness in end milling machining process. Expert Syst Appl 37(6):4650–4659. https://doi.org/10.1016/j.eswa.2009.12.043
13. Hanafi I, Khamlichi A, Cabrera FM, Almansa E, Jabbouri A (2012) Optimization of cutting conditions for sustainable machining of PEEK-CF30 using TiN tools. J Clean Prod 33:1–9. https://doi.org/10.1016/j.jclepro.2012.05.005

14. Sivasakthivel PS, Sudhakaran R, Rajeswari S (2013) Optimization of machining parameters to minimize vibration amplitude while machining Al 6063 using gray-based Taguchi method. Proc IMechE Part B: J Eng Manufact 227(12):1788–1799. https://doi.org/10.1177/095440541 3494921

15. Campatelli G, Lorenzini L, Scippa A (2014) Optimization of process parameters using a Response Surface Method for minimizing power consumption in the milling of carbon steel. J Clean Prod 66:309–316. https://doi.org/10.1016/j.jclepro.2013.10.025

16. Rajemi MF, Mativenga PT, Aramcharoen A (2010) Sustainable machining: selection of optimum turning conditions based on minimum energy considerations. J Clean Prod 18:1059–1065. https://doi.org/10.1016/j.jclepro.2010.01.025

17. Mativenga PT, Rajemi MF (2011) Calculation of optimum cutting parameters based on minimum energy footprint. Annals CIRP 60(1):149–152. https://doi.org/10.1016/j.cirp.2011.03.088

18. Kuram E, Ozcelik B, Bayramoglu M, Demirbas E, Simsek BT (2013) Optimization of cutting fluids and cutting parameters during end milling by using D-optimal design of experiments. J Clean Prod 42:159–166. https://doi.org/10.1016/j.jclepro.2012.11.003

19. Lee CH, Yang MY, Oh CW, Gim TW, Ha JY (2015) An integrated prediction model including the cutting process for virtual product development of machine tools. Int J Mach Tools Manuf 90:29–43. https://doi.org/10.1016/j.ijmachtools.2014.12.003

20. Mori M, Fujishima M, Inamasu Y, Oda Y (2011) A study on energy efficiency improvement for machine tools. Annals of the CIRP 60(1):145–148. https://doi.org/10.1016/j.cirp.2011.03.099

21. Balogun VA, Mativenga PT (2013) Modelling of direct energy requirements in mechanical machining processes. J Clean Prod 41:179–186. https://doi.org/10.1016/j.jclepro.2012.10.015

22. Balogun VA, Mativenga PT (2014) Impact of un-deformed chip thickness on specific energy in mechanical machining processes. J Clean Prod 69:260–268. https://doi.org/10.1016/j.jclepro.2014.01.036

23. Aramcharoen A, Mativenga PT (2014) Critical factors in energy demand modelling for CNC milling and impact of toolpath strategy. J Clean Prod 78:63–74. https://doi.org/10.1016/j.jclepro.2014.04.065

24. Altintas Y (1994) Direct adaptive control of end milling process. Int J Mach Tools Manuf 33(4):461–472. https://doi.org/10.1016/0890-6955(94)90078-7

25. Denkena B, Flöter F (2012) Adaptive cutting force control on a milling machine with hybrid axis configuration. Procedia CIRP 4:109–114. https://doi.org/10.1016/j.procir.2012.10.020

26. Kakinuma Y, Enomoto K, Hirano T, Ohnishi K (2014) Active chatter suppression in turning by band-limited force control. Annals CIRP 63(1):365–368. https://doi.org/10.1016/j.cirp.2014.03.136

27. Zuperl U, Cus F, Reibenschuh M (2011) Neural control strategy of constant cutting force system in end milling. Robotics Comput-Integrated Manuf 27(3):485–493. https://doi.org/10.1016/j.rcim.2010.10.001

28. Yang DL, Chen JC, Chow HM, Lin CT (2006) Fuzzy-nets-based in-process surface roughness adaptive control system in end-milling operations. Int J Adv Manuf Technol 28:236–248. https://doi.org/10.1007/s00170-004-2361-7

29. Kim D, Jeon D (2011) Fuzzy-logic control of cutting forces in CNC milling processes using motor currents as indirect force sensors. Precision Eng 35(1):143–152. https://doi.org/10.1016/j.precisioneng.2010.09.001

30. Zuperl U, Kiker E, Jezernik K (2006) Adaptive force control in high-speed machining by using a system of neural networks. IEEE Int Symp Ind Electron 1:148–153. https://doi.org/10.1109/ISIE.2006.295583

31. Ko TJ, Kim HS (1998) Autonomous cutting parameter regulation using adaptive modeling and genetic algorithms. Precis Eng 22(4):243–251. https://doi.org/10.1016/S0141-6359(98)000 19-1

32. Ghosh, AK, Sharif Ullah, AMM, Kubo, A, Akamatsu, T, D'Addona, DM (2020) Machining phenomenon twin construction for industry 4.0: A case of surface roughness. J Manuf Mater Process 4(1), 4010011

33. Sharif Ullah AMM (2019) Modeling and simulation of complex manufacturing phenomena using sensor signals from the perspective of Industry 4.0. Adv Eng Inform 39:1–13

34. Darwin CR (1872) The origin of species by means of natural selection, or the preservation of favoured races in the struggle for life. London: John Murray. 6th edition; with additions and corrections

35. Coello CAC, Lamont GB, Veldhuizen DAV (2007) Evolutionary algorithms for solving multi-objective problems. Springer

36. Camara M, Ortega J, Toro F J (2007) Parallel processing for multi-objective optimization in dynamic environments. IEEE International Parallel and Distributed Processing Symposium 243, 26–30 March 2007, Long Beach, CA, 1–8. https://doi.org/10.1109/ipdps.2007.370433

37. Konak A, Coit DW, Smith AE (2006) Multi-objective optimization using genetic algorithms: a tutorial. Reliab Eng Syst Safety 91(9):992–1007. https://doi.org/10.1016/j.ress.2005.11.018

38. Deb K, Udaya Bhaskara Rao N, Karthik S (2006) Dynamic multi-objective optimization and decision-making using modified NSGA-II: a case study on hydro-thermal power scheduling. EMO, 803–817

39. Jin Y, Branke J (2005) Evolutionary optimization in uncertain environments—a survey. Evolut Comput IEEE Trans 9(3):303–317. https://doi.org/10.1109/TEVC.2005.846356

40. Jin Y, Sendhoff B (2004) Constructing dynamic test problems using the multiobjective optimization concept. Applications of evolutionary computing, Vol. 3005 of Lecture Notes in Computer Science, Coimbra, Portugal, April 2004, 525–536

41. Hughes EJ (2004) Swarm guidance using a multi-objective co-evolutionary on-line evolutionary algorithm. Congress on Evolutionary computation 2004, cec2004, 2:2357–2363

42. Farina M, Deb K, Amato P (2004) Dynamic multiobjective optimization problems: test cases, approximations, and applications. IEEE Trans Evol Comput 8(5):425–442. https://doi.org/10.1109/TEVC.2004.831456

43. Hatzakis I, Wallace D (2006) Dynamic multi-objective optimization with evolutionary algorithms: a forward-looking approach. Proc of genetic and evolutionary computation conference (GECCO 2006), 12011208

44. Zhang Z, Qian S, Tu X (2010) Dynamic clonal selection algorithm solving constrained multi-objective problems in dynamic environments. Inst Syst Sci Inf Technol Guizhou Univ 6:2861–2865

45. Liu M, Zeng W, Zhao J (2011) An overview of dynamic evolutionary multi-objective optimization. Int Rev Comput Software 6(5):692–699

46. Liu M, Zheng J, Wang J, Liu Y, Jiang L (2014) An adaptive diversity introduction method for dynamic evolutionary multiobjective optimization, 3160–3167

47. Liu M, Zeng W (2013) Memory enhanced dynamic multi-objective evolutionary algorithm based on decomposition. Ruan Jian Xue Bao/J Software 24(7):1571–1588

48. Zhang S, Li Z, Chen S, Li R (2014) Dynamic multi-objective optimization algorithm based on ecological strategy. Jisuanji Yanjiu yu Fazhan/Comput Res Develop 51(6):1313–1330

49. Biswas S, Das S, Suganthan PN, Coello CAC (2014) Evolutionary multiobjective optimization in dynamic environments: a set of novel benchmark functions. Proceedings of the 2014 IEEE congress on evolutionary computation, CEC 2014:3192–3199

50. Coello CAC, EMOO repository, http://neo.lcc.uma.es/emoo/. Accessed 03/03/2017

51. Deb K, Pratap A, Agarwal S, Meyarivan T (2002) A fast and elitist multiobjective genetic algorithm: NSGA-II. IEEE Trans Evol Comput 6(2):182–197. https://doi.org/10.1109/4235.996017

52. Hughes EJ, Zbikowski R, Tsourdos A, White BA (2005) On-line evolutionary algorithm swarm trajectory optimisation. Technical report DAPS/EJH/114/2005, Cranfield University

53. Peng X, Xu D, Zhang F (2011) UAV online path planning based on dynamic multiobjective evolutionary algorithm. 30th Chinese Control Conference (CCC). 22–24 July 2011, Yantai, IEEE, 5424–5429

54. Wang L, Ng AHC, Deb K (2011) Multi-objective evolutionary optimisation for product design and manufacturing. Springer Publishing Company, Incorporated

55. Yusup N, Zain AM, Hashim SZM (2012) Evolutionary techniques in optimizing machining parameters: review and recent applications (2007–2011). Expert Syst Appl 39(10):9909–9927. https://doi.org/10.1016/j.eswa.2012.02.109
56. Davim JP, Davim JP (2012) Computational methods for optimizing manufacturing technology: models and techniques. IGI Global, Hershey, PA, USA, 1St edition
57. Roy R, Mehnen J (2008) Dynamic multi-objective optimisation for machining gradient materials. CIRP Ann Manuf Technol 57:429–432. https://doi.org/10.1016/j.cirp.2008.03.020
58. Wang L (2013) Machine availability monitoring and machining process planning towards cloud manufacturing. CIRP J Manufact Sci Technol 6(4):263–273. https://doi.org/10.1016/j.cirpj.2013.07.001
59. Zoitl A (2009) Real-time execution for IEC 61499. ISA, USA
60. Findeisen R (2005) Nonlinear model predictive control: a sampled data feed- back perspective. PhD Thesis, Universität Stuttgart, Holzgartenstr. 16, 70174 Stuttgart
61. Mills A, Wills A, Ninness B (2009) Nonlinear model predictive control of an inverted pendulum. Proceedings of the 2009 conference on American Control Conference, ACC'09, IEEE Press, Piscataway, NJ, USA, 2335–2340
62. TwinCAT V3.1, Beckhoff Automation GmbH, http://www.beckhoff.com, Accessed 19 Jan 20
63. Butans J (2011) Addressing real-time control problems in complex environments using dynamic multi-objective evolutionary approaches, PhD Thesis, Cranfield University, UK
64. Kienzle O, Victor H (1957) Spezifische Schnittkraefte bei der Metallbearbeitung, Werkstattstechnik und Maschinenbau Bd. 47, H.5
65. Tapoglou N, Antoniadis A (2012) 3-Dimensional kinematics simulation of face milling. Measurement 45(6):1396–1405. https://doi.org/10.1016/j.measurement.2012.03.026
66. Mori Seiki Co. http://en.dmgmori.com, Accessed 19/01/20
67. Durillo JJ, Nebro AJ, Luna F, Dorronsoro B, Alba E (2006) jMetal: A java framework for developing multi-objective optimization metaheuristics. Technical Report ITI-2006–10, Departamento de Lenguajes y Ciencias de la Computación, University of Málaga, E.T.S.I. Informática, Campus de Teatinos

Modeling and Experimental Work on Electrical Discharge Machining

Panagiotis Karmiris-Obratański, Emmanouil L. Papazoglou, and Angelos P. Markopoulos

Abstract Electrical Discharge Machining (EDM) is a non-conventional machining process, widely utilized in the modern industrial environment, especially in applications that involve the manufacturing of complex shapes and geometries, along with high dimensional accuracy. Conceptually EDM is a simple process, which is based on the erosion that accompanies the spark occurrence between two electrically conductive materials, one that acts as working electrode and one as the workpiece. Nevertheless, in practice, and due to the technological advances in the relevant field, EDM has become a multi-parameter machining process. The current chapter aims to familiarize the reader with the process of EDM, while at the same time, to provide useful and practical information concerning more advanced topics. The chapter's first sections are an introduction to the EDM, where a brief historical review, and the basic working principles are presented. The basic physical mechanisms that take place during machining are analyzed, along with the major machining parameters and performance indexes. Moreover, a brief literature review concerning the machining of steel and aluminum alloys with EDM is quoted. Thereafter, the basic principles for modeling and simulation of the process are introduced, aiming to become a helpful reference in model development. Finally, in the last section, a comparative study regarding the machining of two different aluminum alloys (i.e., Al5052 and Al6063) with EDM is presented, indicating how different alloys of the same base may have different behavior during their machining with EDM.

P. Karmiris-Obratański · E. L. Papazoglou · A. P. Markopoulos (✉)
School of Mechanical Engineering - Laboratory of Manufacturing Technology,
National Technical University of Athens, Athens, Greece
e-mail: amark@mail.ntua.gr

P. Karmiris-Obratański
Faculty of Mechanical Engineering and Robotics - Department of Manufacturing Systems,
AGH University of Science and Technology, Cracow, Poland

19

1   A Brief History of EDM

Electrical discharge machining (EDM) is one of the most extensively used non-conventional machining processes, with many applications in the modern industrial environment. The main advantage of EDM is the capability of machining any electrically conductive material, regardless of its mechanical properties, e.g. strength and hardness, in complex geometries and with high dimensional accuracy. EDM finds a wide range of applications in the fields of die and mold manufacturing, aerospace, automotive industries, microelectronics, and biomedical engineering [1, 2]. The original idea of this process came during the eighteenth century when scientist Benjamin Franklin reported the erosion phenomenon of metal workpieces by electrical sparks [3]. About 70 years later the scientist Joseph Priestly discovered the erosive effect of electrical discharges.

A couple of Russian scientists, namely Dr Boris Lazarenko and his wife, Dr Natalia Lazarenko (Fig. 1) were asked to develop a solution for tungsten contact points in the military vehicles distributors to avoid erosion due to friction. At these contacts, occurred small discharges that affected the surface quality of the contact points, and small craters appeared due to the material erosion phenomenon. They discovered that mineral oils could make the sparks more predictable and uniform. These uniform sparks led to more uniform erosion phenomena on the tungsten surface, which was one of the hardest known material at these times. Immediately the Lazarenko couple realized the potential of their discovery, and they decided to create the first.

EDM prototype for industrial machining purposes, they also published their thesis entitled "Investigation of the Effect of Wear on Electric Power Contacts for Manufacturing Purposes" [4]. The following Fig. 1. shows the schematic structure of their EDM prototype which is similar schematic structure to the spark distribution unit.

At the early 1940s was invented the die-sinking EDM process with the advent of pulse generators planetary and orbital motion techniques, CNC and the adaptive control mechanism. So the EDM machine process was in commercial use in 1952 by the "Charmilles" industry which was presented for the first time as the European Machine Tool Exhibition in 1955 [5], and in 1972 "Agie" another company
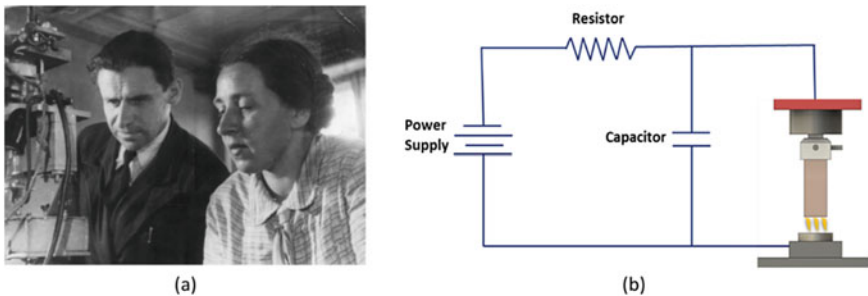

Fig. 1   On the left side **a** Dr. Boris and Dr. Natalia Lazarenko working on their EDM prototype, and on the right side **b** is the schematic representation of their machine

was invented the wire-ED machining process that included powerful generators, improved machine intelligence, better flushing solution and new wire electrodes [6]. "Seibu" developed the first CNC wire EDM machine in 1972 and the first system was manufactured in Japan. Kurafuii and Masuzawa in 1968 demonstrated the development of the first micro- EDM machining process when they drilled a minute hole in a 50 μm thick carbide plate.

2 Introduction and Basic Theory of EDM

The development of modern technology is determined in many respects by new materials difficult to process by conventional methods. Their commercialization and application in industrial conditions involve the development of appropriate machining technologies. One of the modern methods that makes it possible to shape conductive materials, regardless of their hardness, as well as the chemical composition, is electro erosive machining. An unconventional method of material removal, using the phenomenon of electric discharges occurring between two electrodes in the presence of a dielectric, allows obtaining geometrically complex shapes that are difficult to obtain by other methods. EDM machining is divided into two major types: die-sink EDM and the wire-cut EDM. The following Fig. 2 shows the two machine types. The principals are the same for the Die-Sink as well as for Wire EDM process with a small difference in the setup. As it has been mentioned above, EDM is a removable process for conductive materials by means of rapid repetitive spark discharges in the presence of dielectric liquid, while a voltage difference is applied between the electrode and workpiece.

Physical phenomena that occur during the material removal process in an erosion process are of a complex nature. As a result of the applied electrical voltage, in the presence of dielectric fluid (usually deionized water or hydrocarbon oil, which acts as an insulator and coolant) the electrode comes closer to the workpiece material. Upon the conductive workpiece, a column of intense electromagnetic flux is formed. The electrical field is the strongest (energy density of 10^{11}–10^{14} W/m^2) at the point where the distance between the electrode and workpiece is minimum. As the insulating effect of the dielectric fluid breaks down under high electric field, it causes a single spark to be discharged between the tool electrode and the workpiece. EDM utilizes the material erosion due to a spark, occurring between two electrodes, one of which is the workpiece, while both are immersed in the dielectric fluid. The intense electromagnetic flow forms a plasma channel, with plasma temperatures being in the range of 8000–12,000 °C. Part of the discharge energy is transformed into thermal energy, and a part of it is absorbed by the workpiece; as a result, an amount of material is melted and/or ablated. A portion of the molten and ablated material is being flushed away by the dielectric fluid, after the end of the current pulse, and the consequent breakdown of the plasma channel. A series of thousands or even millions of pulses and sparks per second result to the total material removal. This cycle is repeated many times during the machining process. The typical Material Removable Rate (MRR)
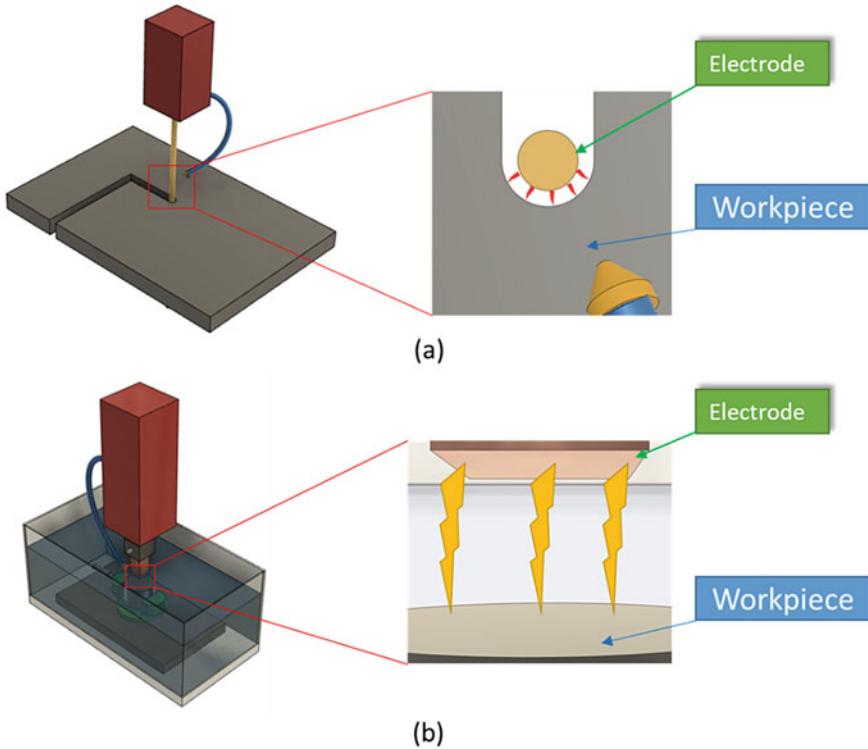
Electrode

Workpiece

(a)

Electrode

Workpiece

(b)

Fig. 2 Graphical representation of **a** Wire EDM and **b** Die-sink EDM

per discharge is in range of 10–6 to 10–4 mm^3, depending on the intensity of the specific application [7, 8]. Since the shaped electrode defines the area in which the spark erosion will occur, the accuracy of the part produced after EDM is fairly high.

In the case of Wire EDM (WEDM), uses a moving wire as a machining tool, whose diameter is between 0.02–0.5 mm to remove material. The workpiece geometry is obtained as a result of electrical dissipation between the wire electrode and the workpiece surface. The wire electrode moves along the programmed path, which allows cutting geometrically complex shapes. Depending on the required dimensions and dimensional accuracy and surface roughness of the cut elements, the treatment is carried out in several electrode passes along the programmed contour for cutting [9].

On the other hand, Die-Sink EDM the erosion mechanism occurs between the shape of the electrode and the workpiece; the geometry of the electrode is reproduced in the object with high accuracy. Modern electro-erosion machine tools are equipped with a numerical control system that enables the production of geometrically complex cavities or holes [10]. As a dielectric medium in die-sink EDM is used commonly hydrocarbon fluids, synthetic fluids or even vegetable oil-based fluids. The surface finish, as well as other parameters, relies on the dielectric decision of dielectric fluid [11].

3 Phases of Electrical Discharge

After 70 years of important applications of EDM in manufacturing processes, it is very difficult to present a complete and define model explaining in all the different processes that take place during one discharge. Makund et al. [12], presented the expanding-circle heat-source model that provides correct erosion curves and explains the low erosion rates. Almost one-decade, later Schumacher [13] tries to cover the gap between different authors and to create a new consensus base. The following Fig. 3 presents the faces of a single discharge pulse, namely:

1. The ignition phase.
2. Formation of the plasma channel.
3. Melting and evaporation of a small part of the workpiece material and the electrode.
4. Ejection of the liquid molten material.

The ignition phase

In the first stage of the process (Fig. 3a), there is a lack of current flux due to the resistance of the dielectric fluid. As the electrode comes closer to the workpiece material, the electric field is increased and occurs the primary emission of the cathode's
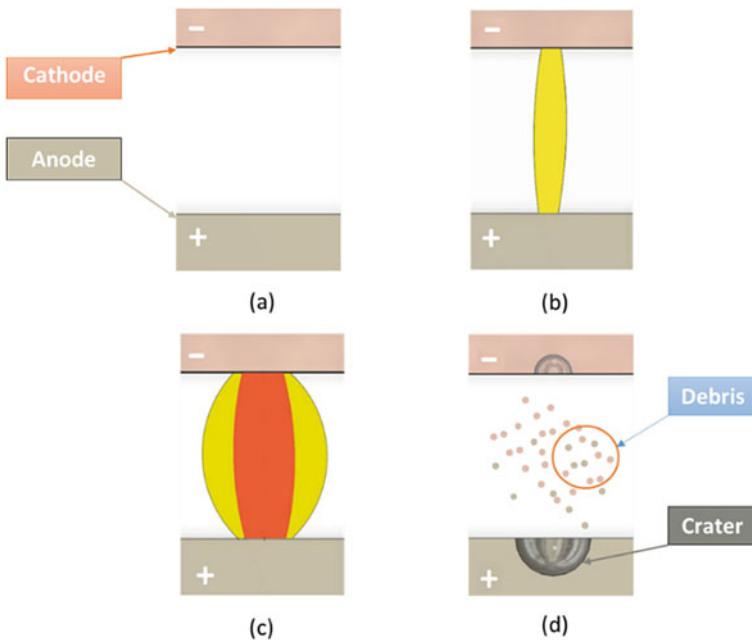

Fig. 3 Graphical presentation of the discharge phases: **a** ignition, **b** plasma formation, **c** plasma channel expand, **d** flashing

electrons. These electrons accelerate by the electric field in the directions of the anode and hit the molecules of the dielectric. Thus, generates secondary electrons and positive ions that move, respectively, to the anode and the cathode causing the ionization.

Formation of the plasma channel

During this phase, the positive ions created from the dielectric collide with the electrodes from the cathode. This process produces more electrons that they are attached to the anode and liberates more electrons. This genesis superheating followed by small evaporation of the dielectric. This causes a reduction of the resistance of the dielectric and increasing the electrical current, creating a discharge tunnel. The plasma channel is created and circled by a vapor bubble, which concentrates all the energy in that small volume. At this moment the open-circuit voltage drops rapidly to the break voltage of the dielectric.

Melting and vaporization of the electrode materials

At this stage, during the generated plasma channel, the increased plasma high energy melts both electrodes by thermal conduction and a portion of the electrode evaporates due to the high plasma pressure over the cathode and anode spots. The explanation of this phenomenon could be that both anode and cathode surfaces are affected by the emission of the electrons and positive ions. The kinetic energy is transformed into thermal energy as in both cases, the positive ions or the electrons hit the cathode or the anode, respectively. As it can be in Fig. 3d, the anode melts quicker than the cathode, due to lower mass of the electrons that collide with the anode compared to the positive ions.

Flushing of the melted material

During the pause period, when the EDM machine stops the current abruptly, the plasma channel collapses and the vapor bubble is formed, causing the superheated molten liquid material of the surfaces (electrode and workpiece) to explode into the dielectric. A part of the material flashes out by the dielectric into the surrounding, while another part resolidifies in the crater. The last part of the material is called "White Layer" (WL) or recast layer. In Fig. 4, the crater formation during a single spark on tool steel utilizing a copper electrode with straight polarity is depicted. A part of the evaporated material has been flushed away, while another part formed a recast layer.

4   Process Parameters—Performance Indexes

Due to the multiparametric nature of the EDM, the process parameters can be branched into two categories, i.e. non-electrical and electrical parameters. The most important electrical parameters that affect the discharge energy are the Pulse-On time (T_{on}), the Pulse-on current (I_p), the duty factor and the polarity. On the other
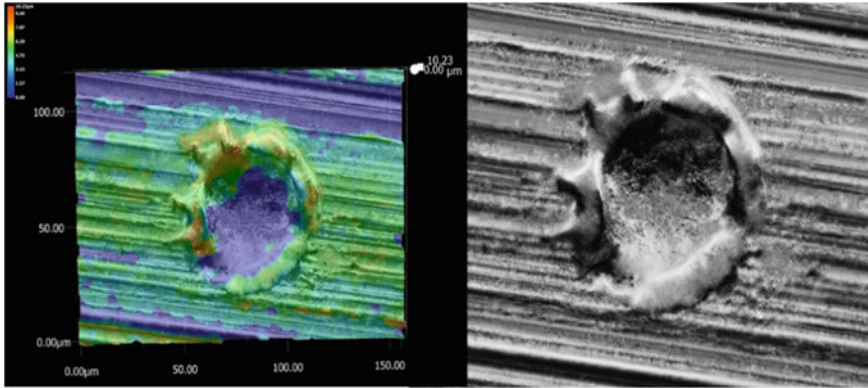
Fig. 4 Crater formation from a single spark experiment

hand, these parameters are strongly related to the process parameters criteria (non-electrical) such as the Material Removable Rate (MRR), Tool Wear Ration, and the Surface Roughness (SR) [14, 15].

The duration of a pulse (T_{on})

Is defined as the time during which there is a current flow between the electrode and the piece and consequently, the time period during which material expulsion is observed. The rate of material expulsion (MRR) is directly related with the machining parameters, especially with the pulse-on current and time, and the machining efficiency. Longer pulses result in a lower quality machined surface, as the craters formed are deeper and broader in diameter. For low roughness, the use of "shorter" pulses is recommended. Finally, the pulse duration of the pulses is related, to the processing speed and surface roughness, to the stability of the treatment.

The pulse interval (T_{off})

The time between the occurrence of two pulses is defined as Pulse-off time. During it, there is no current flow, no spark event. Nevertheless, it is essential, as it is the time during which the waste—products—are removed from the treatment zone. Choosing the right interval is an optimization between the stability and the speed of the processing (increasing the interval makes the processing slower, but at the same time helps to remove the waste, making it more stable more effectively). Typical prices are of the class of μs.

The Potential difference

The potential difference between the piece and the electrode during processing is an essential parameter. Higher values allow for a more significant gap between the electrode and the piece, which makes it easier to flush and remove waste, making processing more stable and increasing the MRR. At the same time, however, it results in treated surfaces with higher surface roughness and more significant electrode wear.

Material Removable Rate (MRR)

It is defined as the volume of material that is removed at a specified reference time. It is usually expressed in units [mm^3/min] and is calculated indirectly by the weight difference of the piece before and after processing. It is an indicator of the processing speed and is affected by the current intensity, the pulse and interval time, the "duty cycle", and the properties of the material to be processed.

Tool Wear Rate (TWR)

In the literature, the tool wear ratio (TWR) is also found as an electrode wear ratio (EWR) or Relative Electrode Wear (REW). There is no difference, and it is essentially the ratio of the volume of material removed from the electrode to the volume of material removed from the piece expressed as a percentage [%]. There are cases where the wear of the electrode on the "front surface" or in the corners, you measure independently in [mm] or [μm]. Nevertheless, the electrode wear ratio (TWR) continues to be the most accurate method of measuring—expressing the wear of the electrode during processing. Understandably, the wear of the electrode must be clearly lower than that of the piece. Low TWR values express more stable, more efficient and more economical treatments. The wear ratio depends directly on the processing conditions (current intensity, vacuum potential, pulse time), the properties of the materials (electrode and piece), but also the polarity used [16].

EDM in Steel Alloys

Steel and its alloys, was one of the first materials that were used experimentally in EDM due to their use, mainly in production dies and molds. Until 1990, the workpiece surface quality was exanimated only by stylus profilometers without considering any material transformation and damage in ultramicroscopic level [17]. As the microscopic technology developed, researchers were able to obtain three-dimensional images of the surface topography as well as to define the particle migration, micro and macrocracks. Haron, Deros and Fauziach [18] investigated the influence of the EDM parameters on an AISI 1045 tool steel. The experimental results show that the MRR and TWR were not depended on the size of the electrode, but it was near related to the current flow. An experimental investigation was conducted by Bleys et al. [19], on the surface and sub-surface properties of tool steel machined by EDM. They considered three types of EDM processes, namely die-sink EDM, WEDM and Milling EDM (MEDM) and they found that the developed of new generators or mixed powder dielectrics will reduce the surface damage. Soni and Chakraverti [20, 21], investigated the TWR, MRR, surface texture, and the dimensional accuracy of steel alloys machined by EDM.

Several researchers [22–30] tried to improve EDM performance in order to increase machining production and decrease the machining time. The main aim is to increase the accuracy and the MRR but at the same time minimizing the TWR. As it has been abovementioned, due to the multiparametric nature of the EDM process, it is not easy to find a single optimal combination for the machining parameters. Thus,

there is a need to apply multi-objective optimization methods to find the solutions to these machining problems.

Khan [31] performed a comprehensive study by EDM mild steel by using copper and brass electrodes. The results show that TWR increases with the increase of voltage and current, also the cross-section of the electrode undergo more wear compared to its length. Guu et al. [32] investigated the surface characteristics of AISI D2 tool steel machined by EDM. They evaluated the recast layer by using Scanning Electron Microscopy (SEM) and X-ray diffraction technique and showed that, an excellent machine surface is produced with lower discharge energy, also at these conditions (lower pule-on time and current) reduces the tensile residual stress. Straka et al. [33] suggested an applied mathematical model to minimize the depth of Heat Affected Zone (HAZ) and the microhardness of an EN X32CrMoV12-28 steel machined by EDM with SF-Cu electrode. According to their study, the most significant parameters that affect the quality of the machined surface are the pulse-on and pulse-off time as well as the pulse-on current. A comparison study performed on a duplex stainless steel alloy machined by EDM with 3 different electrodes (Graphite, Copper-Tungsten and Tungsten electrodes) and 2 different dielectric mediums. Ablyaz et al. [34] found by using Taguchi L18 method that, the most significant parameter that affect the surface roughness is firstly the material of the electrode although for the MRR the dominated factor was the pulse-on current. The study also reported that higher MRR and SR values exhibited the surface wettability. Finally, Mouralova et al. [35] performed a comprehensive study on the influence of the WEDM parameters on Hardox 400 Steel. Among the other parameters (I_p, T_{on}, T_{off} and V), they also analyzed the wire feed and the cutting feed. By using a regression model, the results show that the cutting speed is mainly affected by the pulse-on time and pulse-on current, while the recast layer was between 5 to 20 μm.

EDM in Aluminum Alloys

Aluminum is light, ductile, plastic, non-magnetic; is an excellent conductor of electric current; quickly oxidizes; it is very resistant to tarnishing; is recycled. Aluminum is the third most abundant element (and the most abundant metal) in the earth's crust, which is about 8.1% by mass. It is a reactive element that forms solid compounds, so a lot of energy is required to obtain aluminum from aluminum oxide. As the injection mold technology was getting more and more popular during the past two decades, aluminum molds are competing with harden steel to produce softer materials. Thus, a lot of researchers tried to explore the advantages of machining aluminum and its alloys by using EDM technology [7]. Rao, Ramji and Satyanarayana [36, 37] investigated the generated conditions of residual stresses in Machining AA2014 T6 by using WEDM. The results reviled, a wide range of residual stresses from 8.2 MPa to 405.6 MPa. Besides, the researchers noticed the presence of AlCu and ACu_3 intermetallic. These stresses could cause a susceptible surface to crack formation, which affects not only the corrosion and wear resistance [38, 39] but also the fatigue life [40]. Khana et al. [41] performed an EDM drilling on aluminum alloy 7075. By using Taguchi grey relational theory and ANOVA they were able to analyze the response factors (MRR and TWR) and correlate them with the machining parameters

in order to find the optimal drilling conditions. They also Reported that the MRR and TWR are mainly affected of the pulse-on and off time. By using the same statistical method Bobbili and Gogia [42] machined a ballistic grade aluminum alloy by WEDM. Mathematical models were developed using response surface method to determinate the correlation between machining and performance characteristics. It was demonstrated by Ahmed [43] an experimental investigation of coating deposition on aluminum by EDM. The results show that most significant parameter that affect the layer thickness, material deposition rate and the TWR is the peak current (I_p). In addition, the surface microhardness had a significant improvement with an average hardness of 640HV.

5 Modeling and Simulation of EDM

Modeling and simulation consist a powerful tool in research regarding the EDM process. Additionally, except of the capability to predict the machining results, it provides an insight of the process, allowing the study of mechanisms and phenomena that are almost impossible to be experimentally studied. Since EDM is a multi-parameter process, with complex physical phenomena to take place, some reasonable simplifications and assumptions have to be made, in order the modeling to become feasible. These assumptions have always to be scientifically justified, and be based on robust theoretical background. Each researcher/research team, adopts its own approach regarding the simulation of EDM, developing and presenting different models. Nevertheless, some assumptions/simplifications are common, thus, it is considered useful and helpful to be presented.

At first, all discharges are considered identical, while during each pulse only one spark is occurred. Thus, this "average" spark is simulated, and the results concerning the overall process deduced from correspondence to the real processing time. The into material heat transfer is considered that mainly take place due to conduction, while Joule heating is often neglected. [44] The plasma channel is the main heat source, while the workpiece exchanges heat through convection with the dielectric fluid, and through radiation. Finally, the workpiece material is assumed as isotropic. Some more details will be discussed below.

The conduction heat transfer is mathematically described as:

$$\rho \cdot C \cdot \frac{\partial T}{\partial t} - \nabla \cdot (k \cdot \nabla T) = Q \tag{1}$$

with T the temperature, ρ the density, C the heat capacity (at a constant pressure C_P, or for a constant volume C_v), k the thermal conductivity and Q a heat source or a heat sink. The heat source, i.e. the plasma channel in most simulations is considered to have a Gaussian distribution, hence, the power density can mathematically be expressed:

$$Q(r) = 4.57 \cdot \frac{F_W \cdot V \cdot I_P}{\pi \cdot R_P^2} \cdot e^{-4.5 \cdot \frac{r^2}{R^2}} \tag{2}$$

with V the machining voltage in V, I_p the pulse-on current in A, R_p the plasma channel radius in m, r the distance from the center of the plasma channel in m, and F_w the proportion of energy that is absorbed by the workpiece. At this point, some important clarifications have to be made. At first, and regarding the power distribution of the heat source: in studies different types of heat sources have been adopted, namely, point heat source, or disc heat source. Nevertheless, in many of the models, a heat sources with a Gaussian distribution is utilized, not only because the obtained results are in line with experimental ones, but due to the theoretical background that supports this approach. In the work of Weingärtner et al. [45] a comprehensive comparison between different heat sources models can be found, concluding that the Gaussian distribution is the most consistent with experimental results. Moreover, and regarding the plasma channel radius, there is not a generally accepted model for its calculation, rather experimentally driven semi-empirical relations. Two commonly used relations are [46]:

$$R_p = 2.04 \cdot I_P^{0.43} \cdot T_{on}^{0.44} \tag{3}$$

with R_P the plasma channel radius in μm, I_p the discharge peak current in A and T_{on} the discharge duration in μs.

$$R_p = 0.85 \cdot 10^{-3} \cdot I_P^{0.48} \cdot T_{on}^{0.35} \tag{4}$$

with R_p the plasma channel radius in m, I_p the discharge peak current in A and T_{on} the discharge duration in s. Additionally, in some simulations the plasma channel is considered constant during the whole spark time [47], while in others, the plasma channel growths over time [48], implementing an expanding heat source. Finally, in order the heat source to be fully described, the proportion of power that is absorbed by the workpiece must be defined. Again, there is a deviation between the adopted coefficients. In lots of studies an absorption coefficient of 18.3% is utilized, which emanates from the research of DiBitonto et al. [12]. But this is only an approach; for example, Vishwakarma et al. [49] used an absorption coefficient of 8%, while Singh defined an absorption coefficient between 6.1 and 26.82%. The proportion of energy that is absorbed by the workpiece is strongly depends on the machining parameters, the workpiece and the electrode material, hence, these coefficients must carefully be adopted and as the case may be. The most proper approach, in order the accuracy to be ensured, is its definition by reverse engineering, based on experimental results. Furthermore, this coefficient is preferably not to be constant, but as function of the machining parameters [50].

The convection heat transfer between the workpiece and the dielectric fluid is expressed as:

$$q_{diel} = h_{diel} \cdot (T - T_{diel}) \qquad (5)$$

with q_{diel} the heat flux from the workpiece to dielectric fluid due to convection in W/m^2, h_{diel} the heat transfer coefficient between the workpiece and the dielectric oil in W/m^2K.

At this point, it should be pointed out that in most of the models the assumption of a constant geometry is implemented. In other words, the material erosion is not considered, and the material removal is estimated through a temperature condition. In a different approach, the material erosion is taken into consideration and simulated, through computational methods like moving mesh [51] or deformed geometry [52]. Finally, it must mention, that there are studies concerning consecutive spark, and the surface morphology as the result of them [53]. In those models, a multi-scale approach is adopted, coupling the single spark analysis with a macro scale analysis, where conclusions regarding the surface characteristics and roughness can be deduced.

6 Case Study: The Machining of Aluminum Alloys Al5052 and Al6063 with EDM

The current case study concerns the machining of two different aluminum alloys with EDM, namely the Al5052 and Al6063. The same machining parameters were utilized, aiming in a straight comparison of the machining results, regarding the MRR, Ra and Rt. Al5052 nominally contains 2.5% magnesium & 0.25% chromium, has good workability, very good corrosion resistance, high fatigue strength, weldability, and moderate strength, while it is extensively used in aircraft fuel/oil lines, fuel tanks and other transportation areas. In Al6063 the basic alloying elements are the magnesium (0.45–0.9%) and the silicon (0.20–0.6%), it is a medium strength alloy, with a wide range of applications, including architectural and transportation applications. The alloys' detailed chemical compositions along with their mechanical and thermo-physical properties are listed in Table 1.

The experiments were carried out on an ANGIETRON EMT 1.10 die sinking EDM machine, by using aluminum plates as workpiece material, and utilizing copper working electrode, with nominal dimensions of 38×23 mm. In order any depositions accumulation on electrode's surface to be avoided, in-between the experiments the electrode was properly being cleaned. A highly purified synthetic hydrocarbon oil was used as dielectric fluid, which was properly channeled into the working tank for the efficient debris removal. A nominal 1 mm cutting depth was set for all the experiments, in order a full and uniform machined surface to be formed.

A full-scale experiment was conducted, with control parameters the pulse-on current and time, each of one taking 4 levels of values, thus, 32 experiments were carried out in total. The pulse-on current and time varied from 15 up to 24A and from 100 up to 500 μs respectively, covering that way a wide range of per pulse energies. In Table 2, the machining parameters are listed in details. The experiments

Table 1 Chemical composition, mechanical and thermophysical properties of Al5052 and Al6063

Chemical composition

Element Wt. %	Al	Cr	Cu	Fe	Mg
Al5052	95.7–97.7	0.15–0.35	≤0.1	≤0.4	2.2–2.8
Al6063	≤97.5	≤0.1	≤0.1	≤0.35	0.45–0.9
Element Wt. %	Mn	Si	Ti	Zn	Other total
Al5052	≤0.1	≤0.25	–	≤0.1	≤0.15
Al6063	≤0.1	0.2–0.6	≤0.1	≤0.1	≤0.15

Mechanical and thermophysical properties

	Density [g/cc]	Cp [J/kgK]	Thermal cond. [W/mK]	Melting point [K]	Electrical resistivity [ohm/cm]	HV
Al5052	2.68	880	138	880–922	499e-8	68
Al6063	2.70	900	200	889–927	332e-8	83

Table 2 Machining parameters

Machining conditions	Level 1	Level 2	Level 3	Level 4
Discharge current I_p (A)	15	18	21	24
Pulse on-Time T_{on} (μs)	100	200	300	500
Dielectric	Synthetic hydrocarbon fluid			
Dielectric flushing	Side flushing			
Open circuit voltage (V)	100			
Close circuit voltage (V)	30			

were conducted under straight polarity, with constant voltage difference, and more specific, 100 and 30 V nominal open and close circuit voltage respectively. The Duty Factor (η) was automatically adjusted to optimize the process, thus, only indirectly can be estimated based on the mean current. Taking in mind that voltage pulses can be approximated by square pulses, the Duty Factor is calculated based on Eq. 6:

$$\eta = \frac{\overline{I_p}}{I_p} \tag{6}$$

with Īp with the ammeter indication of the mean current intensity in A and I_p the nominal pulse-on current in A. The MRR is defined as the volume of the removed material per minute, and calculated based on Eq. 2:

$$MRR = \frac{W_{st} - W_{fin}}{\rho \cdot t_m} \tag{7}$$

with MRR the material removal ratio in gr/min, $W_{st.}$, W_{fin} the workpiece weight before and after machining, respectively, in gr, ρ the workpiece material density in gr/mm^3 and tm the machining time in min.

The Surface Roughness was estimated in terms of Ra and Rt, which emerged as the mean value of five consecutive measurements on each machined surface. Finally, the machined surfaces cross sections were grinded, polished and chemically treated with proper etchant, being composed of 92 ml distilled water, 6 ml nitric acid and 2 ml hydrofluoric acid and the etched surfaces were observed in optical microscope in order the formed WL to be studied.

Experimental Results and Discussion

In Table 3 the experimental results are presented.

MMR consists one of the main productivity indexes, directly related with the machining efficiency and sustainability. Although, it is strongly depending on the machining parameters, namely the pulse-on current and the pulse-on time, there is not a linear correlation between the MRR and the machining power and the per pulse energy. More specific, an increase in the machining power, or in the per-pulse energy, does not compulsively result an increase in MRR, as there is an upper limit on the attainable MRR. This behavior can be attributed to three main reasons: the plasma channel growth, the debris concentration in between the electrode and the

Table 3 Experimental Results

I_p [A]	T_{on} [μs]	Al5052			Al6063		
		MRR [mm^3/min]	Ra [μm]	Rt [μm]	MRR [mm^3/min]	Ra [μm]	Rt [μm]
15	100	172.7	10.8	77.2	125.66	8.10	53.40
18	100	207.3	10.7	76.6	189.49	9.30	62.40
21	100	207.3	11.2	76.2	148.15	9.10	64.80
24	100	257.3	11.8	86.4	211.64	10.30	77.60
15	200	179.7	15.1	95.6	139.65	11.20	67.80
18	200	213.2	14.5	98	189.30	12.40	88.60
21	200	252.1	14.4	96.8	194.00	11.80	83.40
24	200	274.4	14.5	101.6	233.92	13.40	85.80
15	300	155.5	14.1	93.8	129.63	14.20	89.20
18	300	216.9	16	113.2	161.62	14.20	96.40
21	300	223.9	15.2	104.2	189.30	13.80	101.00
24	300	259.1	14.4	104.4	219.91	15.00	94.00
15	500	176.7	14.2	94.4	133.10	13.70	94.80
18	500	223.9	17.1	114.8	177.13	16.00	101.40
21	500	234.3	16.7	105	170.37	13.60	85.80
24	500	279.9	19.4	140.6	202.82	16.70	110.20

workpiece and the deposition of carbon the electrode surface. The formed plasma channel expands over the pulse time, consuming significant amounts of energy. Hence the higher the pulse-on time is, the more power is consumed by the plasma channel, decreasing the machining efficiency. At the same time, intense machining parameters lead in increased debris concentration between the electrode and the workpiece, acting like a physical barrier, while a significant amount of energy is spent as they re-melt. The carbon that is decomposed due to high temperatures is being deposited on the surface of the electrode and workpiece, forming a "shield layer" of carbides, which decrease the process efficiency. These underlying mechanisms that taking place during machining significantly affect the MRR, hence, it is of extreme interest to be studied the response of MRR in respect of pulse-on current and time.

Based on the obtained experimental data, which are presented in Table 3, the comparison of MRR for the two aluminum alloys are presented in Fig. 5, along with the corresponding Main Effects Plots. At first, by analyzing the Main Effects Plot of both alloys, it can be deduced that the pulse-on current is the major parameter that mainly affects the MRR, while the pulse-on time has a slight and vaguer influence. More specific, for the Al5052, the mean MRR is constantly increased with increase of I_p, having a total 56.4% increase as pulse-on current is increased from 15 to 24A. On the other hand, as the pulse-on time increased from 100 to 500 μs, the mean MRR only slightly changed, with the pulses of 100–300 μs, and 200–500 μs having almost the same mean MRR. Similar results emerged for the Al6063 as well. The pulse-on
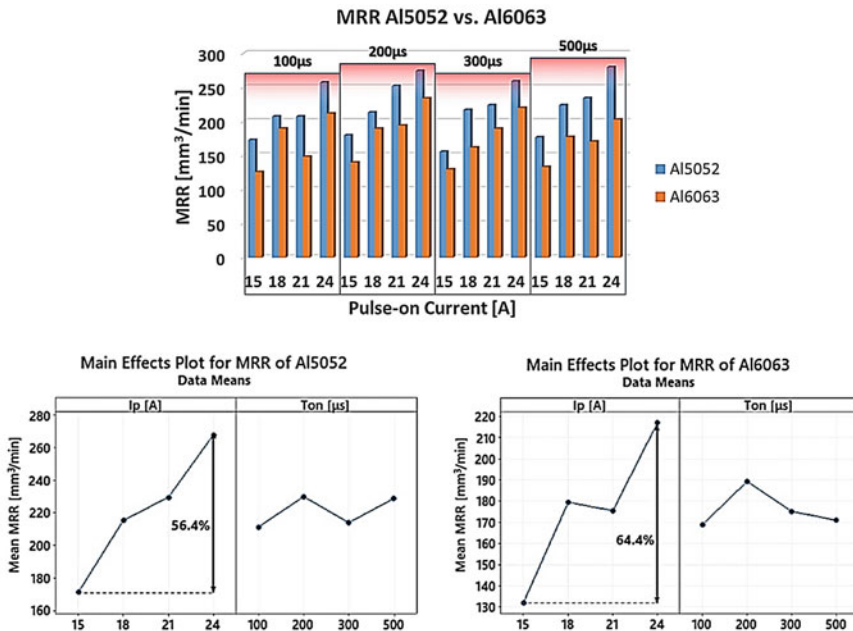

Fig. 5 MRR for Al5052 and Al6063 along with the Main Effects Plot

current mainly affects the MRR, while the pulse-on time has a fuzzy influence. The mean MRR was increased about 64.4% as the I_p increased from 15 to 24A, having only a small decrease between 18 and 21A. On the contrary, as the T_{on} increased from 100 to 300 and 500 μs the mean MRR remained almost constant, with only a slight increase for pulse-on time 200 μs.

Comparing the MRR values of Al5052 and Al6063, for all the sets of machining parameters the MRR of Al5052 is higher, by average 26.36%. This can be attributed to the alloys' thermophysical properties. Namely, Al6063 has higher Specific Heat, Thermal Conductivity and Melting Point than Al5052. Hence, the absorbed energy is more easily distributed in the material, preventing the topical temperature rise that will lead in material melt and removal. At the same time, due to the higher Specific Heat and Melting Point, Al6063 requires more heat energy than Al5052 to be melt, leading in lower MRRs, compared with these of Al5052.

The machined Surface Roughness is another important parameter of EDM, straight related with the surface quality of components that been manufactured with EDM. The Surface Roughness highly depends on the pulse-on current and time, i.e. the machining power and the per-pulse energy. The roughness is the result of the material removal and the craters formation, as well the growth of the White Layer. The craters' geometrical characteristics, (e.g. size, depth and width) are contingent on the pulse-on current and time. Nevertheless, each parameter affects the craters' formation in a distinctive way. Specifically, and as a rule of thumb, the pulse-on time allows the plasma channel to expand, resulting relatively big craters, while the pulse-on current mainly is reflected on the depth of the formatted craters. Nevertheless, the SR is subject to complicated underlying mechanisms, and depends on numerous of parameters, including the workpiece and electrode material, the dielectric fluid, the applied voltage and the utilized polarity during machining. Additionally, a crucial parameter in Surface Quality, and hence for SR is the formation of the WL. During EDM, only a portion of the molten material is removed from the workpiece, with the rest of it being re-solidified. Moreover, ablated material, and debris that remained in a close proximity to the workpiece surface, may re-attaches themselves, as a layer, on the spark cavity forming a layer of re-deposited material. The re-solidified and the re-deposited material form the WL, that drastically reshape the Surface Topology, since the morphology of the machined surface is not only developed by consecutive and/or overlaying craters, but from complex formations of re-solidified and re-condensed material. In Figs. 6 and 7 Ra and Rt of the machined surfaces are presented, along with their Main Effects Plots.

On the contrary with MRR, the Ra is mainly affected by the pulse-on time, while the pulse-on current has a minor, and vaguer influence. More specific, the mean Ra of Al5052 is constantly increased with increase in pulse-on time, having 51.5% higher mean value for T_{on} 500 μs, compared with the mean value for 100 μs pulse-on time. On the other hand, the mean Ra for the different pulse-on currents does not significantly change, showing only a slight increase trend as the pulse-on time (i.e. the machining power) increases. Similarly, in Al6063, increase in pulse-on time results a continuous increase in mean Ra, while, the utilization of higher pulse-on current has a fuzzy affect, leading in both increase and decrease of the mean Ra.
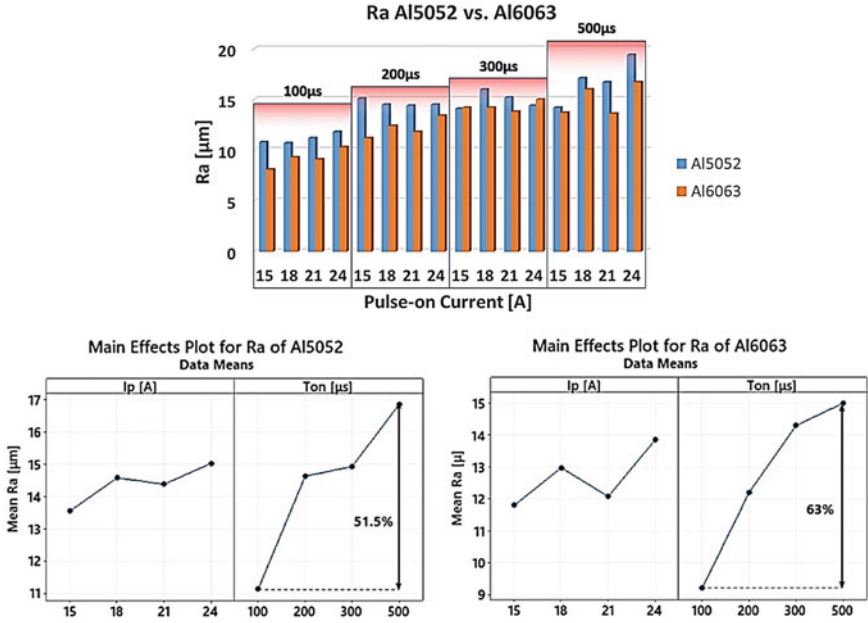
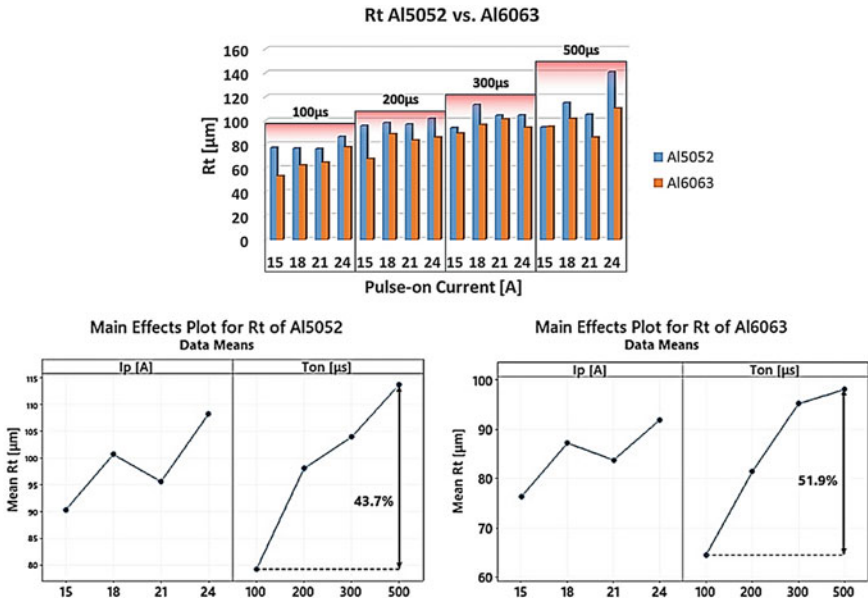Fig. 6 Ra for Al5052 and Al6063 along with the Main Effects Plot

Fig. 7 Rt for Al5052 and Al6063 along with the Main Effects Plot

Comparing the values of Ra for both alloys, they are in the same order of magnitude, with the Ra of Al5052 being, in the vast majority, higher. This can be reasonably attributed to the lower Thermal Conductivity, Specific Heat and Melting Point of Al5052, parameters that, as it has been aforementioned, affect the MRR. Namely, the higher MRR of Al5052, implies that on each spark a greater amount of material is removed, forming a bigger crater.

As it was expected, Rt is mainly affected by the pulse-on time, while the pulse-on current has a fuzzy influence. As the T_{on} increases, the mean Rt also continuously increases, for both alloys, having a 43.7% and 51.9% rise between 100 and 500 µs for the Al5052 and Al6063 respectively. On the other hand, higher pulse-on currents result either an increase or decrease of the mean Rt, hence, any conclusion could be precarious. Finally, it has to be mentioned, that, with only one exception, the Rt of Al5052 is higher than this of Al6063, advocating that in machining of Al5052 bigger and deeper craters are formed.

In Figs. 8 and 9 the cross sections of Al5052 and Al6063 are depicted respectively, for constant machining power (i.e. 24A pulse-on current), and for different per pulse energies (i.e. 100, 200, 300 and 500 µs). Observing the cross sections, it is deduced that the morphological characteristics of the WL are strong related with the pulse-on time. Namely, for T_{on} 100 µs, in both alloys, the WL is thin discontinuous, more like random formations on the surface. Moreover, the formatted craters that can be distinguished are shallow and wide. For 200 µs pulse-on time, the WL becomes thicker, covering greater percentage of the surface. Furthermore, some hollow globules appear, while the formed craters become deeper. The hollow formations are shaped as the result of the material's rapid re-solidification, and the gas entrapment
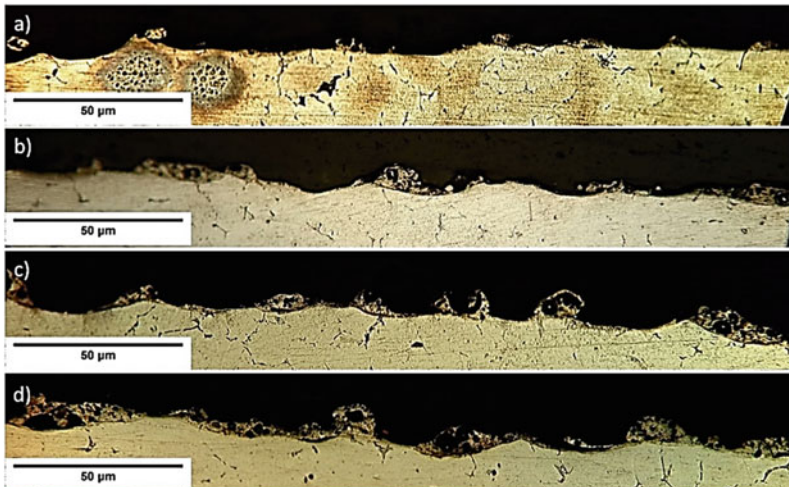

Fig. 8 Surface cross sections of Al5052 for 24A and pulse-on time **a** 100 µs, **b** 200 µs, **c** 300 µs, **d** 500 µs
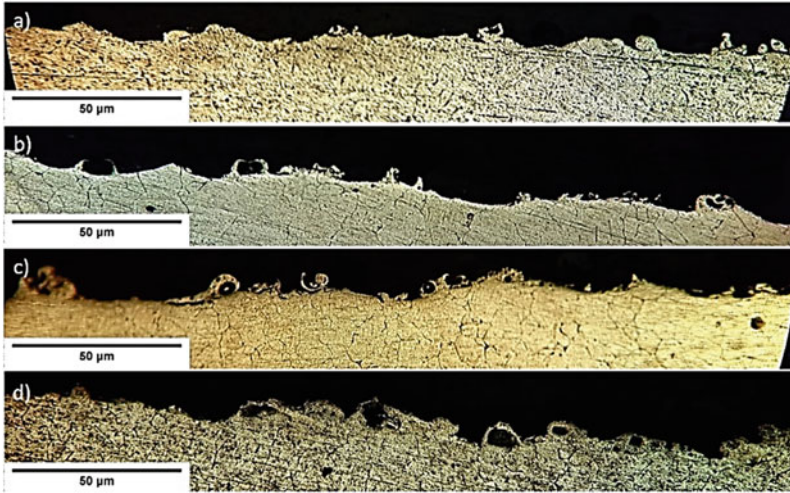
Fig. 9 Surface cross sections of Al6063 for 24A and pulse-on time **a** 100 μs, **b**) 200 μs, **c** 300 μs, **d** 500 μs

inside it. For higher pulse-on times (300 and 500 μs), the WL get almost continuous and thicker, while the aforementioned globules become denser and more bulky.

The juxtaposition of the cross sections for different per pulse energies, and for both alloys, confirm the results of Ra and Rt, which previously presented and analyzed. The WL in Al5052 is thicker in comparison with that of Al6063, while the formed craters appear to be deeper and the globules more bulky. For all those reasons, it is justified that Ra and Rt are higher in Al5052, and their increase in respect of the pulse-on time.

7   Summary

The current chapter concerns the non-conventional machining process of EDM, as well a specific case-study, namely, the machining of aluminum alloys Al5052 and Al6063 with EDM. After a brief historical review, the main operation principles and the underlying mechanisms of the process were presented, along with the most widely used performance indexes. Then a brief review was presented for the machining of steel and aluminum alloys with EDM, providing an adequate relevant literature. In Sect. 5, the basic principles of modeling and simulation of EDM were presented, while some interesting and "scientifically open" issues were pointed out. Finally, in the last section a case study regarding the comparison of machining Al5052 and Al6063 with EDM was presented. A full-scale experiment was carried out, with control parameters the pulse-on current and time. The machining performances were estimated in terms of Material Removal Rate and Surface Roughness (Ra, Rt), while

the machined surfaces cross sections were studied in optical microscope, in order the WL formation to be observed. It was deduced that the pulse-on current mainly affects the MRR, while Ra and Rt mainly depend and affected by the pulse-on time. Finally, it was concluded that the WL morphology is contingent on both the machining parameters, and the workpiece material as well.

References

1. Ho KH, Newman ST (2003) State of the art electrical discharge machining (EDM). Int J Mach Tools Manuf 43:1287–1300. https://doi.org/10.1016/S0890-6955(03)00162-7
2. Markopoulos AP, Papazoglou E-L, Karmiris-Obratański P (2020) Experimental study on the influence of machining conditions on the quality of electrical discharge machined surfaces of aluminum alloy Al5052. Machines 8:12
3. Priestley J (1775) Experiments on the circular spots made on pieces of metal by large electrical explosions. The history and present state of electricity with original experiments, vol. II, 3rd ed. London
4. BR, Lazarenko NJ (1944) Electrical erosion of metals. In Russian: gosenergoisdat leningrad, 27 p, 7 figures
5. Webzell S (2001) That first step into EDM, Machinery, 159, (4040) Findlay Publications Ltd. UK, Kent, p 41
6. Ho KH, Newman ST, Rahimifard S, Allen RD (2004) State of the art wire electrical discharge machining. Int J Mach Tools Manuf 44:1247–1259
7. Markopoulos AP, Papazoglou EL, Svarnias P, Karmiris-Obratański P (2019) An experimental investigation of machining aluminum alloy Al5052 with EDM. Procedia Manufacturing 41:787–794
8. Descoeudres A (2006) Characterization of electrical discharge machining plasmas, PhD thesis, ÉCOLE POLYTECHNIQUE FÉDÉRALE DE LAUSANNE, THÈSE NO, 3542
9. Xu CS (2012) Working principle and performance of wire electrical discharge machining. Adv Mater Res 507:180183. https://doi.org/10.4028/www.scientific.net/amr.507.180
10. Maradia U, Boccadoro M, Stirnimann J, Beltrami I, Kuster F, Wegener K (2012) Die-sink EDM in Meso-Micro Machining, Procedia CIRP, Volume 1. ISSN 166–171:2212–8271. https://doi.org/10.1016/j.procir.2012.04.029
11. Yunus Khan Mohd, Sudhakar Rao P, Pabla BS (2020) Investigations on the feasibility of Jatropha curcas oil based biodiesel for sustainable dielectric fluid in EDM process. Mater Today: Proc 26, Part 2. ISSN 335–340:2214–7853. https://doi.org/10.1016/j.matpr.2019.11.325
12. Di Bitonto DD, Eubank PT, Patel MR, Barrufet MA (1989) Theoretical models of the electrical discharge machining process. I. A simple cathode erosion model. J Appl Phys 66:4095–4103
13. Schumacher BM (2004) After 60 years of EDM the discharge process remains still disputed. J Mater Process Technol 149:376–381
14. Nikalje AM, Kumar A, Srinadh KVS (2013) Influence of parameters and optimization of EDM performance measures on MDN 300 steel using Taguchi method. Int J Adv Manuf Technol 69:41–49. https://doi.org/10.1007/s00170-013-5008-8
15. Karmiris-Obratański P, Zagórski K, Papazoglou EL et al (2020) Surface texture and integrity of electrical discharged machined titanium alloy. Int J Adv Manuf Technol. https://doi.org/10.1007/s00170-020-06159-z
16. Ciubotariu V, Câcu A, Rotundu I, Cucos M-M, Coteata M (2014) Influence of some factors on surface roughness parameters at electrical discharge machining. Appl Mech Mater 657:291–295
17. Guu YH (2005) AFM surface imaging of AISI D2 tool steel machined by the EDM process. Appl Surf Sci 242(3–4):245–250. https://doi.org/10.1016/j.apsusc.2004.08.028

18. Che Haron CH, Deros BM, Ginting A, Fauziah M (2001) Investigation on the influence of machining parameters when machining tool steel using EDM. J Mater Process Technol 116(1):84–87. https://doi.org/10.1016/s0924-0136(01)00846-9
19. Bleys P, Kruth J-P, Lauwers B, Schacht B, Balasubramanian V, Froyen L, Van Humbeeck J (2006) Surface and sub-surface quality of steel after EDM. Adv Eng Mater 8:15–25. https://doi.org/10.1002/adem.200500211
20. Soni JS, Chakraverti G (1991) Investigative study on metal removal rate and wear ratio in EDM of high carbon high chromium die steel J. Ind, Eng., p 71
21. Soni JS, Chakraverti G (1995) Effect of electrode material properties on surface roughness and dimensional accuracy in electro-discharge machining of high carbon high chromium die steel. J Ind Eng 76:46–51
22. Zarepour H, Tehrani AF, Karimi D, Amini S (2007) Statistical analysis on electrode wear in EDM of tool steel DIN 1.2714 used in forging dies. J Mater Process Technol 187–188:711–714. https://doi.org/10.1016/j.jmatprotec.2006.11.202
23. Lin CL, Lin JL, Ko TC (2002) Optimisation of the EDM process based on the orthogonal array with fuzzy logic and gray relational analysis method. Int J Adv Manuf Technol 19:271–277. https://doi.org/10.1007/s001700200034
24. El-Taweel TA (2006) Parametric study and optimisation of wire electrical discharge machining of Al–Cu–TiC–Si P/M composite. Int J Mach Machinab Mater 1(4):380–395. https://doi.org/10.1504/IJMMM.2006.012348
25. Su JC, Kao JY, Tarng YS (2004) Optimisation of the electrical discharge machining process using a GA-based neural network. Int J Adv Manuf Technol 24:81–90
26. Kuriakose S, Shunmugam MS (2005) Multi-objective optimization of wire-electro discharge machining process by non-dominated sorting genetic algorithm. J Mater Process Technol 170:133–141. https://doi.org/10.1016/j.jmatprotec.2005.04.105
27. Tsai KM, Wang PJ (2001) Semi-empirical model of surface finish on electrical discharge machining. Int J Mach Tools Manuf 41:1455–1477. https://doi.org/10.1016/S0890-6955(01)00015-3
28. Wang PJ, Tsai KM (2001) Semi-empirical model on work removal and tool wear in electrical discharge machining. J Mater Process Technol 114:1–17. https://doi.org/10.1016/S0924-0136(01)00733-6
29. El-Taweel TA (2009) Multi-response optimization of EDM with Al–Cu–Si–TiC P/M composite electrode. Int J Adv Manuf Technol 44:100–113. https://doi.org/10.1007/s00170-008-1825-6
30. Straka Ľ, Hašová S (2018) Optimization of material removal rate and tool wear rate of Cu electrode in die-sinking EDM of tool steel. Int J Adv Manuf Technol 97:2647–2654. https://doi.org/10.1007/s00170-018-2150-3
31. Khan AA (2008) Electrode wear and material removal rate during EDM of aluminum and mild steel using copper and brass electrodes. Int J Adv Manuf Technol 39:482–487. https://doi.org/10.1007/s00170-007-1241-3
32. Guu YH, Hocheng H, Chou CY, Deng CS (2003) Effect of electrical discharge machining on surface characteristics and machining damage of AISI D2 tool steel. Mater Sci Eng A 358(1–2):37–43. https://doi.org/10.1016/s0921-5093(03)00272-7
33. Straka L, Corný I, Pitel' J, Hašová S (2017) Statistical approach to optimize the process parameters of HAZ of tool steel EN X32CrMoV12-28 after Die-Sinking EDM with SF-Cu Electrode. Metals 7:35
34. Ablyaz TR, Shlykov ES, Muratov KR, Mahajan A, Singh G, Devgan S, Sidhu SS (2020) Surface characterization and tribological performance analysis of electric discharge machined duplex stainless steel. Micromachines 11:926
35. Mouralova K, Benes L, Bednar J, Zahradnicek R, Prokes T, Fries J (2020) Analysis of machinability and crack occurrence of steels 1.2363 and 1.2343ESR Machined by Die-Sinking EDM. Coatings, 10, 406
36. Rao PS, Ramji K, Satyanarayana B (2014) Effect of wire EDM conditions on generation of residual stresses in machining of aluminum T6 alloy. Alexandria Eng J 55(2). ISSN 1077–1084:1110–168. https://doi.org/10.1016/j.aej.2016.03.014

37. Pujari SR, Koona R, Beela S (2018) Surface integrity of wire EDMed aluminum alloy: a comprehensive experimental investigation. J King Saud Univ—Eng Sci 30(4). ISSN 368–376:1018–3639. https://doi.org/10.1016/j.jksues.2016.12.001

38. Capello E (2004) Residual stresses in turning: Part I: influence of process parameters. J Mater Process Technol 160(2):221–228

39. Bonny K, De Baets P, Quintelier J, Vleugels J, Jiang D, Van der Biest O, Lauwers B, Liu W (2010) Surface finishing: impact on tribological characteristics of WC–Co hardmetals Tribology. Int 43:40–54

40. Ghanem F, Fredj NB, Sidhom H, Braham C (2011) Effects of finishing processes on the fatigue life improvements of electro-machined surfaces of tool steel Int. J Adv Manuf Technol 52:583–595

41. Khanna R, Kumar A, Garg MP et al (2015) Multiple performance characteristics optimization for Al 7075 on electric discharge drilling by Taguchi grey relational theory. J Ind Eng Int 11:459–472. https://doi.org/10.1007/s40092-015-0112-z

42. Ravindranadh Bobbili V, Madhu AKG (2015) Multi response optimization of wire-EDM process parameters of ballistic grade aluminium alloy. Eng Sci Technol Int J 18(4). ISSN 720–726:2215–986. https://doi.org/10.1016/j.jestch.2015.05.004

43. .Afzaal Ahmed (2016) Deposition and analysis of composite coating on aluminum using Ti–B4C powder Metallurgy tools in EDM. Mater Manuf Processes 31(4):467–474. https://doi.org/10.1080/10426914.2015.1025967

44. Papazoglou EL, Markopoulos AP, Papaefthymiou S, Manolakos DE (2019) Electrical discharge machining modeling by coupling thermal analysis with deformed geometry feature. J Adv Manuf Technol https://doi.org/10.1007/s00170-019-03850-8

45. Weingärtner E, Kuster F, Wegene, K (2012) Modeling and simulation of electrical discharge machining. In Procedia CIRP vol 2 74–78

46. Jahan MP (2015) Electrical discharge machining (EDM): types. Nova Science Publishers, Technologies and Applications

47. Mehta HN (2015) Modeling of electrical discharge machining process. Int J Eng Res Technol 4:153–156

48. Tlili A, Ghanem F, Salah NB (2015) A contribution in EDM simulation field. Int J Adv Manuf Technol 79:921–935

49. Vishwakarma UK, Dvivedi A, Kumar P (2012) FEA modeling of material removal rate in electrical discharge machining of Al6063/SiC composites. Int Conf Mech Ind Manuf Eng (ICMIME, 2012), Zurich, Switzerland, Jan. 15–17. 6, 586–591

50. Shabgard M, Ahmadi R, Seyedzavvar M, Oliaei SNB (2013) Mathematical and numerical modeling of the effect of input-parameters on the flushing efficiency of plasma channel in EDM process. Int J Mach Tools Manuf 65:79–87

51. Vignesh Shanmugam S, Krishnaraj V, Jagdeesh KA, Varun Kumar S, Subash S (2013) Numerical modelling of electro-discharge machining process using moving mesh feature. Procedia Eng 64:747–756

52. Papazoglou EL, Karmiris-Obratański P, Karkalos NE, Markopoulos AP (2020) On the use of deformed geometry in EDM modelling: Comparative study. Acta Physica Polonica A https://doi.org/10.12693/APhysPolA.138.268.

53. Liu JF, Guo YB (2016) Modeling of white layer formation in electric discharge machining (EDM) by incorporating massive random discharge characteristics. Procedia CIRP 42:697–702

Simulations and Experiments in Single Point Incremental Forming Process

D. Nasulea and G. Oancea

Abstract In this chapter is presented the entire flow of a single point incremental forming process starting from simulations to experiments for frustum of a cone parts manufactured from DC05 deep drawing steel. To perform the FEM simulations for the considered parts in different dimensional configurations could be used the following software components: ANSYS APDL for the pre-processing stage, LS-DYNA Explicit to solve the analysis, LS-PrePost for results post-processing and an additional software tool developed by the authors for tool path points generating, in a short time. In order to obtain true results, the real mechanical properties of the DC05 material deep drawing steel were experimentally determined and then used as input data in the simulation software. The results obtained in the numerical simulation are validated in practice, for all the parts simulated used FEM analysis were manufactured in good conditions, using a rounded forming tool, a blank fixing device and a three axis CNC machine-tool. Finally, the parts manufactured through single point incremental forming process are digitised using a 3D scanner and dimensional accuracy is obtained

1 Introduction

Nowadays in industry, one of the trends is regarding the products market, consists in changing the production from big volume to small batch production or even unique products manufacturing. This trend is due to the customer's requirements and claims, which are getting to more and more customized products. It is well-known that the Incremental Sheet Forming (ISF) is one of the manufacturing processes, that are able to ensure a great flexibility for industrial companies. In cold-pressing field, the ISF

D. Nasulea · G. Oancea (✉)
Department of Manufacturing Engineering, Transilvania University of Brasov, Mihai Viteazul 5, Brasov, Romania
e-mail: gh.oancea@unitbv.ro

D. Nasulea
e-mail: nasulea.marius.daniel@unitbv.ro

processes, in its different variants, are some of the most flexible processes which are easy to be implemented in a short time and with small investments. Once it was implemented, it can be easily change the process technology in order to adapt it for different shape products manufacturing.

ISF is a relatively new process for sheet metal parts manufacturing, being a flexible "dieless" process, which is suitable for small batch production [1]. In the literature, there are presented two main groups of ISF processes [2]: Single Point Incremental Forming (SPIF), and Two Points Incremental Forming (TPIF). The term SPIF is used when the outside part contour is sustained by a backing plate and it is clamped with a fixing plate on its flange. In SPIF the forming tool is pressing the free inwards material, which is deformed without having support on the opposite blank side. The term TPIF is used when a partial or a full die ensure support for the opposite side of the sheet, mean time the forming tool acts in a similar way with the SPIF process, moving the inside flat blank area gradually downwards. The reason why the ISF processes are called "dieless", even if is not totally true, especially for TPIF [1, 3, 4], is that, for its implementation, it does not require a dedicated die for parts manufacturing, which usually are very expensive to be designed and manufactured.

The ISF process working principle are presented in Fig. 1 [1, 5]. It can be seen the basic elements needed to implement this process: a blank fixing device, a rounded forming tool and a CNC programmed toolpath.

According to the working principle, the sheet metal blank is clamped in the fixing device by contact on its outside contour. The part is deformed based on multiple parallel layers, on each layer, the forming tool follows a toolpath on a constant step depth, usually on a CNC milling machine, and produces a local plastic deformation on the sheet blank. By repeating the contour toolpath, layer by layer, the part is manufactured step by step, until the final shape is obtained [5]. The forming toolpath can be also a continuous one, similar with a spiral toolpath used for milling processes. Thus, the part can be manufactured using multiple layers and a constant step depth toolpath (called Z-level toolpath), or using a continuous spiral toolpath. The distance between two layers or between two consecutive contours is called incremental step down [8], being the reason why this process is named incremental forming process.

SPIF is the most common incremental forming process, being studied in detail by researchers and also by industrial companies. One of the most used methods in investigating forming processes such as SPIF, is the Finite Element Method (FEM), due to its advantage on accuracy prediction and low costs implementation. In this chapter is presented the FEM implementation for frustum of cones in four parts configuration, manufactured through SPIF process, and also experiments which validate the FEM results.
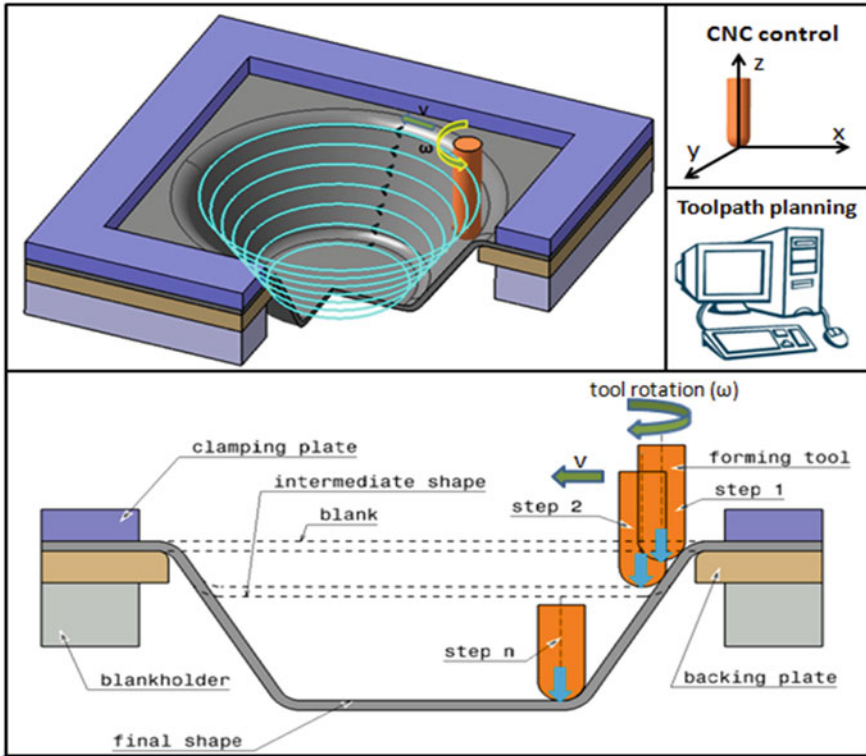
Fig. 1 ISF working principle [1, 5–7]

2 Simulations in Incremental Single Point Incremental Forming Process Using Finite Element Method

In SPIF field, FEM simulations are implemented using common software systems available on the market, such as: ABAQUS, ANSYS or LS-DYNA [5]. The software systems are used in order to investigate different process aspects, of which the most common are: the forces analysis [9], the springback amplitude prediction for tool-path corrections [10], influence of the tool or process parameters and tool path on the deformation behaviour [11], the deformation mechanism, strains and thickness reduction [12], and so on. FEM implementation for SPIF processes is not an easy task, several stages should be followed in order to succeed it, with details on those stages which can be different, depending on what software system has been chosen.

2.1 Stages in Simulation of Single Point Incremental Forming Process

FEM simulation implementation for SPIF process requires several general stages or steps which should be followed, according to the literature [13, 14]. The following three main stages are described [13, 14]:

- *Pre-processing stage*: is the stage when the FEM model is prepared for analysis.
- *Analysis stage*: is the stage when the simulation is made, the FEM model is solved and the FEM results are obtained.
- *Post-processing stage*: is the stage when the results are analysed and processed.

In the present chapter, the FEM simulation was implemented using ANSYS APDL for the pre-processing stage, LS-DYNA Explicit for analysis stage and model solving, and the workbench LS-PrePost from LS-DYNA for results post-processing [5]. The objective of the simulations is to analyse if several frustum of cones can be manufacture through SPIF, without material fracture during processing.

For FEM model preparation in ANSYS APDL, several steps were followed and are further described [5]:

- 3D modelling in ANSYS APDL of the parts assembly involved in the simulation which is presented in Fig. 2. The assembly supposes a sheet metal blank, a forming tool materialized by a simple ball, and the blank fixing device which is composed of a support plate and a fixing plate. The final part shape is not a component of the FEM model assembly, but it is also presented in Fig. 2, in order to show the part shape for which are described the FEM model preparation stages. The sheet blank material is DC05 deep drawing steel, with 1 mm thickness.
- Defining the types of the elements used for each assembly components. It was used the shell elements type specific for ANSYS APDL, called "Thin Shell 163" [15].
- Creating the real constants for each component. When shell elements are used, the neutral fibre of each component are modelled, and the real constants are the parameters which describe the finite element thickness which will be used in the simulation process [15].
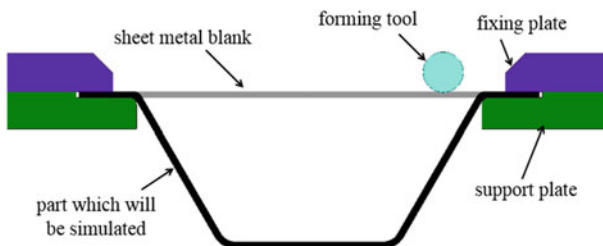

Fig. 2 Components used in FEM simulation process [5]

- Defining the materials for each component. All the components which do not need to be deformed (the forming tool, the support plate and the fixing plate) are defined as rigid bodies, and their material properties are those for general steels, which are available in the literature [5, 13]. For the deformed sheet metal blank, the real DC05 material properties were determined by experiments, those being described later.
- Creating the meshing attributes. An attribute is an association/group of three elements which were defined before: a type of elements, real constants and a type of material. The attributes are individually defined for each component involved in the simulation [5].
- Components discretization. In Fig. 3 is presented a square mapped type of mesh, created for the support plate component [5]. The same mapped mesh was also adopted for sheet metal blank and for device fixing plate, in order to ensure the finite elements vertex coincidence during the model solving stage.
- Mesh refining for the sheet metal blank component. The areas were the forming tool comes in contact with the sheet blank should be analyzed, in detail. Thus, this area was refined to a mesh with a much smaller element type (Fig. 4). Increasing the number of finite elements, a more detailed analysis will be made for those areas, and, in this situation, the analysis results will be more confidence [5].
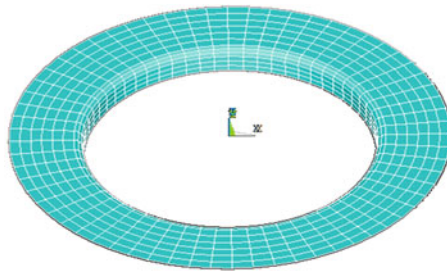

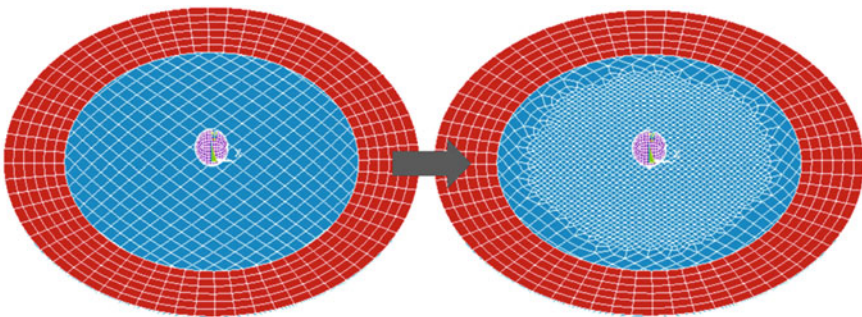**Fig. 3** Square mapped mesh associated to the support plate [5]

Fig. 4 Refined mesh on the blank forming areas [5]

Fig. 5 Parts created for each simulation components [5]

- Defining the parts for all four components involved in simulation. A part in ANSYS APDL, in this case, is an association made by the software system composed of component geometry (part number), component mesh (finite elements), material properties and real constants. In Fig. 5 there is presented the screen of ANSYS APDL, where are described all four parts created for the components involved in simulation [5].
- Toolpath description. The forming tool movements in ANSYS APDL should be exactly the same as the toolpath which will be followed by the tool when the parts are manufactured in reality, in order to obtain confidence results. Describing the toolpath in ANSYS APDL in the same manner as it is described the CNC file used in parts manufacturing is mandatory. Because ANSYS APDL does not allow inserting, as input data, the CNC file or the 3D toolpath curve, the tool movements are described using pairs of array parameters for each tool position which is described in the CNC file. This step is a time-consuming stage in FEM model preparation, because of the big working volume required for array parameters processing, starting from the CNC file. One viable solution to decrease the time and the working volume of this stage are later described in this chapter.
- Creating contacts between components. The recommended type of surface to surface contacts for sheet forming processes is a specific ANSYS APDL type of contact called "forming one way surface to surface (FOSS)", being used also for this study [7, 15]. The friction coefficient used for the contact between forming tool and sheet blank is $\mu = 0.08$ and for the contacts between fixing device components and sheet blank, $\mu = 0.15$ [5, 13, 16].
- Mass scaling. This method is used in order to decrease the analysis run time, which usually exceeds several hours or even days for different part configurations, depending of the computer processing performances [5].
- Generating of the "K" file, being the ANSYS APDL output, which will be further used as running file. The "K" file will be used as input data in by LS-DYNA Explicit, where it will be processed in order to obtain the FEM simulation results.

Two main issues were remarked in the pre-processing stage were the FEM model is prepared, and need to be solved, in order to obtain confidence results from SPIF FEM analysis. The first one is the blank material properties. It is recommended to

avoid using general material properties available in standards, and to determine the real material properties for the used material batch. Those real properties should be used to describe the sheet blank behaviour in FEM simulation. The second issue is the toolpath description in ANSYS APDL exactly the same as it was programmed in the CNC file. Both issues were managed by the authors and are described in the next subsections.

2.2 Real Material Properties Determination

FEM simulations are very powerful virtual tools used to anticipate different aspects for manufacturing processes or products behaviour but those are not always in agreement with the reality [17]. To ensure the confidence of the FEM provided results, the right input data should be introduced for material properties involved in the simulation. How the real material properties were experimental determined for the batch of DC05 deep drawing steel is presented below.

As was already mentioned, the sheet blank material is DC05 deep drawing steel, with 1 mm thickness. The mechanical properties according to the SR EN 10,130:2007 standard are presented in Table 1 [5, 18].

The material properties could be different from batch to batch, thus, the data given by material standards or material suppliers are not always quite accurate. Thus, it was decided to determine the real material properties for the used batch, by applying the uniaxial tensile strength according to the standard SR EN ISO 6892-1:2016. The tensile strength was applied on 15 specimens which have the dimensions presented in Fig. 6.

DC05 deep drawing steel is a blank manufactured by lamination process, and because of the manufacturing process the material properties may be different on each direction. In order to avoid the errors because of the material anisotropy, it was chosen to test five specimens cropped along three different directions related to material rolling direction, as is presented in Fig. 7. Those three cutting directions for the specimens are: S1.1, S1.2,….., S1.5—specimens parallel with the rolling direction, S2.1, S2.2,….., S2.5—specimens perpendicular on the rolling direction and S3.1, S3.2,….., S3.5—specimens at 45º related to the rolling direction. Abrasive water jet cutting process was used for the specimens manufacturing and the tensile tests were made using the LLOYD LS100 Plus uniaxial tensile test machine [5, 18].

Table 1 Material properties for DC05 deep drawing steel according to SR EN 10,130:2007 standard [5, 18]

DC05 deep drawing steel				
Density [Kg/m^3]	Young modulus [MPa]	Poisson's ratio	Yield strength [MPa]	Tensile strength [MPa]
7850	210,000	0.3	180	270…330

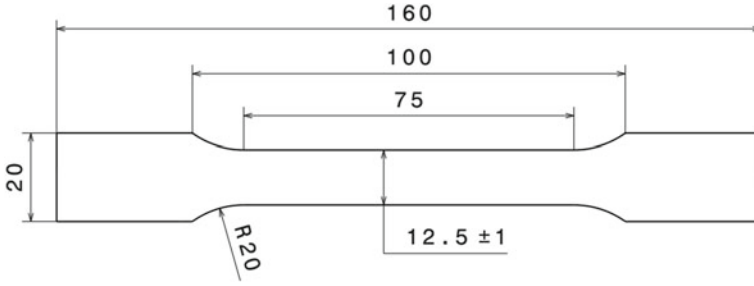**Fig. 6** Specimen dimensions [5, 18]

a)   b)

Fig. 7 Tensile test: **a** specimens on the cutting directions, **b** tested specimens [5, 18]

Before testing, based on the stress-strain values generate by the tensile test machine, the material characteristic curve was graphically represented in Fig. 8, for each tested specimen. Those graphics are also called engineering stress—engineering strain curves (σ, ε), but those are not the real curves.

Those stress-strain values are generated by the machine considering constant values for specimen gauge length L_0 and for gauge section area, S_0. During the tensile test, the specimen are in a continuously streaking which means the gauge length and the gauge section area are in a continuously changing because of the specimen elongation. At each moment the gauge length and the gauge section have different instantaneous values which are notated with S_i and L_i. In order to obtain the true stress—true strain characteristic curve (σ_{real}, ε_{real}) and also the real material properties for the studied DC05 material batch, all the data generated by the tensile test machine should be further processed using an Excel spread sheet and several relations available in the literature [5, 18, 19]:

- According to the law of constant volumes which is valid in material forming field, the following equation available for the initial and instantaneous gauge volume can be [5, 18, 19]:
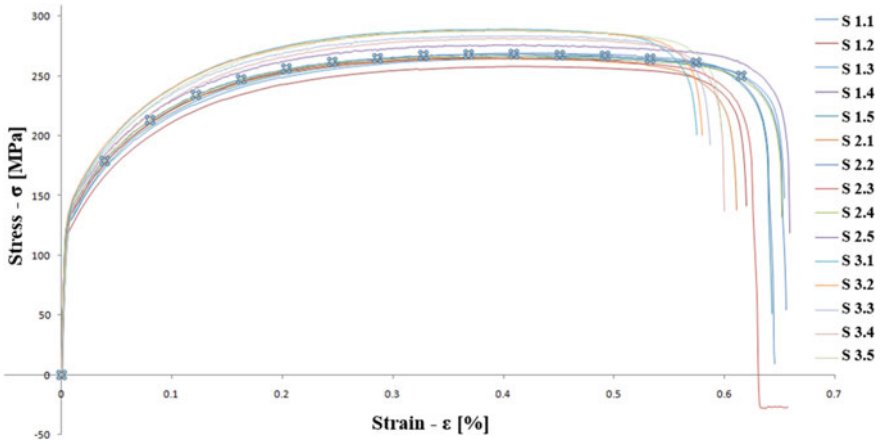
Fig. 8 Engineering stress—engineering strain curves [5, 18]

$$V_0 = V_i \Rightarrow S_0 L_0 = S_i L_i \tag{1}$$

- The instantaneous values for S_i and L_i can be drawn [5, 18]:

$$S_i = \frac{S_0}{1 + \frac{\Delta l}{L_0}} \tag{2}$$

$$L_i = L_0 + \Delta l \tag{3}$$

where Δl is the specimen elongation.

- According the engineering stress equation, the true stress is calculated using relation (4) [13, 18]:

$$\sigma = \frac{F}{S_0} \Rightarrow \sigma_{real} = \frac{F}{S_i} \tag{4}$$

where F is the tensile force, which is known from the tensile test machine.

- Relation (5) describe the real strain values [5, 18]:

$$\varepsilon_{real} = \frac{\Delta l}{L_0} \tag{5}$$

- according to the above relations, the true stress equation becomes [5, 18]:

$$\sigma_{real} = \frac{F}{S_0}(1 + \varepsilon_{real}) \tag{6}$$

Using the above presented steps, the initial set of engineering stress-engineering strain values obtained from the tensile test machine for the specimen which was closest to the average values (S1.3), was further processed in order to obtain the real material properties and the true stress—true strain curve (σ_{real}, ε_{real}), which is, in fact, the real material characteristic curve (Fig. 9). For the same specimen was also calculated the real Young modulus (E), using the Eq. (7) [5, 18].

$$E = tan(\alpha) \tag{7}$$

The real material properties processed for specimen S1.3 are presented in Table 2. Those will be used in the SPIF numerical simulations, in order to ensure that the provided results are closest to the reality.

ANSYS APDL allow also to use, as material property which describe the plastic deformation behaviour, the real characteristic curve, which is introduced in FEM simulation as pairs of values (σ_{real}, ε_{real}), starting from the yield strength graphic point up to the tensile strength graphic point [5].
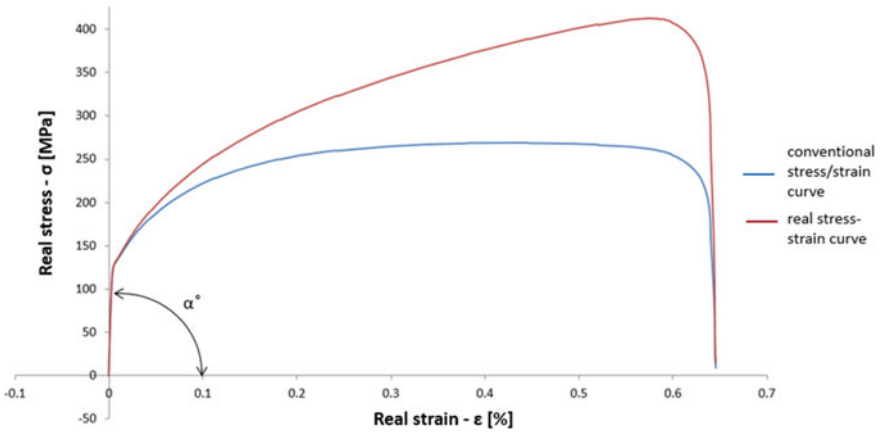

Fig. 9 True stress—true strain curve for S1.3 specimen [5]

Table 2 Real material properties for DC05 deep drawing steel according to the uniaxial tensile test [5, 18]

DC05 deep drawing steel				
Density [Kg/m^3]	Young modulus [MPa]	Poisson's ratio	Yield strength [MPa]	Tensile strength [MPa]
7850	87,952	0.3	190.59	388.67

2.3 Modality of Time Reducing in Simulation of SPIF Process

The time spent for SPIF numerical simulation implementation and also for analysis is considerable in comparison to the simulations for other types of processes. The solving time, also called the computational time (CPU time), has big values because of multiple nonlinear problems in forming processes [20], but also because of the tool trajectory complexity. To decrease the analysis time, multiple solutions were found in the literature [7].

Another reason of time consuming is the difficulty of implementing the forming tool movements in the FEM software, in the same way as it is described for the manufacturing process. Usually, the forming toolpath is generated by using a computer aided manufacturing software system (CAM), and it consist of thousands of integration points followed by the tool during a SPIF process, described in a CNC file, using G-code format. ANSYS APDL and also the others FEM software systems do not allow to introduce directly as input a G-code format, in order to describe the tool movements in numerical simulation. Thus, the CNC file should be further processed to convert it from G-code to a text file containing array parameters for each tool positions coordinates (for X, Y and Z axis) and also for the blank retaining force, all depending of the specific moment (time parameter) when the tool arrives in each position [5, 7].

For ANSYS APDL, five array parameters should be processed from the CNC file, in order to describe the tool movements and the blank retaining forces in SPIF process simulation [5, 7]:

- *UUX*—X coordinate for each tool position during the toolpath.
- *UUY*—Y coordinate for each tool position during the toolpath.
- *UUZ*—Z coordinate for each tool position during the toolpath.
- *TTime*—time moment when the tool arrives in each position.
- *FRET*—retaining force which is equal in each moment.

To convert a CNC G-code toolpath in a specific format, that can be introduced in ANSYS APDL for a SPIF process, suppose an enormous manual or semi-automated working volume, because of a big number of positions occurred by the forming tool during the process. Thus, in order to considerably reduce the time and the working volume spent to generate an ANSYS APDL format able to describe the tool trajectory, a software tool has been developed by the authors. The software tool is a stand-alone application which can be integrated as a supplementary toolpath generation step, in the FEM model preparation stage [5, 7].

The software tool has been developed using Object Pascal programming language under Delphi environment and it was named by the authors Tool Motion Points Generator (TMPG). TMPG working principle is according to the block diagram presented in Fig. 10. It uses, as input data, the toolpath CNC file and it generates, as output data, a text file which includes all five array parameters needed to describe the tool movement during the forming process, in exactly the same way as it was
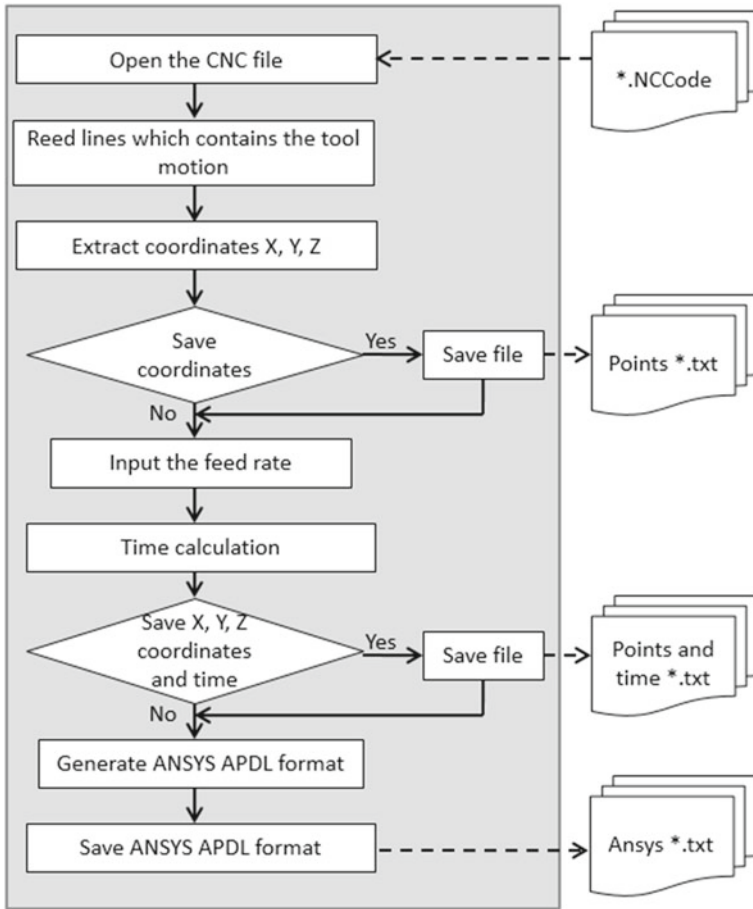
Fig. 10 TMPG block diagram [5, 7]

generated from the CAM software, for parts manufacturing. Even if the retaining force value for each time increment is not extracted from the CNC file, TMPG include in the final output, meaning the ANSYS format, also a parameter f which describe the retaining force value applied by the fixing plate upon the sheet blank margins. The retaining force value can be easily changed by users directly in ANSYS APDL, just by modifying the value for the parameter f. By using the TMPG software tool, the steps for toolpath and the forming force description by generating a specific ANSYS format is converted to a complete automatic stage, substantially reducing the time and the working volume. Thus, the entire FEM model preparation stage is considerably reduced, and further, the implementation time of numerical simulation of SPIF process is reduced, as well [5, 7].
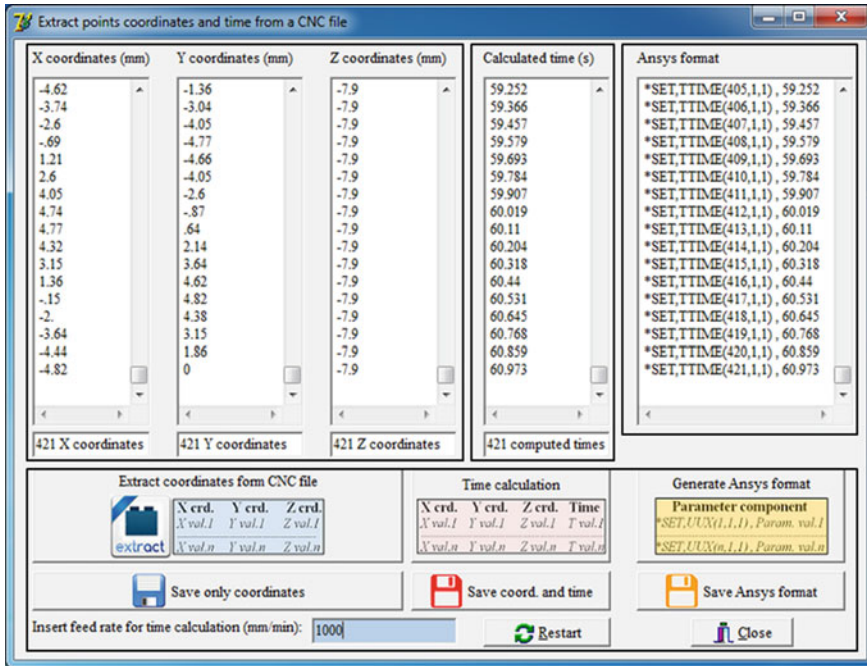
Fig. 11 TMPG graphical user interface [5, 7]

TMPG graphical user interface is presented in Fig. 11 and it is divided into four separate zones according to their role in the use of the software tool. In the first zone, the coordinates X, Y and Z extracted from the CNC file for each tool position during the process are displayed. In the second zone, the time moment when the forming tool arrives each position is displayed. The time is calculated based on the distance between two consecutive tool positions and using the tool feed rate value which is also an input data. The distance between two consecutive points $A(x_a, y_a, z_a)$ and $B(x_b, y_b, z_b)$ is calculated using the following relation [5, 7]:

$$AB = \sqrt{(x_b - x_a)^2 + (y_b - y_a)^2 + (z_b - z_a)^2} \tag{8}$$

In the third interface zone, TMPG automatically generates a list with five successive array parameters: three for each tool position X, Y, Z coordinates, one for time moment in each tool position and one for the retaining force whose value is, in fact, the parameter f value. The last interface zone is the command area where many buttons are placed, which allows users to follow the flow presented in Fig. 10. TMPG allows users to save intermediary files which can be used also for FEM software, other than ANSYS APDL, to describe the tool movements for a SPIF process [5, 7].

```
% O1000
( ***************************************************************
( *   INTELLIGENT MANUFACTORY SOFTWARE WWW.IMS-SOFTWARE.COM   *
( *   IMSPOST VERSION : 7.4R                                  *
( *   USER VERSION : 1                                        *
( ***************************************************************
N1 G49 G54 G17 G80 G40 G90 G23 G94 G01 G98
( TOOL DATA : T1 END MILL D 12)
N2 T1 M6
N3 S500 M3
N4 G0 X9.29 Y-2.15 Z5
N5 G43 Z.78 H1
N6 G1 X9.96 Y-1.04 Z.66 F300.
N7 X10.55 Y.61 Z.51
.......................................
N618 X2.78 Y2.78
N619 Z2.
N620 M30.
```

Fig. 12 CATIA V5 G-code structure [5, 7]

For SPIF process simulation and also for manufacturing, the forming toolpath was generated using CATIA V5, the Advanced Machining workbench. The CNC file was generated and an example of G-code structure is presented in Fig. 12.

The CNC G-code file is automatically processed using the TMPG software tool, and a text file is obtained. It contains the all five array parameters necessary in ANSYS APDL to describe the tool movements for numerical simulation. A general example of how it looks the ANSYS APDL format for all five array parameters is presented in Fig. 13.

The TMPG software tool is integrated in the SPIF simulation flow (FEM model preparation stage) as it is presented in Fig. 14. The parts 3D models which will be manufactured were designed in CATIA V5, the CAD workbench (Part Design) and the CNC forming toolpath was generated further in CATIA CAM workbench (Advanced Machining). The CNC file was further processed using TMPG software tool, and the array parameters for tool movements were obtained. These parameters were used in ANSYS APDL to describe the forming tool trajectory in the FEM model preparation stage. From ANSYS, an output file were obtained (type "k" file) which were further used as input for LS-DYNA Explicit, to solve the analysis. Before analysis, the final results are processed using LS-PrePost workbench [5, 7].

TMPG software tool is an original stand-alone application which proves considerable advantages when it is used for FEM model preparation stages. It succeed to significantly decrease the time spent for FEM simulation implementation for SPIF process, by reducing the FEM model preparation time, in terms of toolpath description in ANSYS APDL. To get the array parameters from the CNC file, before TMPG
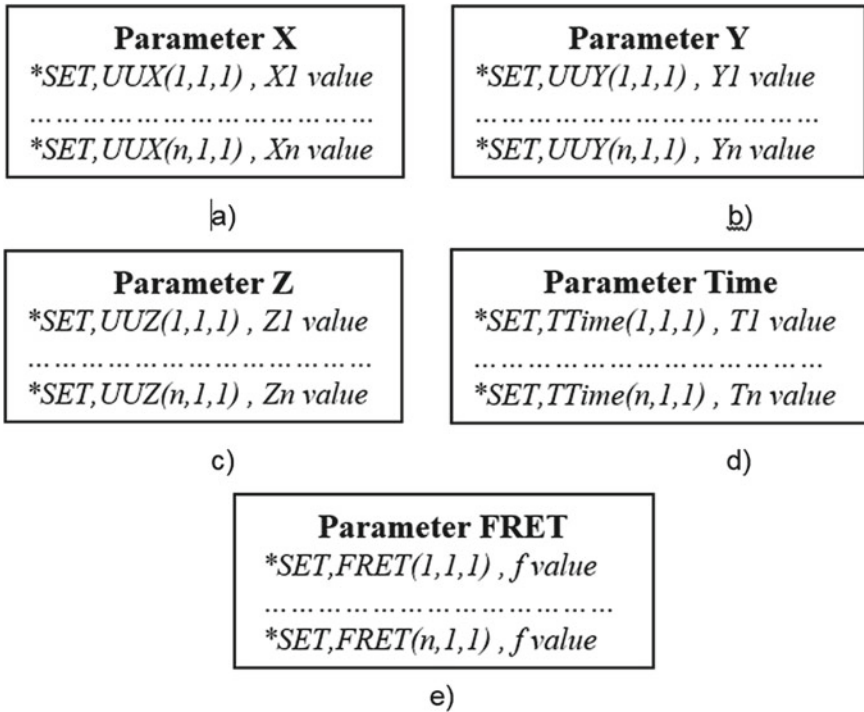
Fig. 13 Parameters format for ANSYS APDL: **a** for X-axis coordinate, **b** for Y-axis coordinate, **c** for Y-axis coordinate, **d** for tool position time, **e** for retaining force parameter f [5, 7]

development, a huge work volume and time were spent by manual and/or semiautomatic processing. Using TMPG, the time was reduced from many hours or even days of manual processing, to a few minutes. Another advantage is that, to use TMPG, the operators does not need additional programing knowledges or others special skills, being very simple to be used by anyone [5, 7].

2.4 Forming Simulation of Frustum of Cone

In this section is presented how FEM simulation is used in order to check if various frustums of the cones shapes, in different dimensional configurations, can be manufactured without material fracture during the process. The goal is to check each part using numerical simulation, before SPIF process implementation and effective manufacturing, avoiding unnecessary costs.

It was decided to simulate the SPIF process for a batch of frustum of cone parts, using as input the real material properties for DC05 deep drawing steel and the forming toolpath description using the array parameters generated using TMPG

Fig. 14 TMPG integration in SPIF simulation stages [7]
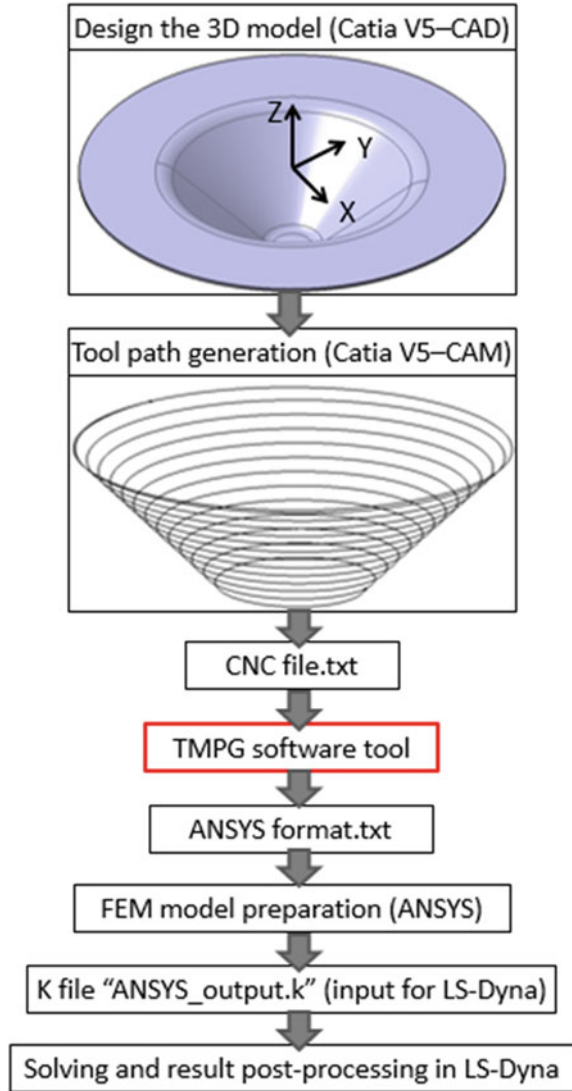
software tool. All the dimensional configurations of the parts have the upper base diameter D = 85 mm, H the parts height, α the draw angle, and Δz the incremental step down used in manufacturing, being the parameters which are different from a part to another one, as follow (Fig. 15) [5]:

- CONE-D85H20α35Δz0.5—part height H = 20 mm, part draw angle α = 35°, being manufactured using an incremental step down of Δz = 0.5 mm.
- CONE-D85H20α35Δz1—part height H = 20 mm, part draw angle α = 35°, being manufactured using an incremental step down of Δz = 1 mm.
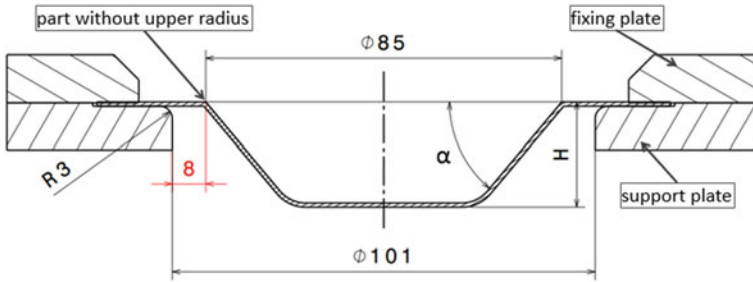
Fig. 15 Part and fixing device [5]

- CONE-D85H35α50Δz0.5—part height H = 35 mm, part draw angle α = 50º, being manufactured using an incremental step down of Δz = 0.5 mm.
- CONE-D85H25α55Δz1.5—part height H = 25 mm, part draw angle α = 55º, being manufactured using an incremental step down of Δz = 1.5 mm.

In Fig. 15 are presented the main dimensions of the fixing device components, which are involved in the SPIF process.

As it was already mentioned before (Sect. 2.1), the FEM models preparation for all parts configurations were done in ANSYS APDL, generating the *K* files, which were solved in LS-DYNA Explicit. The results processed in LS-PrePost workbench are presented in Fig. 16 [5].

The dimensional parts configurations were designed to be deformed by increasing the difficulties in terms of forming conditions, meaning ascending heights, ascending draw angles and rising the step down from 0.5 to 1.5 mm. According to FEM simulation results presented in Fig. 16, all parts configurations should be able to be manufactured without material fracture during the forming process [5].

3 Technological Setup Used in Single Point Incremental Forming Process

SPIF process implementation requests a technological setup which can ensure the forming conditions according to the process working principle presented in Fig. 1. The main elements necessary to implement SPIF process are: a forming tool, a blank fixing device and a CNC milling machine able to drive the forming tool on the trajectory movements.

The forming tool used in the study is presented in Fig. 17. It is similar with a simple rod, with a rounded active head. The tool has two steps in terms of diameters, the active head of 12 mm diameter and the tool tail of 18 mm diameter, for an increased stiffness. The passing between both diameters is made by a smooth conical surface. It can be said that it is a hemispherical forming tool due to its active head shape.
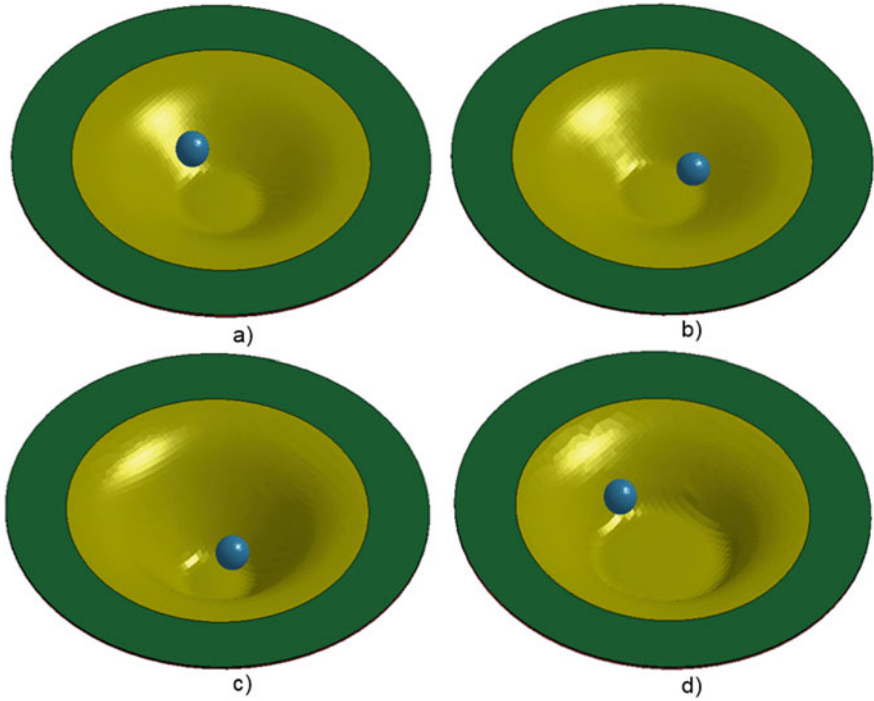
Fig. 16 FEM results for SPIF simulation process: **a** CONE-D85H20α35Δz0.5, **b** CONE-D85H20α35Δz1, **c** CONE-D85H35α50Δz0.5, **d** CONE-D85H25α55Δz1.5 [5]
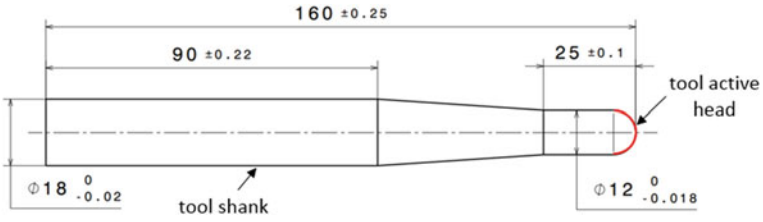

Fig. 17 Hemispherical forming tool [5, 18]

The forming tool is manufactured from C45 carbon steel using turning process, being hardened to increase the tool surface durability [5].

The fixing device was designed to accomplish the SPIF necessity, meaning the planar sheet blank clamping around the outer contour. According to other design variants available in the literature [21, 22], the fixing device designed by the authors is composed of a set of plates which are raised at a certain height on four columns on the base plate (Fig. 18). It allows the parts manufacturing up to 100 mm in diameter and height. By changing only the support plate, the fixing device can be adapted to deform parts as pyramidal frustum parts [17] or other shape parts [23]. In Fig. 18 is
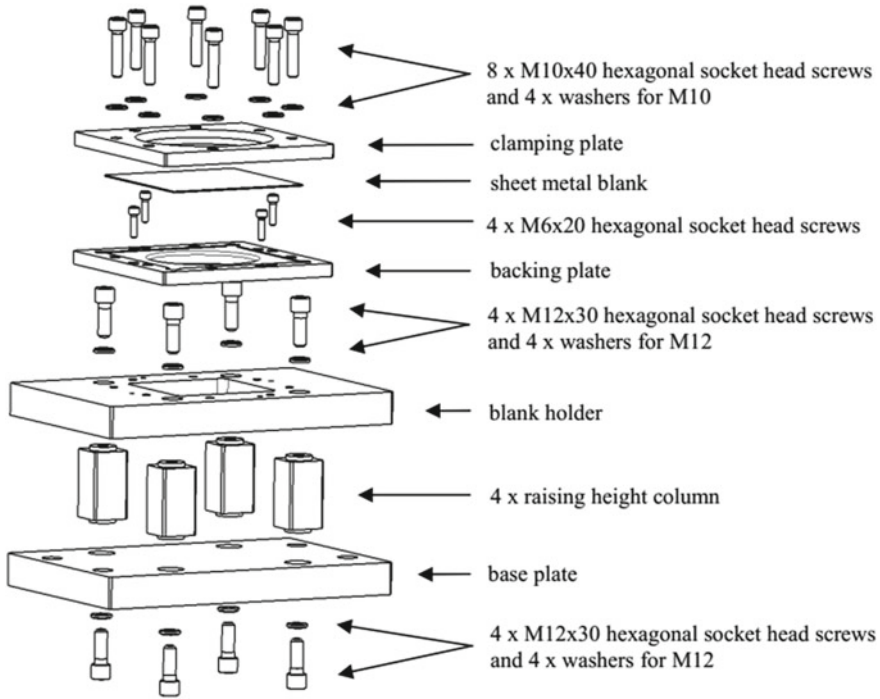
8 x M10x40 hexagonal socket head screws
and 4 x washers for M10

clamping plate

sheet metal blank

4 x M6x20 hexagonal socket head screws

backing plate

4 x M12x30 hexagonal socket head screws
and 4 x washers for M12

blank holder

4 x raising height column

base plate

4 x M12x30 hexagonal socket head screws
and 4 x washers for M12

Fig. 18 Fixing device components [5]

presented an exploded view of the fixing device components. It can be seen that all components are fixed together with different metric screws sizes, the whole assembly being mounted on a solid base plate which will be clamped on the CNC machine table. The device was designed using the Part Design workbench from CATIA V5.

Before the device components manufacturing, the assembly stiffness was also checked by numerical simulation in ANSYS Workbench. It should be able to support the sheet blank during the process, with minimum elastic displacements under the action of the process forces. During SPIF process, three force components act on the part to be deformed: the axial force Fz, in Z direction, the radial force Fx, in X direction and the tangential force Fy on Y direction [1, 24]. The fixing device rigidity was checked by numerical simulation on each direction mentioned above, and the results are presented in Fig. 18. In order to avoid sliding between all four columns and the base plate and the blank holder components, cylindrical bosses were implemented on each column extremity. Those bosses perfectly fits on dedicated holes implemented on the base plate and the blank holder as it is presented in Fig. 19, a. According to FEM results, the final device assembly is able to support the forces which act during the SPIF process, with minimum elastic displacements, being stiff enough in order to not introduce unwanted part dimensional deviations.
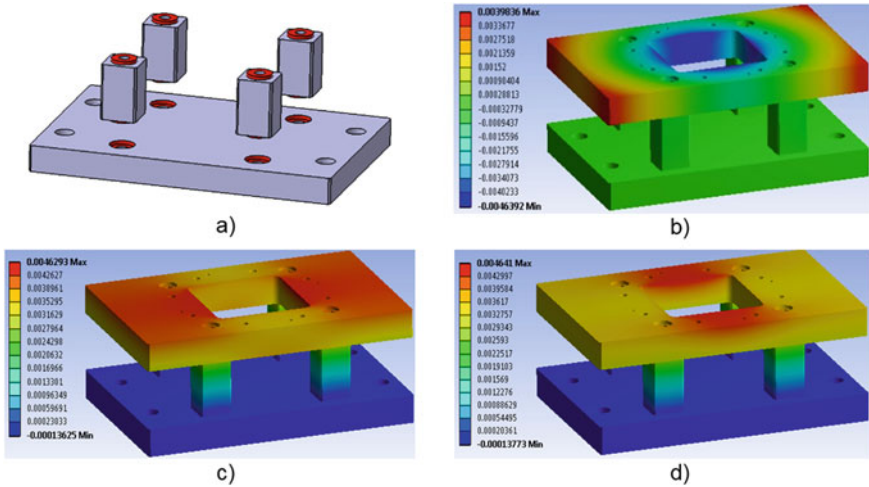
Fig. 19 Fixing device simulation: **a** columns with cylindrical bosses, **b** displacements in Z direction, **c** displacements in X direction, **d** displacements in Y direction [5, 23]

Taking into account the positive FEM results regarding the blank fixing device rigidity, its components were machined and assembled as it is presented in Fig. 20.

The machine-tool used for SPIF process implementation is a 3-axis CNC milling machine, Victor V-Center 55, which is presented in Fig. 21 together with the entire technological setup used in the process.

Therefore, the technological setup used in SPIF process implementation is composed from a 3-axis CNC milling machine, a 12 mm diameter hemispherical forming tool clamped, using a tool holder, on the machine spindle, and a high rigidity blank fixing device which is clamped on the milling machine table by using two parallel vices [5, 7, 23].

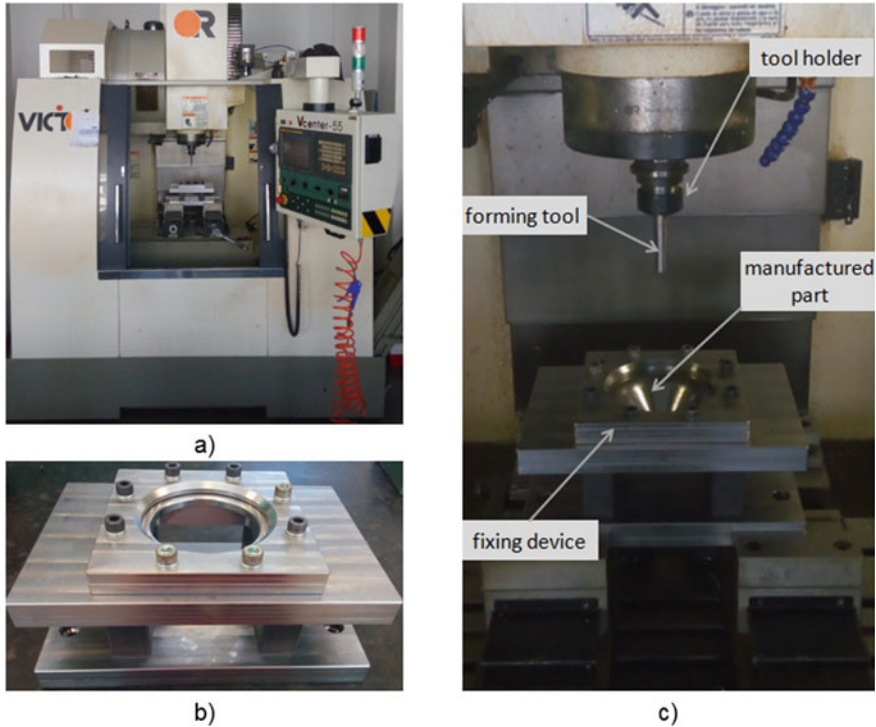**Fig. 20** Final assembly of fixing device [5, 23]
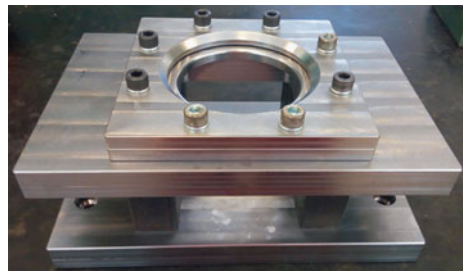
Fig. 21 SPIF technological setup: **a** CNC milling machine, **b** blank fixing device, **c** setup implementation [5, 7, 23]

4 Experiments in Single Point Incremental Forming Process

In research, FEM simulation results are always validated through practical experiments. According to SPIF numerical simulations, all four parts dimensional configurations should be able to be manufactured without material fracture during the forming process. Thus, experiments are required in order to validate the results obtained in a virtual environment.

4.1 Forming Strategy Used for Frustum of a Cone Deforming

Forming strategy used in this study includes all the details about the SPIF process implementation: the manufactured parts shape and dimensions, the blank material, blank shape and its dimensions, the entire technological setup used for process implementation, the process parameters and the type of forming toolpath. The parts shape,
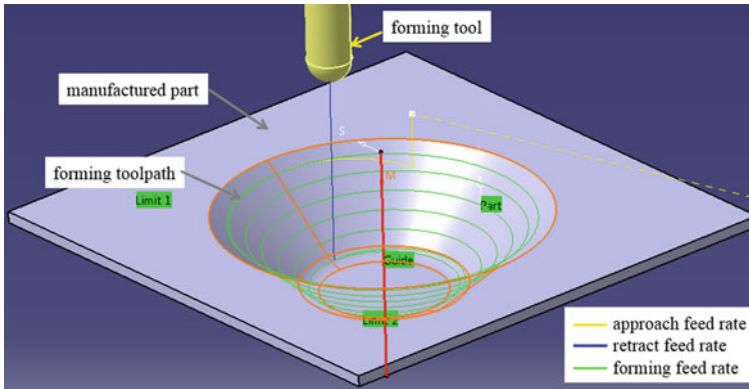
Fig. 22 Forming toolpath [5, 23]

dimensional configurations and the incremental step down value used for its manufacturing and the entire technological setup are presented in details in the previous sections. The blank material (DC05 deep drawing steel with 1 mm thickness) real mechanical properties are also known. The blanks have a square shape, being obtained from the entire sheet plate using abrasive water jet technology. The SPIF process parameters were adopted based on a detailed study of the literature. In order to decrease the friction forces between forming tool and sheet blank, mineral oil was used as lubrication fluid together with a relatively small tool spindle speed of 200 rpm. Taking about the tool feed rate, by association with a milling process, three tool feed rate values are involved in a forming toolpath which are presented in Fig. 22 [5]:

- *Working feed rate* (1500 mm/min) are symbolized with green curves. This is, in fact, the feed rate value used in the local plastic deformation process.
- *Approach feed rate* (500 mm/min) are symbolized with yellow curves. This is a value used to avoid a dynamic contact between forming tool and sheet blank.
- *Retract feed rate* (rapid machine feed rate) is symbolized with a blue line, being used for the rapid tool retraction from the part cavity.

In Fig. 22 is also presented the forming toolpath. A spiral toolpath was chosen for parts manufacturing, because it is a continuous toolpath, in comparison with the Z-level toolpath which can left a visible trace on the part wall when the tool passes from one layer to another [1, 5].

The presented forming strategy was used in exactly the same manner, also for FEM analysis, in order to simulate the real forming conditions for the SPIF process. According to FEM simulations, all four parts designed to the experiments were able to be manufactured without material fracture during the forming process. Those are presented in Fig. 23, in three positions for part: top view, bottom view and isometric view [5].

Taking into account that all four parts were manufactured in good conditions, it can be said the results obtained in the numerical simulations are validated. Thus, FEM
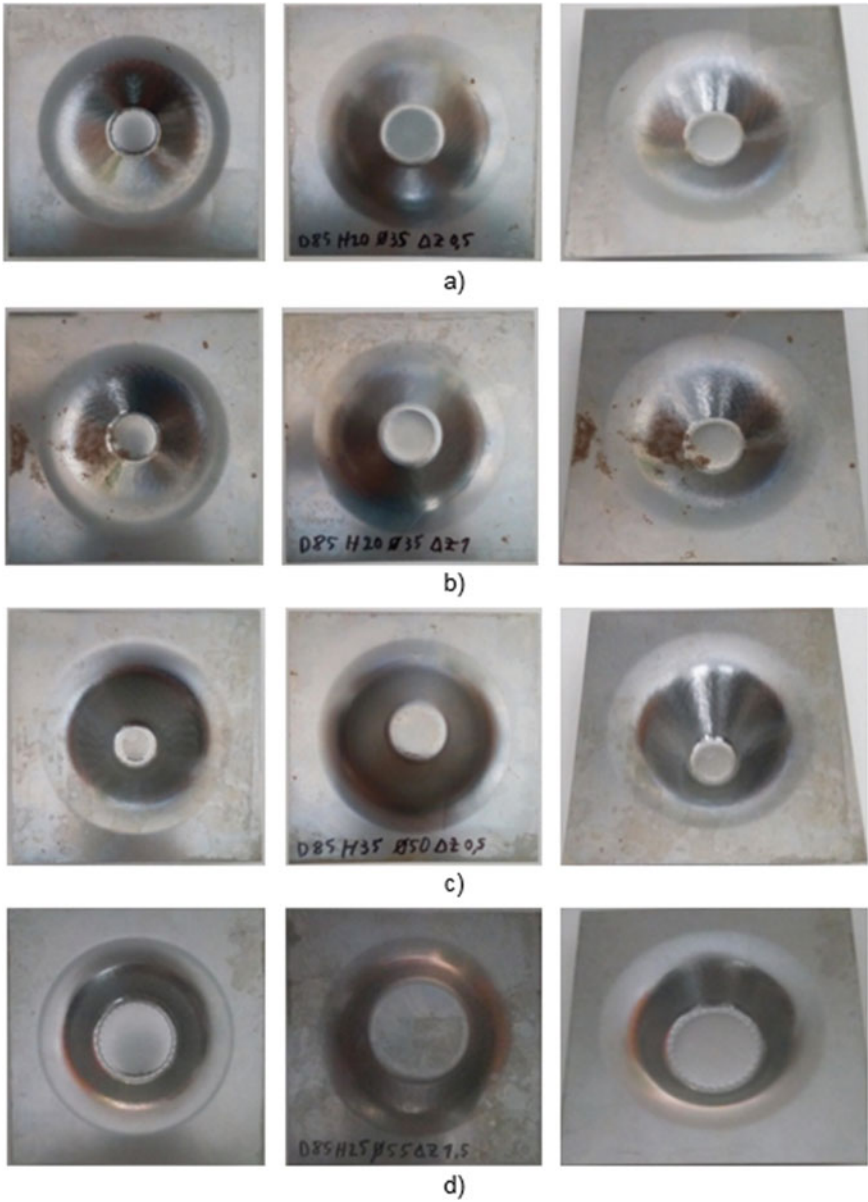
Fig. 23 Manufactured parts through SPIF process: **a** CONE-D85H20α35△z0.5, **b** CONE-D85H20α35△z1, **c** CONE-D85H35α50△z0.5, **d** CONE-D85H25α55△z1.5 [5]

simulations can be successfully used to simulate the SPIF process, but if confidence results are expected, the proper input data in terms of material properties should be used. Because the material properties are usually different from one batch to another, it is recommended to be determined the real material properties, in an experimental manner, for the sheet blank batch which will be used in the part manufacturing [18].

It is well known that, using a conventional SPIF process, the obtained parts dimensional accuracy is a week point in terms of quality. To measure the dimensions for all manufactured parts could be used a measuring method based on 3D scanning technology.

4.2   3D Scanning Used for Parts Measuring

3D scanning is a successfully method used in different fields as reverse engineering but is also used for various parts measurements, including the parts manufactured through SPIF process [5, 25]. Using this method, a 3D model of the digitised surface is obtained, based on which measurements are done, using a CAD software. One of the major advantages in comparison with contact based measurements methods, is that, once obtained the scanned part 3D surface, whenever new measurements are necessary, those can be done without additional preparations [5]. To implement the 3D scanning method, in case of SPIF manufactured parts, several steps should be followed [5, 25]:

- Surface preparation: the sheet metal surfaces which will be digitised, should be prepared previously by cleaning the lubrication oil and by covering the glossy areas with a mat powder, in order to prevent the reflection of light beams used in the scanning process.
- Surfaces scanning: the digitised surfaces are the parts inside surfaces, which were in contact with the forming tool, during the SPIF process. Comet L3D scanner with blue light was used for this purpose. In this stage, a point cloud is obtained. The parts were positioned on the scanner table (Fig. 24), and the point cloud was obtained from one single scan on an inclined position.
- Point cloud processing: the points clouds obtained on the previous stage, should be further processed using a specialized CAD software. In this case, for points clouds processing was used CATIA V5, the Digitized Shape Editor and the Quick Surface Reconstruction workbenches. The scanned 3D surface is obtained, as it is presented in the example from Fig. 25. The processing stage supposes three intermediary steps: point cloud filtering and cleaning the noise points, point cloud meshing and the final surface reconstruction.
- Preparing the assembly for measurements: the scanned surface obtained on the previous stage, is matched with the initial part 3D CAD model which was designed to be manufactured. The surfaces matching is made based on the parts planar flanges and based on the parts axis.
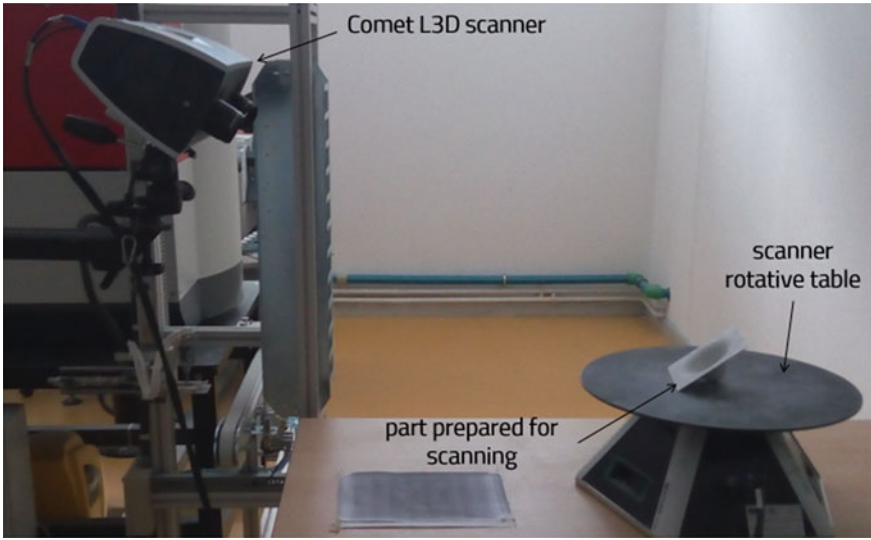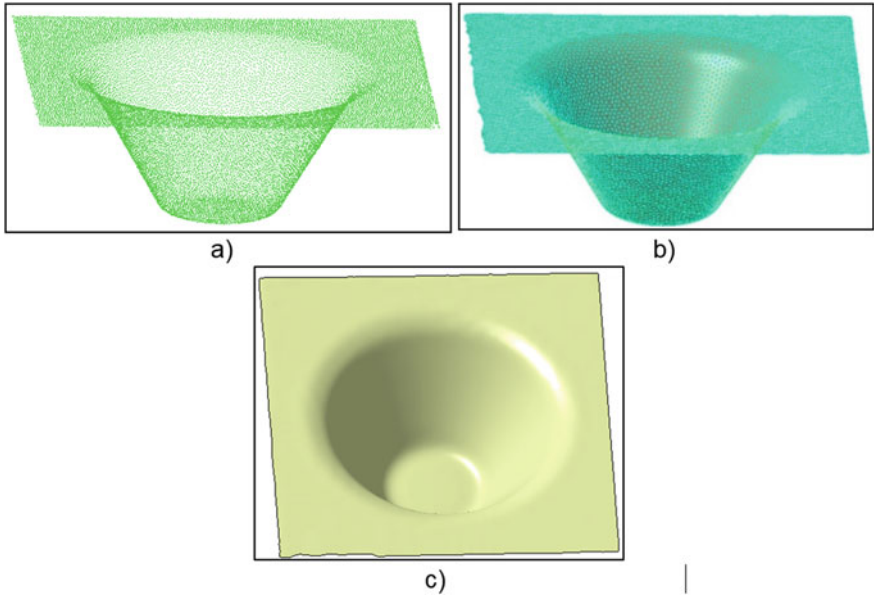
Fig. 24 Part position on Comet L3D scanner [5]

Fig. 25 Points cloud processing stages: **a** point cloud filtering, **b** point cloud meshing, **c** final surface reconstruction [5]

- Deviations measurements: deviations are between the desired parts CAD models, and the real manufactured surfaces, obtained through 3D scanning. This step was also done using CATIA V5.

All the above presented stages were performed for each part configurations manufactured, and for each one, a final 3D surface was obtained.

4.3 Precision of Deformed Frustums of Cone

The dimensional accuracy of the parts manufactured through SPIF process, was measured in CATIA V5, using the matched assembly between the upper surfaces of the initial part CAD model and the surfaces obtained through 3D scanning method. The measurements are done in a section with a plane perpendicular on the part flange, which passes through part symmetry axis. Three deviations are measured: the first on the upper radius areas, the second on the middle parts walls, and the third on the parts bottom. In the Figs. 26, 27, 28 and 29, are presented the deviations between parts CAD models and the scanned digitised surfaces.

For a better overview upon the measured values for the parts deviations, those are centralised in Table 3 [5].

Regarding the dimensional accuracy of the parts manufactured through SPIF process, according to the parts deviations presented in Table 3, several conclusions can be drawn.

The parts accuracy in the upper radius area is decreased for the parts with a bigger draw angle. In this area, to improve parts accuracy, the part flange must be sustained by a support plate, as close as possible to the parts tapered walls. This is also emphasised by other authors [5, 26].

Fig. 26 Dimensional precision for CONE-D85H20α35Δz0.5 part [5]

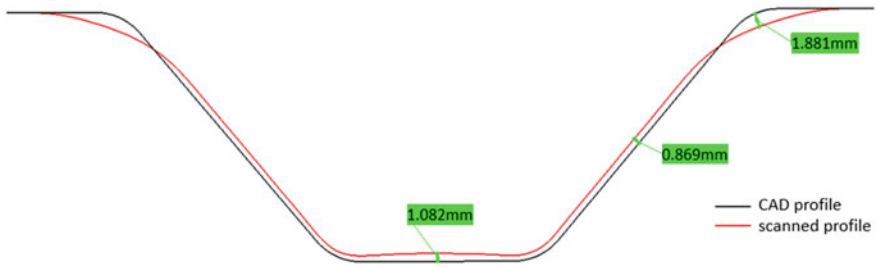**Fig. 27** Dimensional precision for CONE-D85H20α35Δz1 part [5]

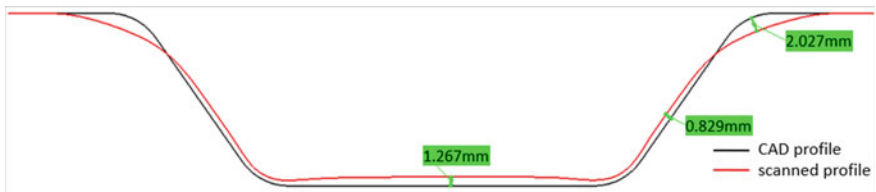**Fig. 28** Dimensional precision for CONE-D85H35α50Δz0.5 part [5]

Fig. 29 Dimensional precision for CONE-D85H25α55Δz1.5 part [5]

Table 3 Deviations measured by 3D scanning method [5]

Dimensional configuration	Upper radius deviation [mm]	Part wall deviation [mm]	Part bottom deviation [mm]
CONE-D85H20α35Δz0.5	1.449	0.909	1.11
CONE-D85H20α35Δz1	1.451	0.947	1.161
CONE-D85H35α50Δz0.5	1.881	0.869	1.082
CONE-D85H25α55Δz1.5	2.027	0.829	1.267

The deviations measured on the parts tapered walls seem to be improved by increasing the draw angle value. On that area, the part precision is affected by an well-known elastic phenomena, which is specific for the parts manufactured through material forming, called springback effect [11].

Finally, the parts accuracy in the bottom area is rising when the bottom surface has a small diameter. The bottom inaccuracies is due to another well-known effect in SPIF field, called pillow effect [27]. For pillow effect reduction, a good solution is to extend the forming toolpath also on the bottom area, this surfaces usually being undeformed [11].

5   Conclusions

This chapter presents the entire flow necessary for parts manufacturing using the single point incremental forming process based on studies made by the authors. These were done from theoretical point of view using the finite elements numerical simulations, and also experimental validation by SPIF process implementation.

In the first section, an introduction of the SPIF process is made, presenting also the working principle and the basic elements necessary for SPIF implementation.

The second section presents aspects regarding the process FEM simulation. It was presented the main stages necessary to be followed to implement the numerical analysis for SPIF process, using ANSYS APDL for the pre-processing stage, LS-DYNA Explicit to solve the analysis and LS-PrePost for results post-processing. There were also presented how the real material properties for DC05 deep drawing steel are determined in an experimental manner. Because the toolpath description is a time-consuming stage, a software tool solution was developed by the authors and it was detailed. At the end, numerical simulations were made and the results are presented for several frustum of cone shapes, in various dimensional configurations.

The third section presents the technological setup used for SPIF implementation. Using this setup, to emphasize the necessity of practical validation of the results obtained in the simulations, the parts dimensional configurations which were simulated using FEM analysis, were also manufactured and presented in section four. In this last section it is also presented how the parts are measured using a scanning method and the dimensional accuracy obtained through SPIF process of frustum of cones parts manufactured from DC05 deep drawing steel.

References

1. Nasulea D, Oancea G (2017) Incremental deformation: a literature review. In: MATEC web conference, vol 121, pp 3017
2. Paniti I, Somló J (2014) Novel incremental sheet forming system with tool-path calculation approach. Acta Polytech Hung 11(7):43–60
3. Devarajan N, Sivaswamy G, Bhattacharya R, Heck DP, Siddiq MA (2014) Complex incremental sheet forming using back die support on aluminium 2024, 5083 and 7075 alloys. In: Proceeding of Engineering 11th International Conference on Technology of Plasticity-ICTP81, pp 2298–2304
4. Sharma V, Gohil A, Modi B (2017) Experimental investigation of single point incremental forming of aluminum sheet in groove test. Appl Mech Mater 867:177–183
5. Nasulea D (2019) Research regarding the incremental forming of DC05 steel sheet parts (Cercetări privind deformarea incrementală a pieselor din tablă de oțel DC05), PhD thesis, Transilvania University of Brasov
6. Jeswiet J, Geiger M, Engel U, Kleiner M, Schikorra M, Duflou J, Neugebauer R, Bariani P, Bruschi S (2008) Metal forming progress since 2000. CIRP J Manuf Sci Technol 1(1):2–17
7. Nasulea D, Oancea G (2018) Integrating of a new software tool used for tool path generation in the numerical simulation of incremental forming process. Strojniški Vestn J Mech Eng 64(10):643–651

8. Liu Z, Li Y, Meehan PA (2013) Experimental investigation of mechanical properties, forma-bility and force measurement for AA7075-O aluminum alloy sheets formed by incremental forming. Int J Precis Eng Manuf 14(11):1891–1899

9. Minutolo FC, Durante M, Formisano A, Langella A (2014) Forces analysis in sheet incremental forming and comparison of experimental and simulation results. In: Intelligent production machines and systems-2nd I*PROMS virtual international conference, 3–14 July 2006, pp 229–234 (January 2014)

10. Fu Z, Mo J, Han F, Gong P (2013) Tool path correction algorithm for single-point incremental forming of sheet metal. Int J Adv Manuf Technol 64(9):1239–1248

11. Gatea S, Ou H, McCartney G (2016) Review on the influence of process parameters in incremental sheet forming. Int J Adv Manuf Technol 87(1):479–499

12. Blaga A (2013) Oleksik V (2013) A study of the influence of the forming strategy on main strains, thickness reduction and forces in single point incremental forming process. Adv Mater Sci Eng 4:2–7

13. Oleksik VŞ (2005) Theoretical and experimental research regarding incremental forming process of indigenous metal sheets (Cercetări teoretice şi experimentale privind procedeul de deformare incrementală a tablelor metalice de fabricaţie indigenă), PhD thesis, Lucian Blaga University of Sibiu

14. Blaga A (2011) Contributions of incremental forming of thin sheets (Contribuţii la deformarea incrementală a tablelor metalice subţiri), PhD thesis, Lucian Blaga University of Sibiu

15. ANSYS Documentation https://www.ansys.stuba.sk/html/elem_55/chapter1/ES1-1.htm. Accessed 23 Nov 2018

16. Petek A, Podgornik B, Kuzman K, Čekada M, Waldhauser W, Vižintin J (2008) The analysis of complex tribological system of single point incremental sheet metal forming-SPIF. Strojniški Vestn J Mech Eng 54(4):266–273

17. Nasulea D, Oancea G (2019) Research on manufacturing of pyramidal frustum parts using single point incremental forming process. In: IOP conference series materials science and engineering, vol 564, no 1, pp 012019

18. Nasulea D, Oancea G (2021) Influence of DC05 deep drawing steel real material properties on numerical simulation of incremental forming process. In: IOP Conference Series: Materials Science and Engineering, vol 1009, no 1, pp 012041

19. Bologa O (2014) Cold forming technologies (Prelucrari prin deformare plastica la rece), Lucian Blaga University Press

20. Nimbalkar DH, Nandedkar VM (2013) Review of incremental forming of sheet metal components. Int J Eng Res Appl 3(5):39–51

21. Borrego M, Morales-Palma D, Martínez-Donaire AJ, Centeno G, Vallellano C (2015) On the study of the Single-stage Hole-flanging process by SPIF. Proc Eng 132:290–297

22. Duflou JR, D'hondt J (2011) Applying TRIZ for systematic manufacturing process innovation: the single point incremental forming case. Proc Eng 9:528–537

23. Nasulea D, Oancea G (2018) Design and manufacturing of a fixing device for incremental sheet forming process. In: MATEC web conference, vol 178, pp 02004

24. Behera AK, De Sousa RA, Ingarao G, Oleksik V (2017) Single point incremental forming: An assessment of the progress and technology trends from 2005 to 2015. J Manuf Process 27:37–62

25. Neagoe I, Filip AC, Manolescu A (2014) Digital scanning method for thickness analysis of hollow parts manufactured by incremental forming on a CNC Lathe. Appl Mech Mater 657:142–146

26. Essa K, Hartley P (2011) An assessment of various process strategies for improving precision in single point incremental forming. Int J Mater Form 4(4):401–412

27. Gupta P, Szekeres A, Jeswiet J (2019) Design and development of an aerospace component with single-point incremental forming. Int J Adv Manuf Technol 103:3683–3702

Designing Novel Synthetic Grafts for Large Bone Defects: Experimental and Numerical Studies

Evangelos Daskalakis, Zhanyan Xu, Abdalla M. Omar, Fengyuan Liu, Anil A. Acar, Ali Fallah, Glen Cooper, Andrew Weightman, Gordon Blunn, Bahattin Koç, and Paulo Bartolo

Large bone defects, usually associated to victims of natural disasters, wars and severe accidents, represent a major clinical problem. The search for an effective and efficient treatment is a key area of research. Our group is exploring a novel and fully automatic approach to produce synthetic grafts anatomically designed to fit on the defect site and able to promote tissue regeneration. These grafts, called bone bricks should be highly porous, for cell attachment and spreading, and presenting appropriated mechanical properties to support the physiological loads once implanted. They must be also degradable, with a degradation rate similar to the regeneration rate of the new tissue. Geometrically, pore size, pore architecture, pore distribution and pore interconnectivity are critical parameters determining mechanical properties, permeability and cell spreading. The design of bone bricks to maximise all of these properties requires extensive experimental work. This Chapter describes the main steps associated to the design and fabrication of biodegradable bone bricks. Three different bone bricks configurations, presenting different porosity levels, are considered, produced using additive manufacturing and mechanically tested under compressive loads. Moreover, a simple simulation approach to predict the mechanical behaviour of bone bricks allowing to determine compressive modulus and to understand the deformation mechanism is also presented. Results show that, by

E. Daskalakis · Z. Xu · A. M. Omar · F. Liu · G. Cooper · A. Weightman · P. Bartolo (✉)
School of Mechanical, Aerospace and Civil Engineering, University of Manchester, Manchester M13 9PL, UK
e-mail: paulojorge.dasivabartolo@manchester.ac.uk

A. A. Acar · A. Fallah · B. Koç
Faculty of Engineering and Natural Sciences, Sabanci University, Orhanli-Tuzla, Istanbul 34956, Turkey

G. Blunn
School of Pharmacy and Biomedical Sciences, University of Portsmouth, Portsmouth PO1 2DT, UK

controlling the architecture of the bone bricks, it is possible to obtain synthetic grafts with compressive modulus in the range of trabecular bone. Results also show a good agreement between numerical and experimental results suggesting that the simulation strategy is a viable tool for the mechanical design of the bone bricks.

1 Introduction

Bone defects associated with non-unions and large bone loss often resulted in extended healing periods, higher complications rates and long-term morbidity. Moreover, the inoculation of microbial pathogens at the time of initial trauma, during the initial fixation surgery or during the healing process may lead to a delay of fracture union, loosening of fixation and chronic osteomyelitis [1]. The treatment of these defects is complex and expensive, placing a burden on the public health system. The costs resulting from the patient's inability to work and mental conditions such as depression as a consequence of the post-traumatic psychological distress are also significant.

A number of surgical techniques exist to address these larger defects but require multiple procedures and significant morbidity with a high rate of complications. Amputation is, in most cases, the clinical approach as it provides short recovery time but with significant loss of limb function. Other techniques include internal fixators, bone shortening, external fixation (distraction osteogenesis) and induced membrane [2–4].

Internal fixation methods such as intramedullary nails or plates to stabilise bone gaps after septic conditions increases the risk for complications as recurrent infections after internal fixation may lead to even larger defects [5, 6]. Recent developments in the field of prosthesis design and manufacturing allows surgeons to replace entire limbs using megaprostheses. These special prostheses, initially developed for the treatment of severe oncological bone loss, have been used in non-oncological conditions, such as acute trauma in severe bone loss and poor bone quality, aseptic and septic post-traumatic failures, major bone loss in prosthetic revision and periprosthetic fractures [7, 8]. However, this approach requires complex surgery and can only be considered in extreme and selected cases.

A successful therapeutic concept is the "diamond concept", based on five factors: osteogenicity (mesenchymal stem cells), osteoconduction (bone graft), osteoinduction (growth factors), mechanical stability and vascularity [9–11]. This concept was explored by Masquelet [12–14], which proposed a two-stage method of treating bone defects to both aseptic and septic conditions. In the first stage, a cement spacer is placed in the bone defect, inducing the formation of a biological membrane. In the second stage, the cement spacer is removed, and a bone graft is placed within the tube of the induced membrane. This membrane is impermeable, hyper-vascular and biologically active. It has enough strength to form a closed biological chamber after the cement removal, maintaining the volume for bone grafting, decreasing resorption of the cancellous bone and preventing ingrowth of soft-tissue. It consists of

ephithelial-like cells, fibroblasts, myofibroblasts, and type I collagen, being also highly vascularised with blood vessels pointing towards the bone defect. It also contains vascular endothelial growth factor (VEGF), transforming growth factor-b1 (TGF-b1) and bone morphogenetic protein-2 (BMP-2). However, infection problems and re-fracture associated with poor corticalization have been reported to be associated to this technique [15–17].

The use of bone grafts, particularly free vascularised bone grafts (e.g. vascularised free fibula graft) that contains an internal vascular network, have been also explored to treat critical-size bone defects (5–12 cm in size) allowing short union times and high union rates [18–21]. These autografts are osteogenic, osteoinductive, osteoconductive and have no risks of immunogenicity and disease transmission [22–25]. Main complications are related to pain and morbidity in the donor site, limited quantity and availability, prolonged hospitalization time, the need for general sedation or anaesthesia, risk of deep infection and haematoma, extended non-weight bearing and the risk of inadequate graft hypertrophy [26–28]. An alternative is the use of allografts obtained from cadavers or living donors. However, they present several limitations such as the risk of rejection, transmission of diseases and infections from donor to recipient, limited supply, and the rate of healing is generally lower than autografts [23].

Recently, additive manufacturing techniques have been used to produce synthetic grafts (scaffolds), using biocompatibe and biodegradable materials, as an alternative to biological grafts [23, 29]. These synthetic grafts can be designed to match the defect site, being produced in a controlled and reproducible way using a wide range of natural and synthetic polymers, ceramics and polymer/ceramic composites. These synthetic grafts provide the substrate for cells to attach, differentiate and proliferate leading to the formation of a new tissue [29]. They must be biocompatible, bioactive, biodegradable (must degrade into non-toxic products with a controlled degradation rate that matches the regeneration rate of the native tissue), must present high porosity to enable high cell seeding and vascularisation, and appropriate mechanical properties (e.g. for in vitro applications, they should maintain their mechanical properties to preserve the required space for cell growth and matrix formation, while for in vivo applications it is important that they mimic as closely as possible the mechanical properties of the native tissue in order to provide a temporary support for tissue regeneration and structural stability to the injured site) [24]. However, these synthetic grafts have been designed considering regular shapes and not considering their potential for large bone defects (~20 cm).

Our group, through the EPSRC/GCRF projects "Bone Bricks: design, fabrication and assessment of composite scaffolds for large bone defects", is designing the next generation of synthetic grafts to treat large bone loss injuries, enabling limb salvage. Through an integrated design-modelling-fabrication approach, this project allows the fabrication of biodegradable and biocompatible modular pieces (bone bricks—modular bone scaffolds), from a pallet of shapes and sizes that fit together in a "lego like" way to form the prosthesis. The assembled prosthesis create a hollow cage which is filled with an infection prevention paste containing calcium sulphate and polymeric microbeads encapsulating gentamycin antibiotic (Fig. 1). The prosthesis
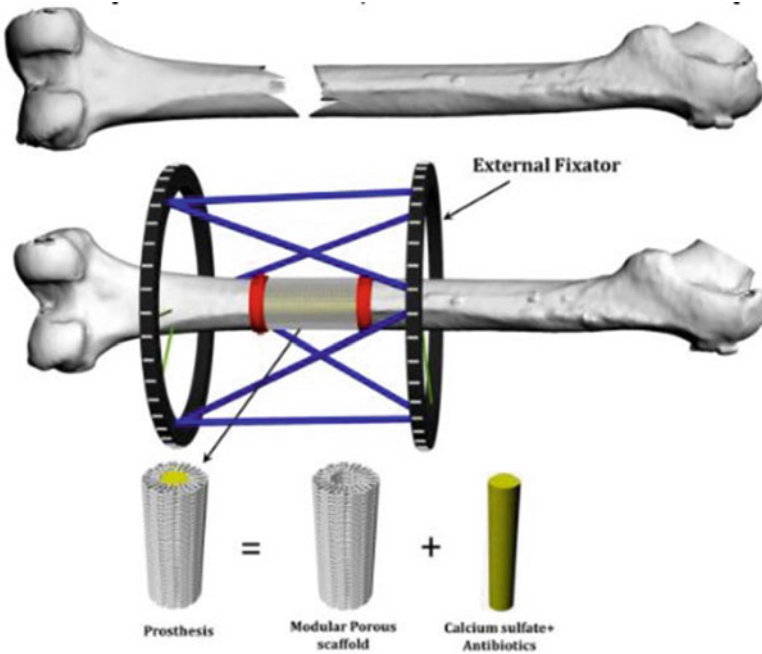
Fig. 1 The bone bricks concept

and paste will prevent infection, promote bone regeneration creating a mechanically stable bone union. This will enable limb salvage as an alternative to amputation, improving recovery time/functional patient outcomes. This Chapters describes the 3D printing fabrication process of polycaprolactone bone bricks considering different printing strategies and a simple and non-expensive simulation strategy to predict the mechanical performance of designed bone bricks, validated against experimental results, considering:

- Linear elastic model: simulations are performed considering small deformations in order to guarantee the structural stability of the bone bricks. Once implanted it is important that the porous channels remain stable to avoid any negative impact on cell spreading and nutrients and oxygen supply. Bone bricks should be designed avoiding plastic deformation or significant deformations.
- Materials are assumed to be homogeneous and isotropic.
- No separation contact condition between the scaffold filaments and the two compressive plates.
- Pore size differences between designed and printed scaffolds are neglected.

2 Bone Bricks Design, Fabrication and Characterization

2.1 Design

A fully automatic and integrated approach is being developed for the design and fabrication of bone bricks. A computational geometry-based tool was developed to model modular porous bone bricks using a parametric femur model based on the frequency of common injuries. The parametric femur model was based on anthropometric data from a total of 1198 males and 1059 females, capturing gender differences. Proper algorithms were developed to create such shapes, to define printing strategies and to send G-code fabrication instructions to 3D printing systems.

```
INPUT: O,h_module ,D_allowable ,R_nail
OUTPUT: {M_q}_q=0…MN
START
   1.  Create_Modules() {
   2.     C_q ←{};CO_q ←{};MO_q ←{};M_q ←{}                      /*Initialization*/
   3.     CO_q ← Intersect (O,Pl_SA ) /*The creation of representative contour curves of defect*/
   4.     While (i < q) {
   5.        j = i+1,m ←0
   6.        While (j < q) {
   7.           k ←0;α ←0
   8.           While (k < DN) {
   9.              P_t_k ←ClosestPoint (P_tCO_jk ,CO_j )
  10.              D = Distance (P_t_k ,P_tCO_jk )
  11.              If (D ≤ D_allowable ) {                        /*Clustering the similar curves*/
  12.                 If (k = DN−1) {
  13.                    C_ma ←CO_j ;k = k+1; j = j+1;a = a+1
  14.                 Else
  15.                    k = k+1    }                             /*End of 2nd If statement*/
  16.                 Else
  17.                    k ←DN ; j ←q    }                        /*End of 1st If statement*/
  18.                 }                                           /*End of 3rd While statement*/
  19.              }                                             /*End of 2nd While statement*/
  20.        i = i+a ;m = m+1    }                                /*End of 1st While statement*/
  21.     For (i =0 to m) {
  22.        For (j =0 to a) {
  23.           C_i ←FitACurve (C_ij ) /*The representative contours of clustered curves*/
  24.                                }                            /*End of 2nd For-loop*/
  25.                             }                               /*End of 1st For-loop*/
  26.     CO_q ←Replace (CO_q ,C_i )  /* Replacing initial contours with fit curves*/
  27.     For (q =0 to MN) {
  28.        MO_q ←Extrude (CO_q ,h_module )
  29.        M_q ←Difference (MO_q ,R_nail ) /*Creation of the final shape of modules*/
  30.                     }                                       /*End of For-loop*/
  31. END                                                        /*End of Create_Modules()*/
END
```

Fig. 2 Algorithm for the design of bone bricks (Algorithm 1) [30]

Figure 2 shows the algorithm used to generate the bone bricks [30]. Briefly, the bone defect volume is sliced to generate a set of contour curves (CO_q). Similar curves are clustered in a set of contours (C_m) and each clustered contour set is then replaced with a fit contour. Finally, each fit contour is extruded along the femoral shaft axis. After the design of the bone bricks, it is necessary to define the path planning, allowing printing material filaments layer by layer in a continuous path with minimum movements between their deposition. The corresponding algorithm is presented in Fig. 3. The path planning will determine pore architecture and pore size. Bone bricks with gradient pore sizes can be easily created using this algorithm.

In this case algorithm 2 was used to create a continuous path planning to create three different bone bricks architectures, using zig-zag (38 double filaments) and spiral-like patterns (6, 9 and 14 filaments) (Table 1). The CAD models used for simulation purposes were created in Solidworks (Dassault Systems, UK), based on the continuous path planning information. As described in Fig. 4, the inner and outer edges of the bone bricks are outlined and joined by straight lines. These straight lines were then divided into 7, 10 and 15 equal segments for the different bone brick groups. After, the segment nodes were connected by curves and swept by a circle to form the filaments for the second layer. To mimic the physical bone bricks an overlap of 0.05 mm between adjacent filaments was considered. A total of 10 layers was considered for all scaffolds. Figure 5 shows the 3D CAD models of the bone bricks considered in this study.

2.2 Fabrication

Bone bricks were produced using the material extrusion additive manufacturing 3D Discovery system (RegenHU, Switcherland) (Fig. 6). The three groups of bone bricks were produced using PCL (CAPA 6500, Mw = 50000 Da), a semi-crystalline linear aliphatic biopolymer commonly used for bone tissue enginnering, supplied by Perstorp Caprolactones (Cheshire, UK) in the form of pellets. Bone bricks were produced considering the following processing conditions: melting temperature 90 °C, deposition velocity of 18 mm/s, screw rorational velocity of 14 rpm and 6 bar of pressure. During the production process the pellets were placed in a heated reservoir, melted and moved into the screw chamber using compressed air and extruded out with the use of a needle with a diameter of 0.33 mm. Printed bone bricks are shown in Fig. 7.

INPUT: $D_n, DN, DNL, \{M_q\}_{q=0,\ldots,MN}$

OUTPUT: $\{P_{t_d}^s\}_{d=1,\ldots,D}$

START

1.   **Create_Layers()** {

2. $d \leftarrow 0;\ P_{t_d}^s \leftarrow \{\}$ /*Initialization*/

3.   **For** $(s = 0$ to $n_l)$ {

4.   **If** $(s(mod\,2) = 0)$ **Then** {

5.   **Create_ZigZag_Layers ( )**

6.   **ElseIf** $(s(mod\,2) = 1)$

7.   **Create_Spiral_Layers ( )**

8.   }   /*End of If statement*/

9.   }   /*End of For-loop*/

10. **Create_Zigzag_Layers ( )** {

11.   **For** $(i = 0$ to $2 * DN - 1)$ {

12.   **If** $(i(mod\,4) = 0)$ **Then** {

13. $P_{t_d}^s \leftarrow P_{t_{CO_{qi}}}^s\ ; d = d + 1$

14.   **ElseIf** $(i(mod\,4) = 1)$ **Then**

15. $P_{t_d}^s \leftarrow P_{t_{CO_{qi}}}^s\ ; d = d + 1$

16.   **ElseIf** $(i(mod\,4) = 2)$ **Then**

17. $P_{t_d}^s \leftarrow P_{t_{CO_{qi}}}^s\ ; d = d + 1$

18.   **ElseIf** $(i(mod\,4) = 3)$ **Then**

19. $P_{t_d}^s \leftarrow P_{t_{CO_{qi}}}^s\ ; d = d + 1$ }   /*End of If statement*/

20.   }   /*End of For-loop*/

21. $s = s + 1$ /*Store $P_{t_d}^s$ information for extrusion-based 3D printer*/

22. **END**   /*End of Create_Zigzag_Layers ( )*/

23. **Create_Spiral_Layers ( )** {

24. $\forall P_{t_{CO_{qi}}}^s$ and $\forall P_{t_{CO_{qi}}}^s$

25. **For** $(i = 0$ to $DN - 1)$ {

26. $l_i^s = Line\,(P_{t_{CO_{qi}}}^s, P_{t_{CO_{qi}}}^s)$ /*Creation of lines that spiral paths lies on*/

27.   }   /*End of 1st For-loop*/

28. **For** $(j = 0$ to $DNL - 1)$ {

29. $P_{t_d}^s \leftarrow P_{t_{u_{(j-1)}}}^s\ ; d = d + 1$

30.   **For** $(i = 0$ to $DN - 1)$ {

31.   **If** $(i = DN - 1)$ **Then** {

32. $P_{t_d}^s \leftarrow P_{t_{u_j}}^s\ ; d = d + 1$

33.   **Else**

34. $P_{t_d}^s \leftarrow P_{t_{u_{ij}}}^s\ ; d = d + 1$ }   /*End of If statement*/

35.   }   /*End of 2nd For-loop*/

36.   }   /*End of 3rd For-loop*/

37. $s = s + 1$ /*Store $P_{t_d}^s$ information for extrusion-based 3D printer*/

38. **END**   /*End of Create_Spiral_Layers ( )*/

END

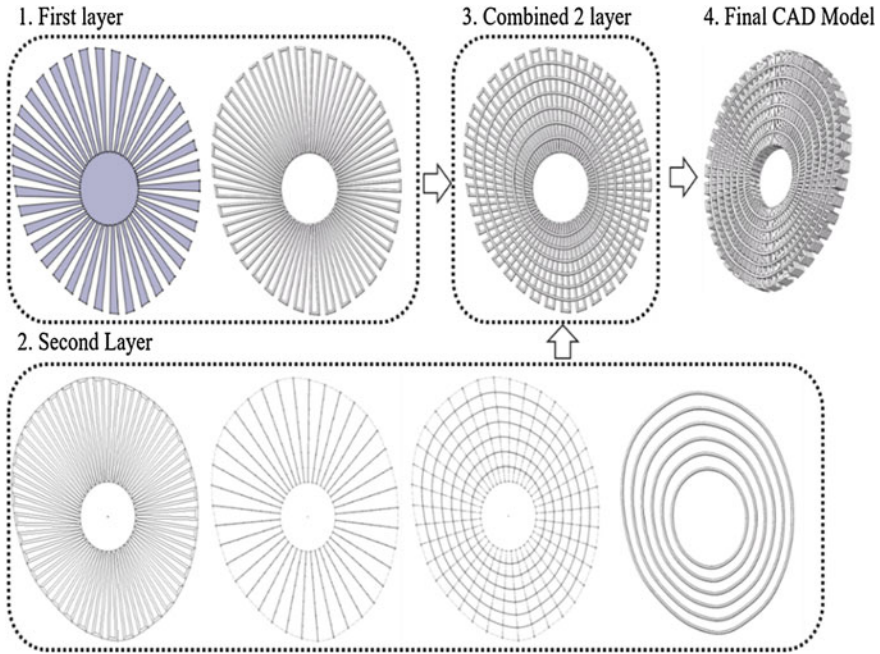**Fig. 3** Algorithm for the creation of continuous path (Algorithm 2) [30]

Fig. 4 Schemtic representation of the main steps to create a 3D bone bricks model. This example corresponds to the 38 double filaments zig-zag and 6 filaments spiral-like pattern
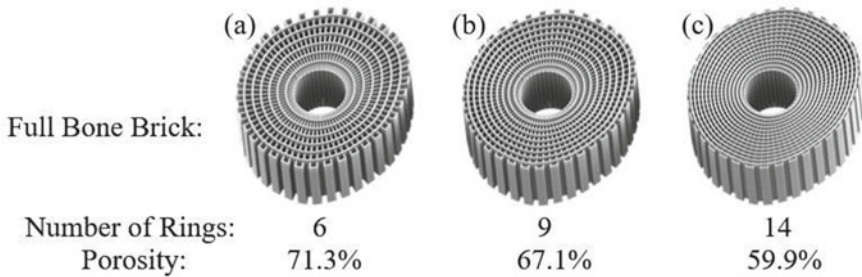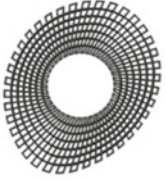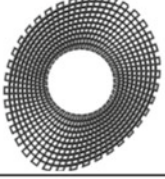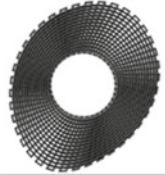

Fig. 5 Bone bricks designs considered in this research, **a** Case 1: 38 double filaments and 6 ring filaments (porosity: 71%); **b** Case 2: 38 double filaments and 9 ring filaments (porosity: 67%); **c** Case 3: 38 double filaments and 14 ring filaments (porosity: 60%)

2.3 Mechanical Characterisation

Bone bricks were mechanically characterized under compression loads. Tests were performed on the INSTRON 3344 (Instron, UK) in dry state following the ASTM D695-15 standards. Bone bricks were tested at a strain rate of 0.5 mm/min with a 2kN

Table 1 Continuous path planning configurations considered in this study

38 Zig Zag Double Filaments	Spiral Layers
	6 Filaments
	9 Filaments
	14 Filaments

load cell. Four bone bricks were tested for each sample group. Before compressive tests, the machine was calibrated according to the supplier guidelines. The Bluehill Universal software (Instron, UK) was used to collect the data and to determine compression modulus (E_c). During the compression tests, the software captured forces, F, and displacement values, automatically converting them into compressive stresses (σ) and strains (ε) as follow:

$$\sigma = \frac{F}{A} \tag{1}$$

$$\varepsilon = \frac{\Delta h}{h_0} \tag{2}$$

where $h0$ is the height of the bone brick sample, A is the initial cross section area and Δh is the height variation.
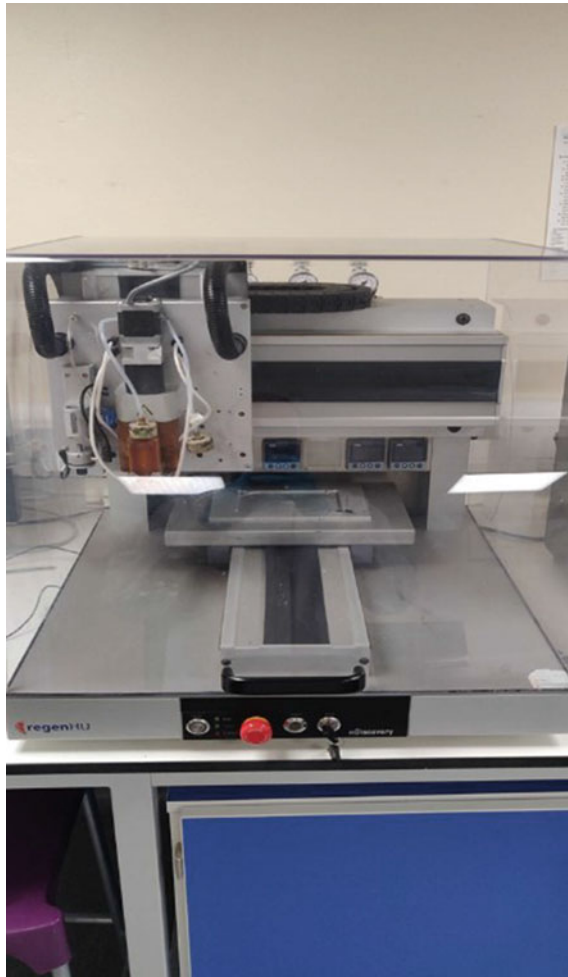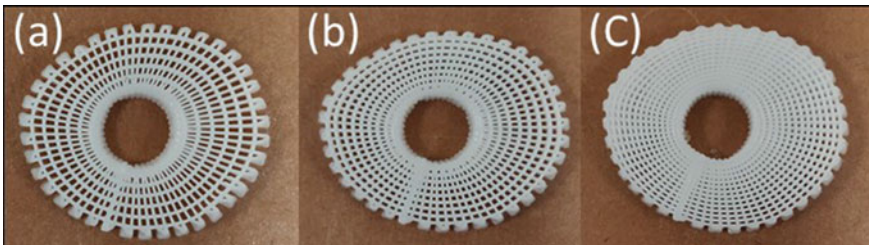
Fig. 6 RegenHU 3D printer

Fig. 7 Printed PCL bone bricks. **a** Case 1: 38 double filaments, 6 ring filaments, **b** Case 2: 38 double filaments, 9 ring filaments, **c** Case 3: 38 double filaments, 14 ring filaments

2.4 Finite Element Simulation

The CAD models created as described in Sect. 2.1 were stored as IGES files and imported into the finite element analysis software Ansys Workbench (Dassault Systems, UK). In order to simulate the experimental work, the scaffolds were positioned in between two compressive titanium plates. A linearly increased compression force up to 400 N was applied across the top plate while keeping the bottom plate fixed (Fig. 8).

Bone bricks were assumed to be made in PCL and the following properties considered for simulation purposes: density of 1.1 g/cm^3; elastic modulus of 400 MPa, and Poisson's ratio of 0.442 [31–34]. Moreover, each adjacent filaments were set to be bonded, with sliding being possible, thus mimicking the bonding of the filaments during the fabrication process. No gap between the scaffold and the plate is considered. For the 6, 9, and 14 ring bone bricks meshs of 168,804, 179,818 and 197,640 tetrahedral elements were considered as in Fig. 9. Convergency analysis was conducted to achieve these optimised mesh densities.

Due to the topology differences between the bone bricks considered in this research, the contact settings for each model are different to allow good accuracy. The settings used for the 14 rings bone bricks are the Ansys default. However, for the other bone bricks configurations the detection method used is the Nodal-normal from contact, and a normal stiffness factor of 0.03 for the 9 rings bone bricks, and 0.01 for the 6 rings bone bricks. The pinball region is used and set as auto.
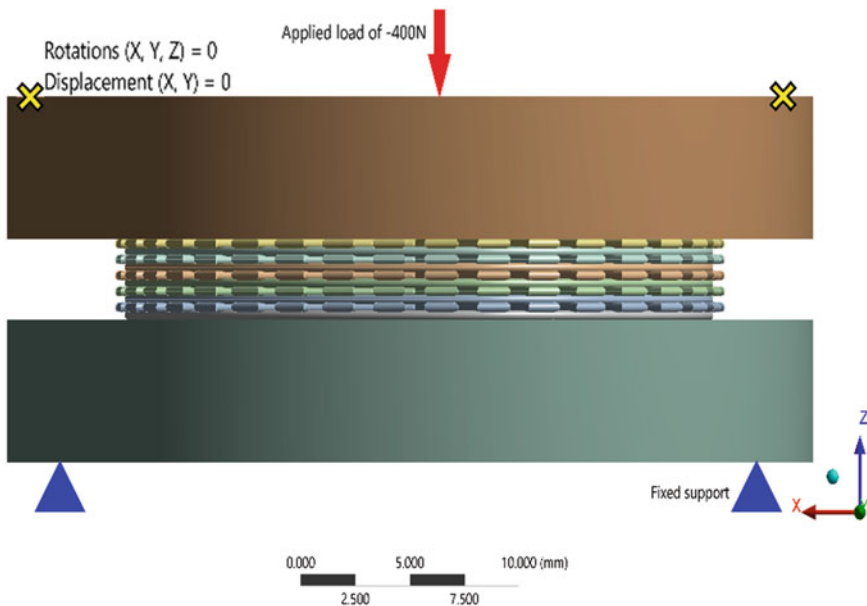

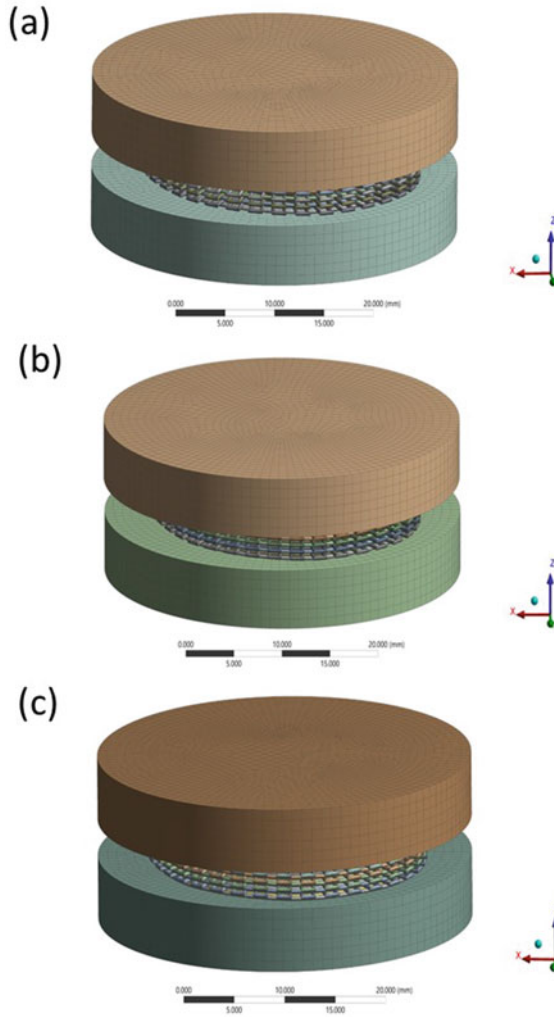**Fig. 8** Boundary and loading conditions

Fig. 9 Meshes considered to simulate the mechanical behavior of the different bone bricks. **a** Case 1: 38 double filaments, 6 ring filaments; **b** Case 2: 38 double filaments, 9 ring filaments; **c** Case 3: 38 double filaments, 14 ring filaments

2.5   *Data Analysis*

Experimental data are represented as mean ± standard deviation. Mechanical results are subjected to one-way analysis of variance (one-way ANOVA) and Tukey's post hoc test with the use of GraphPad Prism software. Significance levels were set at $p < 0.05$.
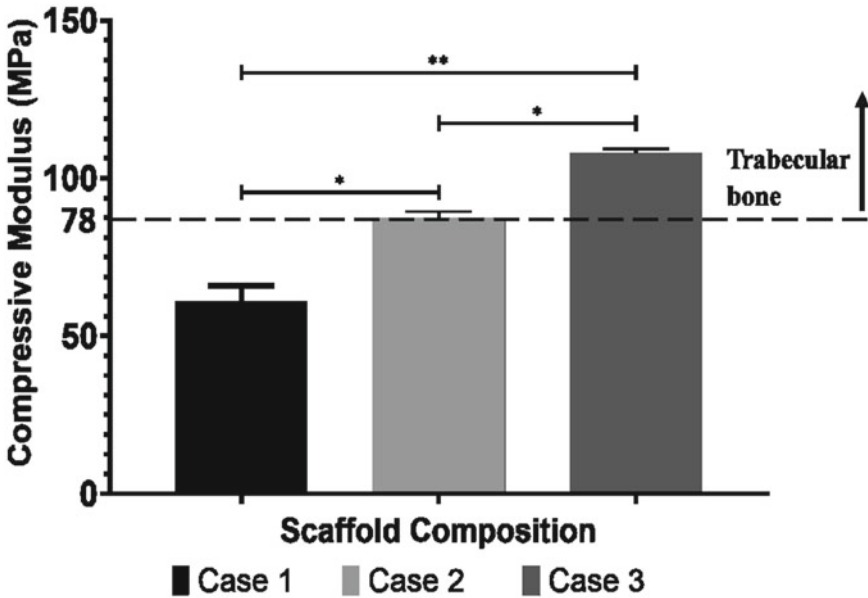
Fig. 10 Compressive modulus of the different bone bricks. Case 1: 38 double filaments, 6 ring filaments; Case 2: 38 double filaments, 9 ring filaments; Case 3: 38 double filaments, 14 ring filaments

3 Results and Discussion

3.1 Mechanical Analysis

As shown in Fig. 10, the mechanical behaviour of the bone bricks strongly depends on the architecture. Results show that by increasing the number of spiral layers (from 6 to 14 spiral layers), the compression modulus increases. This can be explained by the overall decrease in porosity. Results also show that by controlling the number of double and spiral filaments it is possible to create bone bricks with compressive modulus in the trabecular region [35].

3.2 Finite Element Analysis

For the three cases considered in this research, numerically obtained compressive modulus were obtained from the simulated stress-strain curves. Results are presented in Table 2, which compares both numerical and experimentally obtained compressive modulus. Numerical compressive modulus are 74 MPa for the 6 rings bone bricks (Case 1), 90.2 MPa for the 9 rings bone bricks (Case 2), and 110.8 MPa

for the 14 rings bone bricks (Case 3). Experimental results, obtained in the elastic region of the stress-strain curves and for strain values lower than 10%, are 61.0 ± 4.9 MPa for Case 1, 87.2 ± 2.2 MPa for Case 2 and 107.9 ± 1.4 MPa for Case 3. As observed a high level of agreement between experimental and numerical results was obtained (around 92.2%), with differences increasing by increasing porosity. These differences can be attributed to the initial assumptions considered for the numerical simulation [36]. First, simulations were performed considering the bone bricks as homogeneous and isotropic structures. However, printed filaments may contain internal bubbles and all additive manufactured parts are anisotropic not only due to the layer-by-layer approach and layer in-fill strategies but also due to the effect of processing conditions on the material morphological development process during the melting-flow-cooling steps. Previous studies from our group using in situ X-ray diffraction (XRD) experiments, showed the presence of crystalline anisotropy in the printed PCL filaments with the majority of crystals oriented in the direction of flow [37]. Results also showed that an increase on the screw rotational velocity, keeping all the other processing parameters constant, increases the level of orientation improving mechanical properties; while an increase in the melting temperature, keeping all the other processing parameters constant, decreases the level of orientation of the crystalline structure reducing mechanical properties. Secondly, due to the solidification of the molten material being extruded and to the processing conditions being used there are differences between designed and printed filament diameters and pore sizes. Consequently, printed bone bricks usually present different porosities compared to the designed ones. Finally, the mechanical properties used in the simulation model correspond to bulk properties of PCL but not exactly to the same grade of PCL used in the experimental work.

Figures 11, 12 and 13 show the stresses and strains at the bone bricks under a compressive force of 400 N. Due to porosity differences the bone bricks exhibit different behaviours. Bone bricks designed with 38 double filaments and 6 ring filaments exhibited a maximum stress of 20.26 MPa and maximum strain of 7.3% (Fig. 11); while bone bricks designed with 38 double filaments and 9 ring filaments presented a maximum stress of 11.84 MPa and a maximum strain of 3.5% (Fig. 12); and bone bricks designed with 38 double filaments and 14 rings exhibited a maximum stress of 8.31 MPa and a maximum strain of 2.1% (Fig. 13). These results suggest that scaffolds designed with 6 ring filaments are not suitable for bone tissue engineering applications due to the significant deformation of the pores and its negative impact on

Table 2 Experimentally and numerically obtained compressive modulus

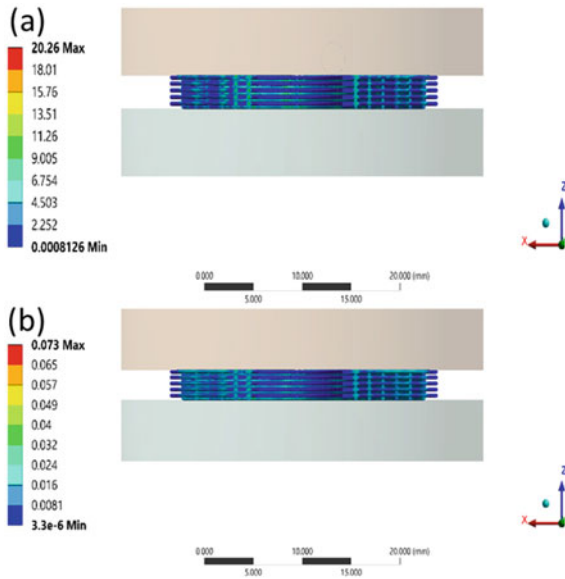| Number of rings	Porosity (%)	Experimental compressive modulus (MPa)	Numerical compressive modulus (MPa)
6	71.3	61.1	74.0
9	67.1	87.2	90.2
14	59.9	107.9	110.8

Fig. 11 Case 1: 38 double filaments, 6 ring filaments. **a** Range of stresses and **b** Range of strains under a 400 N compressive load
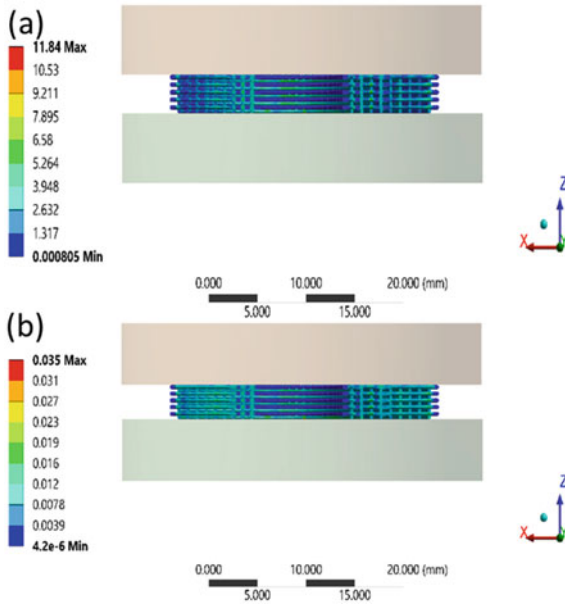

Fig. 12 Case 2: 38 double filaments, 9 ring filaments. **a** Range of stresses and **b** Range of strains under a 400 N compressive load
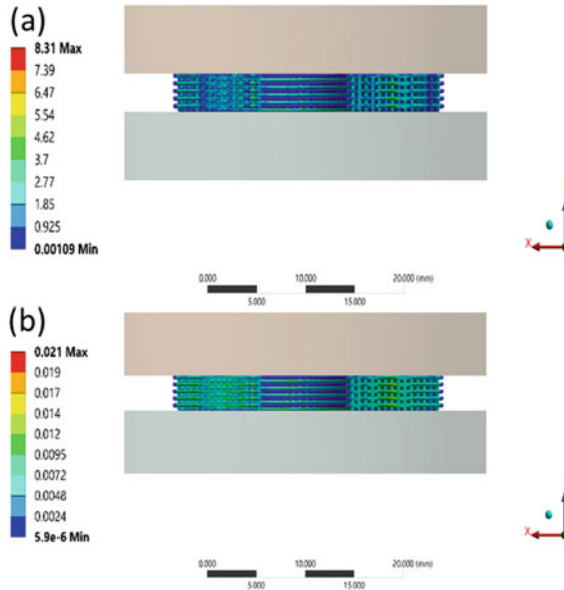
Fig. 13 Case 3: 38 double filaments, 14 ring filaments. **a** Range of stresses and **b** Range of strains under a 400 N compressive load

cell spreading into the internal regions of the bone bricks and the supply of oxygen and nutrients. For a more clear vision of the stresses, Fig. 14 show the stresses considering only half of the bone bricks.

4 Conclusions

This Chapter present a novel strategy to produce synthetic biocompatible and biodegradable porous bone bricks for large bone defects. It also presents a numerical modelling strategy to simulate the mechanical behaviour of bone bricks allowing to determine compressive modulus and deformation. Bone bricks were designed considering different architectures and produced using an extrusion-based additive manufacturing system. The pore size of bone bricks was designed considering different spiral filaments for a fixed number of double zig-zag filaments, with values ranging from 71% (bone bricks based on 38 double filaments and 6 ring filaments) to 60% (38 double filaments and 14 ring filaments). Results also show that bone bricks designed with 9 and 14 ring filaments present compressive modulus in the range
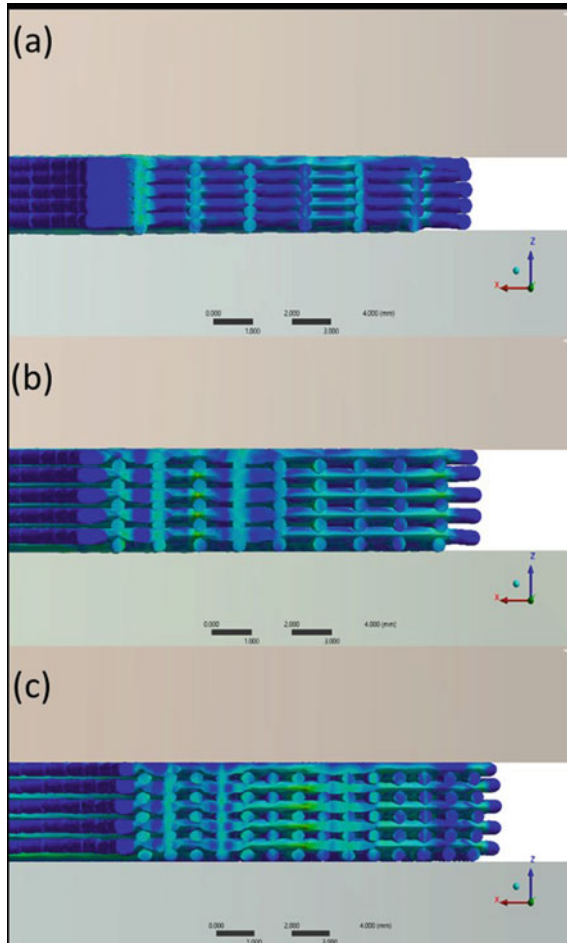
Fig. 14 Zoomed images showing the stresses on half of the bone bricks under a compressive load of 400 N. **a** Case 1: 38 double filaments, 6 ring filaments, **b** Case 2: 38 double filaments, 9 ring filaments; **c** Case 3: 38 double filaments, 9 ring filaments

of trabecular bone. Despite the assumptions initially considered, results also show a good agreement between numerical and experimental results, suggesting that the proposed simulation strategy represents a valid approach to design bone bricks with specific compressive modulus, minimising the need for extensive experimental work.

References

1. Haleem A, Javaid M, Khan R, Suman R (2020) 3D printing applications in bone tissue engineering. Journal of Clinical Orthopaedics and Trauma, 11, 118–124 dimensional printed poly(ε-caprolactone) scaffolds. Biofabrication 9:2
2. Gerdes S, Mostafavi A, Ramesh S, Memic A, Rivero I, Rao P, Tamayol A (2020) Process–structure–quality relationships of three-dimensional printed poly(caprolactone)-hydroxyapatite scaffolds. Tissue Eng Part A 26:271–291
3. Leonchuk SS, Novikov KI, Subramanyam KN, Shikhaleva NG, Pliev MK, Mundargi AV (2020) Management of severe congenital flexion deformity of the knee using Ilizarov method. J Pediatric Orthopaedics B 29:47–52
4. Liu Y, Yushan M, Liu Z, Liu J, Ma C, Yusufu A (2020) Complications of bone transport technique using the Ilizarov method in the lower extremity: a retrospective analysis of 282 consecutive cases over 10 years. BMC Musculoskeletal Disorders 21:354
5. Fragomen TA, Kurtz MA, Barclay RJ, Nguye J, Rozbruch RS (2018) A comparison of femoral lengthening methods favors the magnetic internal lengthening nail when compared with lengthening over a nail. HSS J 14:166–176
6. Al-Tamimi AA, Quental C, Folgado J, Peach C, Bartolo P (2018) Stress analysis in a bone fracture fixed with topology-optimised plates. Biomech Model Mechanobiol 19:693–699
7. Seebah M, Fritz C, Kerschreiter J, Zah FM (2020) Shape accuracy and surface quality of additively manufactured, optimized, patient-specific bone plates. J Med Dev MED-20–1061
8. Yang W, Choi SW, Wong CM, Powcharoen W, Zhu W, Tsoi KJ, Chow M, Kwok K, Su Y (2020) Three-dimensionally printed patient-specific surgical plates increase accuracy of oncologic head and neck reconstruction versus conventional surgical plates: a comparative study. Annals Surg Oncol
9. Huang B, Aslan E, Jiang Z, Daskalakis E, Jiao M, Aldalbahic A, Vyas C, Bartolo P (2020) Engineered dual-scale poly (ε-caprolactone) scaffolds using 3D printing and rotational electrospinning for bone tissue regenera-tion. Add Manuf 36:101452
10. Lin W, Chen M, Qu TLi J, Man Y (2020) Three-dimensional electrospun nanofibrous scaffolds for bone tissue engineering. J Biomed Mater Res B Appl Biomater 108:1311–1321
11. Susmita B, Naboneeta S (2020) Natural medicinal compounds in bone tissue engineering. Trends Biotechnol 38:404–417
12. Wong MT, Lau WT, Li X, Fang C, Yeung K, Leung F (2014) Masquelet technique for treatment of posttraumatic bone defects. Scientific World J 2014:710302
13. Giannoudis VP, Faour O, Goff T, Kanakaris N, Dimitriou R (2011) Masquelet technique for the treatment of bone defects: tips-tricks and future directions. Injury 42:591–598
14. Masquelet A, Kanakaris KN, Obert L, Stafford P, Giannoudis VP (2019) Bone repair using the Masquelet technique. J Bone Joint Surg 101:1024–1036
15. Lasanianos GN, Kanakaris KN, Giannoudis VP (2010) Current management of long bone large segmental defects. Orthopaedics Trauma 24:149–163
16. Vidal L, Kampleitner C, Brennan AM, Hoornaert A, Layrolle P (2020) Reconstruction of large skeletal defects: current clinical therapeutic strategies and future directions using 3D printing. Front Bioeng Biotechnol
17. Zhu G, Mei H, He R, Liu K, Tang J, Wu J (2015) Effect of distraction osteogenesis in patient with tibial shortening after initial union of Congenital Pseudarthrosis of the Tibia (CPT): a preliminary study. BMC Musculoskeletal Disorders 16:216
18. Griffin SK, Davis MK, McKinley OT, Anglen OJ, Chu GT, Boerckel DJ, Kacena AM (2015) Evolution of bone grafting: bone grafts and tissue engineering strategies for vascularized bone regeneration. Clinical Rev Bone Miner Metabolism 13:232–244
19. Pereira RF, Sousa A, Barrias CC, Bayat A, Granja PL, Bártolo PJ (2017) Ad-vances in bioprinted cell-laden hydrogels for skin tissue engineering. Biomanuf Rev 2:1
20. Dzobo K, Thomford NE, Senthebane DA, Shipanga H, Rowe A, Dandara C, Pillay M, Motaung KSCM (2018) Advances in Regenerative Medicine and Tissue Engineering: Innovation and Transformation of Medicine Stem Cells International 2018:2495848

21. Liu F, Vyas C, Poologasundarampillai G, Pape I, Hinduja S, Mirihanage W, Bartolo P (2018) Structural evolution of PCL during melt extrusion 3D printing. Macromol Mater Eng 303:1700494
22. Tang X, Thankappan KS, Lee P, Fard ES, Harmon DM, Tran K, Yu X (2014) Polymeric biomaterials in tissue engineering and regenerative medicine. Nat Synth Biomed Polymers 351–371
23. Lovez-Alvarez M, Rodríguez-Valencia C, Serra J, González P (2013) Bio-inspired ceramics: promising scaffolds for bone tissue engineering. Procedia Eng 59:51–58
24. Vyas C, Pereira R, Huang B, Liu F, Wang W, Bartolo P (2017) Engineering the vasculature with additive manufacturing. Current Opinion Biomed Eng 2:1–13
25. Madrid APM, Vrech SM, Sanchez MA, Rodriguez AP (2019) Advances in additive manufacturing for bone tissue engineering scaffolds. Mater Sci Eng C 100:631–644
26. Hou Y, Wang W, Bartolo P, (2020) Novel poly(ε-caprolactone)/graphene scaffolds for bone cancer treatment and bone regeneration. 3D Print Add Manuf 7:222–229
27. Stevens MM, George JH (2005) Exploring and engineering the cell surface interface. Science 310:1135–1138
28. Hou Y, Wang W, Bartolo P (2020) Investigating the effect of carbon nano-materials reinforcing poly(ε-caprolactone) printed scaffolds for bone re-pair applications. Int J Bioprint 6:266
29. Eivazzadeh-Keihan R, Chenab KK, Taheri-Ledari R, Mosafer J, Hashemi MS, Mokhtarzadeh A, Maleki A, Hablin RM (2020) Recent advances in the application of mesoporous silica-based nanomaterials for bone tissue engineerin. Mater Sci Eng C 107:110267
30. Koc B, Acar AA, Weightman A, Cooper G, Blunn G, Bartolo B,v(2019) Bio-manufacturing of customized modular scaffolds for critical bone defects. CIRP Annals 68:209–212
31. Zhang S, Vijayavenkataraman S, Chong GL, Fuh JYH, Lu WF, (2019) Compu-tational design and optimization of nerve guidance conduits for improved mechanical properties and permeability. J Biomech Eng 141:BIO-18–1350
32. Almeida HA, Bartolo PJ (2014) Design of tissue engineering scaffolds based on hyperbolic surfaces: structural numerical evaluation. Med Eng Phys 36:1033–1040
33. Lu L, Zhang Q, Wootton DM, Chiou R, Li D, Lu B, Lelkes P, Zhou J (2014) Mechanical study of polycaprolactone-hydroxyapatite porous scaf-folds created by porogen-based solid freeform fabrication method. J Appl Biomater Function Mater 12:145–154
34. Almeida HA, Bártolo PJ (2013) Numerical simulations of bioextruded poly-mer scaffolds for tissue engineering applications. Polymer Int 62:1544–1552
35. Misch EC, Qu Z, Bidez WM (1999) Mechanical properties of trabecular bone in the human mandible: implications for dental implant treatment planning and surgical placement. J Oral Maxillofacial Surg 57:700–706
36. Xu Z, Omar MA, Bartolo P (2020) Experimental and numerical simulations of 3D-printed Polycaprolactone scaffolds for bone tissue engineering applications. Biomech Model Mechanobiol
37. Liu F, Wang W, Mirihanage W, Hinduja S, Bartolo PJ (2018) A plasma-assisted bioextrusion system for tissue engineering. CIRP Annals 67:229–232

CAD Software Integration with Programming Tools for Modelling, Measurement and Verification of Surfaces

Rafael Gella-Marín, Anastasios Tzotzis, César García-Hernández, José-Luis Huertas-Talón, and Panagiotis Kyratsis

In modern industry, surface verification is usually performed with the aid of manual instruments or machines such as Coordinates Measuring Machines (CMM) along with the appropriate software. The goal is comparing the manufactured product with a pattern in order to detect deviations from the desired dimensions. This pattern is usually a 2D or 3D model developed using a Computer Aided Design (CAD) program performing manual commands. Most CAD software allow modelling automation either through its own programming language or through third party languages which connect to the CAD software. This chapter presents methodologies and procedures to automate the modeling of parts, the assembly of mechanical sets, the processing of these parts via milling, turning and Wire Electrical Discharge Machining (WEDM) in order to obtain the Numerical Control (NC) program and, finally, the verification of the measures of the simulated parts. This can be done either through the built-in programming language available in the CAD software or by using external developing tools. Several examples are presented. First it is applied to the verification

R. Gella-Marín (✉) · A. Tzotzis · C. García-Hernández · J.-L. Huertas-Talón
Department of Design and Manufacturing Engineering, University of Zaragoza, Campus Rio Ebro, C/Maria de Luna 3, 50018 Zaragoza, Spain
e-mail: rafaelmariagellamarin@gmail.com

A. Tzotzis
e-mail: atzotzis@unizar.es

C. García-Hernández
e-mail: cesarg@unizar.es

J.-L. Huertas-Talón
e-mail: jhuertas@unizar.es

P. Kyratsis
Department of Product and Systems Design Engineering, University of Western Macedonia, 50100 Kila Kozani, Greece
e-mail: pkyratsis@uowm.gr

process of a 2D spur gear. A tool to generate an ideal gear using the gear data is presented. Then a manufactured gear with these data is measured using a CMM. A second tool is presented to compare the ideal gear with the manufactured gear and obtain the manufacturing accuracy. Finally, a tool is presented to simulate the CMM measurement with Solid Edge™. In this case, the virtual gear can show the errors to be considered, so users can take into account the inaccuracies in the gear.

1   Introduction

The manufacturing industry today relies heavily on simulation methods for product design and development, manufacturing processes and material testing. This is because simulations provide results in a safer, faster and more economical way compared to a physical setup. The implementation of Application Programming Interface (API) tools in modern Computer Aided Design (CAD) systems have been used by researchers, engineers and designers since the CAD invention. API is a computer interface that allows multiple software intermediaries to interact between each other. Since developing CAD models can be very time consuming, APIs allow to automatize this process allowing engineers to focus on the results of the model they are developing. An early example of CAD based programming for manufacturing purposes is the simulation system that was presented by Dillmann and Huck [1]. The system allows the modelling of various objects that take part into a manufacturing process and in addition it can display the controls graphically.

Almost every type of the simulation models that are currently in use can be developed by using the API of a CAD system; typical examples are the Computer Aided Manufacturing (CAM) simulation of milling tool fabrication [2] and gear manufacturing [3]. There are studies where CAM systems or sometimes Computer Aided Engineering (CAE) systems are also used for simulation purposes; with the aid of the API, researchers have developed tools that integrate both CAD and CAE modules [4] and in some cases all three modules (CAD/CAM/CAE) [5]. Moreover, CAD systems along with their APIs are used for machining simulations [6, 7] in order to increase the productivity and the effectiveness of CNC machines.

As described above, the advantages that derive from the use of the API and similar programming resources are multiple. First of all, the user can automate various tasks in a short amount of time and in a relatively easy way [8] or simplify the design process of complex parts and assemblies [9–11].

Secondly, each of the tasks that can be automated, can be integrated also into a graphical interface; a typical interface of a CAD based developed application is presented in the work of Tzotzis et al. [12, 13]. Graphical interfaces are usually Object Oriented Programming (OOP). These include forms that contain several graphics like buttons, textboxes, menus and lists that help the user perform a number of actions such as select an option, type a value, execute a process, etc. The type of automation is related to the software used. If the user programs with the API of a CAD system then the result could be the automation of certain design routines [14], the automation

of an assembly process [15, 16] or the automatic creation of engineering documents [17]. In some cases, researchers use CAD systems and the programming resources for calculation purposes of the cutting forces, chip morphology and other parameters involved in machining processes [18–20]. Another area of API implementation related to calculation purposes is Finite Element Model (FEM) Analysis. Since FEM can involve a CAD model preprocessing, it is possible to automate tasks that are related to finite element model preparation such as feature recognition and meshing [21, 22].

As we explained, the API can be used to establish communication between different pieces of software; a typical example would be the connection between a CAD system with Visual Studio™ or an equivalent Integrated Development Environment (IDE) which allows developing computer applications to automate tasks. Another example would be the connection between a CAD system and an office productivity software. This interconnectivity process is important when the user wishes to link a macro with an external environment. In the case of Visual Studio™, the user can link the macro with an interface that can be operated outside the CAD system, whereas in the second case, the user can link certain output data that are exported from the CAD system with an office suite software for management and analysis purposes. The API provides the user with the necessary tools that are required to create simple macros, complete applications or even full grade software systems. These tools are usually in the form of a programming interface.

Finally many scientific studies found in literature that take advantage of the programming resources of CAD, CAM or CAE systems focus on the automation of design tasks or engineering calculations and in some cases on analysis of engineering problems. Measuring and virtual verification with the aid of CAD based techniques is an equally interesting research area that can benefit from the API. A CAD based approach on measurement and verification can be found on the work of He et al. [23].

In this chapter the use of APIs to automate spur gears generation, verification and measurement simulation is described. First, a macro to generate the profile points of an ideally manufactured gear is presented. Then, another macro is introduced to make possible the comparison between this ideally manufactured gear and a manufactured gear with the same gear data, which has been measured with a CMM. This makes possible the comparison of the real gear with the ideal one and obtaining the manufacturing accuracy.

Even though many commercially available software are available, such as Mitutoyo Gearpak™ and Zeiss Gear™ Pro that can be used for these purposes, they are still too expensive for training activities and usually require the "continuous touch" feature for the verification process [24].

Finally, the API of a common CAD system, Solid Edge™, and a proposed programming technique is used as the basis for the development of an interactive tool that can be used to simulate the measuring and verification processes of a spur gear. This tool aims to provide assistance both in academic and professional environment, with respect to advanced machine measuring techniques.

As we can see, the aim of this chapter is showing how to develop macros to generate and simulate spur gears and how to use this technique to link it to a CAD program.

2 Methodology

2.1 Implementation of CAD API

A classification of the simulation areas in manufacturing engineering were published in the work of Negahban and Smith [25]. According to this classification, this work can be framed in "general simulation models", either applied to simulation with teaching purposes or as support to machine programming, avoiding errors and collisions or allowing off-line programming.

There are several possibilities for the development of these types of simulation software: by using general purpose development systems (C++ , Java, Visual Net, etc.), starting from the beginning, in order to represent the geometric elements and their operations and, finally, by using libraries, transforming the programming language into a library administrator.

There is a third way, which uses the advantages offered by the 3D CAD software systems. Some of them use their own development language (e.g., AutoCAD's AutoLisp), or allow the use of their own libraries for developing external applications, i.e., using the API as described by Kyratsis et al. [26].

In the presented research, the Solid Edge™ APIs, and the Object Linking Environment (OLE) with the Dynamic Data Exchange (DDE) technology have been used. They are a series of techniques which allow the programmer to design specific applications in the Windows™ environment, importing / exporting data (exchanging) with an external program and, at the same time, manipulating these data with the commands and methods of the external program.

The most important element in OLE automation is the object. An object refers to a unit or an organized collection of data supplied by an application. The types of objects and their parameters can be very diverse. In this paper, it is described how Solid Edge™ becomes a Visual Basic.NET™ object, which has been the programming language applied. In this way, the programming language uses the CAD instructions and supplies the data and, at the same time, the numerical data obtained in Solid Edge™ are processed by Visual Basic™, applying the DDE technology.

2.2 Development of Application

This first part of the chapter focuses on the development of an API to verify the manufacturing accuracy of spur gears. First a macro application will be developed to

generate the profile points of a spur gear and save them to a Comma Separated Values (CSV) file. Then a CMM will be used to measure the profile of a manufactured spur gear with the same data (Module, number of teeth, profile correction) as the profile which was generated with the app. A CSV file with the measured points will be generated. Finally, a second app will be described which compares the measured points with the generated points. This comparison will quantify the manufacturing accuracy. This process is explained in the flowchart in Fig. 1.
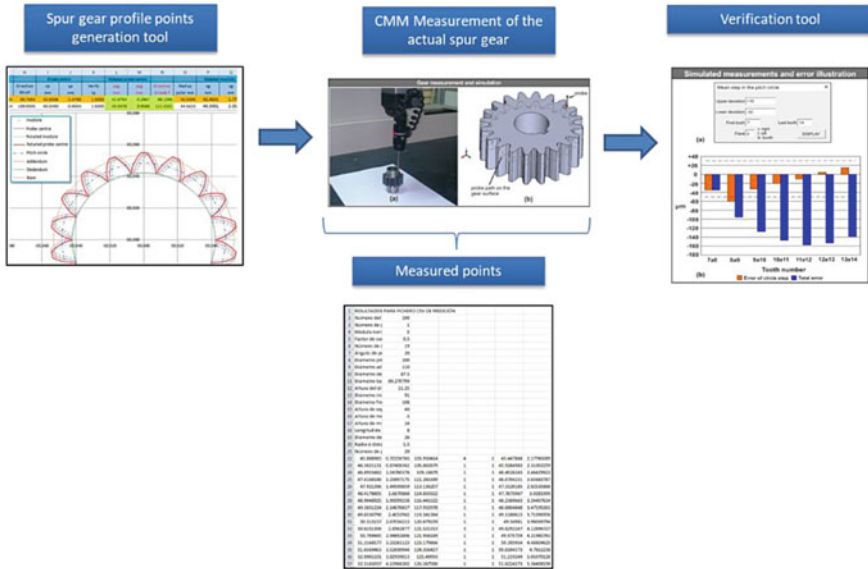
Fig. 1 Workflow chart

Fig. 2 Involute profile of a spur gear tooth
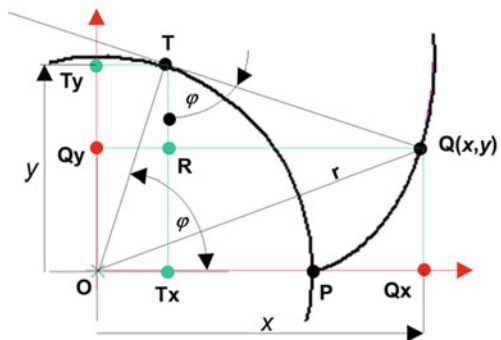
2.2.1 Spur Gear Profile Points Generation Tool

Mathematical Context

The mathematical part of this simulation in a CMM is similar to the one needed for WEDM machining [27, 28] and profile milling [29]. The process is described below.

The profile of a spur gear tooth is an involute (Fig. 2) which can be described with Eq. 1:

$$
\begin{aligned}
x &= r_b \cdot \cos \varphi + \varphi \cdot r_b \cdot \sin \varphi \\
y &= r_b \cdot \sin \varphi - \varphi \cdot r_b \cdot \cos \varphi
\end{aligned}
\tag{1}
$$

Here there are two parameters to obtain the coordinates: The base radius rb and the angle parameter φ for a polar radius of the given involute (Eq. 2).

$$
\varphi = \sqrt{\left(\frac{r_p}{r_b}\right)^2 - 1}
\tag{2}
$$

We will obtain points between an initial angle φ_i and a final angle φ_e in the parametric equation. These initial and final angles can be calculated as follows (Eq. 3):

$$
\varphi_i = \sqrt{\left(\frac{r_i}{r_b}\right)^2 - 1} \quad \varphi_e = \sqrt{\left(\frac{r_e}{r_b}\right)^2 - 1}
\tag{3}
$$

They depend on the base radius and an initial r_i and final radius r_e of measurement. Since the outer and inner diameters in the tooth are the addendum and dedendum diameters, *ri* should be equal or higher than the dedendum and re should be equal or lower than the adendum. In this way, using the parametric equation we will cover the entire involute arc.

Now that we have the initial and final points in the parametric equation, we have to calculate the points between them to generate the whole involute arc. The criteria that we will follow is obtaining points at the same arc length distance.

Given the initial and final angles, we can calculate the arc length between these angles (Eq. 4).

$$
\bar{s} = \frac{1}{2} r_b \left(\varphi_e^2 - \varphi_i^2\right)
\tag{4}
$$

If we set a number of arcs, we can obtain the individual arc length (Eq. 5).

$$
\bar{s}_j = \frac{\bar{s}}{n - 1}
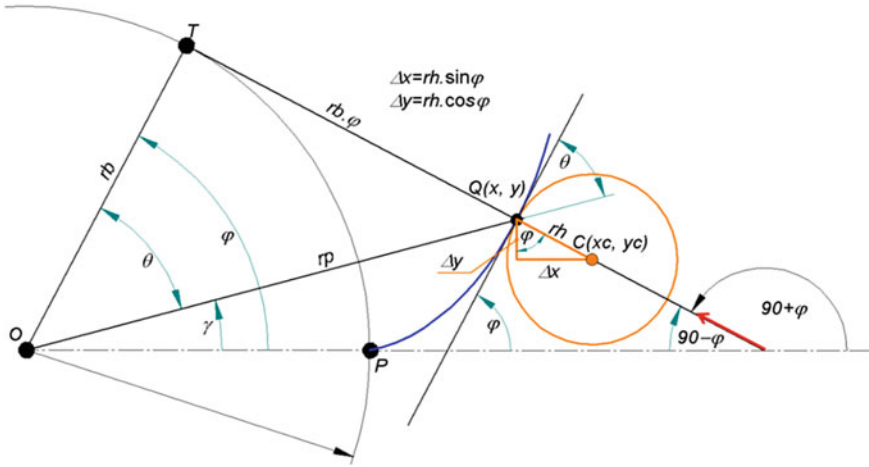\tag{5}
$$

Fig. 3 Probe center positioning and implementation of the measuring direction

With this individual arc length we can calculate each parametric angle from the initial angle φi until the final angle φe (Eq. 6).

$$\bar{s}_j = \frac{1}{2} r_b \left(\varphi_2^2 - \varphi_i^2 \right) \Rightarrow \varphi 2 = \sqrt{\frac{2\bar{s}_j}{r_b} + \varphi_i^2}$$

$$\bar{s}_j = \frac{1}{2} r_b \left(\varphi_3^2 - \varphi_2^2 \right) \Rightarrow \varphi 3 = \sqrt{\frac{2\bar{s}_j}{r_b} + \varphi_3^2} \tag{6}$$

We substitute each of the angles in the involute equation and we will obtain one side of the tooth profile. We have to take into consideration that if we measure the tooth profile with a CMM probe we must include the probe radius (Eq. 7). Therefore, the probe coordinates must include the correction in Fig. 3:

$$x_C = x + r_h \sin \varphi \; y_C = y - r_h \cos \varphi \tag{7}$$

Next we have to obtain the other side of the tooth profile. We will perform symmetry (Eq. 8) on each tooth point of the involute (Fig. 4).

$$x_s = x - 2e \sin \varphi$$
$$y_s = y + 2e \cos \varphi \tag{8}$$

To use this formula on each involute point we need the angle ϕ and the distance to the symmetry axis e. The angle ϕ is obtained from Fig. 5.

In intersection point P between the involute and the primitive circle we can calculate angle φ (Eq. 9):
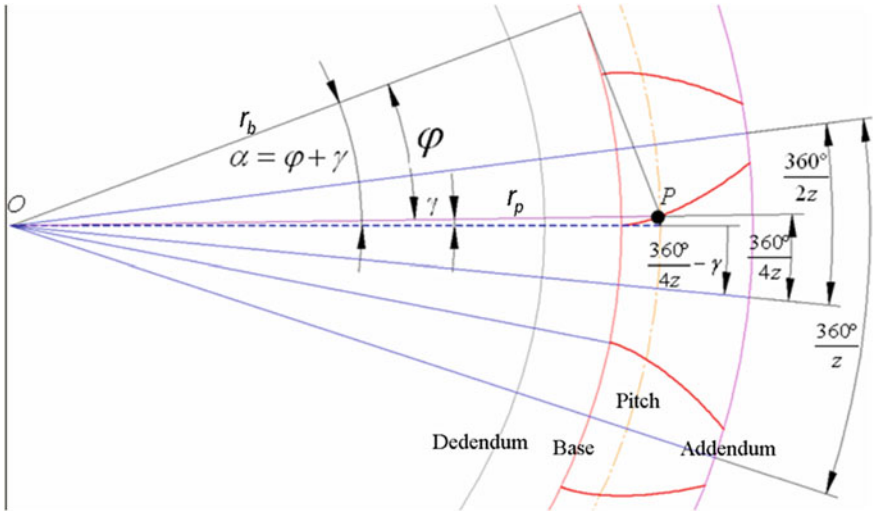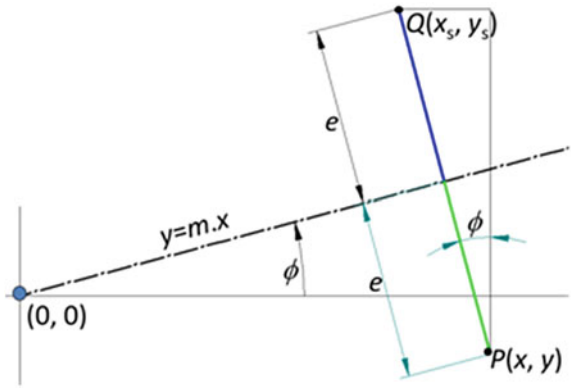
Fig. 4 Symmetry on an involute point

Fig. 5 Symmetry angle calculation

$$\cos \varphi = \frac{r_b}{r_p} = \frac{m \cdot z \cdot \cos 20}{(m \cdot z + 2 \cdot k \cdot m)}$$
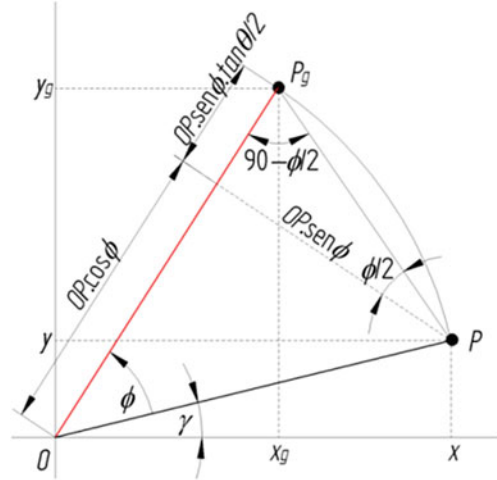
$$\varphi = \cos^{-1}\left[\frac{m \cdot z \cdot \cos 20}{(m \cdot z + 2 \cdot k \cdot m)}\right] \tag{9}$$

At the same time we can calculate angle α (Eq. 10):

$$r_p^2 = r_b^2\left(1 + \alpha^2\right)(m \cdot z + 2 \cdot k \cdot m)^2 = (m \cdot z \cdot \cos 20)^2 \cdot \left(1 + \alpha^2\right)$$

$$1 + \alpha^2 = \frac{(m \cdot z + 2 \cdot k \cdot m)^2}{(m \cdot z \cdot \cos 20)^2} \quad \alpha = \sqrt{\frac{(m \cdot z + 2 \cdot k \cdot m)^2}{(m \cdot z \cdot \cos 20)^2} - 1} \tag{10}$$

Fig. 6 Rotation
transformation ϕ

Therefore we can calculate angle γ (11):

$$\alpha = \varphi + \gamma \Rightarrow \gamma = \alpha - \varphi \tag{11}$$

Now we can calculate the symmetry axis (Eq. 12):

$$\varphi = \frac{2\pi}{4z} - \gamma \tag{12}$$

The distance e is obtained by substituting in the symmetry axis equation the coordinates of point P. The symmetry axis crosses the origin of coordinates and we know its slope. Therefore we can calculate the distance e (Eq. 13):

$$e = \frac{x \sin \phi - y \cos \phi}{\sqrt{\sin^2 \phi + \cos^2 \phi}}$$
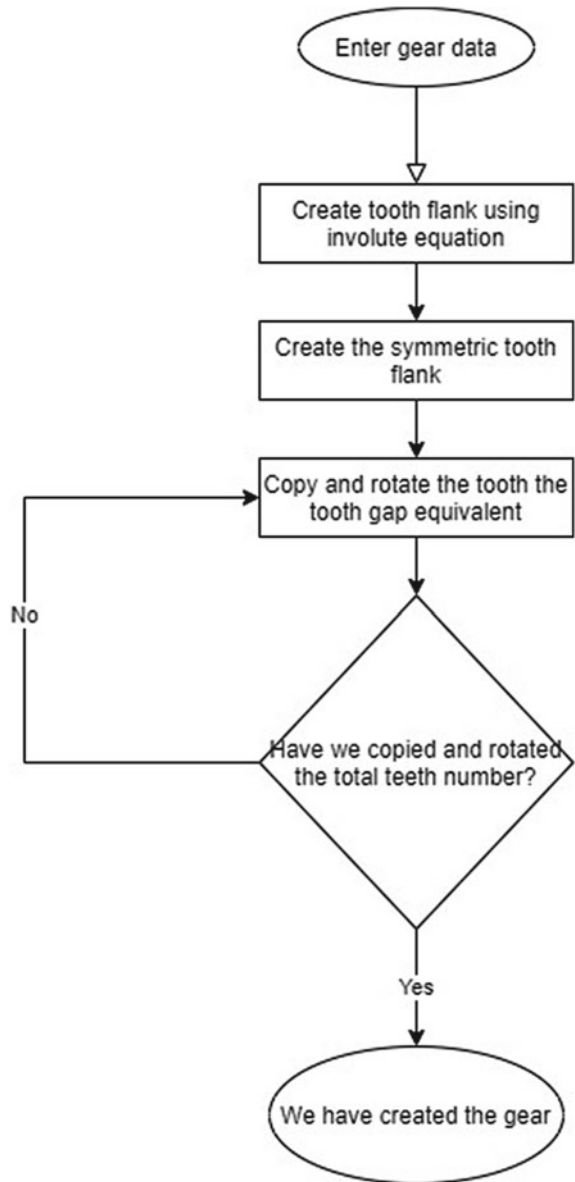$$e = x \sin \phi - y \cos \phi \tag{13}$$

Once that we have calculated a tooth, we can obtain the rest of the teeth by using a rotation matrix (Eq. 14) on each point of the tooth profile (Fig. 6).

$$\begin{bmatrix} x_g \\ y_g \end{bmatrix} = \begin{bmatrix} \cos \varphi & -\sin \varphi \\ \sin \varphi & \cos \varphi \end{bmatrix} \begin{bmatrix} x \\ y \end{bmatrix} \tag{14}$$

The flowchart of the gear generation we have described is shown in Fig. 7.

Table 1 describes all the variables used.

Fig. 7 Gear generation
flowchart

With this algorithm it is possible to create an Excel Macro which given the gear
data generates the spur gear profile including the probe measuring coordinates. This
tool is shown in Fig. 8.

Table 1 Variables used in gear profile generation

Variable	Use
x, y	Involute coordinates
rb	Base radius
φ	Involute angle for the parametric equation
rp	Pitch radius
ri	Initial radius of the involute
re	Final radius of the involute
$\bar{s}$	Arc length between two involute angles
φi	Initial involute angle
φe	Final involute angle
$\bar{s}_j$	Individual arc length
n	Number of arcs
x_s, y_s	Symmetric x, y involute coordinates
e	Distance to symmetry axis
ϕ	Symmetry axis angle
m	Module
z	Teeth number
k	Spur gear mounting factor
γ	x, y points angle with respect to OX axis
α	Base diameter angle with respect to OX axis
x_g, y_g	x, y involute coordinates rotated φ angle
x_c, y_c	Probe center coordinates
r_h	Probe radius
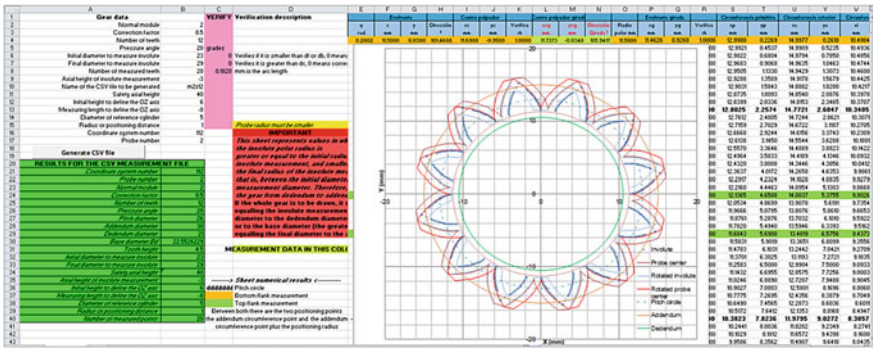
Fig. 8 Gear generation macro

Table 2 Setup of the CMM parameters for the measuring test

Parameter	Unit	Value
Resolution	mm	0.0005
Sampling points per tooth		100
Approaching speed	mm/s	200
Approaching acceleration	G	0.12

2.2.2 Experimental Setup

In order to acquire the coordinates from the measuring procedure of the physical gear that was used in this study, a Mitutoyo EURO-C544 CMM was utilized. The set up time of the gear and the CMM took about 20 min and the measuring time of all the teeth around 15 min.

The measuring range of the machine is 505 mm on X axis, 405 mm on Y axis and 405 mm on Z axis with a resolution of 0.0005 mm, which was enough for the needs of the test. Table 2 shows the important parameters of the measuring test setup along with their values. The number of the measured sampling points was roughly 100 per tooth. It was selected to ensure that the measuring process was accurate enough. The more sampling points during a measurement the better the accuracy is. On the other hand, a measurement with an increased number of sampling points requires longer time to complete. This means that a balance between accuracy and completion time must be determined, which depends on the size and complexity of the item that is going to be measured and the capabilities of the CMM.

The number of the sampling points was chosen so that the arc length between two consecutive points in a tooth flank is always the same [24]. Figure 9 shows the measurement process.

Figure 10a illustrates part of the gear's measuring procedure after the WEDM process, whereas Fig. 10b illustrates the simulation of the same procedure. The profile of the specific gear is an involute according to DIN 867, DIN 868 and DIN 3960 standards. Additionally, the tool generates the simulated points using the UNE 18,066 international standard, whereas the error measurement is performed according to ISO 1328.

After the CMM has completed the measurement, a CSV file with the measured points is generated.

2.2.3 Verification Tool

Now that we have the generated profile points and the measured points, we can compare them to verify the manufacturing quality and the deviations from the ideal profile. A Verification Tool has been programmed with an Excel macro as shown in Fig. 11.
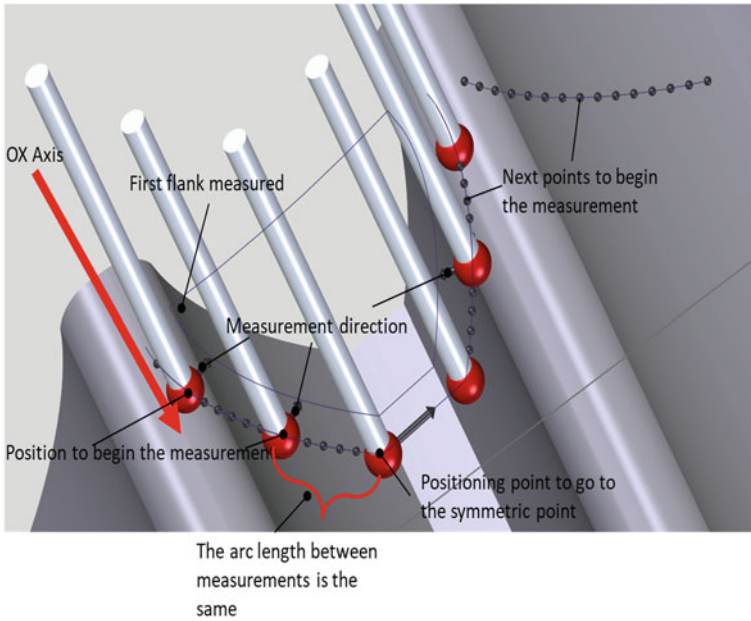
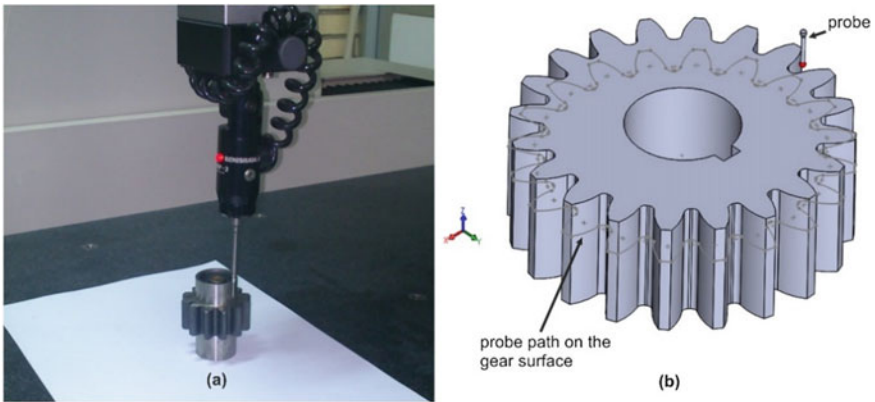The macro has four buttons:

Fig. 9 CMM Measurement process

Fig. 10 Measuring procedure of the gear with the CMM (**a**) and the equivalent measuring simulation (**b**)

- Read Measurement file. This macro reads the measurement file and the generated points from the Generation Tool and loads them in the Verification Tool.
- Verify tooth profile. This macro selects a tooth and compares the profile from the generated points with the measured points.

	Data		Added ending
1			
2	CSV File Name	m2z12	_medido.CSV
3			
4			
5	Read measurement file		
6			
7	Verify tooth profile		
8			
9	Tooth width in		
10			
11	pitch circle		
12			
13	Tooth pitch in		
14			
15	pitch circle		
16			
17			
18	Probe radius=	0.984107	
19			
20	RESULTS FOR MEASUREMENT CSV FILE		
21	Coordinates system number	112	
22	Probe number	2	
23	Normal module	2	
24	Profile shift modification	0.5	
25	Number of teeth	10	
26	Pressure angle	20	
27	Pitch diameter	22	
28	Addendum diameter dc	26	
29	Dedendum diameter df	17	
30	Base diameter db	18.79385242	
31	Tooth height	4.5	
32	Involute initial measurement diameter	23	
33	Involute finale measurement diameter	29	
34	Safety height za	40	
35	Involute measurement height	-3	
36	Inital height to define OZ axis	6	
37	Measurement length to define OZ axis	-8	
38	Reference cylinder diameter dr	5	
39	Radius or positioning distance rh	1	
40	Number of measurement points	20	
41			

Fig. 11 Verification tool

- Tooth width in pitch circle. This macro selects a tooth and compares the tooth width in pitch circle from the generated points with the measured points.
- Tooth pitch in pitch circle. This macro selects a number of teeth and compares the tooth width in pitch circle from the generated points with the measured points.

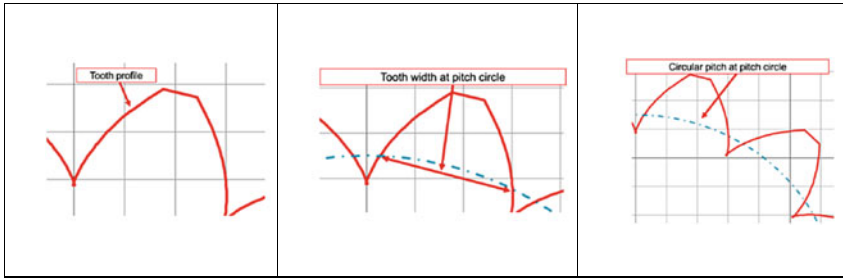The points that are compared are shown in Fig. 12.

Fig. 12 Points compared in verification tool

2.3 Virtual Simulation

This second part of the chapter deals with the development of an API to simulate the CMM measurement process. This API developed with Microsoft Visual Studio™ connects the CAD program Solid Edge™ with a CSV file using the coordinates obtained from the measurement of an actual gear. The virtual simulation process is based on strategies similar to those found in WEDM and milling machining simulations [27–29]. With the aid of Solid Edge™ and its APIs the user can simulate the movement of the probe just like any cutting tool by generating a trajectory.

Before explaining the development of the API, we have to briefly touch the Solid Edge™ structure. Solid Edge™ has three modules:

- The part module, which is used to design 3D workpieces from profiles and applying geometric operations.
- The assembly module, wich is used to assemble different workpieces.
- The draft module, which is used to draw construction plans and sections.

All of them are related. If an operation is modified in the part module, this modification is transferred to the assembly and draft modules [30]. Each module consists of a number of objects and each object consists of a number of members. An object member can either be a method or a property. Each of the modules has their own hierarchy. The assembly module is used in this chapter.

Using a 3D part piece of the theoretical gear, another 3D part piece of the CMM probe and the CSV measurement file of the actual gear, the main flowchart of the process is shown in Fig. 13.

The flowchart in Fig. 14 summarizes the whole simulation process. First both the CMM API Simulator and Solid Edge™ must be opened. Then the user has to enter the measurement file path and run the Simulator by pushing the simulator button in the form. This runs the code, which opens an assembly file in Solid Edge, imports the Gear CAD, the Probe CAD and the Measurement file. It reads the measurement points and moves the Probe CAD to the read point in the Gear CAD until the End of File.

Fig. 13 Workflow of the application's code
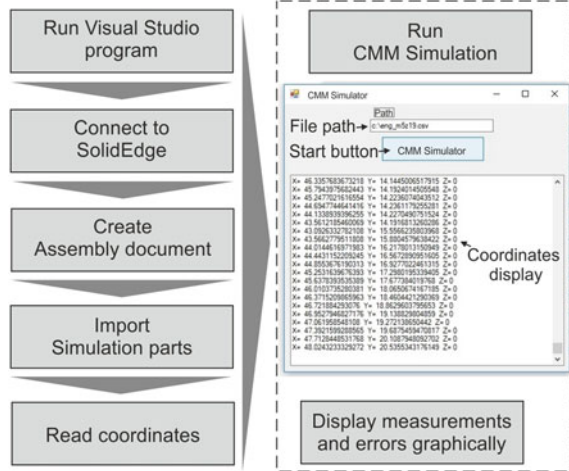
Now that we have seen the whole simulation process we can start describing the API development. We will start by taking a look at the CMM Simulator Form (Fig. 13) created in Visual Studio™. It is made up of a window to introduce the path where the measurement file is stored. Below there is a button to start the application. Finally there is a window to display the coordinates in real time as the API reads them from the CSV measurement file and moves the CAD probe to the CAD gear.

Figure 15 shows how the application looks when it is running.

Now that the API workflow has been explained, we will take a look at how it was developed.

As it was stated above, the API was developed with MicrosoftVisual Studio™. It is an IDE used in Graphical User Interfaces (GUI) such as apps, mobile apps, and cloud and web services. It supports code writing in 36 programming languages. In this case Visual Basic (VB) was the language chosen, since it is one of the two languages available in the.NET Programmer's Guide book for Solid Edge™ with Synchronous Technology API, the other one being C#.

The first step to develop the CMM Simulator API with Visual Studio™ is creating a Windows Form Application. Next we have to add references, which are the Solid Edge™ DLL libraries which will allow to connect the API to Solid Edge™ and to access its commands. These are the first steps to allow the data and commands interaction between the API, the CSV measurement file and to Solid Edge™. Next we can start creating the form and developing the code (Fig. 16).

Next take a look at the structure of the CSV measurement file obtained from the CMM measurement as shown in Fig. 17. The first 21 rows describe the gear characteristics and the probe information that has been used to perform the measurement. The next rows are the actual measurement coordinates.

Summarizing, what the API has to do is read the CSV measurement file up to line 21 and from then until the end of file, read the coordinates, move the CAD probe to the measured coordinates gear position and display them in the API.
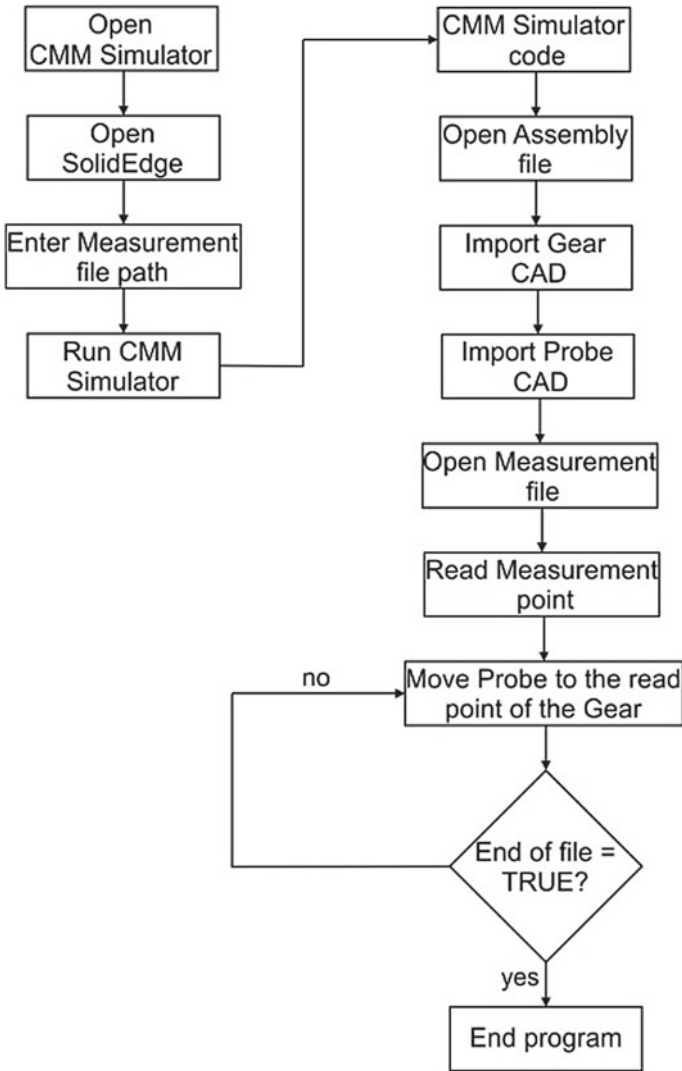
Fig. 14 Simulation process flowchart

We have to highlight that the measured points in the measurement file were scanned at the same probe height. The measurement file displays only X and Y coordinates. The API is programmed to accept X, Y and Z coordinates, but since the original measurement file did not include the Z coordinate, we have modified the Move command to not include the Z variable from the read file.

Now that we have described all the considerations that must be taken into account to develop the API, we can start describing the code. As explained before after creating the windows form application in Visual Studio™and adding the Solid
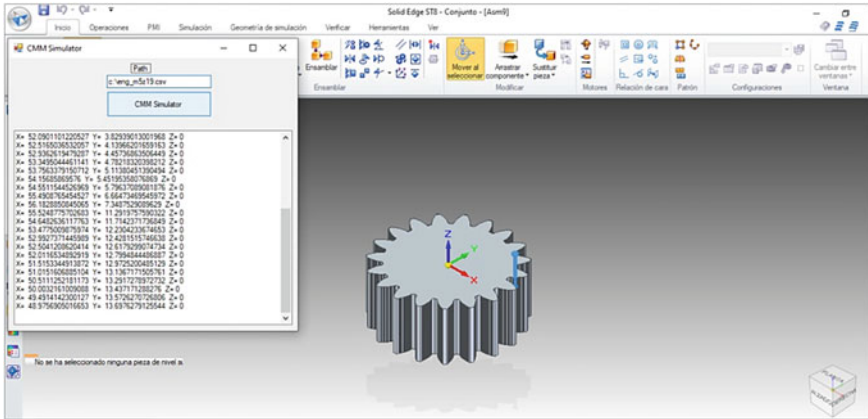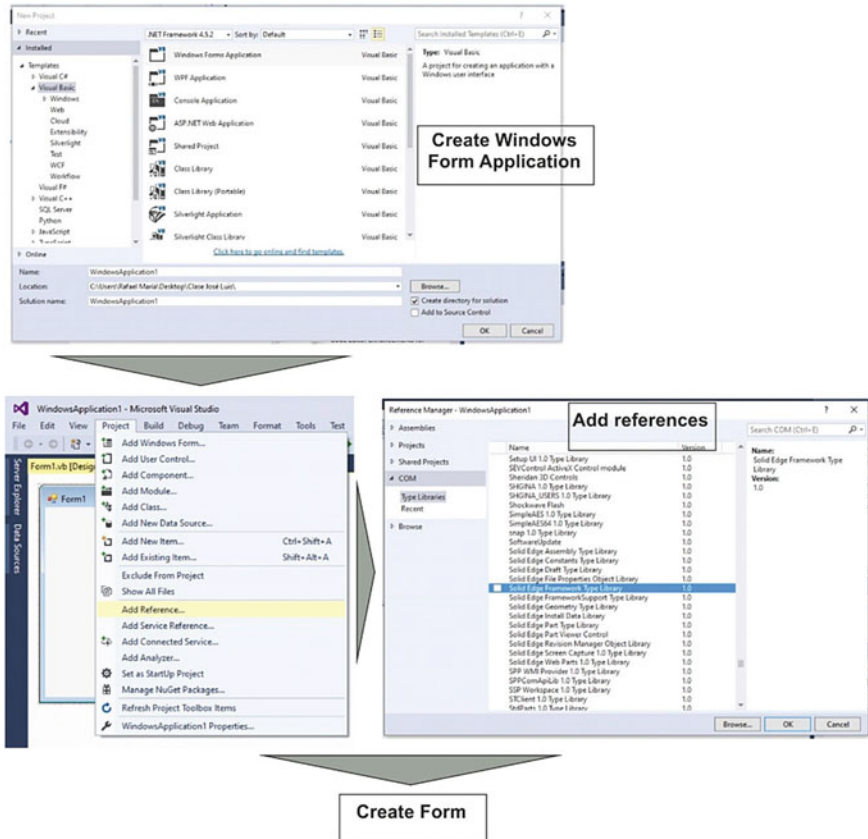
Fig. 15 CMM simulation

Fig. 16 Windows form application creation in Visual Studio™ and Solid Edge™ references addition

1	CSV MEASUREMENT FILE RESULTS	
2	Coordinates system number	100
3	Probe code number	1
4	Module	5
5	XM	0.5
6	Number of teeth	19
7	Pressure angle	20
8	Pitch diameter	100
9	Addendum	110
10	Dedendum	87.5
11	Base diameter	89.270799
12	Tooth height	11.25
13	Involute measurement initial diameter	91
14	Involute measurement final diameter	108
15	Safety measurement probe height	40
16	Involute measurement height	-3
17	Initial height to define OZ axis	16
18	Measurement length to define OZ axis	8
19	Reference cylinder diameter dr	26
20	Radius or positioning distance (rh=rp+distance	1.5
21	Number of measured points by tooth	20
22		45.45403445	2.17845361
23		45.93088383	2.30370947
24		46.39668278	2.47254142
25		46.85584361	2.64465958
26		47.34145325	2.8316298
27		47.77386726	3.02562088
28		48.24784486	3.25279074
29		48.67667086	3.4858112
30		49.1292049	3.69765667
31		49.56329668	3.95631851
32		49.8299707	4.13698062
33		49.96236416	4.22238138
34		50.39501498	4.48199121
35		50.81411818	4.76965844
36		51.2121628	5.04408154
37		51.63232133	5.35382004
38		52.02268344	5.65958761
39		52.42435676	5.94494503
40		52.80437242	6.28258013
41		53.17183256	6.59086193

General gear and probe information

X and Y coordinates

Fig. 17 Structure of the CSV measurement file

Edge™ references, we can create the form which will be the interface to simulate the CMM Measurement. As shown in Fig. 15, the form includes a button which starts the simulation. If we open this button in the form, we can write the code that will run when it is pushed.

First we have to enable the data reading and connection with Solid Edge™ and the CSV file. This is shown in Fig. 18.

Next we have to define the general variables and the variables which are used to access Solid Edge™. Figure 19 shows this definition step.

Now that we have defined all the variables, we have to start designing the sequence of events. Figure 20 shows these steps:


```
1    Imports System.IO                              Enable text file reading
2    Imports SolidEdgePart              Enable data connection with Solid Edge
3    Imports System.Runtime.InteropServices              Enable COM interoperability
```

Fig. 18 Code header

```vbnet
1     ⊟Imports System.IO
2       Imports SolidEdgePart
3       Imports System.Runtime.InteropServices
4
5
6     ⊟Public Class Form1
7
8     ⊟    Private Sub Button1_Click(sender As System.Object, e As System.EventArgs) Handles Button1.Click
9
10              Dim path As String
11              Dim line As String
12              Dim linecounter As Integer
13              Dim aryTextFile() As String
14              Dim XSolidEdge As Double
15              Dim YSolidEdge As Double
16              Dim ZSolidEdge As Double
17              Dim Xant As String
18              Dim Yant As String
19              Dim Zant As String
20              Dim Xsig As String
21              Dim Ysig As String
22              Dim Zsig As String
23              Dim X1, X2, X3 As Double
24              Dim Y1, Y2, Y3 As Double
25              Dim Z1, Z2, Z3 As Double
26              Dim X4, Y4, Z4 As String
27
28
29              Dim objApp As SolidEdgeFramework.Application = Nothing
30              Dim objApplication As SolidEdgeFramework.Application = Nothing
31              Dim objDocuments As SolidEdgeFramework.Documents = Nothing
32              Dim objAssembly As SolidEdgeAssembly.AssemblyDocument = Nothing
33              Dim objAsmRefPlanes As SolidEdgeAssembly.AsmRefPlanes = Nothing
34              Dim objAsmRefPlane As SolidEdgeAssembly.AsmRefPlane = Nothing
35              Dim objPPlane As SolidEdgeAssembly.AsmRefPlane = Nothing
36              Dim objPart As SolidEdgePart.PartDocument = Nothing
37              Dim objRefPlanes As SolidEdgePart.RefPlanes = Nothing
38              Dim objRefPlane As SolidEdgePart.RefPlane = Nothing
39              Dim objType As Type
40              Dim objOccurrences As SolidEdgeAssembly.Occurrences = Nothing
41              Dim objOccurrence As SolidEdgeAssembly.Occurrence = Nothing
42              Dim objOccurrence1 As SolidEdgeAssembly.Occurrence = Nothing
43              Dim objOccurrence2 As SolidEdgeAssembly.Occurrence = Nothing
```

General variables definition

Solid Edge variables

Fig. 19 Variables declaration


```
path = TextBox1.Text              → We read the path where the measurement file is located
linecounter = 0

Dim sr As StreamReader = New StreamReader(path)    → We use the Streamreader command to read the .csv file

objApp = Marshal.GetActiveObject("SolidEdge.Application")   → Connect to Solid Edge
objApp.Visible = True             → Make Solid Edge Visible
objApp.DisplayAlerts = False      → Turn off alerts
objDocuments = objApp.Documents   → Get a reference to the Documents collection

objAssembly = CType(objDocuments.Add("SolidEdge.AssemblyDocument"), SolidEdgeAssembly.AssemblyDocument)   → Create an Assembly Document

objOccurrences = objAssembly.Occurrences   → Insert part file in Assembly Document. Get a reference to the occurrences collection

objOccurrence1 = objOccurrences.AddByFilename("C:\CAD palpapador y engranaje medido\z19x5_de diente.par")   → Add the gear to the Assembly Document
objOccurrence2 = objOccurrences.AddByFilename("C:\CAD palpapador y engranaje medido\Palpador.Asm")          → Add the probe to the Assembly Document

objOccurrence1.Move(0, 0, 0)      → We place the gear in the coordinates origin. (Units: 1 = 1000 mm

objApp.StartCommand(CType(SolidEdgeConstants.AssemblyCommandConstants.AssemblyViewISOView, SolidEdgeFramework.SolidEdgeCommandConstants))   → We change to Isometric view

linecounter = 0
While linecounter < 21            → We read and display the coordinates until the end of file. The coordinates
    line = sr.ReadLine              begin in line 22. This loop reads the file until line 21 but does not display it
    linecounter = linecounter + 1   since it is only the gear and probe general information
End While
```

Fig. 20 Connect to Solid Edge, creation of an assembly document and import of Gear and Probe CAD

- Read the location of the measurement file in the text box in the app form.
- Connect to Solid Edge.
- Create the assembly document.
- Import the Probe CAD and the Gear CAD in the assembly document.
- Read the first 21 rows in the CSV measurement which as explained before don't contain information useful for the CMM Simulation.

When we reach row 22 we move the Probe CAD to the read position. This is the beginning position of the measurement.

After row 22 we can start reading the rows until the End of File. They contain the measurement coordinates. We can read each row and move the probe to the position. This part of the code is shown in Fig. 21.

Now the process until the End of File is a loop which reads the rows and moves the Probe CAD to the read coordinates.

The whole code is displayed in the flowchart in Fig. 22.

Table 3 explains the variables used in the code.

The variables described as Solid Edge™ variables are used as part of the syntax to access Solid Edge™ and therefore they are not explained.

Finally it is possible to include this API as a button in Solid Edge. When the API is compiled and run in Visual Studio™, an executable file with the same name of the project API is created in the project folder. First in Solid Edge™ we have to select More Commands from the Quick Access Toolbar. Then we have to Select Macros in the Choose Commands from the drop down. This process is shown in Fig. 23.
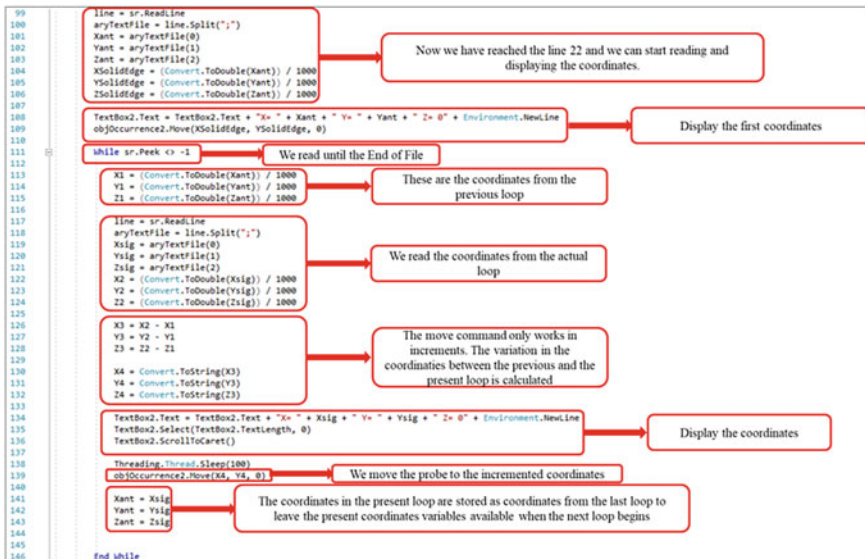
Fig. 21 Loop to read measurement coordinates in CSV file and to move the probe
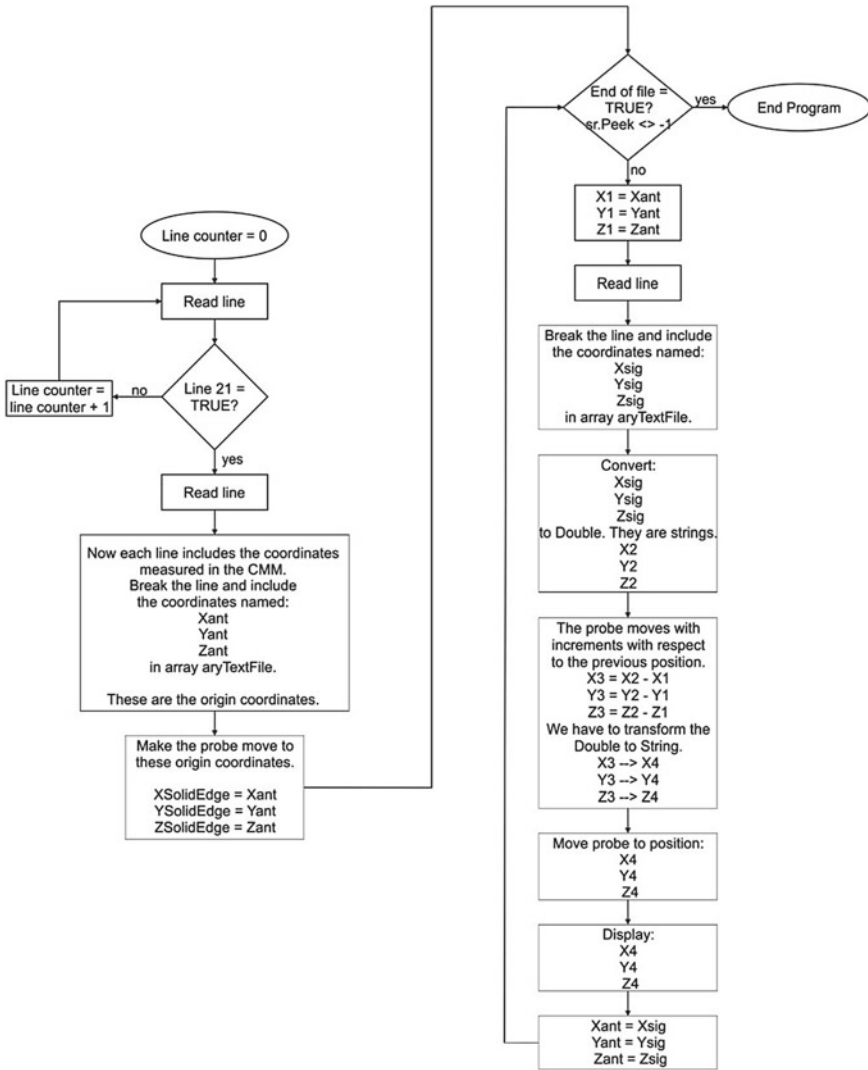
Fig. 22 CMM simulation code flowchart

Next we have to browse the executable file in the project folder and it will be added as button. Now we don't have to use Visual Studio™ to run the API. We can just open Solid Edge™ and run the API from the button in the Quick Access Toolbar.

Table 3 CMM Simulator variables

Variable	Description
Path	Path of the CSV measurement file
Line	Line of the CSV file
Linecounter	Line counter
aryTextFile	Array which contains the X, Y and Z coordinates
Xant, Yant, Zant	When we reach line 22, these are the first coordinate points where the probe must be displayed
XSolidEdge, YSolidEdge, ZSolidEdge	Coordinates used in the Move command in SolidEdge when we reach line 22
Xsig, Ysig, Zsig	In the loop until the End of File, these are the coordinates in the current iteration
X1, Y1, Z1	These are the coordinates from the previous iteration
X2, Y2, Z2	These are the coordinates from the current iteration transformed to Double
X3, Y3, Z3	These are the coordinates increment from

3 Conclusions

This chapter shows how it is possible to use macros to verify the manufacturing accuracy of spur gears and how to use APIs in CAD software as a simulation tool in the metrology field. Furthermore, a WEDM CAM and the graphical simulation have been successfully developed and have been particularized for a spur gear. Even more, the whole measurement process is equivalent to the one in the CMM, being possible to apply it to different types of gears by altering the application's code. Even though the presented application was developed for the specific CMM, the code can be changed in such way that it can be applied to different machines as well.

If the CMM is programmed with standardized software, as in this case, then the CMM program can be developed with any text processor (like in CNC machines). This means that the described methodology is valid to create offline programs, being even possible to visualize the physical CMM configuration in the CAD software.

Finally, the presented tools aim is to become a useful and valuable asset in training seasons for both academic and industrial environments, because it provides the following advantages:

- Automatic comparison between the critical dimensions of the virtual part, as an ideal reference part, with the equivalent measurements taken from the manufactured part with minimal effort and in very short time.
- Verification within the limits specified in this study, of machined gears and possibly other machine elements.
- Cost-effective and easy to set up compared to using a real CMM and commercially available CMM software.
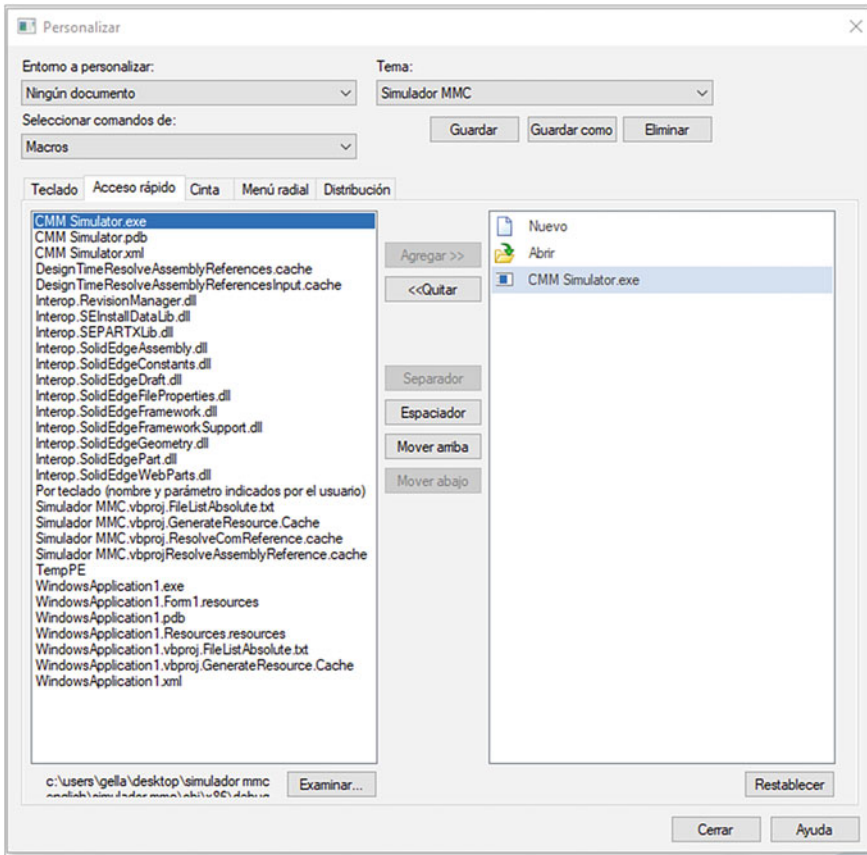
Fig. 23 Macro button implementation in Solid Edge

- Can be used in pair with either a real CMM (even without the "continuous touch" feature) or a virtual simulator.

References

1. Dillmann R, Huck M (1986) A software system for the simulation of robot based manufacturing processes. Robotics 2:3–18
2. Kim J, Park J, Ko TJ (2008) End mill design and machining via cutting simulation. Comput Des 40:324–333
3. Dimitriou V, Vidakis N, Antoniadis A (2007) Advanced computer aided design simulation of gear hobbing by means of three-dimensional kinematics modeling. J Manuf Sci Eng Trans ASME 129:911–918
4. Wu Y, Zhou Y, Zhou Z et al (2018) An advanced CAD/CAE integration method for the generative design of face gears. Adv Eng Softw 126:90–99

5. Wang L, Chen ZC (2014) A new CAD/CAM/CAE integration approach to predicting tool deflection of end mills. Int J Adv Manuf Technol 72:1677–1686
6. Kyratsis P, Tapoglou N, Bilalis N, Antoniadis A (2011) Thrust force prediction of twist drill tools using a 3D CAD system application programming interface. Int J Mach Mach Mater 10:18–33
7. Vakondios DG, Kyratsis P (2020) An innovative CAD - based simulation of ball - end milling in microscale. Adv Comput Des 5:13–34
8. Tzivelekis CA, Yiotis LS, Fountas NA, Krimpenis AA (2015) Parametrically automated 3D design and manufacturing for spiral-type free-form models in an interactive CAD/CAM environment. Int J Interact Des Manuf 11:223–232
9. Yicong G (2019) Quantifying the complexity of subassemblies in a fully automated assembly system. Assem Autom 39:803–812
10. Zhang S, Wang G, Zhang L, Fang X (2009) CNC programming system for complex components based on KBE within integrated environment of CAD/CAPP/CAM. Front Mech Eng China 4:97–102
11. Roberto V, Osorio-Gómez G (2012) Assembly planning with automated retrieval of assembly sequences from CAD model information. Assem Autom 32:347–360
12. Tzotzis A, Garcia-Hernandez C, Talón JLH, Kyratsis P (2020) CAD-Based Automated Design of FEA-Ready Cutting Tools. J Manuf Mater Process 4:1–14
13. Tzotzis A, Garcia-Hernandez C, Huertas-Talon J-L et al (2017) Engineering applications using CAD based application programming interface. In: MATEC web of conferences, pp 1–7
14. Mok H-S, Kim C-H, Kim C-B (2011) Automation of mold designs with the reuse of standard parts. Expert Syst Appl 38:12537–12547
15. Du B, Wang X, Feng Y et al (2014) Intelligent assembly technology based on standard parts feature of CATIA. Mod Appl Sci 8:49–55
16. Sapidis N, Chatziparasidis I (2017) Framework to automate mechanical-system design using multiple product-models and assembly feature technology. Int J Prod Lifecycle Manag 10:124–150
17. Nasulea D, Oancea G, Neagoe I (2017) Parametric design of dies for cutting and drawing using Catia. Bull Transilv Univ Braşov 10:1–8
18. Tapoglou N (2019) Calculation of non-deformed chip and gear geometry in power skiving using a CAD-based simulation. Int J Adv Manuf Technol 100:1779–1785
19. Tapoglou N, Antoniadis A (2012) CAD-based calculation of cutting force components in gear hobbing. J Manuf Sci Eng 134:1–8
20. Xu J, Liu W, Sun Y (2008) Optimal localization of complex surfaces in CAD-based inspection. Front Mech Eng China 3:426–433
21. Qisheng W (2019) Triangular mesh generation on free-form surfaces based on bubble dynamics simulation. Eng Comput 36:646–663
22. Bartłomiej S (2013) Method of spiral bevel gear tooth contact analysis performed in CAD environment. Aircr Eng Aerosp Technol 85:467–474
23. He G, Huang X, Ma W et al (2017) CAD-based measurement planning strategy of complex surface for five axes on machine verification. Int J Adv Manuf Technol 91:2101–2111
24. García-Hernández C, Gella-Marín R, Huertas-Talón JL, Berges-Muro L (2016) Algorithm for measuring gears implemented with general-purpose spreadsheet software. Measurement 85:1–12
25. Negahban A, Smith J (2014) Simulation for manufacturing system design and operation: literature review and analysis. J Manuf Syst 33:241–261
26. Kyratsis P, Bilalis N, Antoniadis A (2011) CAD-based simulations and design of experiments for determining thrust force in drilling operations. Comput Des 43:1879–1890
27. Talón JLH, Ortega JCC, Gómez CL et al (2010) Manufacture of a spur tooth gear in Ti–6Al–4V alloy by electrical discharge. Comput Des 42:221–230
28. Garcia-Hernandez C, Marín R, Talón J et al (2016) WEDM manufacturing method for noncircular gears using CAD/CAM software. Strojniški Vestn J Mech Eng 62:137–144

29. Özel C, Özler L (2005) An investigation on manufacturing of the straight bevel gear using end mill by CNC milling machine. J Manuf Sci Eng 127:503–511
30. González DE, Peña JL, Pérez ST (2013) Manual práctico Solid Edge ST6. Servicios Informáticos DAT, SL

Experimental Investigation of Process Parameters Effect on Laser Engraving Process Quality

Evangelos Nikolidakis and Aristomenis Antoniadis

In this chapter it is presented an experimental investigation of stainless steel SAE304, aluminium 7075, pressure vessel steel P355GH and yellow brass C26000 nanosecond pulsed Q-switched Nd:YAG 1064 nm laser engraving process. Laser engraving experiments were performed using a LASERTEC 40 laser machining center made by DMG MORI for various sets of process parameters (average power, repetition rate, scanning speed) and engraving geometry characteristics. The effect of process parameters on removed material layer thickness, material removal rate, average surface roughness and kerf taper angle formation was examined.

1 Introduction

Laser beam machining is a thermal energy based non-conventional machining process that belongs to the large family of material removal processes. A subcategory of these processes is the nanosecond pulsed laser engraving process. Laser engraving process has a wide range of applications in industry. It is used for example for the micro-engraving of molds, cutting tools, micro-channels and medical tools. It allows the engraving of small and complex geometries with high precision on a wide variety of materials, glass, plastics, and composite materials.

In the laser beam machining process, a laser beam is generated by a CNC (Computerized Numerical Control) laser machine which is focused and directed appropriately to the workpiece to be engraved. Material removal is achieved through the interaction between the laser beam and the target material of the workpiece. When the

E. Nikolidakis · A. Antoniadis (✉)

Micromachining & Manufacturing Modeling Laboratory, School of Production Engineering & Management, Technical University of Crete, University campus, Building E4.026- Kounoupidiana, 73100 Chania, Greece
e-mail: antoniadis@dpem.tuc.gr

beam interacts with the target material, the electrons of the material are excited by the photons of the laser beam [1]. Therefore, the electron subsystem heats up to a high temperature and the absorbed energy is transferred to the atomic lattice. The energy absorbed by the pulse gradually causes the material to melt and heats it until it reaches a temperature at which the atoms have gained enough energy to convert it into a gaseous phase of the melt [2]. In other words, the energy of the photons of the beam is transferred to the target material in the form of heat and the material is removed immediately mainly through its vaporization.

Compared to conventional machining processes, laser beam machining processes have significant advantages that have to do with the nature of the process. A key advantage is the ability to focus the beam on diameters of a few microns. Thus, a high-intensity heat source is focused on a very small area, making it possible to engrave micro-geometries without significantly affecting the surrounding areas. In other words, the heat affected zone (HAZ) and the deformations are significantly reduced. In addition, due to the absence of direct tool-workpiece contact no problems occur that take place in conventional machining such as wear and tear of the cutting tools, self-excited oscillations (chattering) and machine deformations. Also, an important advantage is the ability to steer-maneuver the beam using beam steering systems so that machining is possible in areas that would not normally be accessible with conventional tools. Finally, another advantage is the limited pollution of the environment due to the non-use of cutting fluids which pollute the natural environment after their use and removal. However, laser beam machining processes also have some drawbacks that make them less suitable for some applications. The main disadvantage is that it is unsuitable for processing metals with high reflectivity in laser beams. Also, a disadvantage is its low efficiency-productivity compared to conventional processes. Finally, the equipment required for the laser beam machining processes (laser machining center) has a high acquisition cost and during its operation is characterized by high energy consumption.

2 Laser Engraving Process

As far as pulsed laser engraving process is concerned, the material is removed by passing the laser beam in multiple layers. At each layer scanned, overlapping craters are generated in a specific way coming from the laser beam pulses ablated material [3] as shown in the Fig. 1. Thus, by removing in each level a layer of material with a specific thickness and shape and by making gradual passes in multiple levels, the geometry to be engraved is formed. The movements of the beam to scan the workpiece are performed through CNC laser machining centers. These machines take as input programs that have been created using appropriate CAM (Computer Aided Manufacturing) software that include all the beam movements as well as the parameters required for the engraving process. In order to achieve high speed machining with high accuracy in most cases for small areas machining the workpiece remains stationary on the machine table and the laser beam [4] is moved using a
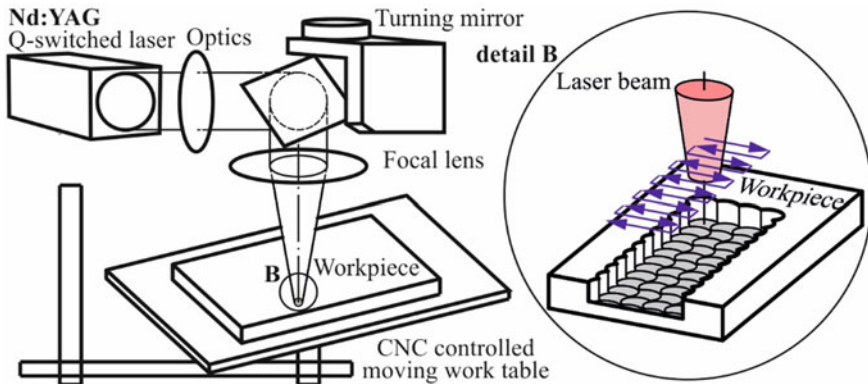
Fig. 1 Schematic illustration of pulsed laser engraving process

suitable steering system [5]. The work table is moved only in cases where the size of the geometry exceeds the maximum allowable range for moving the beam. The final result is directly affected by parameters related to the beam characteristics such as the intensity, focus diameter, beam quality and scanning speed as well as the pulses characteristics such as pulse duration, repetition rate and more. Also, as this is a level-by-level material removal process, the determinant size for the final result is the removed material layer thickness.

Of the various types of lasers available, carbon dioxide CO_2 lasers and neodymium-doped yttrium aluminum garnet Nd:YAG lasers have prevailed in laser beam processes. CO_2 lasers have a wavelength of 10.6 μm, high average power, high efficiency and good beam quality. Nd:YAG lasers with a wavelength of 1064 nm have less power but when used as pulsed lasers with nanosecond pulses then they achieve high peak power [6] which makes them suitable for processing either for small or large machining depths [7]. Due to the shorter wavelength, Nd:YAG lasers have lower reflectivity for some metals than CO_2 lasers [8]. Thus, they can be used to process metals with high reflectivity that would be difficult to accomplish with CO_2 lasers. However, due to the fact that Nd:YAG lasers have entered the industrial manufacturing industry recently and their acquisition cost is higher, they are not as widespread as CO_2.

Lasers fall into two main categories: continuous wave (CW) lasers and pulsed lasers. In continuous wave lasers the output power of the beam is constant over time and find applications in processes such as welding and metal cutting. Pulsed lasers produce a series of high-power pulses with a specific duration t_{pulse} and a repetition rate F. Pulsed lasers produces pulses with a maximum peak power P_{peak} much higher than the average power P_{avg} of the beam as shown in the Fig. 2 that is calculated using the Eq. (1). This is because the energy is stored when no pulse is sent and it is released concentrated thereafter. The most common method for generating pulses of the order of nanoseconds is Q-switching. The flexibility provided by pulsed lasers
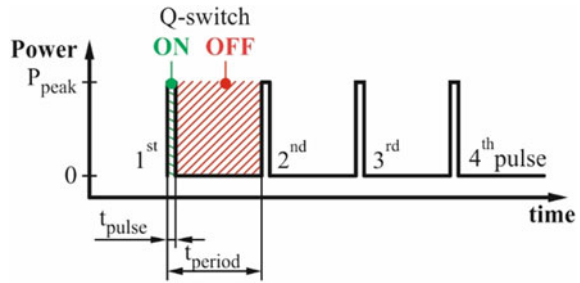
due to the fact that a variety of combinations of process parameters can be performed makes them more suitable for processes such as laser engraving.

$$P_{peak} = \frac{P_{avg}}{t_{pulse} F} \tag{1}$$

The power density or fluence I of the beam at the focus point is determined as a function of the peak power P_{peak} of the beam and the diameter of the laser beam D from Eq. 2. As Meijer et al. [9] have shown, based on the power density of the laser beam as well as the pulse duration, a classification can be made about the type of process (hardening, welding, drilling, cutting, engraving) a laser beam can be used as shown in the Fig. 3. As shown in the Fig. 3, laser engraving process requires laser beams with a minimum power density of 10^8 W/cm^2 and pulses of the order of nanoseconds.
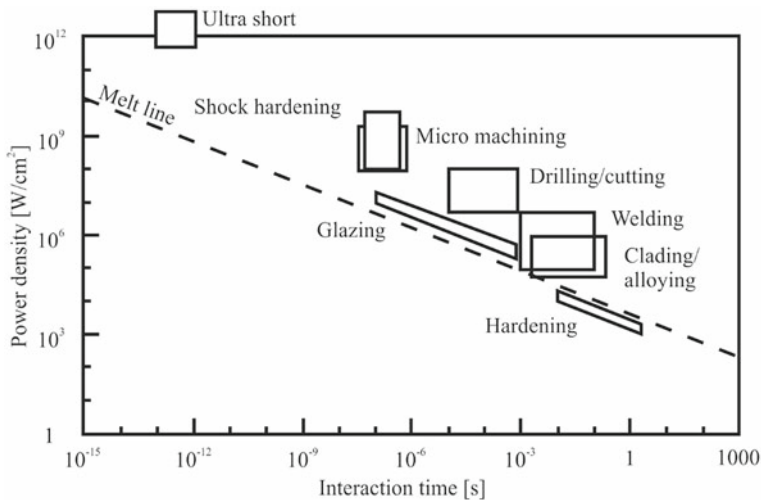
Fig. 3 Power density and laser beam pulse duration required for each type of process

Fig. 4 Correlation between laser wavelength and reflectivity on metal surfaces
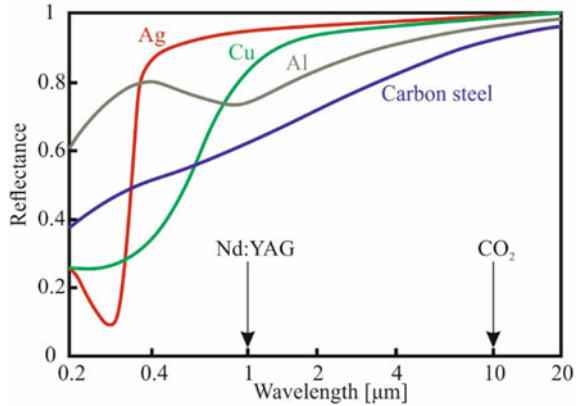
$$I = \frac{4P}{\pi D^2} \qquad (2)$$

During the interaction between the laser beam and the material a significant amount of the incident radiation is absorbed by the material and a temperature field gradually develops in the workpiece. The rest is reflected back to the environment. The reflectivity depends on both the material and the wavelength of the beam. As shown in Fig. 4 [10], metals have less reflectance at the 1064 nm wavelength corresponding to Nd:YAG lasers than the 10.6 μm CO_2 lasers for temperatures below the melting point. The reflectivity decreases with increasing temperature for a given wavelength. The reflectivity of a material also depends on the quality of its surface (roughness) or whether any surface treatment processes such as anodizing, sandblasting or coating has been applied. However, these changes in the reflectivity of the material due to the surface only affect the early stages of the laser engraving process until the initial melting of the material takes place.

When the irradiance of the beam absorbed by the target material is high enough then the ablation mechanism takes place, i.e. the irradiated material vaporizes and enters the gaseous phase. As a result, a dense plume of metal vapor forms over the surface of the workpiece as shown in the Fig. 5. Due to the high temperatures, ionization occurs in the vapor plume atoms resulting in the formation of plasma
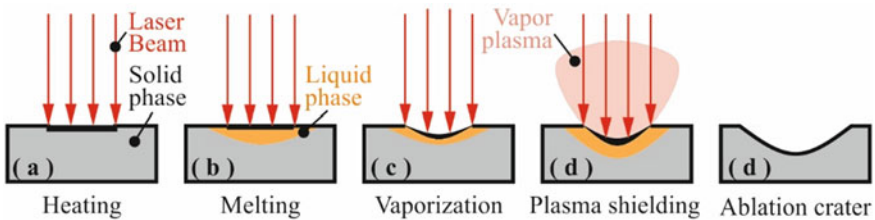
Fig. 5 Basic phenomena that occur during the interaction of the laser beam with the material

[11]. Since the frequency of plasma oscillation generated during metalworking is in most cases significantly lower than the frequency of lasers used then the laser beam propagates through the plasma. However, during the laser beam-plasma interaction, a significant portion of the beam irradiance is absorbed by the plasma. Thus, the intensity of the laser beam that eventually strikes the workpiece after passing through the plasma is significantly reduced. This phenomenon is known as plasma shielding [12]. The above phenomena are shown schematically [13] in the Fig. 5.

3 Laser Engraving Process Research: State-of-the-Art

Laser engraving process is a layer by layer process, that means each time a single layer is scanned with laser pulses in straight tracks. Each layer of material removed has a specific thickness and shape. Thus, by performing multi-level scans and removing layers of material with a predefined geometry in each one, cavities with various geometries can be engraved. So, the removed material layer thickness has a direct correlation with the productivity of the laser engraving process. Furthermore, as it is affected by the positioning and characteristics of the laser beam pulses it directly affects the surface roughness. There are several researchers involved in the experimental investigation of laser engraving process under different perspectives and for different applications each. The following are some state-of-the-art research papers on the investigation of removed material layer thickness and surface roughness formed during laser engraving process.

Campanelli et al. [14] investigated the influence of the main parameters involved in the laser milling process on the success of the ablation process in terms of depth of removed material and surface roughness. Laser milling tests were conducted on aluminium–magnesium alloy specimens using a laser marking machine (the Trumark VMc5 from Trumpf) equipped with a pulsed Nd:YVO4 laser and having a wavelength of 1064 nm, a pulse width of 5 ns, a focus diameter of 40 μm and an average laser power of 30 W. The maximum depth of removed material for a single layer was found to be 17.9 μm and it is obtained for the minimum overlapping (distance between two consecutive spot diameters) 5 μm and the pulsing frequency 30 kHz. A good surface finishing with a roughness less than 7 μm can be obtained choosing the above values for overlapping and frequency and using a scanning strategy with parallel lines to the lamination direction for the first layer and rotation with 45° angular increase for the following layers. To minimize roughness, it was found that maximizing the overlapping distance is required with the optimal value to appear for overlapping 20 μm.

Orazi et al. [15] presented an empirical model which by excluding the physical factors, allows the material removal rate MRR (μm/layer) to be correlated to the process parameters. Experimental tests were performed in aluminium 7075 and mild steel AISI 1040 using a 20 W IPG pulsed ytterbium fiber laser emitting at 1060 nm with spot diameter of 31 μm and pulse duration of 100 ns. The material removal rate is evaluated by producing a series of 2.5 mm square pockets for various combinations

of the most important process parameters: laser power density, pulsing frequency and scanning speed. Pockets were scanned and the depths were measured using a conoscopic interferometer mounted on board the laser machine. From the statistical analysis of the experimental results a database was created with the use of which can be predicted the configuration that guarantees the maximum removal rate. A practical example realized on mild steel AISI 1040 was presented. The maximum MRR was found to be 4.64 µm/layer for laser current 70%, pulsing frequency 37.7 kHz and scanning speed 400 mm/s.

Teixidor et al. [16] investigated the influence of laser process parameters on dimensional precision and surface quality in laser milling of hardened AISI H13 tool steel. Experiments were performed using a Deckel Maho LASERTEC 40 machine, a nanosecond Nd:YAG lamp pumped solid-state laser with 100 W average laser power, 1064 nm wavelength and a laser beam spot diameter of 0.03 mm. In the experiments the scanning speed (200–400 mm/s), the pulse frequency (35–40 kHz) and the pulse intensity levels of a percentage of the ideal maximum pulse intensity (35–45%) were considered as input process parameters. The experiments were carried out machining 54 micro-channels of 200 mm in width and 50 mm in depth. Dimensional measurement was performed with a ZEISS SteREO Discovery.V12 stereomicroscope attached to DeltaPix digital camera. The measurement of the surface roughness parameter Ra on the micro-channel bottom surface was conducted with a stylus instrument Mitutoyo SV2000. From the analysis of the experimental results they concluded that a lower surface roughness will result in a higher depth dimensional error. The lowest depth error was found to be around 10 µm with a surface roughness of 0.53 µm.

Campanelli et al. [17] performed an experimental investigation of the nanosecond Nd:YAG laser milling process of the 5754 aluminum. Square samples with dimension of 15 × 15 mm were manufactured with constant number of 25 removed layers in 3 mm thick aluminum-magnesium alloy 5754 rolled sheets. A nanosecond Q-switched 1064 nm Nd:YAG laser machine was used with a maximum average power of 20 W and a spot diameter of 70 µm. The investigation was conducted using a full factorial plan of experiments characterized by 3 factors: scanning speed (400–1600 mm/s), repetition rate (25–40 kHz) and hatching mode (parallel, mix). The parameters used to evaluate the ablation process were the depth of the removed material, the material removal rate and the surface roughness Ra. The analysis of laser fluence suggested that the highest values of MRR correspond to the highest values of fluences. The use of the mix mode hatching strategy produces higher values of roughness than the parallel one. The highest values for roughness were observed for lower overlapping for both scanning strategies. The smallest value for roughness was 2.6 mm corresponding to a degree of overlap between 40 and 60%.

Anita Pritam [18] studied the effects of process parameters laser power (12–30 W), scan speed (200–800 mm/s), frequency (25–55 kHz) and fill spacing (10–40 µm) on the laser deep engraving of AISI 1045 stainless steel. A laser marking machine equipped with a ytterbium-doped fibre laser having a wavelength of 1064 nm with 30 W maximum laser output power and a beam spot diameter of 100 µm was used for machining square pockets of 10 × 10 mm. The engraving depth and the surface

roughness were measured using a Mitutoyo SJ 301 stylus profilometer. The analysis of the results revealed some important conclusions. The scan speed and laser power have main effect on the surface roughness. For higher scan speed and lower laser power, surface roughness is better. The effect of frequency on the surface roughness is not significant but the engraving depth increases with the increase of frequency. Therefore, in order to achieve deeper cavity result, the scan repetition rate should be increased at lower power and higher scan speed.

Sugar et al. [19] studied experimentally the relationship between laser beam machining parameters and machined surface quality for aluminium bronze as working material using a nanosecond pulsed ytterbium fibre laser. Series of experiments were carried out using a five axis highly dynamic laser precision machining center LASERTEC80 Shape equipped with the low-power nanosecond ytterbium-doped fiber laser (wave length 1064 nm, maximal average output power 100 W, pulse duration 120 ns, repetition rate 80 kHz) and aluminium bronze (AMPCO 25®) as working material. The influence of laser pulse energy (1.27–2.6×10^8 W/cm^2), scanning speed (1000–2200 mm/s) and laser track distance (12.5–27.5 μm) on the surface roughness of machined surface has been studied. Roughness parameters were measured using a contact-gauge profilometer Zeiss Surfcom 5000. They confirmed that the high values of pulse intensity in combination with the minimal scanning speed lead to the worst surface finish quality. Only minimal effect has been reported in the case of laser track distance.

Ahmed et al. [20] investigated the machinability of titanium alloy for laser milling process. Slots of rectangular cross section with 5 mm length 3 mm width and 12 μm depth were machined on titanium alloy (Ti-6Al-4 V) substrates having an average surface roughness of Ra 6.38 μm prior to laser machining. The laser milling process was performed using a DMG LASERTEC 40 Q-switched Nd:YAG pulsed laser machine with 30 W maximum power, beam diameter of 20 μm, pulse duration 10 μs and wavelength of 1064 nm. The process parameters selected to be investigated were: lamp current intensity (75–85%), pulse frequency (10–20 kHz), laser scanning speed (200–400 mm/s), track displacement between two successive laser tracks (8–12 μm), and thickness of the substrate layer to be removed per laser scan (1–3 μm). Material removal rate MRR (μm^3/s) and surface roughness SR Ra (μm) of the milled area were considered as the machinability indicators. The analysis of the results revealed the following conclusions: Increase in laser intensity increases the surface roughness SR as well as material removal rate MRR, whereas by increasing the values of remaining four parameters (pulse frequency, scanning speed, layer thickness, and track displacement), MRR and SR decrease. Mathematical models were developed which can effectively be used to estimate the resulting surface roughness at any settings of laser parameters. It was found that the milled surface having minimum surface roughness of Ra $= 0.965$ μm can be achieved using the following optimal combination of laser parameters: laser intensity 75%, pulse frequency 10.33 kHz, scanning speed 250 mm/s, track displacement 12 μm and layer thickness 1.11 μm.

For laser engraving process of cavities with vertical walls, it has been observed that the walls of the engraved cavity are not in practice vertical. That is, the walls are not vertical as they should ideally be but show a significant slope towards the

inside of the engraved cavity. This phenomenon is referred to in the literature as kerf formation and the angle formed by the side walls with the vertical axis is called kerf taper angle. The research works on the study of kerf formation specifically for laser engraving process are very few.

Mohammed et al. [21] investigated the effects of laser power intensity, pulse overlap and scanning pattern on material removal rate and dimensional accuracy on microchannels fabrication in alumina ceramic using Nd:YAG laser. The experiments were carried out on a LASERTEC 40 machine from Deckel Maho Gildemeister, equipped with a 1064 nm wavelength Nd:YAG pulsed laser with a maximum average power of 30 W and a spot diameter of 30 µm. A 10 mm thick Aluminum Oxide (Al2O3, 99.7%) was used as a workpiece material to engrave microchannels having dimensions of 200 µm width and 5 mm length by performing 24 laser scans without specifying any target depth. The repetition rate was kept constant at 6 kHz throughout all the process while varying values for laser power intensity (75–95%), pulse overlap (58–75%) and scanning pattern (unidirectional, rotating) were tested. The laser machined microchannels were cut through the cross-section and the cross-sections were analyzed using JEOL JSM-6610LV SEM to measure channel top width, bottom width, total depth obtained and machined area. The process performance was measured in terms of four parameters i.e., depth obtained per laser scan, top width error, bottom width error and material removal rate. The following conclusions emerged from the analysis of the experimental results: An increase in intensity and an increase in overlap both contribute to increase in depth of material removed per laser scan whereas scanning pattern and other interactions are comparatively less significant. For each overlap value the top width error increases with depth of material removed per laser scan. Bottom width error is found to be more dependent on pulse overlaps and increases rapidly with increase in pulse overlaps. A combination of high pulse overlap and intensity gives rise to v-shaped channels. Low intensity and low to medium pulse overlap are recommended to minimize the dimensional errors.

Mohammed et al. [22] presented an investigation of the effect of process parameters on the laser machining quality of microchannels in Nickel–Titanium (NiTi)-based shape-memory alloys (SMA) using experimental design methodology. Rectangular cross-section channels of 200 µm width and 100 µm depth were machined in NiTi (Ni 50% Ti 50%) sheet of dimension 40 × 40 × 1 mm. The LASERTEC 40 from DMG/Sauer laser machine was used that is equipped with the Q-switched Nd:YAG laser operating with a wavelength of 1064 nm, having a maximum average power of 10 W, a 10 µs pulse duration and a 30 µm spot diameter. The effect of the following five parameters was examined in the experiments: frequency (25–40 kHz), scan speed (200–600 mm/s), layer thickness (1–3 µm), track displacement (8–12 µm) and scan strategy (unidirectional, cross hatching, rotating). The cross-section cuts of the microchannels were analyzed using scanning electron microscope SEM JEOL JSM-6610LV. The output responses considered were top-width error, taper, spatter and MRR. The conclusions that emerged are the following: In general, higher values of speed and layer thickness, along with unidirectional scan strategy were found to produce microchannels with least dimensional error. The low

layer-thickness resulted in microchannels with least taper angle. Low levels of speed and layer thickness along with unidirectional scan strategy was found to produced microchannels with least spatter. Higher values of speed, layer thickness and track displacement result in higher MRR. Multi-objective optimization was successfully carried out using MOGA-II algorithm for minimizing taper angle and spatter. The optimal solution resulted in a minimum taper of 12.5° and a spatter of 30.8 µm for frequency 40 kHz, scan speed 400 mm/s, layer thickness 1 µm, track displacement 8 µm and rotating scan strategy.

4   Research Objectives

From the previous analysis it becomes apparent that the removed material layer thickness parameter plays a decisive role in the laser engraving process. This is because although this is not a process parameter that is directly defined in the machine, its value is required in advance in order for the CAM software to be able to calculate how many passes-layers will be made and what will be the geometry of each one in order to be engraved the required cavity. Because there are currently no suitable diagrams or nomograms available to determine the removed material layer thickness as a function of the process parameters, it is determined each time through an experimental trial and error method specified by the laser machine manufacturer. However, this trial and error method is very time consuming and requires the existence of a remnant from the material of the workpiece to perform the tests. In addition, a major problem is that there is no information on the surface roughness that will result from process depending on the parameters used. It is worth noting that as shown in Fig. 6 the differences that appear on the laser processed surface for different process parameters are significant. There is therefore a need to know the removed material layer
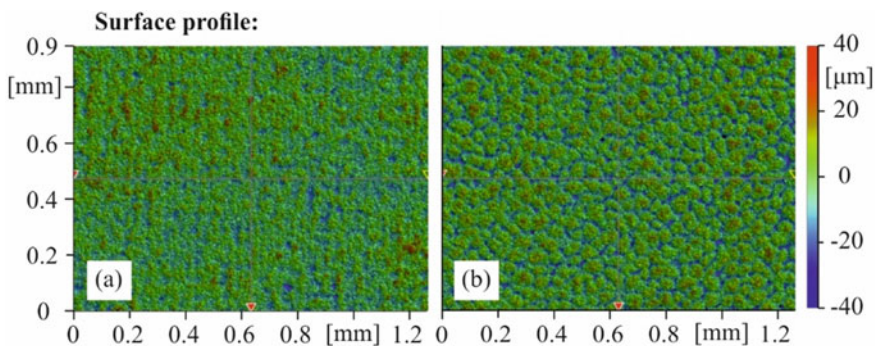
Fig. 6 Surface topology measured by a ContourGT-K 3D optical microscope of yellow brass C26000 surface after laser engraving process made by a LASERTEC 40 laser machining center with the following process parameters: **a** Average power 16 W, Repetition rate 50 kHz, Scanning speed 300 mm/s **b** 12 W, 60 kHz, 800 mm/s

thickness and the corresponding surface roughness that arises for different materials depending on the process parameters used and the characteristics of the laser beam.

During laser engraving process the kerf formation is observed which means that it is not possible to achieve vertical walls. The sidewalls show a slope called kerf taper angle which means that the actual dimensions of the engraved geometry deviate from the required ones. For example, when a cavity is engraved as shown in Fig. 7, the opening at the top level of the cavity (surface of the workpiece) is significantly larger than that at the bottom of the cavity. The need for high dimensional accuracy at laser engraving process, which means the minimization of the kerf taper angle, makes it imperative to study the effect of process parameters on the kerf formation.

The purpose of this study is to experimentally investigate the effect of process parameters on the quality and productivity of the laser engraving process. Laser
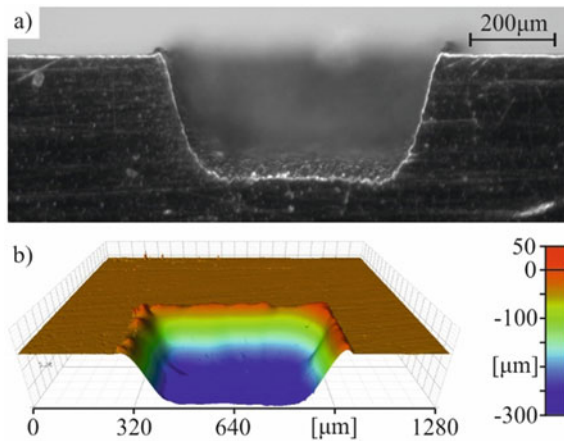
Fig. 7 Sloped sidewalls formation on a $600 \times 300\,\mu m$ laser engraved square pocket **a** picture taken by Leica M125 Stereomicroscope **b** 3D scanned geometry by ContourGT-K 3D optical microscope
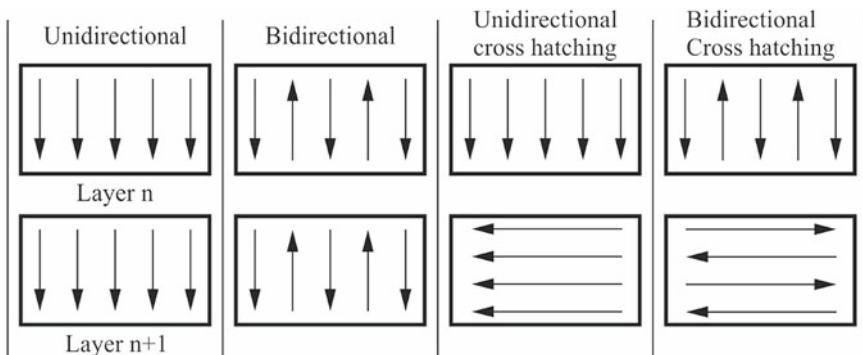
Fig. 8 LASERTEC 40 basic scanning strategies

Fig. 9 Unidirectional cross hatching strategy used for experimental tests
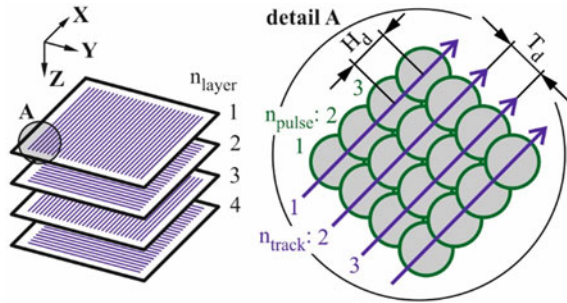
engraving tests were performed using a LASERTEC 40 laser machining center made by DMG MORI. This is a nanosecond pulsed Q-switched Nd:YAG laser machine emitting at 1064 nm with a nominal average power of 20 W, a pulse duration of 100 ns and a spot diameter of 30 μm. 5 mm thick plates from the following materials were used as workpieces for the experiments: stainless steel SAE304, pressure vessel steel P355GH, yellow brass C26000 and aluminium 7075. All measurements in the experimental samples were performed using Bruker Contour GT-K 3D optical microscope made by Bruker. The basic parameters examined to study their effect on the final laser engraving process result are the average power, the repetition rate, the scanning speed and the engraving depth. Removed material layer thickness and material removal rate was chosen as indicators for productivity. Surface roughness and kerf taper angle were chosen as quality indicators. From the analysis of the results, conclusions were drawn regarding the process parameters that must be selected each time to achieve the desired result.

5　Equipment and Materials

The implementation of the experimental procedure was divided into two parts. Laser engraving experiments were first performed to study the effect of process parameters on the removed material layer thickness and surface roughness. Then, new experiments were performed to study the appearance of kerf formation. All engraving experiments were performed using the LASERTEC 40 laser machining center made by DMG MORI. The technical data as specified in the manufacturer's technical data sheet for the LASERTEC 40 laser machining center are presented in Table 1.

The procedure followed to engrave a geometry on a workpiece using LASERTEC 40 laser machining center is summarized in the following basic steps. Using a CAD (Computer-aided design) software, the three-dimensional model of the geometry to be engraved is initially designed. The machine accepts three-dimensional volume files in.stl (stereolithography) format as input that describes the surface geometry of a three-dimensional object to be engraved. It is worth noting that the file with the geometry that will be given as input to the laser machine should refer to the

Table 1 LASERTEC 40 laser machining center technical data

		Manufacturer	DMG MORI
		Model	LASERTEC 40
		Laser type	Q-switched Nd:YAG
		Wavelength	1064 nm
		Pulse width	100 ns
		Spot diameter	30 μm
		Focal length	100 mm
		Average power (nom.)	20 W
		Peak power (nom.)	10 kW
		Pulse energy (nom.)	1 mJ
		Pulse repetition rate	20–80 kHz
		Scanning speed	50–1000 mm/s
Table size	400 × 300 mm	Max. load	50 kg
Rapid traverse	20 m/min	Acceleration	0.3 g
Work area X/Y/Z	400/300/500 mm	Laser range	60 × 60 mm
CAM software	LPSWin	Control software	LaserSoft 3D

geometry of the material to be removed. The.stl file is transferred to the controller of the machine using a usb stick and its processing follows in order to determine the parameters required for the machining. Software LPSWin is used to generate the laser beam tool path.

Software LPSWin is provided by the machine manufacturer and works like a CAM (Computer-aided manufacturing) software. As input the LPSWin software takes the.stl file with the geometry to be engraved as well as some parameters related to the laser processing such as the workpiece zero point, the removed material layer thickness, the scanning strategy and the track distance. The removed material layer thickness refers to the thickness of the layer of material to be removed at each level that the laser beam scans the workpiece for the specific process parameters selected to be used. Knowledge of the removed material layer thickness prior to machining is necessary for the LPSWin software to calculate how many passes-layers must be made to achieve the final desired machining depth. The laser machine scans the workpiece by making pulses in straight tracks parallel to each other in multiple layers. The distance between two successive straight tracks of pulses is called track distance and the way one layer is scanned over the next is called a scanning strategy or scanning type. The basic scanning strategies available on LASERTEC 40 are shown in Fig. 8. Apart from these, there is also the possibility for rotary hatching, during which the

laser tracks of one level form a specific angle in relation to the previous ones, and there is also the possibility for random hatching. The choice of the appropriate scanning strategy and the track distance is made empirically depending on the geometry that is engraved. As has been shown by experimental tests in the literature, they indirectly affect the time and quality of the laser engraving process. The scanning strategy chosen to be applied for all the experiments is unidirectional cross hatching with track distance $\mathbf{T_d}$ (distance between two successive laser beam tracks) to be equal with the hatching distance $\mathbf{H_d}$ (distance between two successive laser beam pulses in the same track) as shown in Fig. 9. The hatching distance $\mathbf{H_d}$ is calculated by the Eq. 3. The overlap degree $\mathbf{O_d}$ between two following laser pulses which shows how two successive laser beam pulses overlap each other is calculated from the hatching distance $\mathbf{H_d}$ and the laser spot diameter $\mathbf{D}$ by the Eq. (4). A file with .l4d extension is extracted from software LPSWin which contains all the movements of the laser beam for the engraving process which is then given as input to software LaserSoft 3D.

$$H_d = \frac{V}{F} \tag{3}$$

$$O_d = \left(1 - \frac{H_d}{D}\right)\% \tag{4}$$

LaserSoft 3D software is the one that controls the LASERTEC 40 CNC laser machining center. The other process parameters such as average power, scanning speed and repetition rate are entered in LaserSoft 3D software. In addition, through the LaserSoft 3D software the part zero is located on the CNC laser machine. The zero point of the workpiece in laser machine is selected and defined at the appropriate point on the surface of the workpiece so that it is identical with the position where the zero point in the.l4d file has been set. The locating process of the zero point takes place in two phases. At first, using a camera as shown in Fig. 10a, the origin of the
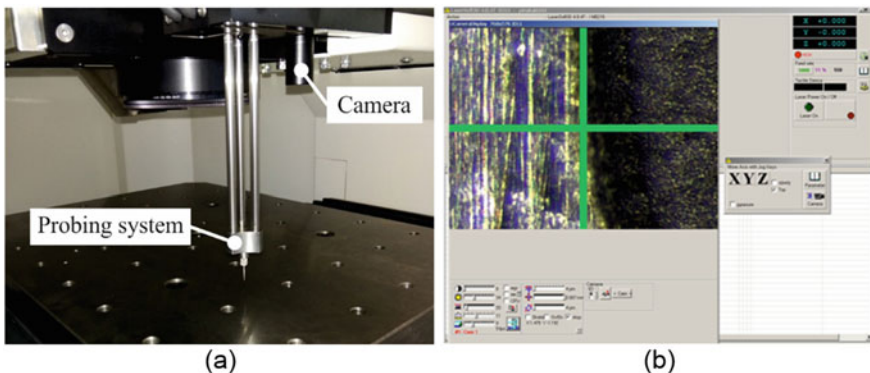
Fig. 10 **a** LASERTEC 40 camera and probing system **b** setting the origin of the X–Y coordinate system using camera

X–Y coordinate system is placed in the desired position of the workpiece. Then, the Z = 0 plane is determined with high accuracy using a touch probing system that is presented in Fig. 10b. Once all the above procedures have been completed, the laser machine is ready to perform the laser engraving process.

The engraving experiments performed were measured using a ContourGT-K 3D optical microscope-profilometer made by Bruker. The profilometer is a measuring instrument used to measure the profile of a surface and extract topographical data, with the aim of quantifying certain quantities related to it such as the engraving depth, the slope of the sidewalls and the roughness of the surface for the case studied here. The characteristics of profilometer ContourGT-K are presented in detail in the Table 2.

The experiments were performed on stainless steel SAE304, pressure vessel steel P355GH, yellow brass C26000 and aluminium 7075 plates with dimensions of approximately 200 × 200 mm and 5 mm thick. The materials used show strongly different behaviors during laser processing due to the differences in thermophysical properties and the differences in the absorption of the laser beam of each one [23] as shown in Table 3.

6 Removed Material Layer Thickness and Roughness

6.1 Experimental Procedure

This section presents the experimental procedure followed for conducting experiments with the aim of studying the effect of process parameters on the removed material layer thickness and roughness. Square pockets of dimensions 4 × 4 mm were engraved as shown in Fig. 11a on 5 mm thick stainless steel SAE304, pressure vessel steel P355GH, yellow brass C26000 and aluminium 7075 plates. The pockets was chosen to be engraved keeping a constant number of layers equal to 50 for stainless steel, pressure vessel steel, yellow brass and 30 for aluminium. The number of layers for the different materials was chosen so that to be large enough to reduce the error that will occur for the removed material layer thickness and at the same time the total engraving depth of the pocket to not exceed the thickness of the plate.

The laser engraving process was performed using the LASERTEC40 laser machining center. The process parameters examined are the following: Average Power **P**, Scanning Speed **V**, Repetition Rate **F**. For each of the materials it was chosen to test 3 levels for average power, 7 levels for scanning speed and 7 levels for repetition rate as shown in Table 4. In other words, 147 experiments were performed for each material, which means that the total number of experiments was 588. In Fig. 12 it is presented stainless steel plate with the laser engraved square pockets on it. The range of parameters tested was selected according to the instructions of the machine manufacturer.

Table 2 ContourGT-K 3D Optical Microscope technical data

		Manufacturer	Bruker
		Model	ContourGT-K
		Type	3D Optical Microscope
		Max scan range	Up to 10 mm
		Vertical resolution	<0.01 nm
		RMS repeatability	0.01 nm
		Lateral resolution	0.38 µm min (Sparrow crit.) 0.13 µm (with AcuityXR™) 0.01 µm (with NanoLens)
		Step height accuracy	<0.75%
		Step height Rep/ty	<0.1% 1 sigma repeatability
		Max. scan speed	47 µm/sec
		Z scan range	0.1–10 mm
		Z focusing	100 mm
		Sample reflectivity	0.05–100%
		Max. sample slope	Up to 40° (shiny surfaces) Up to 87° (rough surfaces)
Sample Height	Up to 100 mm	XY sample stage	150 mm
Max. sample weight	4.5 kg	Tip/Tilt function	±6° manual in stage
Calibration	Via traceable step standards	Objectives	Parfocal: 2.5x, 5x, 10x, 20x, 50x LWD: 2x,5x,10x
Camera	Monochrome: 640 × 480	System software	Vision64 operation and analysis software

Table 3 Reflectivity (%) of polished metals for 1.06 µm Nd:YAG lasers
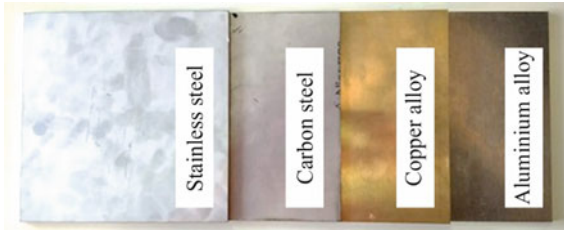
Material	Room temp.	Melting temp.
Aluminium alloys	94.1	79.8
Copper alloys	95.1	83.9
Carbon steels	91.3	61.8
Stainless steels	69.3	55.8
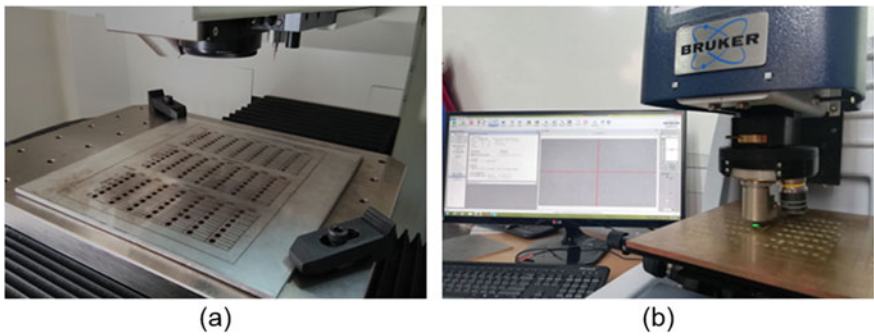
Fig. 11 **a** square pockets engraved using LASERTEC40 laser machining center **b** square pocket measuring process using ContourGT-K 3D optical microscope-profilometer

Table 4 Process parameters levels

Process parameters	Units	Levels			
		Stainless steel SAE304	Aluminium 7075	Pressure vessel steel P355GH	yellow brass C26000
Average power P	W	8, 12, 16	8, 12, 16	8, 12, 16	8, 12, 16
Scanning speed V	mm/s	100, 200, 300, 400, 500, 600, 700	100, 200, 300, 400, 500, 600, 700	200, 300, 400, 500, 600, 700, 800	200, 300, 400, 500, 600, 700, 800
Repetition rate F	kHz	20, 30, 40, 50, 60, 70, 80	20, 30, 40, 50, 60, 70, 80	20, 30, 40, 50, 60, 70, 80	10, 20, 30, 40, 50, 60, 70
Layers n		50	30	50	50
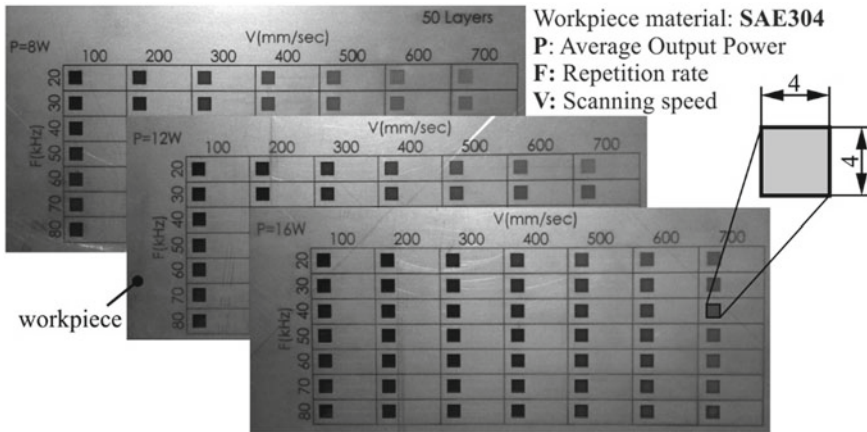
Fig. 12 Stainless steel plate with the laser engraved 4 × 4 mm square pockets on it

Each of the square pockets engraved was measured using ContourGT-K 3D optical microscope-profilometer as shown in Fig. 11b. Using the optical profilometer, the 3D geometry of each pocket was scanned and its topographic data were obtained. Due to the limited scanning range of the profile meter (1.26 × 0.9 mm) it was chosen for each pocket to scan a section around the border so that both the top surface of the plate-workpiece and the bottom of the pocket are visible in the measurement. From the analysis of the topographic data, the average total engraving depth **Dzn** of each pocket was calculated as shown in Fig. 13. The removed material layer thickness **Dz** was calculated by dividing the average total engraving depth by the number of layers **n** made.

The engraved pockets were measured again using the ContourGT-K 3D optical profilometer to measure the surface roughness. ContourGT-K 3D optical profilometer is based on the principle of two-beam optical interferometry and confocal profilometry to perform non-contact 3D surface measurements. The Vision64 analysis software provided by the profilometer's manufacturer is equipped with the Analysis Toolbox plugin which either modifies the data output or performs a specific analysis according to user-selected analytical functions to calculate parameters that characterize the profile data such as the **Ra** (average roughness). The arithmetical mean roughness **Ra**, the most commonly used international parameter of roughness, calculates the arithmetic average deviation from the mean line within the assessment length. Measurements were made at the bottom of the pocket. Figure 14 schematically shows an example of a roughness measurement at a specific position of a square pocket engraved in stainless steel SAE304 with the following process parameters: average power **P** = 12 W, repetition rate **F** = 40 kHz and scanning speed **V** = 500 mm/s. Five separate roughness measurements were performed in different areas for each pocket. The final arithmetical mean roughness value **Ra** was calculated as the mean value of the five individual roughness values measured (Figs. 15, 16 and 17).
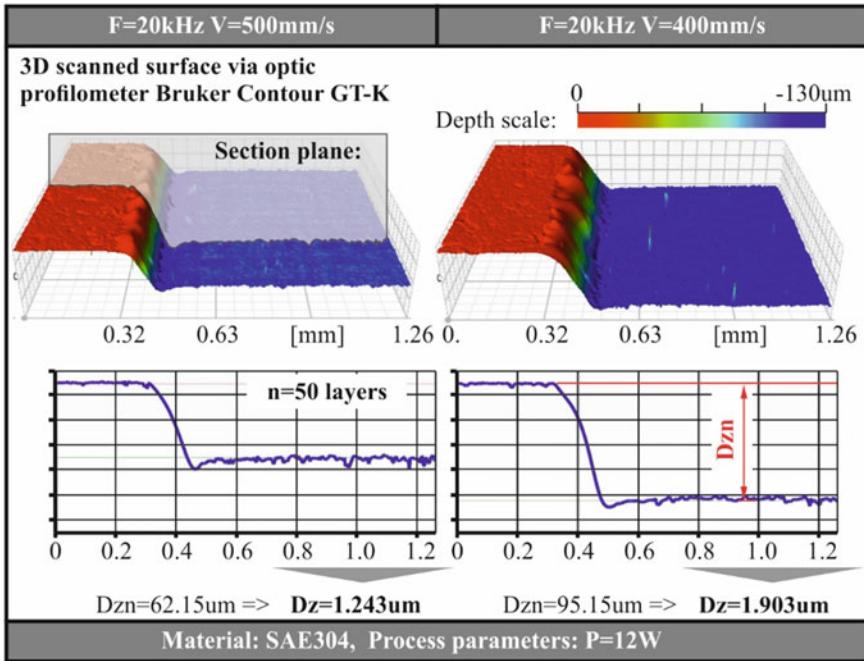
Fig. 13 Determination of the removed material layer thickness **Dz** from the 3D scanned geometry

6.2 Removed Material Layer Thickness Results

The results of the measured removed material layer thickness **Dz** from the experiments as function of the average power **P**, the repetition rate **F** and the scanning speed **V** for stainless steel SAE304, aluminium 7075, pressure vessel steel P355GH and yellow brass C26000 laser engraving process are presented in Fig. 18, Fig. 19, Fig. 20 and Fig. 21 respectively. Observing the diagrams with the results some conclusions can be drawn regarding the effect of the process parameters on the removed material layer thickness **Dz**.

First, the stainless steel SAE304 laser engraving process is studied. Visually observing the engraved pockets, as far as the selection of the range of parameters studied, it is observed that for the scanning speed **V** = 100 mm/s the engraving process has not been performed in a proper way. Regardless of the value of the average power and the repetition rate, the quality of the engraving for the scanning speed **V** = 100 mm/s is poor. That is, although great depth has been achieved, the engraved surface does not have the desired shape and form and is characterized by strong non-uniformity as shown in Fig. 15.

The removed material layer thickness **Dz** measured results for stainless steel SAE304 are presented Fig. 18. Initially it is observed that for any values of repetition rate **F** and scanning speed **V** an increase in average power **P** leads to a significant
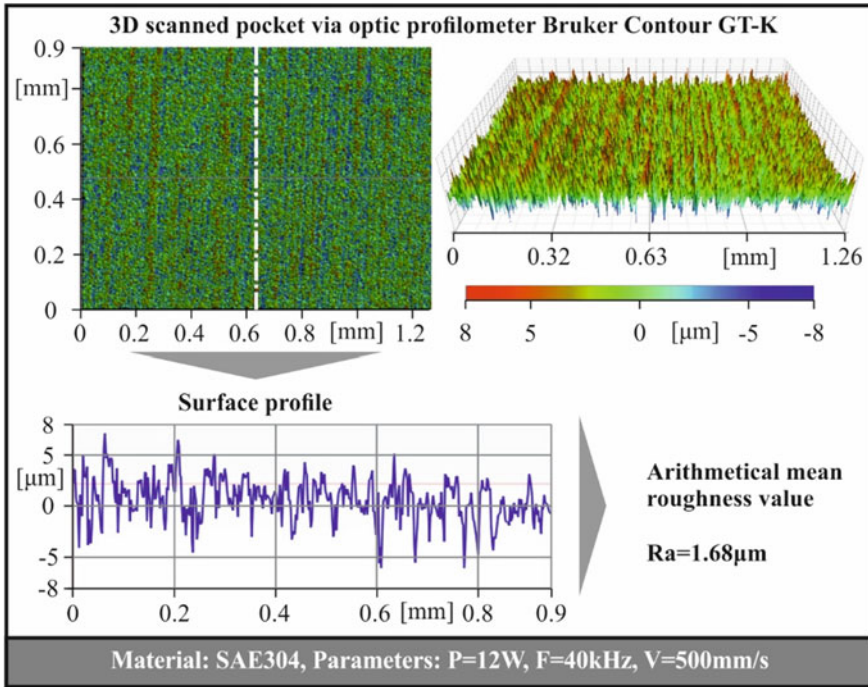
Fig. 14 Roughness **Ra** measurement using Bruker Contour GT-K optical profilometer
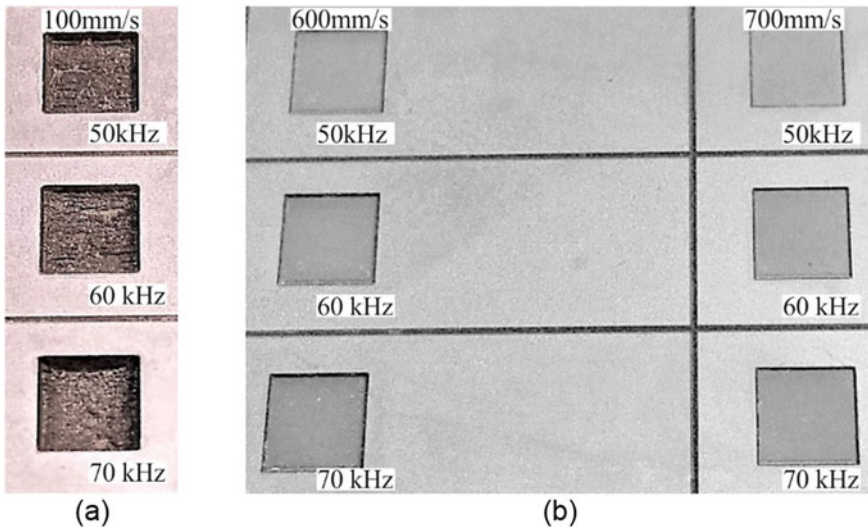
Fig. 15 Poor laser engraving quality for scanning speed **V** = 100 mm/s on stainless steel SAE304: pockets engraved with **P** = 16 W, **F** = 50, 60, 70 kHz and **a** V = 100 mm/s **b** V = 600, 700 mm/s

increase in the removed material layer thickness **Dz**. Furthermore, a reduction in scanning speed **V** leads to a significant increase in the removed material layer thickness **Dz**. As far as the repetition rate **F** effect, considering that the scanning speed **V** = 100 mm/s is ignored due to poor engraving quality, some cases are distinguished depending mainly on the imposed average power but also the scanning speed. For the low average power of **P** = 8 W it is observed that for small values of the repetition rate **F** the removed material layer thickness **Dz** is kept low, for repletion rate around **F** = 40 kHz it shows a maximum and for high repetition rates it is kept low again. Similar behavior occurs for medium average power **P** = 12 W and high average power **P** = 16 W with the difference that the maximum removes material thickness **Dz** occurs around repetition rate **F** = 60 kHz and around **F** = 70–80 kHz respectively with the exception of the scanning speed **V** = 200 mm/s which shows the maximum in all cases at **F** = 40 kHz. Based on the above, assuming that speed **V** = 100 mm/s is ignored, for average power **P** = 16 W the maximum removed material layer thickness **Dz** = 19.392 μm is found for repetition rate **F** = 40 kHz and scanning speed **V** = 200 mm/s and the minimum **Dz** = 0.814 μm is found for **F** = 20 kHz and **V** = 700 mm/s. For average power **P** = 12 W the maximum removed material layer thickness **Dz** = 12.858 μm is found for **F** = 40 kHz and **V** = 200 mm/s and the minimum **Dz** = 0.701 μm is found for **F** = 20 kHz and **V** = 700 mm/s. For average power **P** = 8 W the maximum removed material layer thickness **Dz** = 7.838 μm is found for **F** = 40 kHz and **V** = 200 mm/s and the minimum **Dz** = 0.272 μm is found for **F** = 80 kHz and **V** = 700 mm/s. If it is assumed that the quality of the process is not a criterion but the maximum possible removed material layer thickness needs to be achieved, for example when roughing operation is performed, then the process parameters **P** = 16 W, **F** = 80 kHz and **V** = 100 mm/s that give the maximum removed material layer thickness **Dz** = 41.622 μm could be used.

Afterwards, the aluminium 7075 laser engraving process is studied. Regarding the range of process parameters, it was observed that as shown in Fig. 16 for some cases
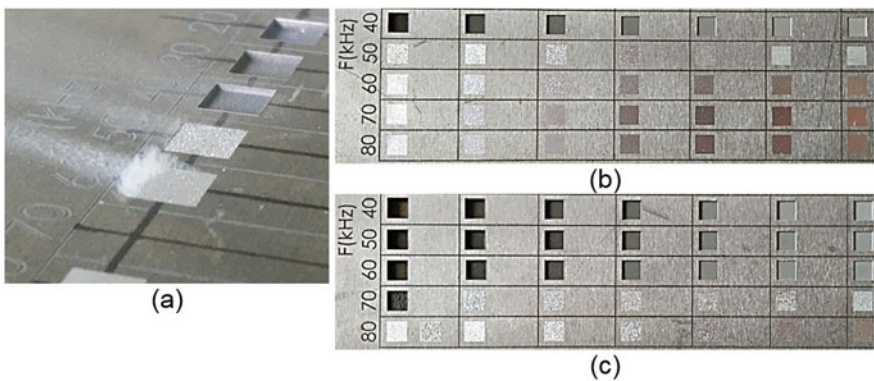

Fig. 16 **a** No material ablation for some process parameters of aluminium 7075 laser engraving process **b** pockets that no material ablation took place for average power **P** = 8 W and **c** **P** = 12 W

it was not possible to engrave the aluminum. More specifically, for square pockets with average power $\mathbf{P} = 8$ W and repetition rates of $\mathbf{F} = 50, 60, 70, 80$ kHz as well as for pockets with average power of $\mathbf{P} = 12$ W and repetition rates of $\mathbf{F} = 70, 80$ kHz no material removal was performed and consequently the removes material layer thickness $\mathbf{Dz}$ was measured to be zero. The reason that no material is removed is that the maximum peak power P_{peak} of the laser beam pulses is not enough to vaporize the aluminum. Based on the process parameters values of the experiments in which no material ablation was performed using Eq. (1) it is calculated that the minimum peak power to perform the aluminum laser engraving process is $P_{peak} = 1.7$ kW which is equivalent to a laser beam pulse fluence about 24 J/cm^2.

The removed material layer thickness $\mathbf{Dz}$ measured results for aluminium 7075 are presented Fig. 19. For aluminum 7075, same as previously mentioned for stainless steel, increasing the average power $\mathbf{P}$ and decreasing the scanning speed $\mathbf{V}$ lead to a significant increase in the removed material layer thickness $\mathbf{Dz}$. Regarding the effect of repetition rate, there are three cases depending on the average power. For the case of the low average power $\mathbf{P} = 8$ W the removed material layer thickness $\mathbf{Dz}$ increases by decreasing the repetition rate $\mathbf{F}$ for scanning speed between 100 and 500 mm/s whereas the removed material layer thickness $\mathbf{Dz}$ initially increases by decreasing the repetition rate $\mathbf{F}$ until it reaches a maximum value for repetition rate $\mathbf{F} = 30$ kHz and then decreases for scanning speed $\mathbf{V} = 600, 700$ mm/s. In the case of the medium average power $\mathbf{P} = 12$ W for scanning speed $\mathbf{V}$ from 200 to 700 mm/s it is observed that decreasing the repetition rate $\mathbf{F}$ increases the removed material layer thickness $\mathbf{Dz}$ until it reaches its maximum value for $\mathbf{F} = 30$ kHz and then decreases with the exception of scanning speed $\mathbf{V} = 100$ mm/s where the increase of the removed material layer thickness $\mathbf{Dz}$ is continuous. In the case of the high average power $\mathbf{P} = 16$ W for scanning speed $\mathbf{V}$ from 300 to 700 mm/s it is observed that decreasing the repetition rate $\mathbf{F}$ increases the removed material layer thickness $\mathbf{Dz}$ until it reaches its maximum value for $\mathbf{F} = 40$ kHz and then decreases. For the scanning speed $\mathbf{V} = 200$ mm/s it is observed the same behavior with the only difference that the maximum value of $\mathbf{Dz}$ is for $\mathbf{F} = 30$ kHz. For scanning speed $\mathbf{V} = 100$ mm/s decreasing the repetition rate $\mathbf{F}$ leads to a continuous increase in removed material layer thickness $\mathbf{Dz}$. Based on the above, the maximum removed material layer thickness $\mathbf{Dz}$ for aluminium 7075 laser engraving process appears in all cases for scanning speed $\mathbf{V} = 100$ mm/s and repetition rate $\mathbf{F} = 20$ kHz and is equal to $\mathbf{Dz} = 30.902$ μm for average power $\mathbf{P} = 8$ W, with $\mathbf{Dz} = 51.289$ μm for $\mathbf{P} = 12$ W and $\mathbf{Dz} = 62.458$ μm for $\mathbf{P} = 16$ W.

The removed material layer thickness $\mathbf{Dz}$ measured results for pressure vessel steel P355GH are presented Fig. 20. In the same way as in the previous materials, in pressure vessel steel P355GH an increase in average power $\mathbf{P}$ and a decrease in scanning speed $\mathbf{V}$ lead to an increase in removed material thickness $\mathbf{Dz}$. Regarding the repetition rate $\mathbf{F}$ effect it is observed that regardless of scanning speed for low average power P = 8 W the removed material layer thickness $\mathbf{Dz}$ is maximized for repetition rate $\mathbf{F}$ around 40 kHz, for medium average power $\mathbf{P} = 12$ W is maximized for repetition rate $\mathbf{F}$ around 50–60 kHz and for high average power $\mathbf{P} = 16$ W is maximized for frequency around 70 with 80 kHz with the exception of the scanning

speed $V = 200$ mm/s which at $P = 12$ W and $P = 16$ W gives maximum Dz for F = 50 kHz. Therefore, the maximum removed material layer thickness $Dz = 18.921$ μm is obtained for average power $P = 16$ W, repetition rate $F = 50$ kHz and scanning speed $V = 200$ mm/s.

As far as yellow bras C26000 engraving is concerned, it was observed that all the square pockets engraved with repetition rate $F = 10$ kHz, regardless of the average power P, have poor engraving quality. On the engraved surface as shown in Fig. 17 the ablated material from the laser beam pulses gave the material a chessboard pattern. The reason for the above phenomenon is that because the repetition rate $F = 10$ kHz is too low it leads to negative overlap degrees O_d. This means that there is no overlap between the successive pulses, with the result that the pulses create craters that deepen at each layer but leave between them a quantity of material that remains unaffected. In addition, it was observed that for repetition rates $F = 50, 60, 70$ kHz at low average power $P = 8$ W and for repetition rate $F = 70$ kHz at medium power $P = 12$ W the material removal was not performed and consequently the removed material layer thickness Dz was measured to be almost zero. The reason this happens, as mentioned for aluminum, is that maximum peak power P_{peak} of the laser beam pulses is not enough to start the material ablation. Thus, based on the experiments, it appears that for laser engraving in yellow brass C26000, a peak power P_{peak} greater than 1.7 kW is required or respectively a laser beam fluence greater than 24 J/cm^2.

The removed material layer thickness Dz measured results for yellow brass C26000 are presented Fig. 21. As far as the effect of average power P and scanning speed V is concerned, it is observed that in the same way as in the other materials the removed material layer thickness Dz increases by increasing the average power P and decreasing the scanning speed V. Regarding the effect of repetition rate F, there are three cases depending on the average power P. For low average power the
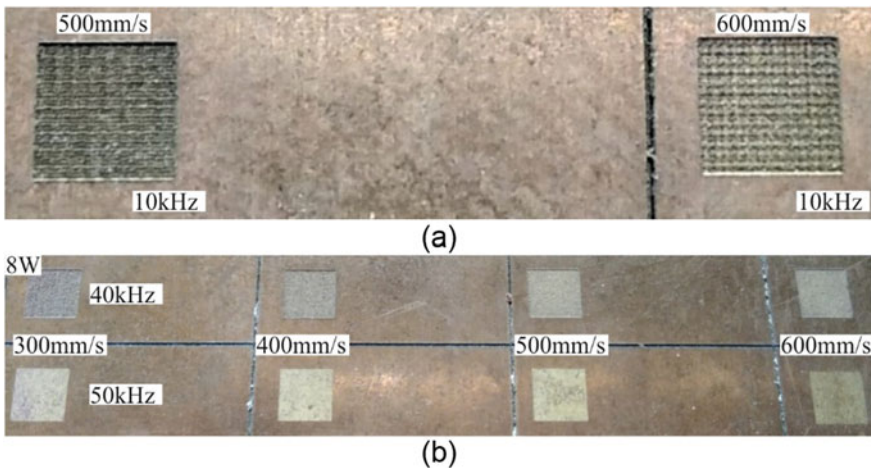
Fig. 17 a Poor pockets quality for repetition rate $F = 10$ kHz b inability to be engraved pockets for repetition rate $F = 40, 50$ kHz for average power $P = 8$ W
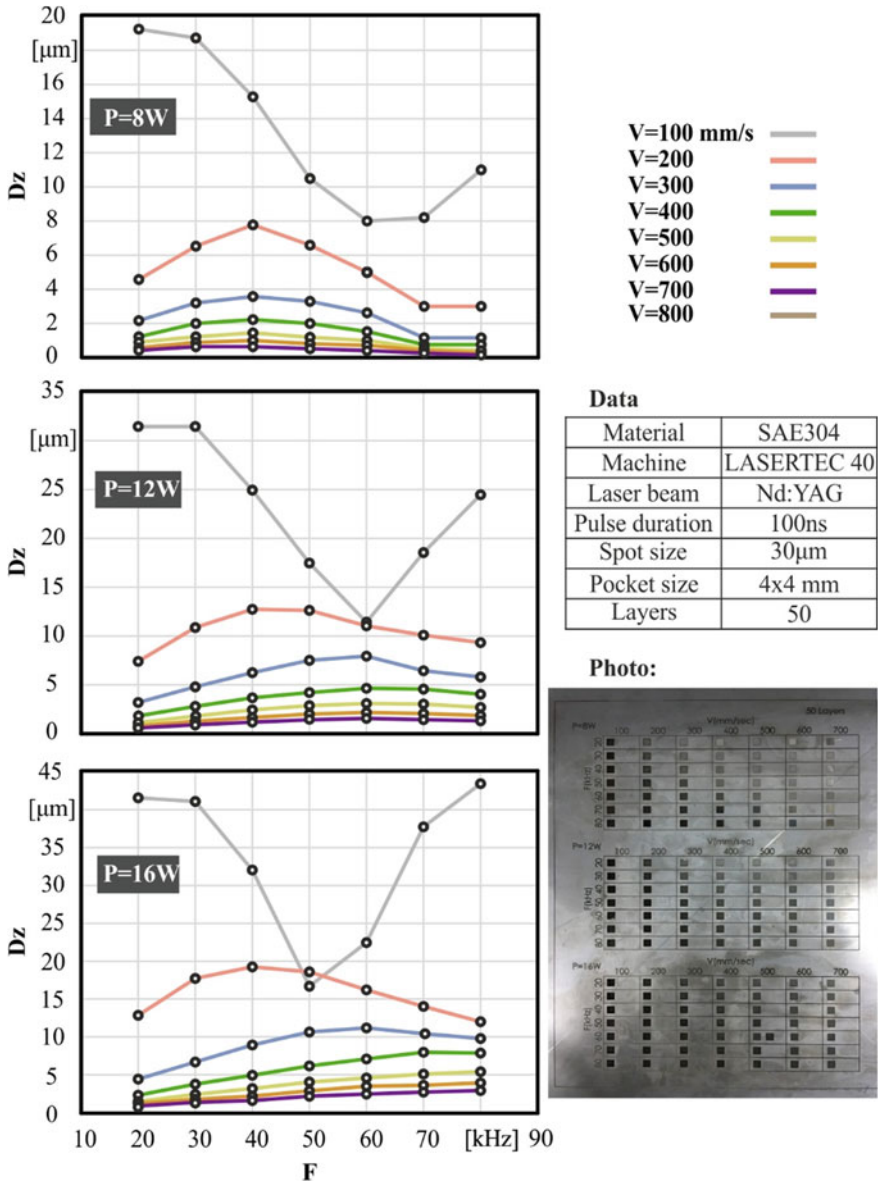
Fig. 18 Removed material layer thickness **Dz** for stainless steel SAE304
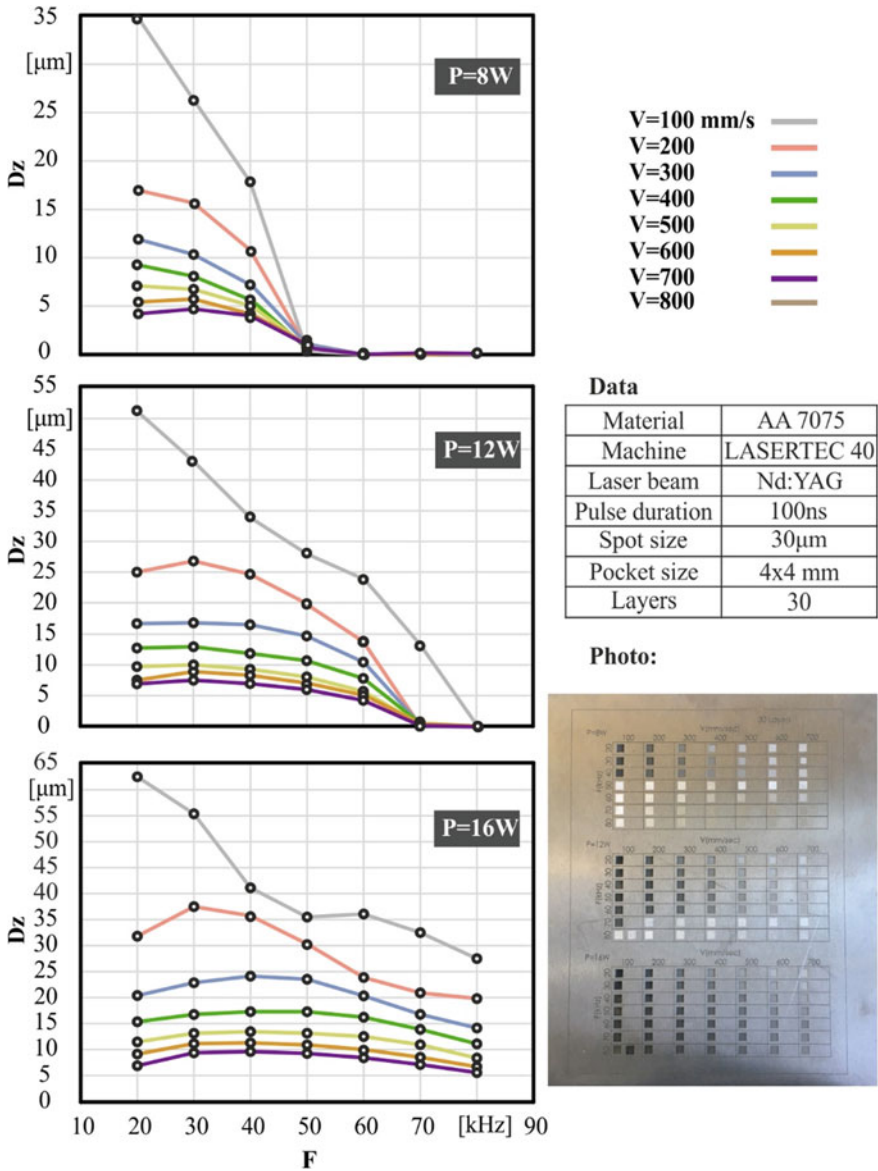
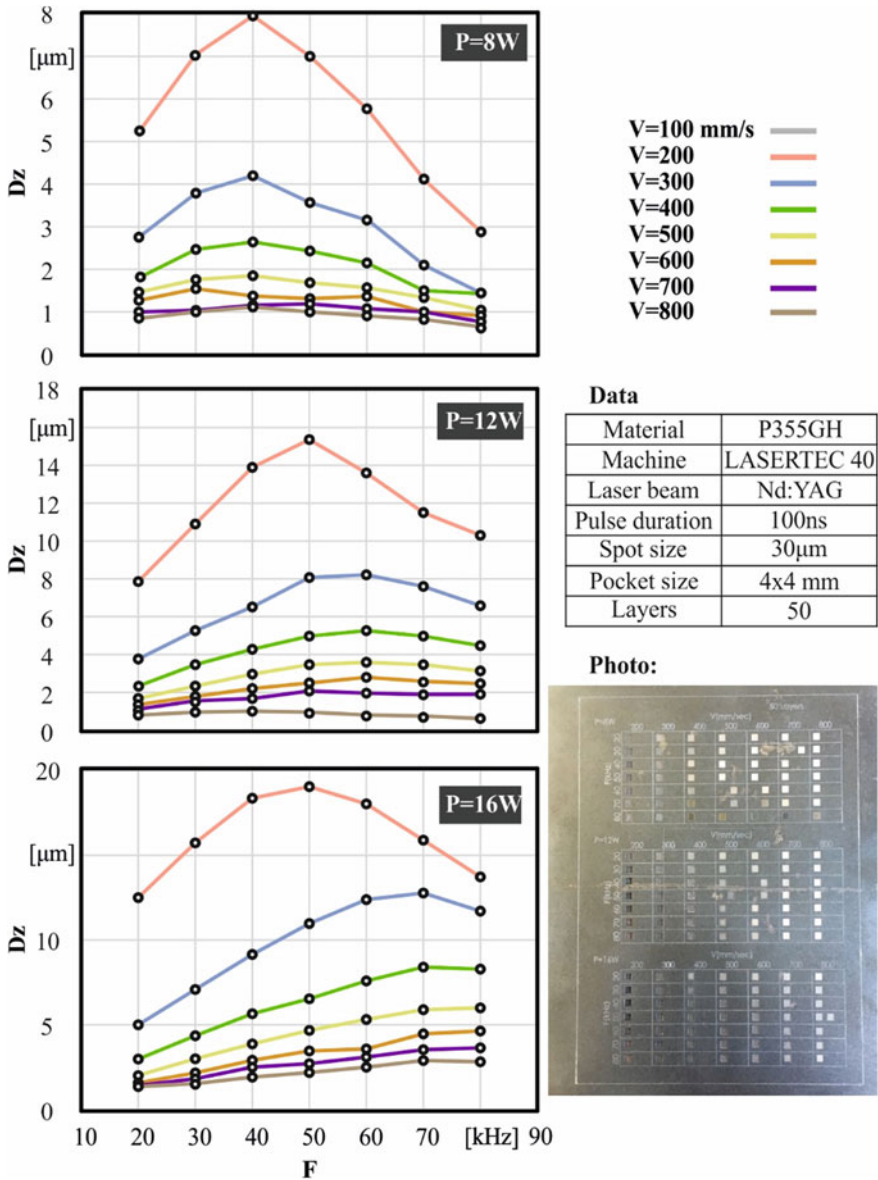**Fig. 19** Removed material layer thickness **Dz** for aluminium 7075

Fig. 20 Removed material layer thickness **Dz** for pressure vessel steel P355GH

removed material layer thickness **Dz** is maximized for repetition rate **F** = 20 kHz. For the medium average power **P** = 12 W it is observed that for low scanning speeds **V** = 200,300 mm/s the **Dz** is maximized for **F** = 40 kHz whereas for high scanning speeds **V** = 400–800 mm/s is maximized for **F** = 30 kHz. Finally, for high average power **P** = 16 W it is observed that for all scanning speeds the **Dz** is maximized for **F** = 40 kHz with the exception of scanning speed V = 200 mm/s for which the **Dz** is maximized for **F** = 50 kHz.

Knowing the values of the removed material layer thickness is not enough to evaluate the effect of process parameters on productivity. This is because the final machining time is not only determined by how big the thickness of each layer is removed each time but also by the time required to scan it. For example, when a surface is scanned with a laser beam using low speed then the thickness of the layer to be removed will be large but at the same time the time required to scan it will be high. Therefore, for the evaluation of productivity, a parameter should be used that will take into account both the thickness and the rate at which the surface is scanned. This parameter is the material removal rate **DV**. The material removal rate **DV** was calculated for each rectangular pocket as a function of scanning speed **V**, track distance **T_d** and removed material layer thickness **Dz** using the following equation:

$$DV[mm^3/s] = V[mm/s] * T_d[\mu m] * Dz[\mu m] * 10^{-6} \tag{5}$$

The diagrams showing the material removal rate **DV** during laser engraving process as a function of the process parameters stainless steel SAE304, aluminium 7075, pressure vessel steel P355GH and yellow brass C26000 are shown in Fig. 22. The results presented in Fig. 22 concern the high average power **P** = 16 W as it is known that increasing the average power of the beam leads to an increase in the material removal rate and hence to an increase in productivity. By observing the diagrams it is concluded that increasing the scanning speed **V** up to its maximum value (700 for stainless steel, aluminum and 800 for pressure vessel steel, yellow brass) and decreasing the repetition rate **F** (up to the value of 20 kHz for all materials) increases the material removal rate **DV**. The maximum material removal rate **DV** for aluminum 7075 is equal to 0.173 mm³/s for the average power **P** = 16 W, scanning speed **V** = 700 mm/s and repetition rate **F** = 20 kHz. The maximum **DV** for pressure vessel steel P355GH is equal to 0.046 mm³/s for **P** = 16 W, **V** = 800 mm/s and **F** = 20 kHz. The maximum **DV** for yellow brass C26000 is equal to 0.072 mm³/s for **P** = 16 W, **V** = 800 mm/s and **F** = 20 kHz. An exception as far as the scanning speed at which the maximum material removal rate is concerned is the stainless steel SAE304 as long as the maximum **DV** occurs for **P** = 16 W, **V** = 200 mm/s and **F** = 20 kHz and is equal to 0.026 mm³/s.

It is therefore worth noting that although in most cases high scanning speeds lead to small removed material layer thicknesses they lead to a higher material removal rate and consequently to higher productivity. Another important observation is that while in aluminum 7075 and yellow brass C26000 for small values of peak power P_{peak} it is not possible to carry out the material ablation (in stainless steel SAE304
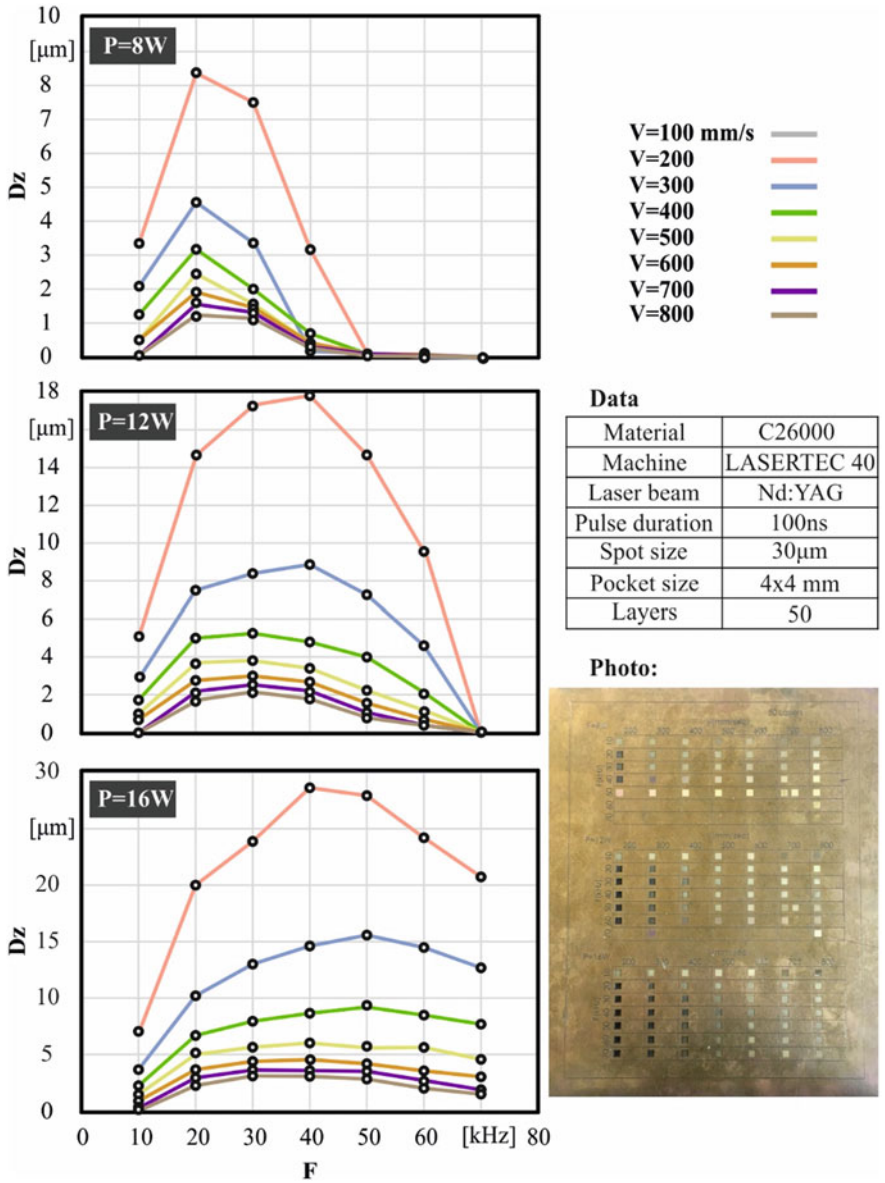
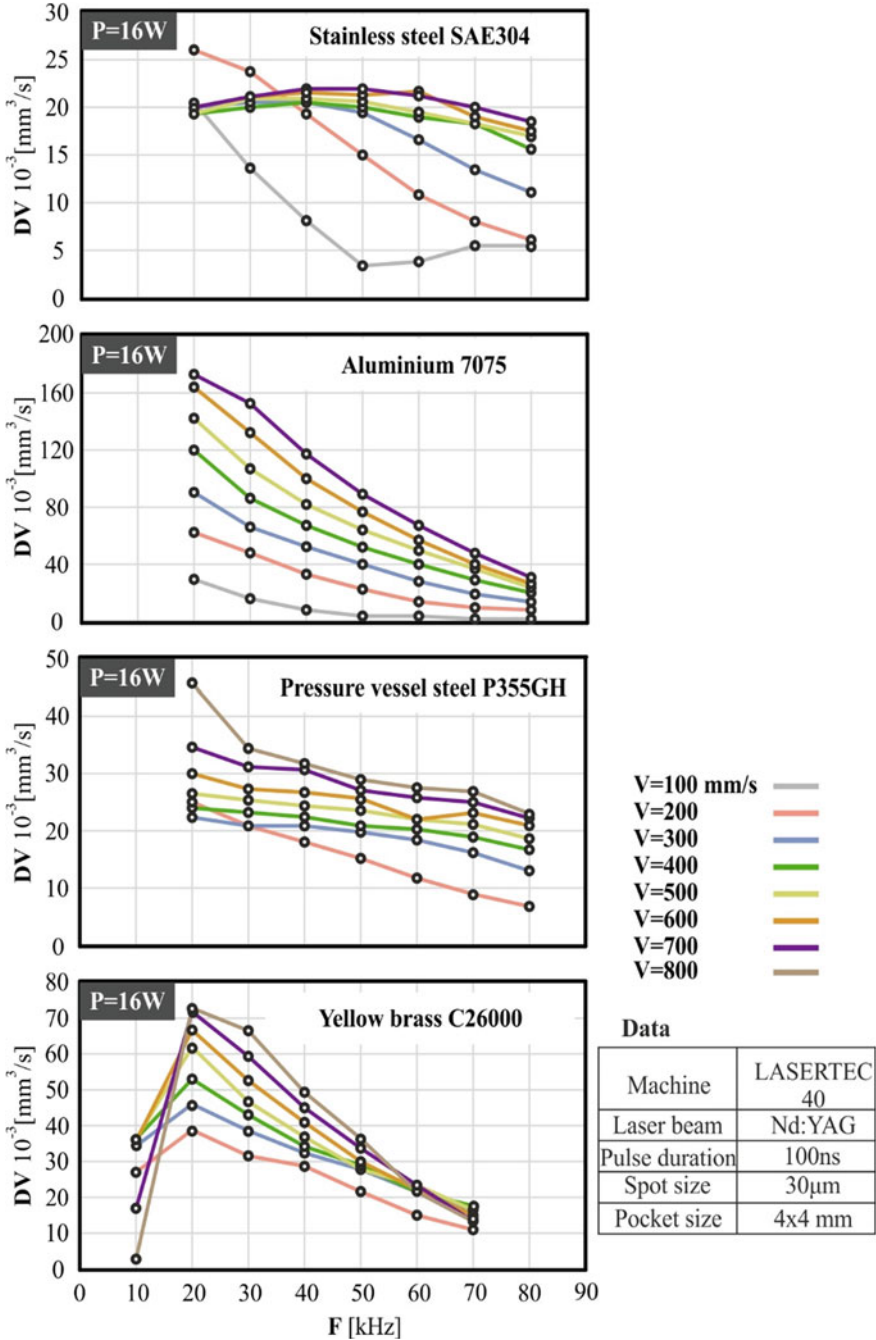**Fig. 21** Removed material layer thickness **Dz** for yellow brass C26000

Fig. 22 Material removal rate **DV** for stainless steel SAE304, aluminium 7075, pressure vessel steel P355GH and yellow brass C26000 as a function of repetition rate **F** and scanning speed **V** for average power **P** = 16 W

and pressure vessel steel P355GH there is no similar problem), at high values of peak power P_{peak} they cause a higher material removal rate **DV** than stainless steel SAE304 and pressure vessel steel P355GH. The reason that there is difficulty in starting the material ablation for aluminum and yellow brass is that they have much higher reflectivity in the laser beam at temperatures below the melting temperature compared to other materials as presented in Table 3. When the power is enough to start the material ablation, aluminium and brass show a higher material removal rate due to the fact that at the melting temperature all materials have almost similar laser beam absorption coefficients and furthermore they have more propitious thermophysical properties for material vaporization.

6.3 Roughness Results

This section presents the results concerning the measured roughness for the engraved square pockets. In Fig. 23 it is presented a correlation between measured removed material layer thickness **Dz** and roughness **Ra** for the engraved square pockets in stainless steel SAE304 and aluminium 7075. In Figs. 24, 25 and 26 are presented the diagrams showing the roughness **Ra** formed during laser engraving process as a function of the process parameters for stainless steel SAE304, aluminium 7075 and yellow brass C26000. Figure 24 shows the results of the roughness **Ra** measured for stainless steel SAE304. As mentioned in a previous chapter due to the fact that for the scanning speed **V** = 100 mm/s the engraving was not successfully performed the roughness for it was not measured. In the case of pockets engraved with low average power **P** = 8 W it is observed that for scanning speeds **V** from 400 to 700 mm/s low surface roughness **Ra** values around 1.2 µm appear and there is a tendency to decrease the roughness with increasing scanning speed **V** and increasing the repetition rate **F**. For scanning speeds 200 and 300 mm/s the roughness is much higher compared to the other scanning speeds. For the low average power **P** = 8 W the minimum roughness was measured for repetition rate **F** = 70 kHz, scanning speed **V** = 700 mm/s and is equal to **Ra** = 0.88 µm. For the pockets engraved with medium average power **P** = 12 W, it is observed that for the scanning speeds 500–700 mm/s low values of roughness around 1.6 µm are achieved. For scanning speeds 200–400 mm/s the roughness values are increased. Regarding the effect of scanning speed, it is observed that increasing the scanning speed leads to a decrease in roughness. The repetition rate for high scanning speeds 500–700 mm/s does not seem to have any effect while for low scanning speeds 300 and 400 mm/s increasing the repetition rate leads to an increase in roughness. For the medium average power **P** = 12 W the lowest value of the roughness measured is **Ra** = 1.28 µm for **F** = 80 kHz and **V** = 700 mm/s. For the high average power **P** = 16 W, similar to the previous one, for low scanning speeds 200–400 mm/s the values of the roughness are high while for high scanning speeds 500–700 mm/s there are low values of the roughness around 2.0 µm. Increasing the scanning speed here also leads to a reduction in roughness while reducing the repetition rate leads to a reduction in roughness. For the high average power **P** =

16 W the minimum value of roughness results for $\mathbf{F} = 20$ kHz, $\mathbf{V} = 700$ mm/s and is equal to 1.54 µm. Regarding the effect of the average power $\mathbf{P}$, the conclusion is that in general the reduction of the average power reduces the value of the surface roughness with the minimum roughness of 0.88 µm for the $\mathbf{P} = 8$ W to be about half of the minimum roughness 1.54 µm for the $\mathbf{P} = 16$ W.

The results for the roughness measured for aluminum 7075 are shown in Fig. 25. As mentioned in a previous chapter for average power $\mathbf{P} = 8$ W at repetition rates $\mathbf{F} = 50, 60, 70, 80$ kHz and for $\mathbf{P} = 12$ W at $\mathbf{F} = 70, 80$ kHz it was not possible to perform the laser engraving process and therefore the corresponding roughness values were not measured. In addition, the pockets were not measured at scanning speed of 100 mm/s because their total depth was large and the lens of the optical profilometer could not get close enough to the bottom of the pocket to be focused for the measurement. For the low average power $\mathbf{P} = 8$ W it is observed that increasing scanning speed $\mathbf{V}$ leads to a decrease of roughness $\mathbf{Ra}$. Regarding the repetition rate $\mathbf{F}$, for the scanning speeds 200, 300, 700 mm/s the minimum value of the roughness seems to appear for $\mathbf{F} = 30$ kHz. For the remaining scanning speeds 400, 500, 600 mm/s reduction of repetition rate leads to reduction of roughness. For the low average power $\mathbf{P} = 8$ W the minimum roughness $\mathbf{Ra}$ was measured equal to 2.4 µm for $\mathbf{F} = 30$ kHz, $\mathbf{V} = 700$ mm/s. For the medium average power $\mathbf{P} = 12$ W the increase of the scanning speed $\mathbf{V}$ leads to a decrease of the roughness. Regarding to the repetition rate $\mathbf{F}$ the roughness minimizes for $\mathbf{F}$ around 40–50 kHz. The minimum roughness for the medium average power $\mathbf{P} = 12$ W appears for $\mathbf{F} = 40$ kHz, $\mathbf{V} = 700$ mm/s and is equal to 2.9 µm. For the high average power $\mathbf{P} = 16$ W, behaviors similar to the previous one occurs: an increase in scanning speed $\mathbf{V}$ leads to a decrease in roughness $\mathbf{Ra}$ and the roughness minimizes for repetition rate $\mathbf{F}$ of 50–60 kHz. For the high average power $\mathbf{P} = 16$ W the minimum roughness is equal to 3.75 µm for $\mathbf{F} = 50$ kHz, $\mathbf{V} = 700$ mm/s. As in stainless steel, so in aluminum it appears that the increase in average power has a negative effect on the surface roughness formed.

Figure 26 shows the roughness measured for the yellow brass C26000. For exactly the same reasons mentioned above for aluminum, the roughness for the scanning speed $\mathbf{V} = 100$ mm/s as well as the repletion rates $\mathbf{F} = 50, 60, 70$ kHz for $\mathbf{P} = 8$ W and $\mathbf{F} = 70$ kHz for $\mathbf{P} = 12$ W was not measured. In addition, the pockets with repetition rate $\mathbf{F} = 10$ kHz were not measured because they had poor engraving quality for the reasons discussed in a previous chapter. For the low average power $\mathbf{P} = 8$ W from the diagrams it is observed that there is a general tendency to decrease the roughness with increasing scanning speed and decrease the repetition rate with the exception of a few cases that show different behaviors. For the low average power $\mathbf{P} = 8$ W the minimum roughness is $\mathbf{Ra} = 1.5$ µm for repetition rate $\mathbf{F} = 30$ kHz and scanning speed $\mathbf{V} = 800$ mm/s. For the medium power $\mathbf{P} = 12$ W it is observed that with increasing scanning speed the roughness decreases with the exception of the scanning speed $\mathbf{V} = 200$ mm/s which shows less roughness than the next ones. Regarding the repetition rate, it is observed that for the scanning speeds 200–400 mm/s a reduction of the repetition rate leads to a reduction of the roughness while for the scanning speeds 500–800 mm/s the roughness is minimized for a repetition rate of about 30–40 kHz. For the medium average power $\mathbf{P} = 12$ W

the minimum roughness is **Ra** = 1.7 μm for **F** = 30 kHz, **V** = 700 mm/s. For the high average power **P** = 16 W the roughness decreases with increasing scanning speed and decreasing repetition rate with the exception of the speeds 200, 300 mm/s which for repetition rates greater than 50 kHz form lower roughness than the next ones. For the high average power **P** = 16 W the minimum value of roughness results for **F** = 20 kHz, **V** = 800 mm/s and is equal to 1.8 μm. As in the previous materials, so in the yellow brass, with the increase of the average power **P** a small increase in the surface roughness **Ra** is caused.

The roughness of the pockets engraved on the pressure vessel steel P355GH plate could not be measured accurately and therefore are not shown. When scanning the bottom of the pocket with the optical profilometer, the data points obtained were not enough to calculate the roughness. The inability to obtain several data points from the optical profilometer is probably due to the intense black color that the surface got after the laser processing. Because the surface got this intense black color, its reflectivity in the light emitted by the optical profilometer was greatly reduced and went beyond the permissible limits set by the manufacturer for a correct measurement.

In order to determine whether the removed material layer thickness **Dz** affects the surface roughness **Ra** at laser engraving process, the diagrams of Fig. 23 for stainless steel and aluminum were created. Each plotted point in the diagram corresponds to a pocket engraved for a specific average power, repetition rate and scanning speed for which the measured values of removed material layer thickness **Dz** and surface roughness **Ra** are presented. From both the stainless steel and the aluminum diagrams it is clear that all cases of engraving with high values of removed material layer thickness **Dz** lead to high values of roughness **Ra**. In order to achieve low roughness
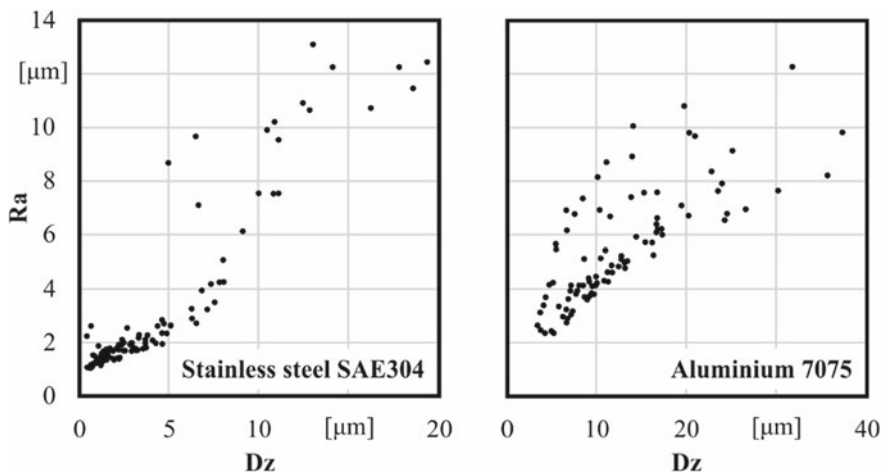
Fig. 23 Correlation between measured removed material layer thickness **Dz** and roughness **Ra** for the various cases of square pockets laser engraving process in stainless steel SAE304 and aluminium 7075

Ra which means good surface quality it is necessary to use process parameters for the laser engraving process that lead to small removed material layer thickness **Dz**.
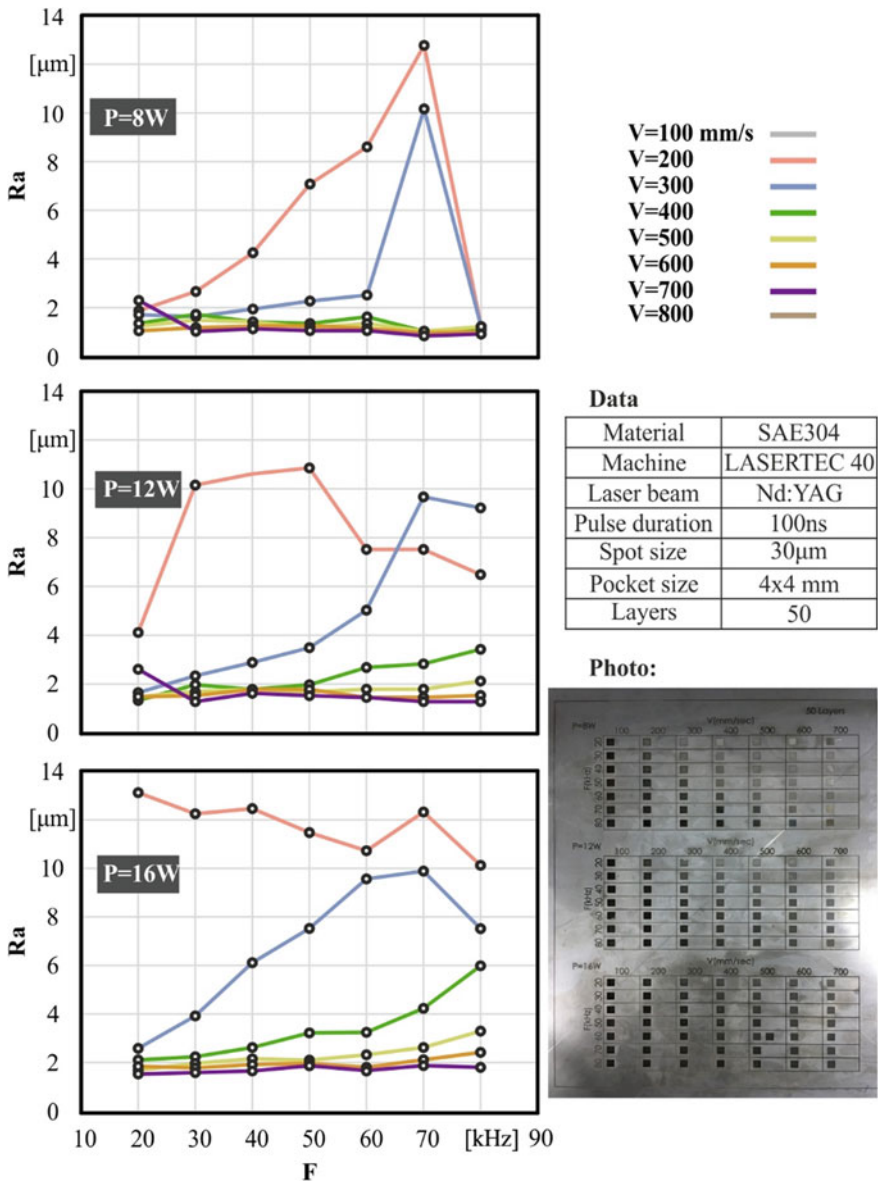
Fig. 24 Roughness **Ra** for stainless steel SAE304
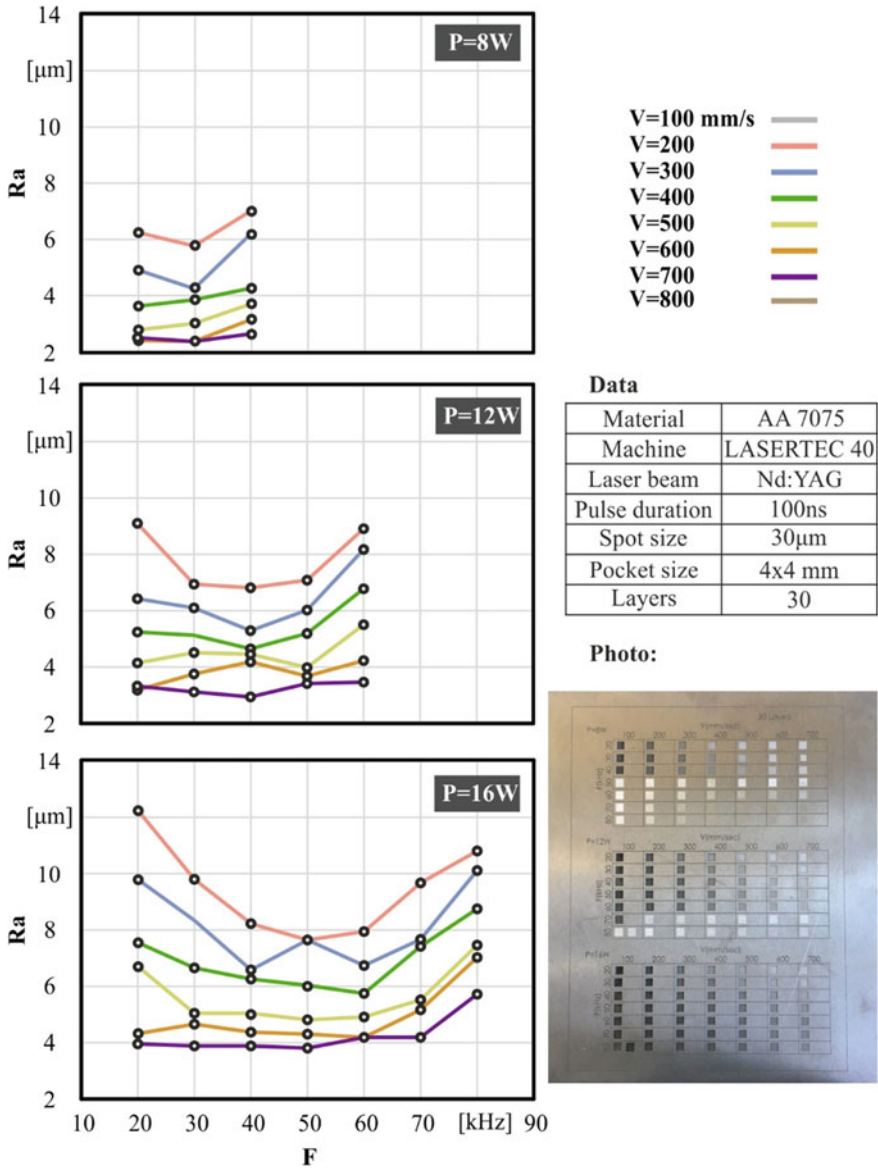
Fig. 25 Roughness **Ra** for aluminium 7075
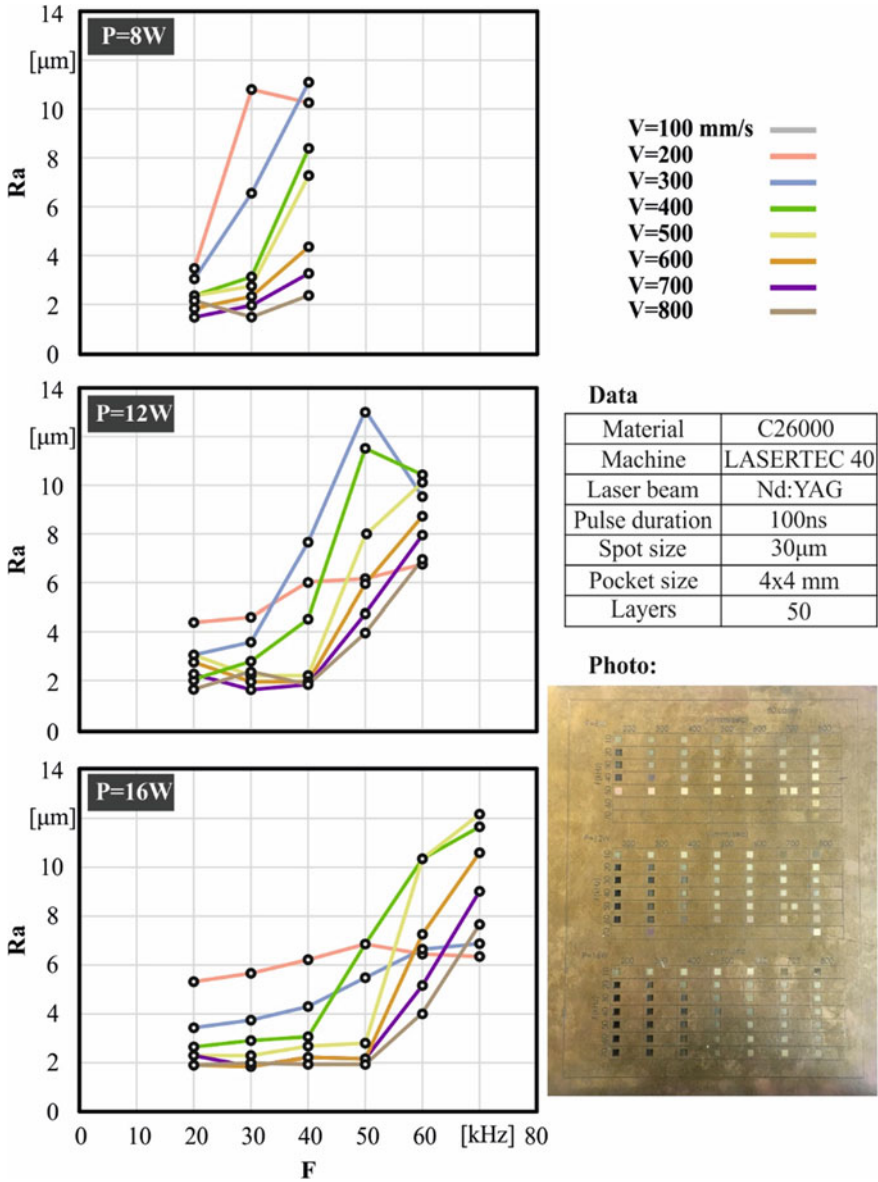
Fig. 26 Roughness **Ra** for yellow brass C26000

7   Kerf Formation

7.1   *Experimental Procedure*

This chapter describes the experimental procedure followed to study the kerf formation during laser engraving process. To study the kerf formation during laser engraving process, square pockets were engraved on a 5 mm thick stainless steel SAE304 plate using the LASERTEC 40 laser machining center. The parameters whose effect was examined are divided into two categories: the parameters related to the way the laser engraving process is performed and the parameters related to the geometry to be engraved. The parameters related to the laser engraving process are the following: average Power **P**, scanning Speed **V**, repetition Rate **F**. The parameters related to the geometry to be engraved are the pocket depth **z** and the pocket side **a.** The levels examined for each parameter are presented in Table 5.

The values of the process parameters examined are those used in most stainless steel laser engraving applications and are at the same time in accordance with the instructions of the machine manufacturer. The ContourGT-K 3D optical profilometer is equipped with a lens that has X5 zoom which allows scanning a surface with dimensions of 1.26×0.9 mm. Therefore, the values for the pocket side **a** were chosen so that the whole pocket is within the available measuring range.

In order to engrave the square pockets, the procedure presented earlier was followed. More specifically, the 3D models of square pockets were designed using a CAD design software. The 3D geometry of each designed square pocket was exported in an STL file. This STL file was given as input to the CAM software called LPSWin that is provided by the machine manufacturer. In this software for each pocket to be engraved the following data was given as input: the scanning strategy type and the thickness of the material to be removed at each layer in order to be calculated the total number of layers to be made. The pockets were engraved using unidirectional cross hatching the scanning strategy, as in the experiments presented in the previous chapters. As far as the thickness of the material to be removed per layer is concerned, the value of which is necessary for the software to calculate the total number of passes to be made by the machine, the values from the removed material layer thickness **Dz** measurements for stainless steel presented in the previous chapter were used. From LPSWin an L4D format file was extracted which contains the toolpath or laser map required to engrave the pocket. The L4D file was given as input to LaserSoft 3D

Table 5 Examined parameters levels

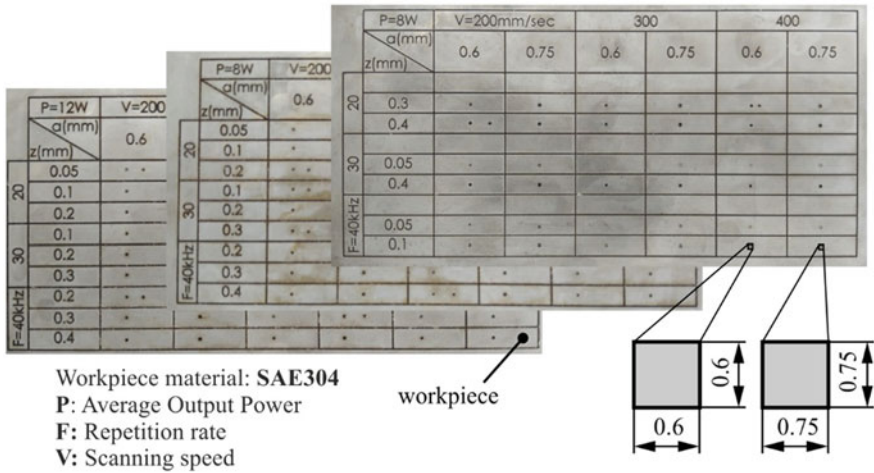| Process parameters	Units	Levels
Average power *P*	W	8, 12
Scanning speed *V*	mm/s	200, 300, 400
Repetition rate *F*	kHz	20, 30, 40
Pocket depth z	mm	0.05, 0.1, 0.2, 0.3, 0.4
Pocket side a	mm	0.6, 0.75

Fig. 27 Laser engraved square pockets for the analysis of kerf formation

software that controls the machine. The values of the process parameters (average power, scanning speed, repetition rate) were also given in this software and the zero point of the workpiece was defined according to the procedure described extensively previously. Following the above procedure for each pocket separately, the stainless steel plate with the engraved square pockets on it shown in Fig. 27 was obtained.

Once the pockets were engraved, it was observed that there were deposits of burnt materials inside them. The LASERTEC40 machine is equipped with a vacuum cleaner that sucks the particles from the material that has re-solidified. However, due to the extremely small dimensions of the pockets, the vacuum cleaner was not able to adequately clean the pockets to their full depth. Therefore, after the laser processing, the engraved pockets were cleaned. The stainless steel plate was immersed for a short time in hydrochloric acid with percentage purity of 15% (w/w), then rinsed with water and finally each engraved pocket was cleaned with high pressure compressed air. Then, the square pockets were measured using the optical profilometer ContourGT-K. The 3D geometry of each pocket was scanned through the optical profilometer to gain the three-dimension surface profile. Cross-sections were made considering cutting planes perpendicular to the surface of the stainless steel plate with a direction defined by the X-X and Υ-Υ axis for each scanned 3D geometry. The corresponding diagrams with the cross-section points of the pocket's surface resulting from the cross-section cut were obtained as shown in Fig. 28.

The data obtained for each cross-section were processed in order to calculate the values top kerf width **TKW**, bottom kerf width **BKW**, pocket depth **z** and kerf taper angle **KT** which are the parameters related to the basic dimensions of the geometry of the engraved pocket. The parameters top kerf width **TKW** and bottom kerf width **BKW** are defining the opening of the pocket on its upper side and its bottom respectively, the pocket depth **z** defines the depth of the pocket and the kerf
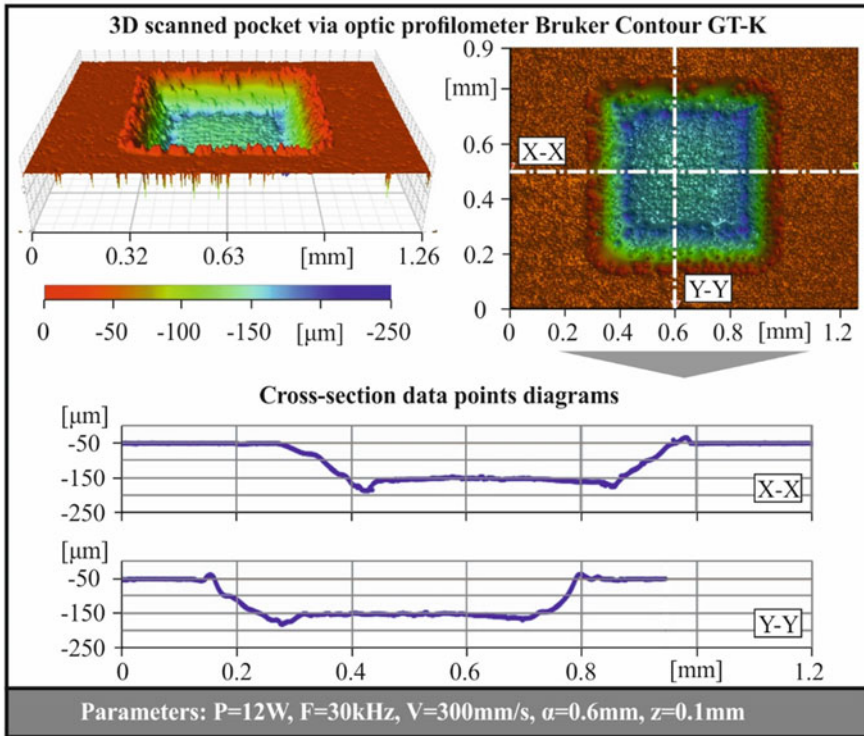
Fig. 28. 3D scanned square pocket and cross-sections

taper angle **KT** defines the slope of the sidewalls of the pocket. The analysis of the cross-section data performed is shown schematically in Fig. 29. At first the horizontal regression line **ε1** (horizontal line of best fit) was calculated taking into account the left and right ends of the diagram that corresponds to the points on the upper surface of the workpiece. After, the horizontal regression line **ε2** was calculated taking into account the points located in a certain range around the middle of the diagram which corresponds to the points of the bottom of the pocket. Then, the points of the sloped side walls located between the lines **ε1** and **ε2** were identified and the regression lines **ε3** and **ε4** were calculated by them. From the intersection points of the lines **ε1**, **ε2**, **ε3** and **ε4** the simplified geometry of the engraved pocket emerges from which the values top kerf width **TKW**, bottom kerf width **BKW** and pocket depth **z** are calculated. The value of kerf taper angle **KT** is calculated by the following equation:

$$KT = \tan^{-1}\left(\frac{TKW\text{-}BKW}{2z}\right) \tag{6}$$

For each engraved pocket, three cross-sections were taken in the direction of the X-X axis and 3 cross-sections in the direction of the Y-Y axis. According to the

Fig. 29 Determination of top kerf width **TKW**, bottom kerf width **BKW**, pocket depth **z** and kerf taper angle **KT** from the cross-section data

① Measurement data points of the engraved square pocket as received from the optical profilometer

② Determination of regression lines: top surface line ε_1, bottom line ε_2 and left, right slopped walls lines ε_3, ε_4

③ Determination of top kerf width **TKW**, bottom kerf width **BKW**, depth **z** and kerf taper angle **KT**
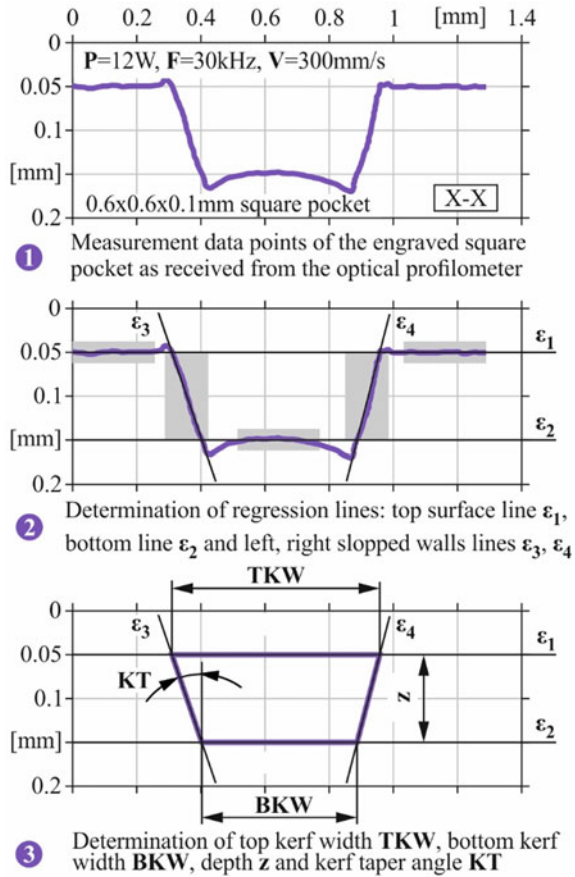
analysis presented above the kerf taper angle **KT** was calculated for each cross-section data set. The average kerf taper angle of the pocket in the direction of the X-X axis was calculated as the average of the three values of kerf taper angle coming from the three cross-sections in the direction of the X-X axis. The average kerf taper angle of the pocket in the direction of the Y-Y axis was calculated in a similar way.

7.2 Kerf Taper Angle Results

Figure 30 shows the values of an introduced average kerf angle $KT_{X-X,Y-Y}$ resulting for the different values of the process parameters for both scanning directions as a function of the side length a, pocket depth z and the average power **P**. Diagrams in Figs. 31, 32, 33, 34, 35, 36, 37 and 38 show the results of the kerf taper angle **KT** for all the engraved pockets as they were measured according to the experimental

Table 6 Summary of average values of the kerf taper angles

KT[deg]	**P = 8 W**					
	a = 0.6 mm			**a = 0.75**		
z	KT_{X-X}	KT_{Y-Y}	$KT_{X-X,Y-Y}$	KT_{X-X}	KT_{Y-Y}	$KT_{X-X,Y-Y}$
0.05 mm	48.7	47.6	48.2	48.4	49.9	49.2
0.1	44.7	44.2	44.5	42.1	45.4	43.7
0.2	29.5	32.2	30.8	31.0	31.6	31.3
0.3	23.5	22.8	23.1	22.3	23.1	22.7
0.4	19.6	18.3	18.9	18.3	18.4	18.4
	P = 12					
	a = 0.6			**a = 0.75**		
z	KT_{X-X}	KT_{Y-Y}	$KT_{X-X,Y-Y}$	KT_{X-X}	KT_{Y-Y}	$KT_{X-X,Y-Y}$
0.05	50	41	45.3	51	39	45.0
0.1	39	42	40.5	42	40	40.9
0.2	32	33	32.1	32	32	31.9
0.3	23	25	23.9	25	24	24.5
0.4	18	20	19.0	18	21	19.5

procedure presented previously. These diagrams were studied as will be presented below in order to investigate the effect of process parameters and the geometry dimensions on the formed kerf taper angle **KT**. Also, these diagrams are a useful tool for the designers of parts manufactured by laser engraving process but also the operators of laser machining centers to predict the dimensional deviations in the produced parts due to the appearance of slope on the sidewalls.

At first it is examined whether the kerf taper angle **KT** formed is affected by the dimensions of the pocket and whether there is a difference in the kerf taper angle formed on the sides in the direction of the X-X axis with those in the direction of the Y-Y axis. For this purpose, Table 6 is presented, which contains a summary of some average values of the kerf taper angles that have emerged, categorizing the data based on the average power **P**, pocket depth **z**, pocket side **a** and the direction of the measurement (X-X or Y-Y).

Examining comparatively the diagrams concerning the kerf taper angle formed in the direction of the X-X axis with those concerning the same angle in the direction of the Y-Y axis it is observed that they do not show any particular difference between them as far as the range of kerf taper angle values is concerned. In order to quantify the differences that appear in the kerf taper angles of the two directions, the parameters KT_{X-X} and KT_{Y-Y} were used. The KT_{X-X} and the KT_{Y-Y} are the average of kerf taper angles formed by all the repetition rate and scanning speed combinations examined in the X-X and Y-Y axis directions respectively. Using KT_{X-X} and KT_{Y-Y}, a comparison can be made between the resulting kerf taper angles in the direction of the X-X and Y-Y axis based on the average power **P**, side length **a** and depth **z** of the pockets. Comparing the values of KT_{X-X} and KT_{Y-Y} it becomes obvious that for each case

examined the average kerf taper angle formed for the sidewalls in the direction of the X-X axis has almost the same value with the average kerf taper angle formed for the sidewalls in the direction of the axis Y-Y since there are differences between them that do not exceed 3° as shown in the Table 6. The fact that the angles in the direction of the X-X and Y-Y axis do not show significant differences between them is mainly due to the unidirectional cross hatching strategy used for experimental tests. A characteristic of the unidirectional cross hatching strategy is that between two successive layers the laser tracks of first layer (let's say they are parallel to the X-X axis) are perpendicular to the direction of the next layer's laser tracks (they are parallel to the Y-Y axis). In this way, when a sufficient number of layers are engraved, then the number of the layers with laser tracks parallel to the X-X axis is equal to the number of the layers with laser tracks parallel to the Y-Y axis, thus leading to similar geometries for all sidewalls of the engraved square pockets.

The pockets that have the minimum depth $\mathbf{z} = 0.05$ mm and are engraved with the maximum examined average power $\mathbf{P} = 12$ W show a differentiation as the average kerf taper angle KT_{X-X} is about 10° greater than the average kerf taper angle KT_{Y-Y}. Due to the high average power the value of the removed material layer thickness is high which in combination with the small value of the depth lead to a very small number of layers during the laser engraving process. For example, when engraving a pocket with a depth of $\mathbf{z} = 0.05$ mm with process parameters $\mathbf{P} = 12$ W, $\mathbf{F} = 40$ kHz and $\mathbf{V} = 200$ mm/s the corresponding removed material layer thickness $\mathbf{Dz}$ is 12.858 µm which means that only $\mathbf{n} = 3$ layers were performed. According to unidirectional cross hatching strategy, when only $\mathbf{n} = 3$ layers are performed, then the number of layers whose laser tracks will be parallel to the X-X axis will be twice the number of layers whose laser tracks will be parallel to the Y-Y axis (two layers for X-X and one layer for Y-Y), thus causing a difference between the resulting kerf taper angles for the two directions.

Another conclusion that results from comparing the diagrams for the pockets with side $\mathbf{a} = 0.6$ with the corresponding ones for the pockets with side $\mathbf{a} = 0.75$ is that the length of the sides of the pockets does not significantly affect the formed kerf tapper angle $\mathbf{KT}$. To verify this conclusion, based on the previous finding that the kerf taper angle in the direction of the X-X axis does not differ significantly from the angle in the direction of the Y-Y axis, parameter $KT_{X-X,Y-Y}$ was used. The $KT_{X-X,Y-Y}$ is the average of the kerf taper angles formed by all the repetition rate and scanning speed combinations tested for both the X-X axis direction and the Y-Y axis direction. Using $KT_{X-X,Y-Y}$, which values are plotted in Fig. 30, some important conclusions can be drawn about the effect of the average power $\mathbf{P}$, side length $\mathbf{a}$ and depth $\mathbf{z}$ of the pockets on the kerf formation. Comparing the values of average kerf angle $KT_{X-X,Y-Y}$ for the pockets with side length $\mathbf{a} = 0.6$ mm with the corresponding ones with side length $\mathbf{a} = 0.75$ mm it is observed that the difference between them is very small and in no case exceeds 1°. It is therefore clear that the side length $\mathbf{a}$ of the pockets does not affect the kerf formation. The reason for this is based on the fact that the mechanisms that contribute to the development of the kerf taper angle and the phenomena that take place have to do only with the border sides of the pocket. The size of the flat area at the bottom of the pocket does not affect what will happen
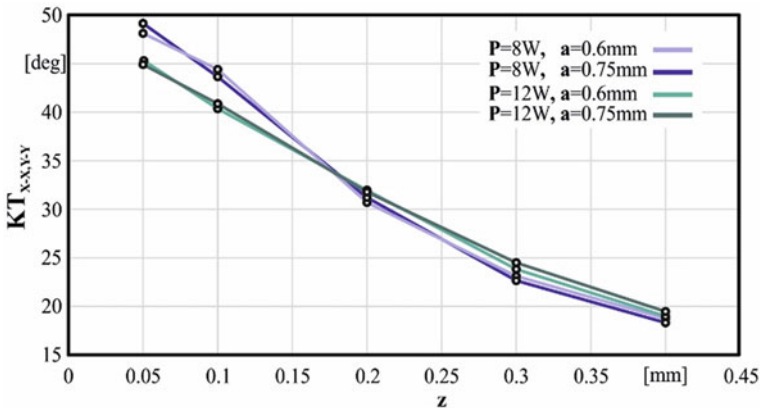
Fig. 30 Average kerf angle $KT_{X-X,Y-Y}$ as a function of the side length **a**, pocket depth **z** and the average power **P**

to the sidewalls. However, it should be noted that the side length **a** of the pocket does not affect the kerf formation when the pocket is large enough to form a flat area at the bottom. Otherwise, if the pocket's side length is very small due to the slope on the side walls there is a chance that they will converge with each other and give a V-shape to the engraved pocket.

In contrast to the side length of the pocket, the effect of the pocket depth **z** on the formed kerf taper angle **KT** is strong as observed in all the diagrams. The effect of pocket depth **z** on the kerf taper angle becomes more apparent in Fig. 30 using the average kerf taper angle $KT_{X-X,Y-Y}$ as an indicator. As we can see in the diagram in Fig. 30 the maximum average kerf taper angle $KT_{X-X,Y-Y}$ is formed for the minimum depth of **z** = 0.05 mm and is around 49° for average power **P** = 8 W and 45° for average power **P** = 12 W. For small values of the pocket depth up to **z** = 0.2 mm there is a high slope in the curves which corresponds to a decrease of about 10° of the kerf taper angle **KT**| per 0.1 mm increase of the depth **z**. As the depth increases the slope of the curves decreases. Thus, for depths from 0.3 to 0.4 mm there is a smaller decrease on kerf taper angle of about 5° per 0.1 mm increase in depth. If it was tried to achieve much greater engraving depths, it would be possible that the kerf taper angle would converge to a specific value which depends on many factors, with the predominance being the convergence cone half-angle and the quality of the laser beam.

So far it has been analyzed how the kerf taper angle is affected by the geometry characteristics of the engraved pocket. Equally important is the study of the effect of process parameters on the kerf formation. Regarding the effect of the average power **P** according to the diagram of Fig. 30, two cases can be distinguished. For small values of the pocket depth **z** from 0.05 to 0.1 mm it is observed that the high average power **P** = 12 W leads to a smaller kerf taper angle **KT** and the reduction in relation to the low average power **P** = 8 W ranges around 4°. Gradually, however, the reduction decreases until just before the depth of **z** = 0.2 mm, where both high
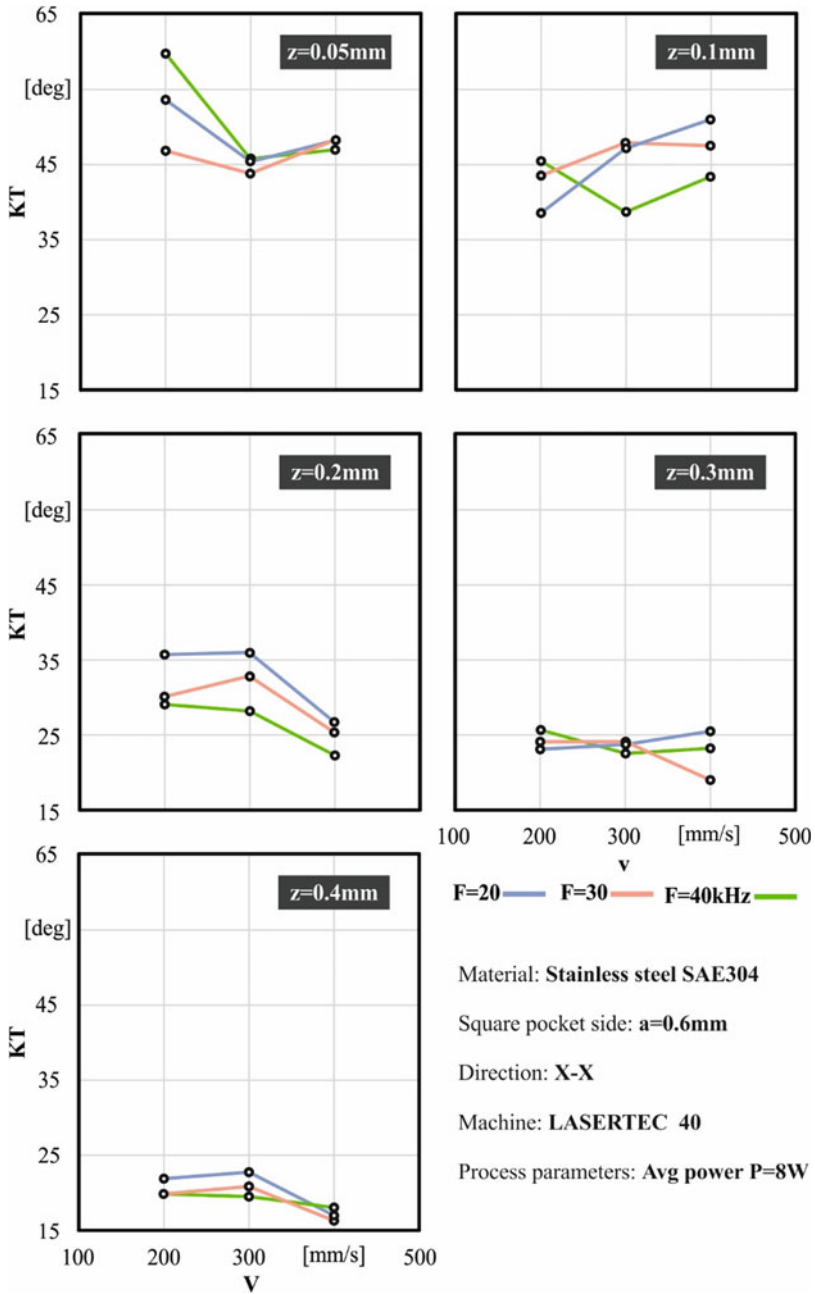
Fig. 31 **KT** angle in the X-X axis for a 0.6 mm pocket engraved with P = 8 W
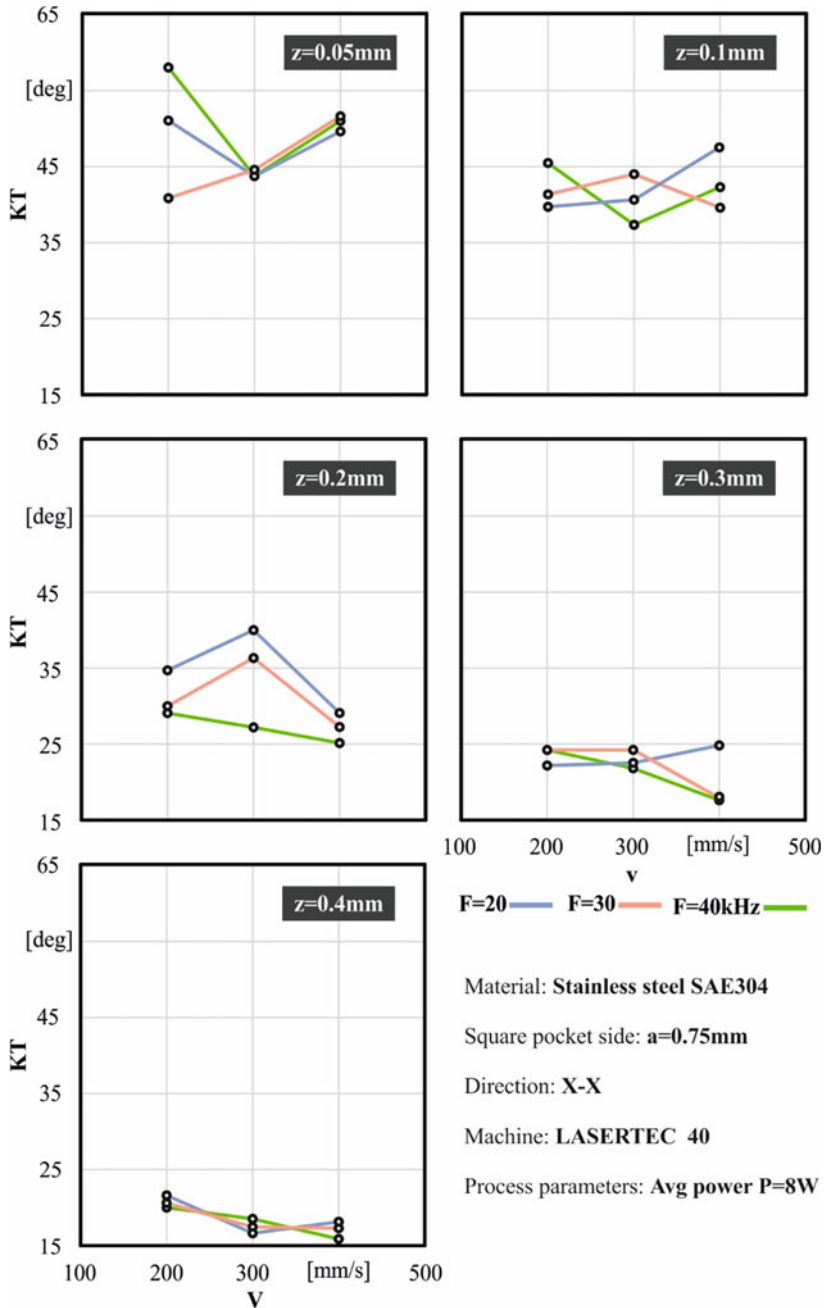
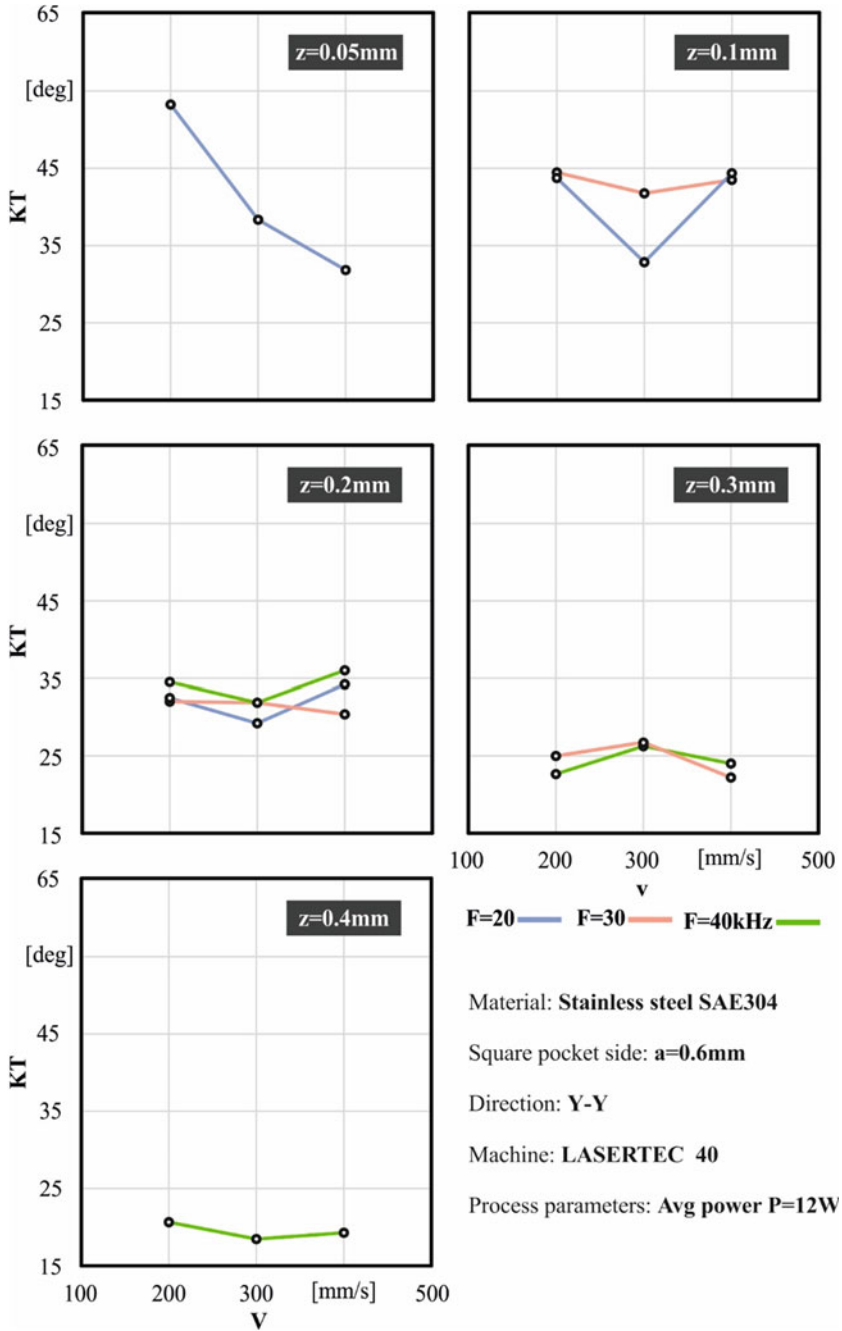**Fig. 32** **KT** angle in the X-X axis for a 0.75 mm pocket engraved with P = 8 W
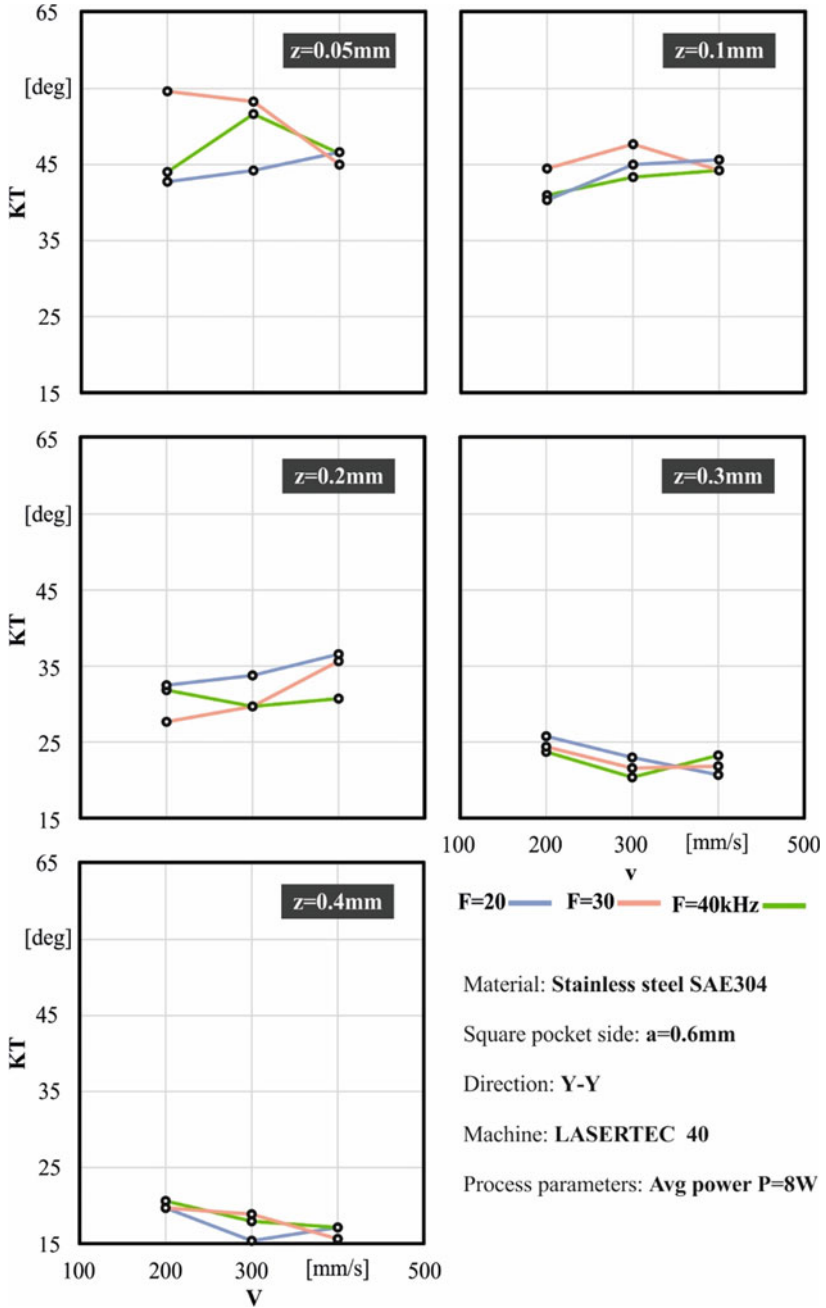
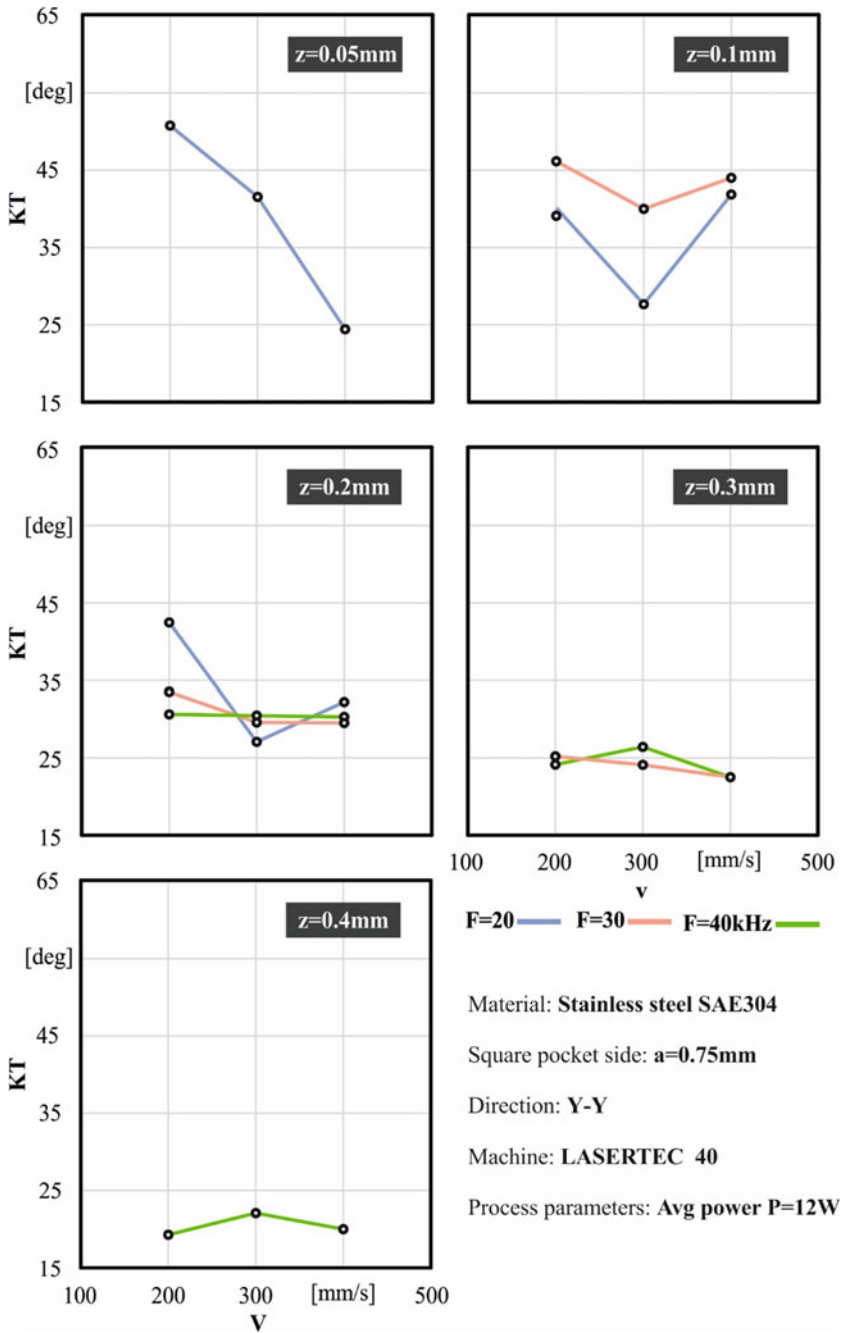**Fig. 33 KT** angle in the Y-Y axis for a 0.6 mm pocket engraved with P = 8 W
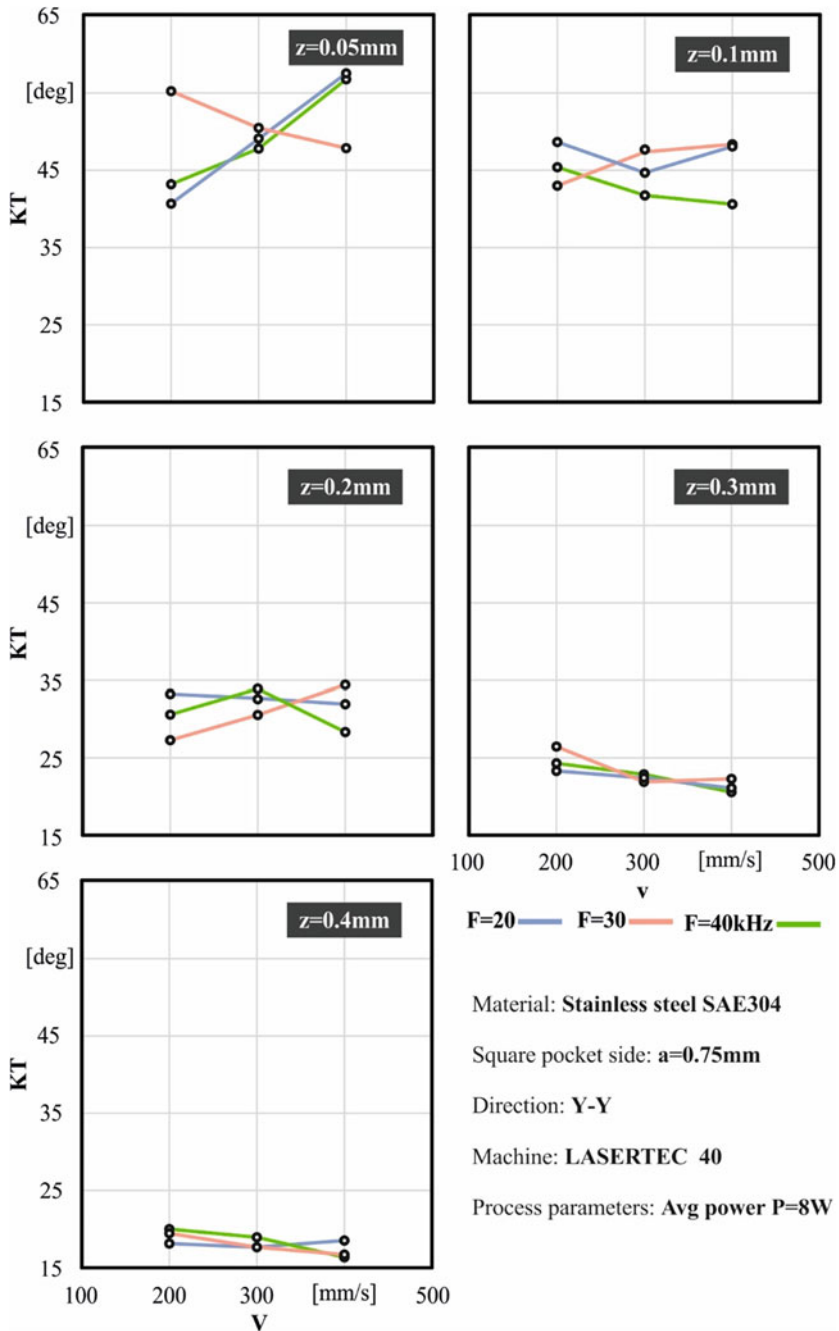
Fig. 34 **KT** angle in the Y-Y for a 0.75 mm pocket engraved with P = 8 W
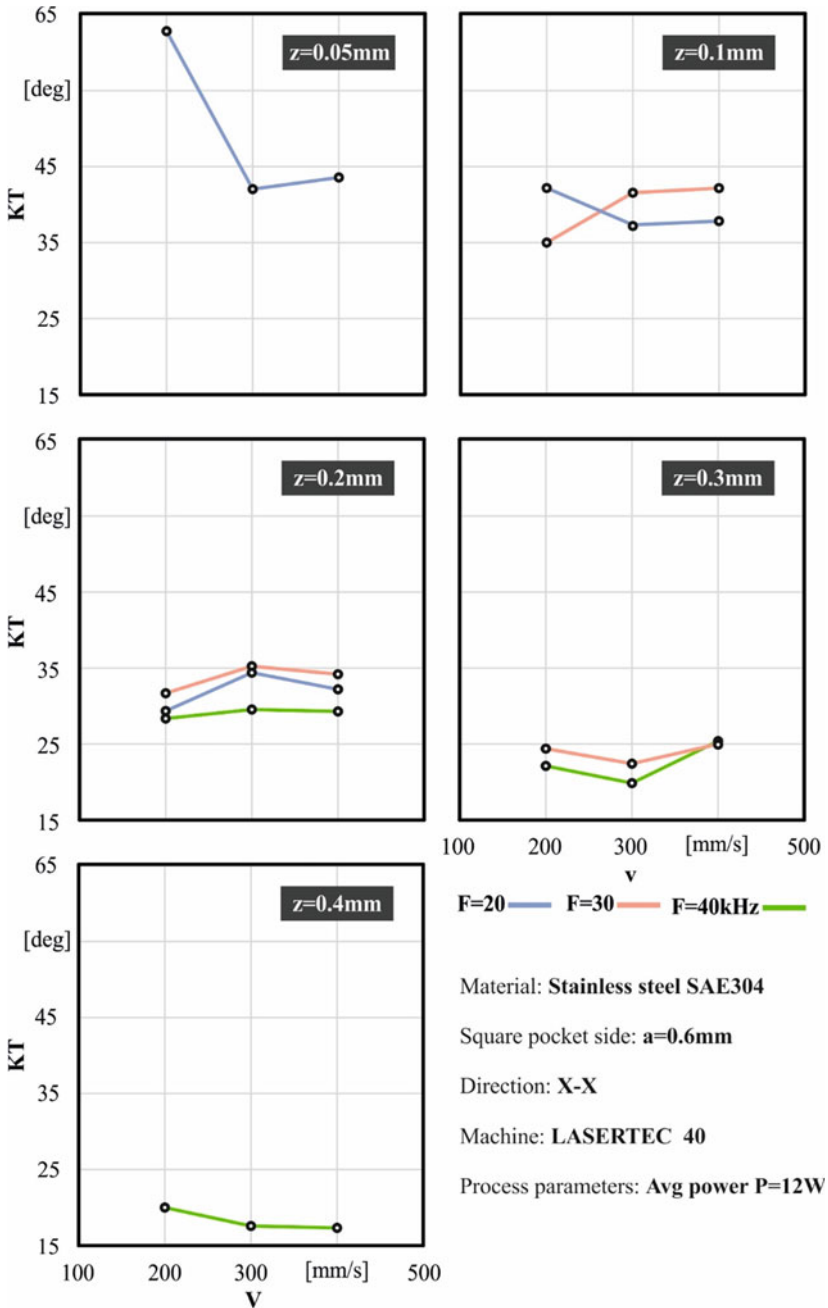
Fig. 35 KT angle in the X-X axis for a 0.6 mm pocket engraved with P = 12 W
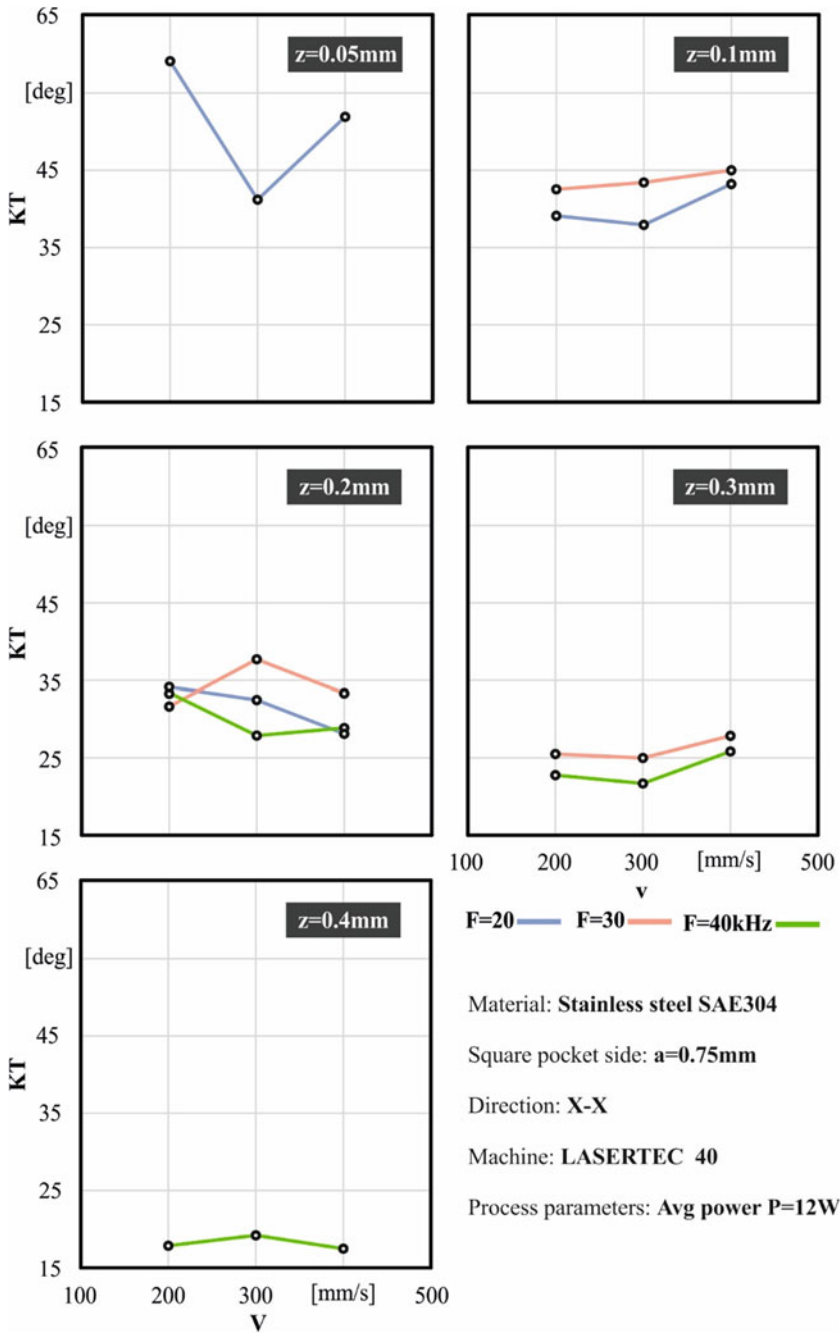
Fig. 36 **KT** angle in the X-X axis for a 0.75 mm pocket engraved with P = 12 W

Fig. 37 **KT** angle in the Y-Y axis for a 0.6 mm pocket engraved with P = 12 W

Fig. 38 **KT** angle in the Y-Y axis for a 0.75 mm pocket engraved with P = 12 W

and low average power **P** lead to approximately the same result. Unlike before, for engraving depths **z** greater than 0.2 mm the low average power **P** = 8 W leads to a slightly smaller kerf taper angle **KT** than the high average power **P** = 12 W with the reduction being around 1–2° which although it is a small reduction it cannot be considered negligible.

Next, the effect of the process parameters repetition rate **F** and scanning speed **V** on the kerf taper angle **KT** is studied. The differences that occur in the effect of repetition rate **F** and scanning speed **V** in kerf taper angle depending on the direction of the measured angle X-X or Y-Y, the pocket depth **z** and the average power **P** seem to be more intense, do not show any uniformity and will be examined separately. Regarding the minimum depth examined **z** = 0.05 mm as previously mentioned angle **KT** in the direction of the X-X and Y-Y axis shows deviations. Thus, the effect of repetition rate **F** and scanning speed **V** on the formation of the **KT** angle in each of the two directions appears different. For the direction of the X-X axis at low average power **P** = 8 W for both the pocket with side length **a** = 0.6 mm and the one with **a** = 0.75 mm the minimum **KT** angle is formed for repetition rate **F** = 30 kHz and low scanning speeds: **V** = 300 mm/s for the pocket with side length **a** = 0.6 mm and **V** = 200 mm/s for the one with **a** = 0.75 mm. For the direction of the X-X axis at high average power **P** = 12 W for both pockets the minimum **KT** angle is formed for the scanning speed **V** = 300 mm/s. For the direction of the Y-Y axis at low average power P = 8 W for both pockets the minimum angle **KT** is formed for **F** = 20 kHz and **V** = 200 mm/s whereas for the high average power **P** = 12 W the maximum scanning speed **V** = 400 mm/s is required. The set of process parameters among all that gives the minimum kerf taper angle **KT** for engraving depth **z** = 0.05 mm is **P** = 12 W, **F** = 20 kHz, **V** = 400 mm/s and is equal to 24.6° in the direction of Y-Y axis of the **a** = 0.75 mm pocket.

As far as the pocket depth **z** = 0.1 mm is concerned for the case of low average power **P** = 8 W in all cases the minimum kerf taper angle **KT** appeared for repetition rate **F** = 40 kHz and the scanning speed **V** = 300 mm/s for the direction of the X-X axis while for the direction of the Y-Y axis the optimal speed does not show the same behavior for both pockets dimensions. For the case of high average power **P** = 12 W in all cases the minimum angle **KT** appeared for repetition rate **F** = 20 kHz and the scanning speed **V** = 300 mm/s except for the case of the pocket with side length **a** = 0.6 mm where in the direction X-X the minimum angle appeared for **F** = 30 kHz, **V** = 200 mm/s. For the case of the engraving depth **z** = 0.1 mm the minimum kerf taper angle is **KT** = 27.0° in the direction of the Y-Y axis of the **a** = 0.75 mm pocket for process parameters **P** = 12 W, **F** = 20 kHz, **V** = 300 mm/s.

As for the depth **z** = 0.2 mm for the low average power **P** = 8 W the minimum kerf taper angle **KT** appears for both pockets a = 0.6 mm and a = 0.75 mm in the direction of the X-X axis for **F** = 40 kHz, **V** = 400 mm/s while in the direction of the Y-ϒ axis for **F** = 30 kHz, **V** = 200 mm/s. For the high average power **P** = 12 W in the direction of the X-X axis the minimum **KT** angle is formed for the repetition rate **F** = 40 kHz and the scanning speed **V** = 200 mm/s for the pocket with side length **a** = 0.6 mm and the speed **V** = 300 mm/s for the pocket with side length **a** = 0.75 mm. For depth **z** = 0.2 mm the minimum angle **KT** of all was found to be

equal to 22° for the $\mathbf{a} = 0.6$ mm pocket in the direction of the X-X axis for process parameters $\mathbf{P} = 8$ W, $\mathbf{F} = 40$ kHz, $\mathbf{V} = 400$ mm/s.

For the depth $\mathbf{z} = 0.3$ mm at low average power $\mathbf{P} = 8$ W the scanning speed $\mathbf{V} = 400$ mm/s provides the minimum angle $\mathbf{KT}$ for all cases while for the effect of the repetition rate $\mathbf{F}$ no clear conclusions can be drawn. For the high average power $\mathbf{P} = 12$ W the minimum angle $\mathbf{KT}$ is formed for $\mathbf{F} = 40$ kHz, $\mathbf{V} = 300$ mm/s in the direction of the X-X axis and for $\mathbf{F} = 30$ kHz, $\mathbf{V} = 400$ mm/s in the direction of Y-Y axis. For depth $\mathbf{z} = 0.3$ mm the minimum angle $\mathbf{KT}$ of all was found to be equal to 17.9° for the $\mathbf{a} = 0.75$ mm pocket in the direction of the X-X axis for process parameters $\mathbf{P} = 8$ W, $\mathbf{F} = 40$ kHz, $\mathbf{V} = 400$ mm/s.

Regarding the maximum depth $\mathbf{z} = 0.4$ mm it is observed that the changes that appear in the kerf taper angle $\mathbf{KT}$ for the various values of repetition rate $\mathbf{F}$ and scanning speed $\mathbf{V}$ are too small, they do not show uniformity and so it is not easy to draw a safe conclusion about their effect. For low average power $\mathbf{P} = 8$ W there seems to be a slight tendency to decrease the $\mathbf{KT}$ angle with increasing scanning speed $\mathbf{V}$ which however does not appear in all cases. For the engraving depth $\mathbf{z} = 0.4$ mm the minimum kerf taper angle is $\mathbf{KT} = 15.5°$ in the direction of the Y-Y axis of the $\mathbf{a} = 0.6$ mm pocket for process parameters $\mathbf{P} = 8$ W, $\mathbf{F} = 20$ kHz, $\mathbf{V} = 300$ mm/s.

8 Conclusions

In the present work an experimental investigation of laser engraving process was presented. The aim was to investigate the effect of process parameters and the dimensions of the geometry to be engraved on the final result. A large number of engraving experiments were performed using a LASERTEC 40 laser machining center on stainless steel SAE304, aluminium 7075, pressure vessel steel P355GH and yellow brass C26000 plates which were measured using a ContourGT-K 3D optical profilometer. The productivity of the laser engraving process was initially studied by examining the removed material layer thickness and the material removal rate. Then the engraving quality was studied by examining surface roughness as well as the dimensional accuracy by examining the kerf taper angle. The study of the experimental results revealed important conclusions that show that by selecting suitable process parameters, engravings can be achieved with high productivity, good surface quality and acceptable dimensional accuracy. In future work, the experimental results could be statistically processed to create a statistical prediction model. Using the prediction model, the CNC laser machining center operator will be able to find the optimal set of process parameters depending on the application, the material used and the engraving quality requirements.

References

1. Johander P, Goenaga I, Gomez D, Moldovan C, Nedelcu O, Petkov P, Kaufmann U, Ritzhaupt-Kleissl H-J, Dorey R, Persson K (2006) Design and manufacturing of micro heaters for gas sensors, 4 M 2006 - Second International Conference on Multi-Material Micro Manufacture

2. Quintana I, Etxarri J, Sanz C, Aranzabe A, (2008) Laser micro–milling and drilling using microsecond pulses. applications for mould and aeronautical industry. In: Proceedings of the 3rd international conference on material, mechanical and manufacturing engineering

3. Schnell G, Duenow U, Seitz H, (2020) Effect of laser pulse overlap and scanning line overlap on femtosecond laser-structured Ti6Al4V surfaces, materials (basel)

4. Jofre M, Anzolin G, Steinlechner F, Oliverio N, Torres JP, Pruneri V, Mitchell MW (2012) Fast beam steering with full polarization control using a galvanometric optical scanner and polarization controller. Express, Opt

5. Dongyun W, Xinpiao Y (2014) An embedded laser marking controller based on ARM and FPGA processors. Sci World J

6. Pantawane M, Joshi S, Dahotre N (2018) Laser beam machining of aluminum and aluminum alloys. Aluminum Science and Technology, ASM International, pp 519–541

7. Dubey AK, Yadava V (2008) Laser beam machining-a review. Int J Mach Tools Manuf

8. Ghany KA, Rafea HA, Newishy M (2006) Using a Nd:YAG laser and six axes robot to Cut Zinc-Coated steel. Int J Adv Manuf, Technol

9. Meijer J, Du K, Gillner A, Hoffmann D, Kovalenko VS, Masuzawa T, Ostendorf A, Poprawe R, Schulz W (2002) Laser machining by short and ultrashort pulses, state of the art and new opportunities in the age of the photons. CIRP Ann.-Manuf, Technol

10. Li L (2000) Advances and characteristics of high-power diode laser materials processing. Opt Lasers Eng

11. Bäuerle D (2011) Laser processing and chemistry

12. Duanming-Zhang Liu D, Zhihua-Li Sipu-Hou, Boming-Yu Guan L, Xinyu-Tan Li L (2006) Effects of plasma shielding on pulsed laser ablation. Phys Lett B, Mod

13. Nee AYC (2015) Handbook of manufacturing engineering and technology

14. Campanelli SL, Ludovico AD, Bonserio C, Cavalluzzi P, Cinquepalmi M (2007) Experimental analysis of the laser milling process parameters. J Mater Process Technol

15. Orazi L, Cuccolini G, Fortunato A, Tani G (2010) An automated procedure for material removal rate prediction in laser surface micromanufacturing. Int J Adv Manuf Technol

16. Teixidor D, Ferrer I, Ciurana J, Özel T (2013) Optimization of process parameters for pulsed laser milling of micro-channels on AISI H13 tool steel. Robot Comput Integr Manuf

17. Campanelli SL, Casalino G, Contuzzi N (2013) Multi-objective optimization of laser milling of 5754 aluminum alloy. Opt Laser Technol 52:48–56

18. Pritam A (2016) Experimental investigation of laser deep engraving process for AISI 1045 Stainless Steel by Fibre Laser, 03(8), pp 1730–1734

19. Šugár P, Šugárová J, Frnčík M, Ludrovcová B (2018) Nanosecond YB fibre laser milling of alluminium bronze: effect of process parameters on the surface finish. Adv Sci Technol Res J

20. Ahmed N, Ahmad S, Anwar S, Hussain A, Rafaqat M, Zaindin M (2019) Machinability of titanium alloy through laser machining: material removal and surface roughness analysis. Int J Adv Manuf, Technol

21. Mohammed MK, Umer U, Rehman AU, Al-Ahmari AM, El-Tamimi AM (2018) Microchannels fabrication in alumina ceramic using direct Nd: YAG Laser Writing, Micromachines

22. Mohammed MK, Al-Ahmari A (2020) Laser-machining of microchannels in NiTi-based shape-memory alloys: experimental analysis and process optimization, materials (Basel)

23. Xie J, Kar A (1999) Laser welding of thin sheet steel with surface oxidation. Weld J (Miami, Fla)

The Effects of 3D Printing Structural Modelling on Compression Properties for Material Jetting and FDM Process

Marek Płaczek, M. K. A. Ariffin, B. T. H. T. Baharudin, and Mohammadreza Lalegani Dezaki

3D printing is a well-known technique in producing parts in safe and efficient way. One of the famous techniques in producing high quality product is by using MultiJet printing (MJP) technique and the fastest process is Fused deposition modelling (FDM) technique. Usually, products are produced using these techniques were associated with the complex shape that tends to have defects on the product quality. It is well known that direction of printing is one of the parameters that affects surface quality. In this research, the authors determined the effects of structure's design and applied technology of printing with relation to strength of the designed structure. Different design variants were designed with Computer aided design (CAD) system and fabricated using the MJP and FDM machine. Simulation and experimental analysis were conducted to analyze the strength of complex structures. Results showed there was a slight difference between simulation and experimental process with the percentage of error within 10% for FDM technology and very significant error in the case of MJP technology. Moreover, structures made in the FDM technology are characterized by higher strength and stiffness compared to elements made in the MJP technology. However, with MJP technology it is possible to obtain better

M. Płaczek (✉)
Department of Engineering Processes Automation and Integrated Manufacturing Systems, Silesian University of Technology, 44-100 Gliwice, Poland
e-mail: marek.placzek@polsl.pl

M. K. A. Ariffin · B. T. H. T. Baharudin · M. Lalegani Dezaki
Department of Mechanical and Manufacturing Engineering, Universiti Putra Malaysia, Serdang, 43400 Putrajaya, Selangor, Malaysia
e-mail: khairol@upm.edu.my

B. T. H. T. Baharudin
e-mail: hangtuah@upm.edu.my

M. Lalegani Dezaki
e-mail: Lalegani.mr@gmail.com

171

surface quality and higher print accuracy. In brief, this research has shown that proper design and optimum printing technology and parameters ensure the required structure stiffness for the printed products.

1 Introduction

Additive manufacturing (AM) or 3D printing (3DP) is one of the pillars for industrial revolution 4.0 (IR4.0) which is highly important for industries. Most of the applications use this technology for producing complex shape due to flexibility and freeform capabilities of design [1]. Vast number of products utilizing the 3D printer can be found in automotive, aerospace, medical, construction, and others [2]. There is no doubt that the 3D printing has become one of the most important technology in industries. AM can be categorized according to its processes based on solid, liquid, and powder [3]. Classification of 3D printing can be named according to Material extrusion [4], Binder jetting (BJ) [5], Material jetting (MJ) [6], Powder bed fusion (PBF) [7], Sheet lamination [8], and Direct energy deposition (DED) [9]. These processes use a wide range of material from metal, polymer, composite, hybrid material, and biomaterial [10]. Therefore, due to various materials involve, the quality of the printed products depends on special treatment on the process and requirement needs.

As mentioned in [11], the 3DP is based on layer-by-layer manufacturing technique. The material is adding up step by step until the product is finished. With this technology, industries are able to produce complex products without sacrificing material properties with less cost and build products which are impossible to be machined with traditional processes. With such techniques, the quality of the produced layer in each process determines the product's quality. Generally, the intended product is designed by Computer aided design (CAD) software. Further, the design is translated to the proper format which is known as Standard Tessellation Language (STL) by exclusive softwares. These softwares generate G-codes that are readable by 3D printers. The machine follows these codes to print the products layer by layer from bottom to top [12]. CuraEngine® and Slic3er® are amongst the famous softwares used by the 3D printing machines for slicing operation [13]. In addition, process parameters need to be properly controlled in order to ensure the product quality is achieved according intended design. There are lots of factors that contribute to the quality of the part produce using these technologies. Finding the optimum quality of the product which is produced by the 3D printer depends on infill pattern, infill density, layer thickness, build orientation, material type, laser power, printing speed, and temperature [14].

One of the process that promises good printing quality is MultiJet printing (MJP) or Material jetting (MJ) process [15]. MJP is known as one of the precise 3D printing technique in the world. The capability of using this technique is the user can produce product with finest detail and quality. Normally, the capability of printing is within the range of 0.1–0.2 mm in size. MJP is a process that required the ultraviolet (UV)

laser to react on the photopolymer resin. This technology builds products in drop-by-drop deposition. Sometimes due to its characteristics, this process is also known as Drop-on-demand (DOD) process. The liquid resin is heated to achieve optimal viscosity. Then, Inkjet head drops the liquid and these droplets are cured by UV laser. The resolution of head to print resins is 10–30 μm layer thick. This process is similar to the traditional 2D document printing. Most application of the produced part by using this technology is for medical usage. MJP also is required the support structure material which is used to prevent deflection due to gravity and pressure resistance or can be used as the support to maintain the original structure. All those situations are required support structure to enhance mechanical properties and surface quality [16]. Subsequently, the support platform is removed manually or using other techniques such as heat treatment which is called post-processing [17]. The support material can be from the same material or different materials. Support material can affect the surface finish or structure integrity of the product. Hence, selection of the support material is crucial in this process. Usually, companies use different materials in MJ process to save the production cost.

One of the main limitations in this process in the cost of material which is more expensive compared to the Fused deposition modeling (FDM) or Stereolithography (SLA) process. A barrage range of materials can be used in this process but the main material is thermosets and thermoplastics due to the good properties [18]. Due to the process features, multiple materials can be delivered by inkjet head simultaneously and full-color printing is achievable by combination of different materials. For example, Salcedo et al. [19] analyzed physical tensile test on Digital material (DM) and Functionally graded material (FGM)by using experimental and simulation process. Two based material (ABS-like and rubber-like) and elastic materials (Tango Black + , DM95, DM60, and Vero White +) were used due to the MJ process capabilities. Results showed the simulation predicted the maximum strain in the matrix material within 5% error and the surface quality in DM 60 was smooth compared to the DM 95. Because of high resolution and multi-material printing, this process is suitable for microfluidic applications [20, 21]. Various parameters have effect on surface quality and mechanical properties in this process such as build orientation, infill density, laser speed, layer thickness, and material properties [22]. To achieve the best quality and mechanical properties, finding optimal parameters is crucial. As an example, build orientation may cause distortion and warpage in this process [23]. Another issue in MJP process is limitation in controlling the droplets and inconsistent anisotropic trends due to the staircase defects in printed products [24, 25].

There have been researches on MJ or MJP process to determine the effects of process on mechanical properties and surface quality to eliminate issues and limitation [26]. Surface quality is an important aspect in AM processes (in this case MJP process). Smooth surface quality without defects can be conducted by assigning proper process parameters [27]. Besides, better mechanical properties can be achieved when the surface texture is in the best condition. Udroiu et al. [28] examined the effects of build orientation (artifact orientation, platen orientation, and finish type) on surface quality in a case study by analyzing average surface roughness (R_a) in PolyJet process. Results illustrated these elements affected surface quality

and the lowest R_a value was 0.5–4 μm for the glossy finish type. Hafsa et al. [29] investigated build orientation in MJ process and found out parts had better accuracy at 90° orientation with 0.01% average percentage. On the other hand, 0° had the lowest average surface roughness. Another study has been conducted on mechanical properties in different printing directions by Barclift et al. [30].In this study, results showed x–y plane had significant effect on mechanical properties while in printed samples in z-plane did not improve so much. Moreover, Khoshkhoo et al. [31] found XY orientation had the best dimensional accuracy. The height and functional parameters are highly dependent on stair-stepping. Also, results showed 0° had the best surface quality among other orientations. Surface angle was also investigated which showed dimensions, surface quality, printing time were affected due to this feature. Kim et al. [32] proposed a novel technique to make the simulation process faster compared to Finite element analysis (FEA) in 3DP process. This solution was highly effective to increase the performance and speed in MJ fusion process. In addition, He et al. [33] worked on printing temperature and found that by optimizing this parameter and drop spacing, film quality can be enhanced for Polycaprolactone (PCL) ink in MJ process. In this work [34], fatigue characteristic of Tango Black+ material was analyzed. Fatigue life was reduced by a reduction in cross-sectional area and it leads to stress concentrations reduction. On the other hand, fatigue life was increased by 37% using glossy finish. Bass et al. [35] examined the effects of build orientation and part age on tensile stress, elastic modulus, and elongation at break by analyzing Vero White+ and Tango Black+ materials. They found flat parts (x–y direction) were the strongest while z-x direction samples were the weakest. The lowest elasticity and highest elongation at break were conducted for x-axis printed samples. Also, by increasing the part age, the ultimate tensile strength of VW+ increased as well while elongation at break decreased over time and modulus of elasticity remained unchanged. Moreover, Yap et al. [36] found build orientation had an extraordinary effect on height accuracy. Results indicated thin wall could be printed if the wall thickness were more than 0.4 mm. Furthermore, to achieve highest accuracy width and height, 0° along the y-direction was the optimum parameter in this research. Studies have shown by decreasing the part thickness, the surface quality increased but the printing time increased. In brief, by finding optimal condition in MJP process, issues and limitation can be eliminated to reach the best quality and mechanical properties.

In contrast to MJP, FDM is a user-friendly technology that utilizing the material extrusion. FDM is the most suitable process that can be used as a domestic 3D printer due to compatibility of the size. Main materials for FDM are plastic-based materials namely as Polylactic acid (PLA), Acrylonitrile butadiene styrene (ABS), Polypropylene (PP), Polycarbonate (PC), Nylon, and Thermoplastic polyurethane (TPU) [37]. Other materials such as composite can be extruded using this machine with some necessary modification. Materials exists in shape of filament with different colors. The nature of this process is to extrude and deposit the melted material through nozzle. FDM consists of different components, as shown in Fig. 1 [38]. Extruder (nozzle) is the heart of FDM which can affect surface quality and mechanical properties of products. There are several issues highlighted while using this process such as warpage, poor layer binding, shrinkage, and others due to unproper setup
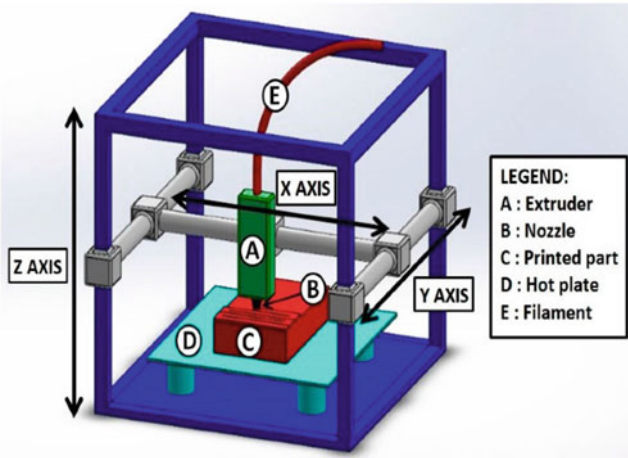
Fig. 1 FDM components [38]

of the process parameters or temperature variation [39, 40]. Most parameters for both MJP and FDM are quite same that optima condition need to be found. In this process, main parameters are layer thickness, infill pattern, percentage of infill, build orientation, nozzle temperature, nozzle diameter, and printing speed [41]. These parameters affect surface quality and mechanical properties. Thus, it is necessary to optimize the pre-process conditions to eliminate mentioned issues. Also, this process used support structure to print products but the support can be removed easily However, post-processing techniques were also needed to enhance surface quality such as machining process or chemical treatment [42–44].

The main goal in this study is to make a comparison between FDM and MJP process to find out their capability and differences. However, researches on FDM parameters and its capabilities are also helpful to find out the nature of this process. Various studies have been conducted on strength and stiffness of FDM products to find out the optimal process parameters mechanical properties [45]. Researchers investigated the nozzle condition and its effects on mechanical properties [46–48]. As an example, Sukindar et al. [49] analyzed the effects of nozzle die angle, nozzle diameter, and liquefier design on 3D printed PLA products by conducting tensile and compressive test. Another parameter which is one of the most critical factors that affects surface quality and mechanical properties is build orientation [50]. Products can be printed from 0° to 180° angle and each angle shows different characteristics. The best surface quality and mechanical properties can be achieved by selecting proper angle. Samykano et al. [51] developed mathematical model and also investigated the process parameters in printing ABS material by FDM. Results showed 80% infill percentage, 0.5 mm layer thickness, and 65° raster angle were the proper parameters in this case. Tensile strength was done and 31.57 MPa ultimate tensile strength,

774.50 MPa elastic modulus, and 19.95 MPa yield strength were achieved, respectively. Wang et al. [52] proposed a novel technique by combining FDM process with thermal treatment. Microsphere content, heating temperature and heating time were investigated by tensile and compressive test. Samples' tensile strength and compressive strength increased 25.4 and 52.2 by adding 2wt% microsphere at 140 °C heating temperature for 120 s compared to the untreated specimens. In this study [53], the effects of infill pattern on mechanical properties were examined. Rectilinear, honeycomb, and line patterns with 20, 50, and 100% infill density were analysed. They found infill pattern and infill density had significant effects on mechanical properties. Rectilinear pattern with 100% density showed the highest tensile strength with the value of 36.4 MPa for ABS material. Another study examined the effects of build orientation and infill patterns on strength in printed PLA parts [54]. Results indicated flat samples had highest strength and infill density had direct effect on stiffness and strength of printed dog-bone shaped samples. Also, strongest samples were found with concentric and rectilinear pattern with 100% density. Masood et al. [55] examined the tensile strength of 3D printed PC products and found out they had good strength in the range of 70–80% compared to injection moulded process. Also, solid infill, 0.6064 mm raster width, and 45° raster angle showed the highest strength in this study. In brief, many parameters should be considered that play a vital role in this technology compared to other AM processes. Moreover, these parameters affect surface roughness and dimensional accuracy as well [56, 57].

Both MJP and FDM are capable to produce complex features with stipulated time. Generally, due to the nature of MJP, the printing time is longer compared to the FDM. There is no doubt that the printed products with the MJP process possess high quality but this process can be toxicity due to the existence of chemical reaction. On the other hand, FDM is most suitable process to produce toy for kids. Both MJP and FDM are looking for the product's quality in term of surface finished and sometimes neglected the strength of the product. As an example, Salmi et al. [58] analyzed the effects of build orientation in 3DP processes. Results showed build orientation is highly effective in material extrusion and MJ processes while by adding samples to the build platform, printing time per parts was reduced in MJ process. The results showed how AM processes are capable in terms of product developments and their effects on surface quality. However, parameters play an important role in these technologies, design and product's features are also effective during printing. Hence, It is necessary to analyze and predict, how printing process affects surface quality when it comes to complex structures [59]. This means, design for AM should be considered to eliminate obstacles and increase the productivity [60].

Nevertheless, controlling and finding proper parameters lead to the finest quality and the strongest products. Studies has shown that the strength of the 3D printed part plays an important role in industry. There have not been many studies on the structure integrity of the 3D printed in both MJP and FDM. As mentioned before, various factors affect the strength and mechanical properties of the 3D printed part. To find these capabilities, specimens must be printed according to ASTM standard and go through the test. Since much study has not been done yet to compare the product's strength between MJP and FDM. Hence, this study tends to investigate

the effects of different thicknesses on the structure strength in a complex specimen for both MJP and FDM. This goal was done by compressing the 3D printed parts with different thickness. The effects of different thickness were analyzed based on compression strength. Also, FEA was used to investigate the compression strength before the experimental process was done to analyze the defects and deflections.

2   Materials and Methods

A wide range of simple to complex products have been used in industries based on requirements. Products become more complex with different features and designs due to the aesthetic and mechanical properties [61, 62]. This structure can be used in construction due the stiffness and strength under loads [63]. Therefore, by scaling up the design into large system, it can be used in buildings and bridge based on requirements. Also, by increasing the density of details and adding extra details, porous structure can be achieved. The main applications of this design are scaffold and porous products. These structures have been used in in medical and construction field due to the complex features [64]. Researches have been conducted on bone scaffold by using 3D printing due to its capabilities [65, 66]. Hence, the features in this design can be modified and used in various fields.

This research was divided into three sections which were FEA, MJP and FDM process. Procedure was started by designing a novel complex structure with 3 different thicknesses. Siemens NX PLM Software® was used to design these structures. Light products have been widely used in different applications. Weight reduction without sacrificing mechanical properties is the main goal in industries. By optimizing the design, material wastage can be reduced and the final cost is affected as well. Specimens' details are provided in Fig. 2 to show the size and the differences between these products for MJP process. This design is highly effective to distribute the pressure and minimize the concentrated forces. As shown in Fig. 3, specimens were chosen to reduce the weight and achieving highest strength. Therefore, the parts' thickness was increased from 2 to 6 mm to find out the deflection and also how different thicknesses react under pressure.

The following step was printing samples by using MJ and FDM process. Poly lactic acid (PLA) material was used for both processes to eliminate differences in material properties. However, the material in this process was liquid while it was solid for FDM process. The properties of PLA material are provided in Table 1.

ProJet 3510 HD (3D Systems, Rock Hill, South Carolina, United States) machine which is a MJP (MJ) process was used to print samples. ProJet® 3D Modeling Accelerator software was used to slice the CAD design. Build orientation with 0° angle (x–y plane) and 0.05 mm layer thickness were chosen to print specimens due to the high quality and best mechanical properties. The infill density was 100% and all samples were printed in solid form. Due to the machine limitations and long process (42 h to print one sample), samples were scaled down by 50% to make the process faster. This machine uses two material to build products. The main material was black
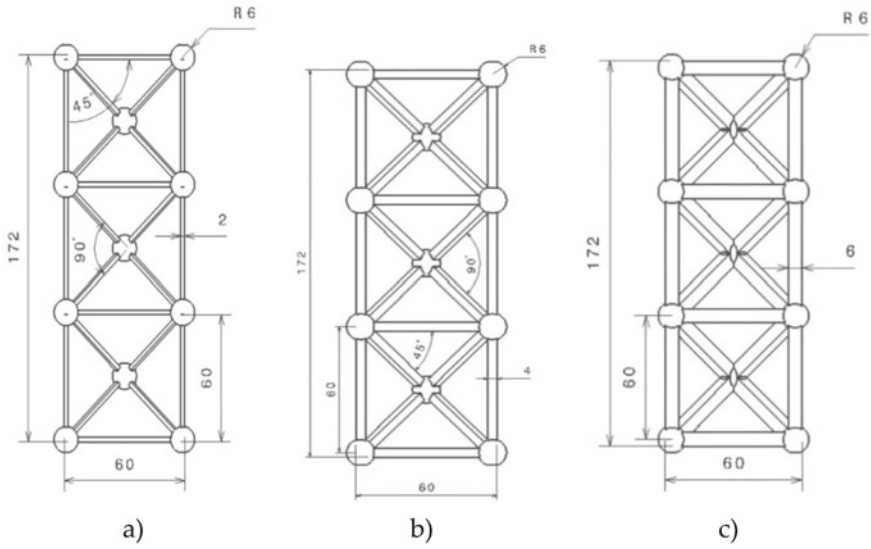
**Fig. 2** Details of each structure, **a** 2 mm, **b** 4 mm, and **c** 6 mm wall thickness
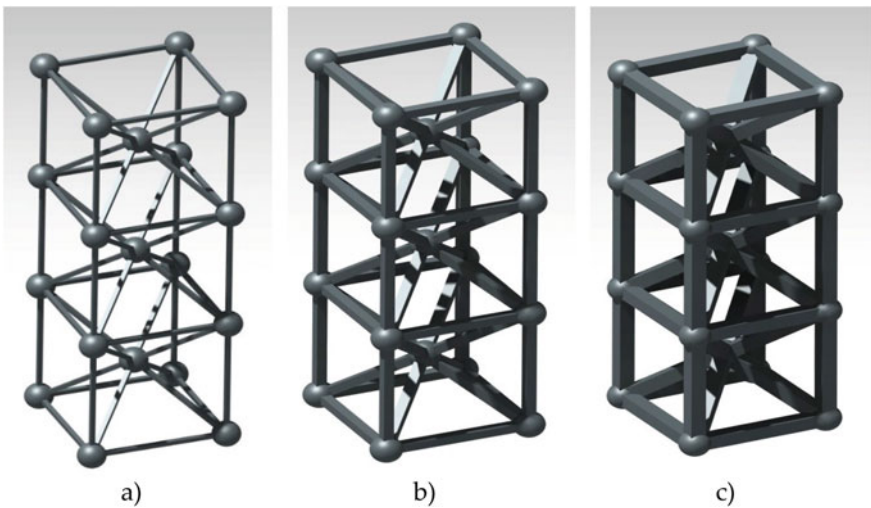
Fig. 3 Schematic of complex specimens with **a** 2 mm, **b** 4 mm, and **c** 6 mm wall thickness

PLA and Wax was used to build support structure in this process. Printed samples with support structure are shown in Fig. 4. The printing time to finish all samples simultaneously was 21 h. Due to the existence of support material in this process, post-processing techniques is necessary to remove excessive material from products. This post process was done by heat treatment. To remove supports, samples were put

Table 1 Material properties

Material	PLA
Density (g/cm^3)	1.17
Printing temperature (°C)	190–230
Printing speed (mm/s)	40–60
Bed temperature (°C)	25–60
Tensile strength (MPa)	46.6 ± 0.9
Young's Modulus (MPa)	2636 ± 330

Fig. 4 Printed samples with support structure
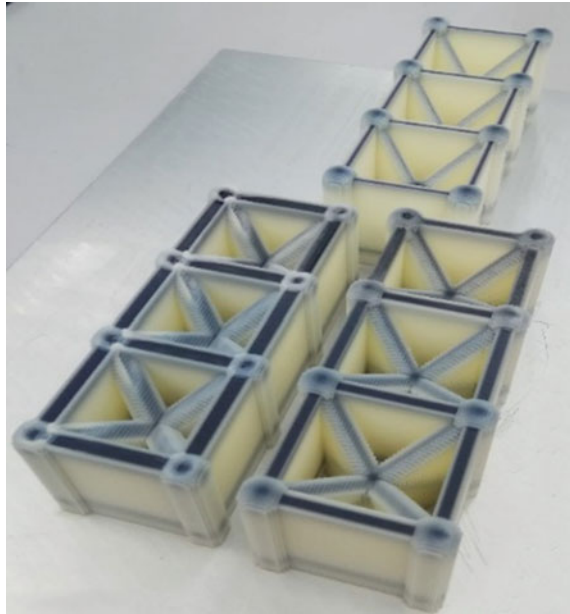
into the UF260 oven (Memmert, Schwabach, Germany) with 60 °C temperature. As shown in Fig. 5, a little bit of wax still attaches to the samples which were removed by hand or washing.

Meanwhile, FDM process was also used to print samples to make a comparison between these two processes. In this section, samples were limited to two modules. Creality Ender 3 machine (Creality, Shenzhen, China) was used to print samples. Red PLA from Devil Design with 1.75 mm filament diameter was used in this study. Simplyfy3D® software (4.0 version, Simplyfy3D, Cincinnati, US) was used to slice the design and converted them into G-code. Nozzle with 0.4 mm diameter was used to have better accuracy and reasonable printing time. The infill density in the printout was 100%. Printing parameters are provided in Table 2. The machine print samples with support structure to avoid material drops (see Fig. 6). Two samples were printed
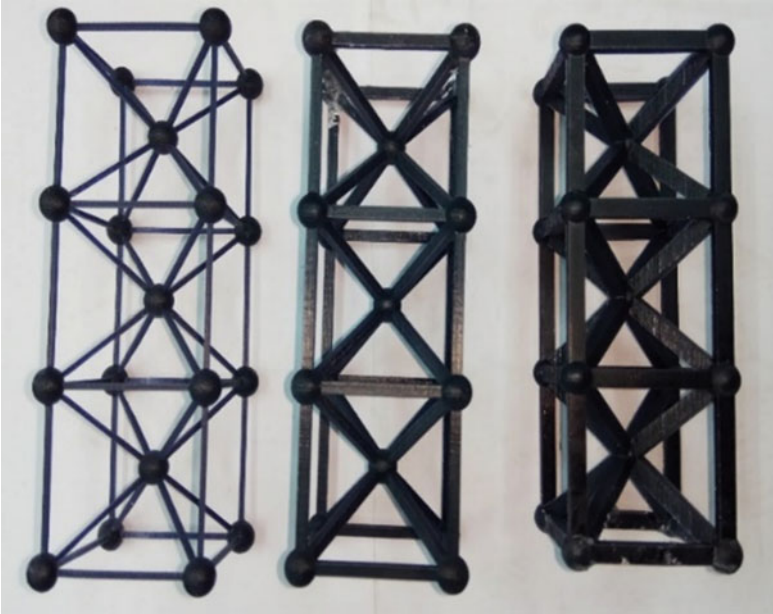
Fig. 5 Samples after wax removing

Table 2 FDM printing parameters

Parameter	Value
Build orientation (degree)	0
Nozzle temperature (°C)	210
Printing speed (mm/s)	50
Bed temperature (°C)	60
Infill pattern	Rectilinear
Infill density (%)	100
Layer thickness (mm)	0.2

Fig. 6 FDM printing procedure
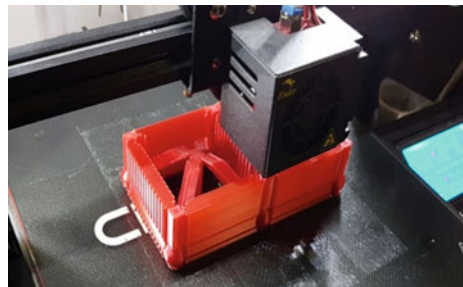
Fig. 7 3D printed PLA
samples in FDM process
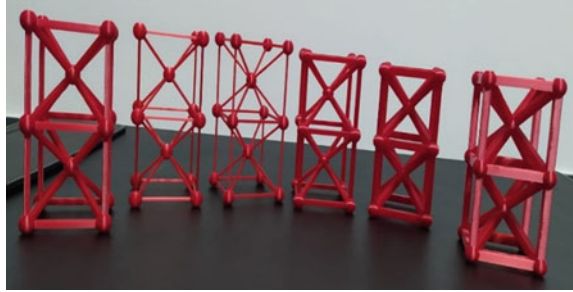
for each design to achieve more accurate result. As shown in Fig. 7, supports were removed by hand after printing process.

After printing samples in FDM and MJP process, the next step was to test their strength in compression test. The machine to conduct this test was INSTRON 3366 (INSTRON, Norwood, Massachusetts, United States) with 10 kN maximum capacity and 500 mm/min speed for MJP samples and Zwick/Roell Z010 (ZwickRoell GmbH & Co. KG, Ulm, Germany) with 10 kN maximum capacity and 1000 mm/min speed for FDM samples.

Printed samples were put for a compression test and 1 mm/min speed was applied for the upper jaw while the second jaw was constant during the process. Each sample was analyzed separately and the maximum loads were recorded for all of them to find out which process can produce stronger product in this case. Also, there was a brief look at the quality of the printed samples refer to details and curves.

Moreover, to find out the deflection and displacement of each sample, FEA was used to achieve accurate results. Finite element analysis was performed in order to validate the CAD model and assess the compliance of the obtained simulation results with laboratory tests. Positive validation of CAD models will enable subsequent modifications of the designed structures in order to optimize the strength parameters in relation to the mass of the designed elements, without the need to make time-consuming and expensive prints of many modified elements and subjecting them to compressive strength tests in laboratory conditions.

The analysis of the tested elements' strength using the finite element method was performed in the Siemens NX 12 environment, using the Pre/Post module. It is a tool that provides a wide selection of solutions for multitasking finite element simulation and provides comprehensive functions for model preparation, solving and post-processing. A mesh made of CTETRA (10) finite elements with a finite element size of 1 mm was used. After splitting the models into finite elements, the correctness of the finite element mesh was verified using the "Element quality" tool that detects elements that are too distorted to yield good analysis results. The analysis was carried out assuming a fixed constraint of the base of the tested elements as shown in Fig. 8a and assuming the load in the form of a force distributed evenly on the planes on the opposite side of the model−see Fig. 8b. The model with the created mesh of
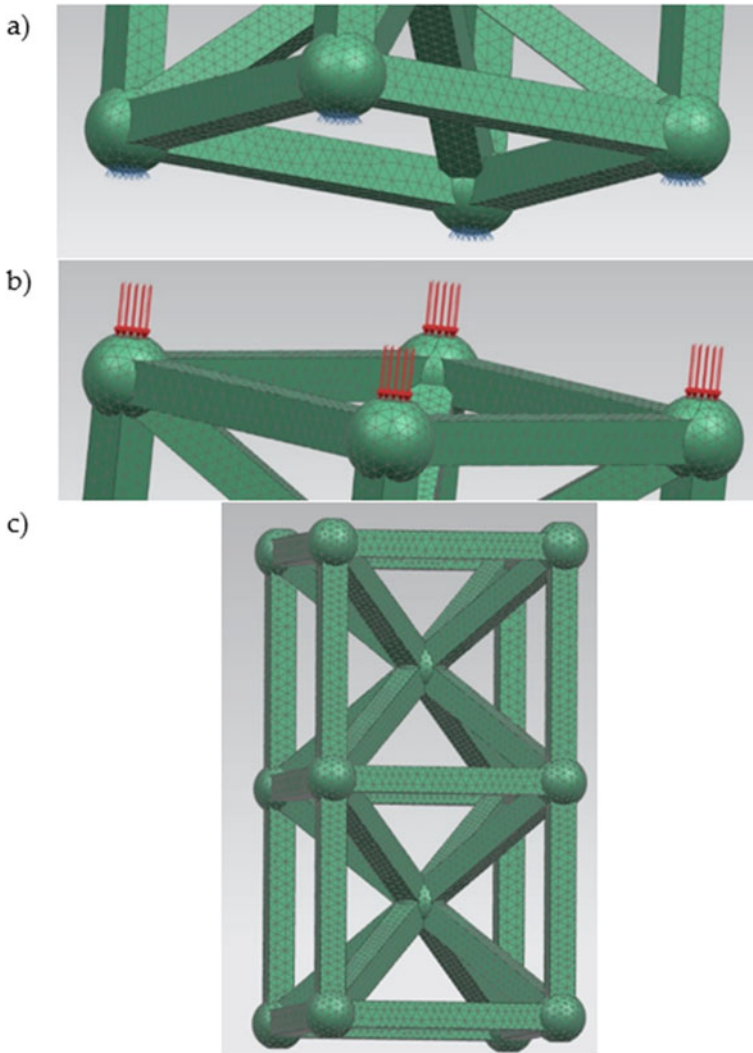
Fig. 8 A fixed constraint of the base of the tested elements (**a**), the load (**b**) and The model with the created mesh of finite elements

finite elements is shown in Fig. 8c. The NX Nastran solver was used to perform the calculations.

The analyzes were carried using parameters of the PLA material in accordance with the data presented in Table 1. The values of the forces loading the individual models were determined during the compressive strength tests of the printed elements.

3   Results and Discussion

Various factors have effects on mechanical properties and surface quality of 3D printed products. As discussed in literature, a vast range of parameters in both FDM and MJP are critical and should be controlled to enhance products quality. Therefore, by looking at the printed samples in FDM and MJP process, it would be possible to find out which samples have better quality. As shown in Fig. 9, samples with 6 mm wall thickness were chosen to analyze the quality of printed specimens. Based on information in printing parameters, the layer thickness in MJP process was 0.05 mm while the thickness in FDM was 0.2 mm. This means lower layer thickness leads to better surface quality due to the better layer binding. Also, when the layer thickness

a)

b)
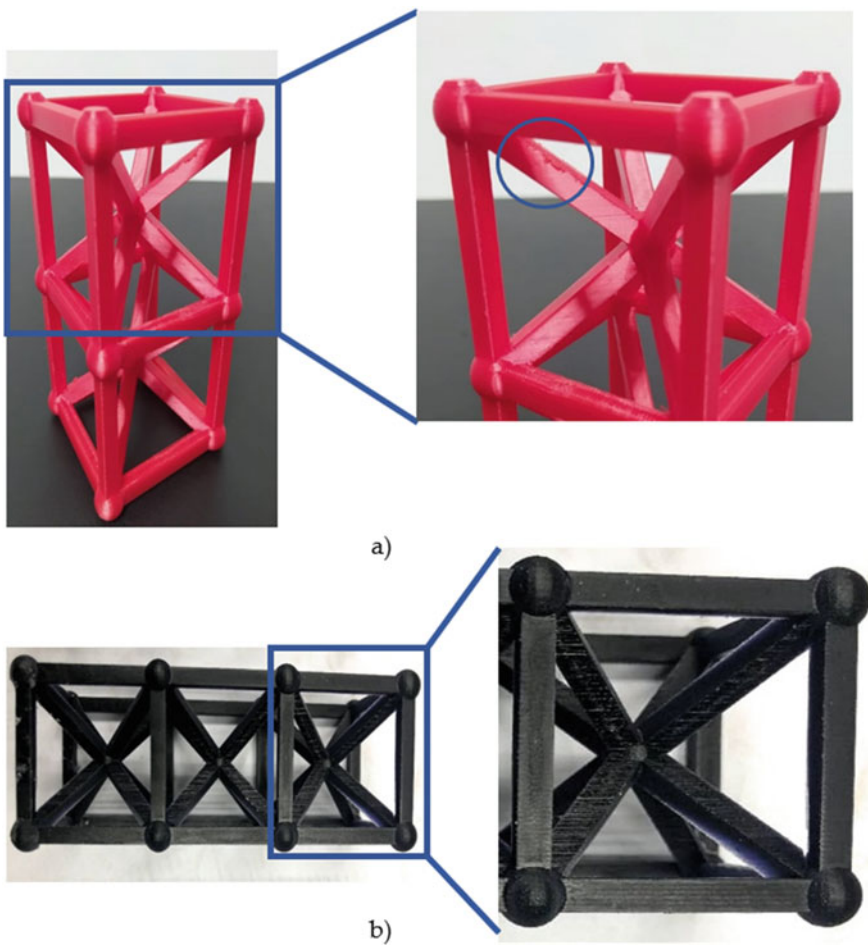
Fig. 9 Printing quality in **a** FDM process and **b** MJP process

decreases, the stair-step in texture is minimized as well. Figure 9a shows defect in surfaces with perpendicular directions in FDM process due to the poor layer adhesion which did not happen for MJP because of the support structure all over the samples. In brief, the quality of samples in MJP process was better compared to the FDM and surface smoothness was observed for MJP products. However, post-processing was needed to remove Wax support from printed specimens while FDM parts did not need any post-processing.

As shown in Fig. 10a, specimens 3D printed using MJP technology and scaled down by 50% from the designed dimensions cracked at different points. Part with 2 mm thickness was the weakest among MJP samples and cracked at 12.98 N. The 4 mm and 6 mm specimens cracked at 172.33 N and 587.21 N, respectively. Since, sample with 2 mm thickness did not show reasonable result, compression test was recorded step by step to show the deflection in samples. The results showed by increasing the part thickness, they could tolerate much pressure. Figure 10b shows the results of laboratory tests of the compressive strength of samples printed in
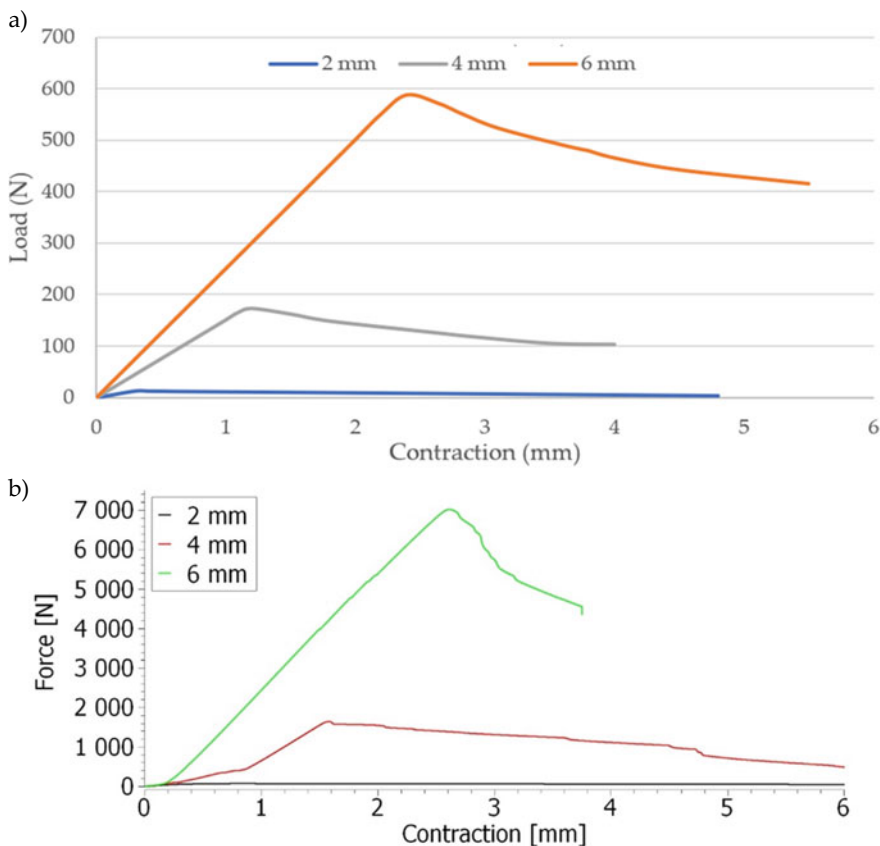
Fig. 10 Load/contraction chart for MJP (**a**) and FDM (**b**) samples

the FDM technology. The much higher strength of the samples is clearly visible compared to the elements printed in the MJP technology. However, it should be remembered that in this case the tested samples were not scaled in relation to the designed dimensions, and were also made of two modules. Larger cross-sections of the elements translated directly into their higher strength. Part with 2 mm thickness of course was also the weakest among FDM samples and cracked at 72.45 N. The 4 mm and 6 mm specimens cracked at 1652,20 N and 7072,45 N, respectively.

Deflection under different loads was recorded in Fig. 11 for MJP samples to illustrate how specimens acted. This Figure shows the samples' displacements and deflections based on produced pressure. It can be clearly seen, all specimens cracked from outer wall and failure did not happen for interconnection lines inside each cube.

Deflection under different loads was recorded in Fig. 12 for FDM samples. This Figure shows the samples' displacements and deflections based on produced pressure. It is easy to notice that the tested samples behaved differently from the samples made in the MJP technology. Not only the outer wall lines failure but failure happen also for interconnection lines inside each cube were damaged can be observed. What's more, taking into account the much greater loads carried by the tested elements, their small displacements can be observed compared to samples made in the MJP technology. This clearly indicates a higher strength of the elements produced in the FDM technology, which, however, are prone to brittle fracture when the load limit of the sample is exceeded.

Table 3 compares the results obtained during the compressive strength tests of samples produced with the FDM and MJP technology with the results carried out using the finite element method. Differences in the obtained results of the analyzes are clearly visible. In the case of analyzes of elements produced with the use of FDM technology, a very high compliance of the results obtained by numerical analyzes with the results of laboratory measurements of the produced samples was obtained. This allows to infer the correct preparation of the model, the definition of material parameters and the computer-aided calculations. In the case of analyzes of elements produced with the MJP technology, very large discrepancies between the results obtained using FEM method and the results of laboratory strength tests are visible. Figure 13 summarizes the obtained results of analyzes using the finite element method in the form of maps of strains and stresses determined for individual models of elements produced in the MJP technology. Figure 14 shows an analogous comparison with regard to the models produced in the FDM technology.

The obtained, very significant discrepancies in the comparison of the results in the case of printed elements in the MJP technology may be the result of the fact that in this technology the element is produced from a liquid material, while in the FDM technology the material is fed in a solid form and then melted. The differences in the technologies used translate directly into the strength properties of the products obtained. During the strength tests of the printed elements, differences in their behavior during increasing the load to which the elements were subjected are clearly visible. Samples made in the MJP technology show greater flexibility and no tendency to brittle cracking. In the case of samples made in the FDM technology, greater stiffness of the elements can be observed, which, however, is related to their
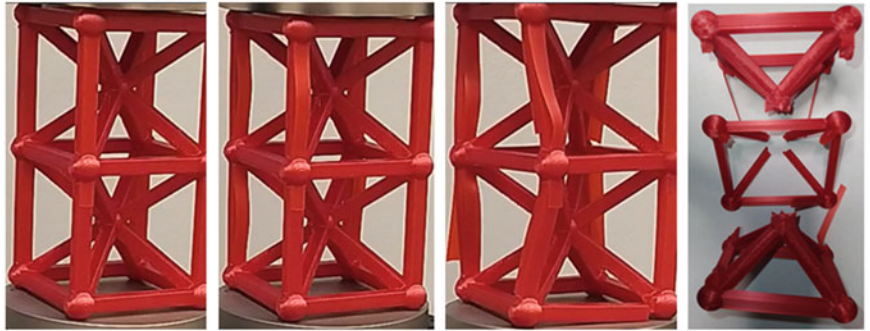
Fig. 11 Deflections and cracks in **a** 2, **b** 4, and **c** 6 mm of MJP samples
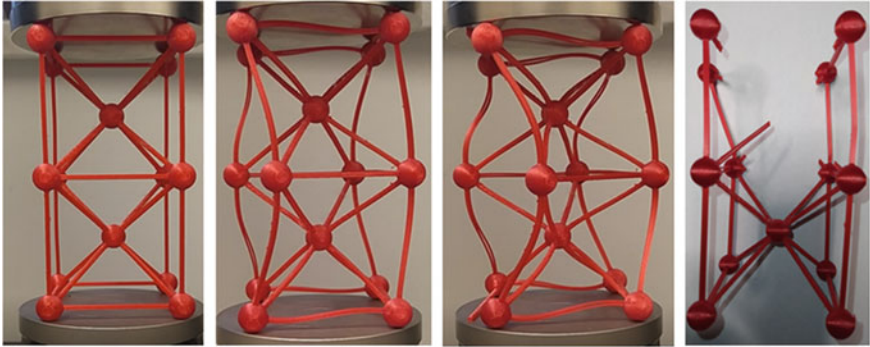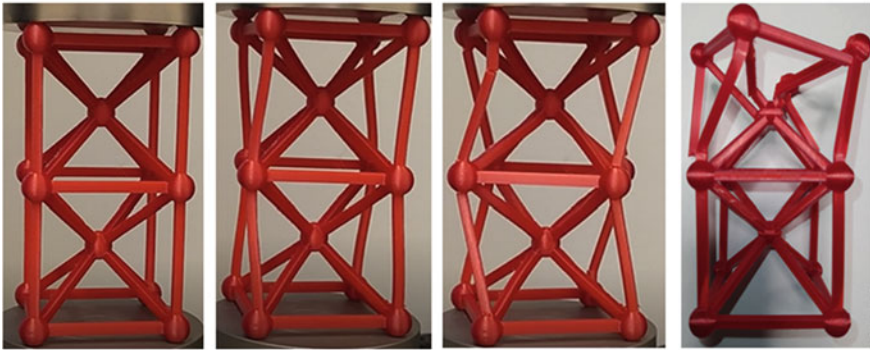
Fig. 12 Deflections and cracks in **a** 2, **b** 4, and **c** 6 mm of FDM samples

Table 3 Comparison of the results of strength tests and FEM analysis

Thickness [mm]	FDM printed elements				MJP printed elements			
	Force [N]	Displacement		Error [%]	Force [N]	Displacement		Error [%]
		Lab	FEM			Lab	FEM	
2	72.45	0.39	0.35	10.26	12.98	0.41	0.09	78.05
4	1652.20	1.58	1.50	5.06	172.33	1.22	0.33	72.95
6	7072.45	2.60	2.61	0.38	587.21	2.48	0.55	77.82

brittleness and complete destruction of the samples when the compressive strength is reached. This is particularly evident in the case of a specimen with a structural element thickness of 6 mm (see Fig. 12). You can also observe the separation of individual print layers.

Figure 15 shows the places of stress concentration on the example of a model with a structural element thickness of 6 mm.

It is clearly possible to observe the compliance of the places of stress concentration determined in the mathematical model using the FEM method with the places of damage to the printed elements during the strength tests.

4 Conclusions

Additive manufacturing (AM) is the next industrial revolution. Each process in this technology has different characteristics. Finding optimal condition in these processes leads to better quality and mechanical properties. In this study, MJP and FDM processes were analyzed to find out their capabilities and differences. Complex products with different part thicknesses were designed and printed. Surface quality in MJP process was better due to the lower layer thickness compared to the FDM process. Which is obvious, in both FDM and MJP process, the results showed part thickness had an extraordinary effect on mechanical properties and the strongest part was sample with the higher structural element thickness. However, a very interesting conclusion from the conducted research is the fact that there is a very significant difference in the mechanical properties of elements made of the same material with the use of different technologies. Elements printed in FDM technology show much higher stiffness and strength than elements printed in MJP technology, which show much greater flexibility, but also lower compressive strength. The reasons for such a phenomenon can be seen in the difference in the form of the material from which the print is made, which in the MJP technology is in a liquid form, and FDM in a solid form. However, the quality of the printed elements in the MJP technology significantly exceeds the surface quality of the elements obtained in the FDM technology. In the FDM technology, the print layers can be clearly observed, as well as their separation during durability tests of elements printed in this technology.
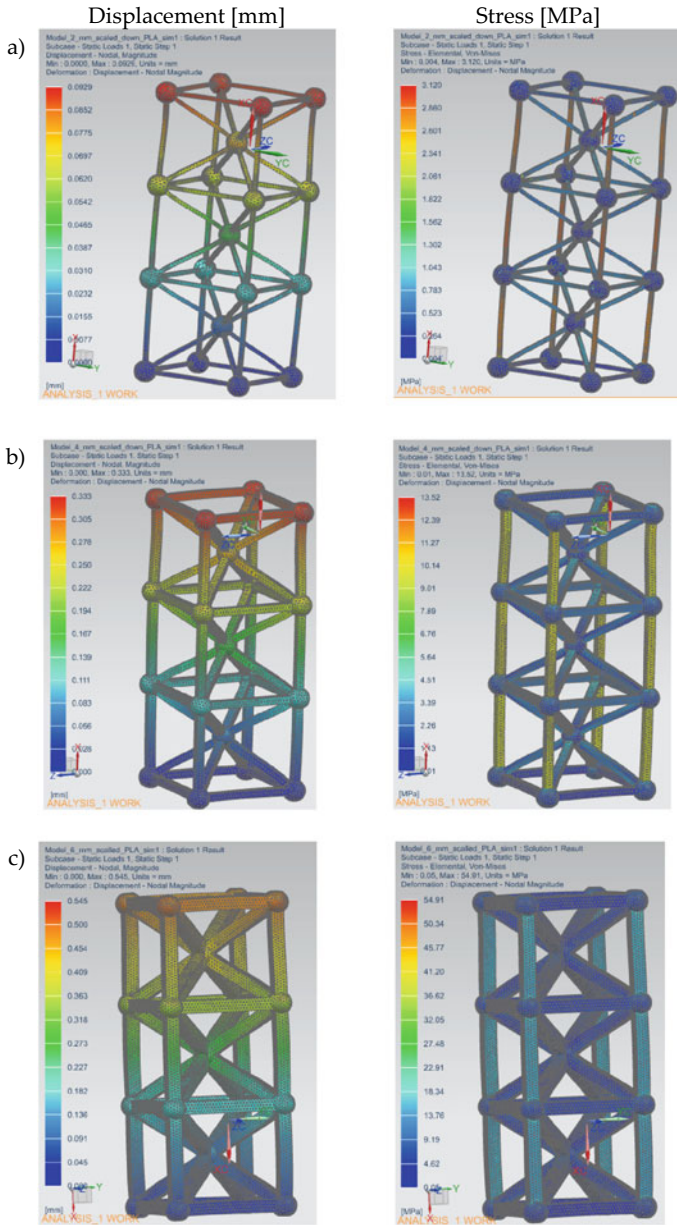
Fig. 13 Results of FEM analysis for **a** 2, **b** 4, and **c** 6 mm MJP samples
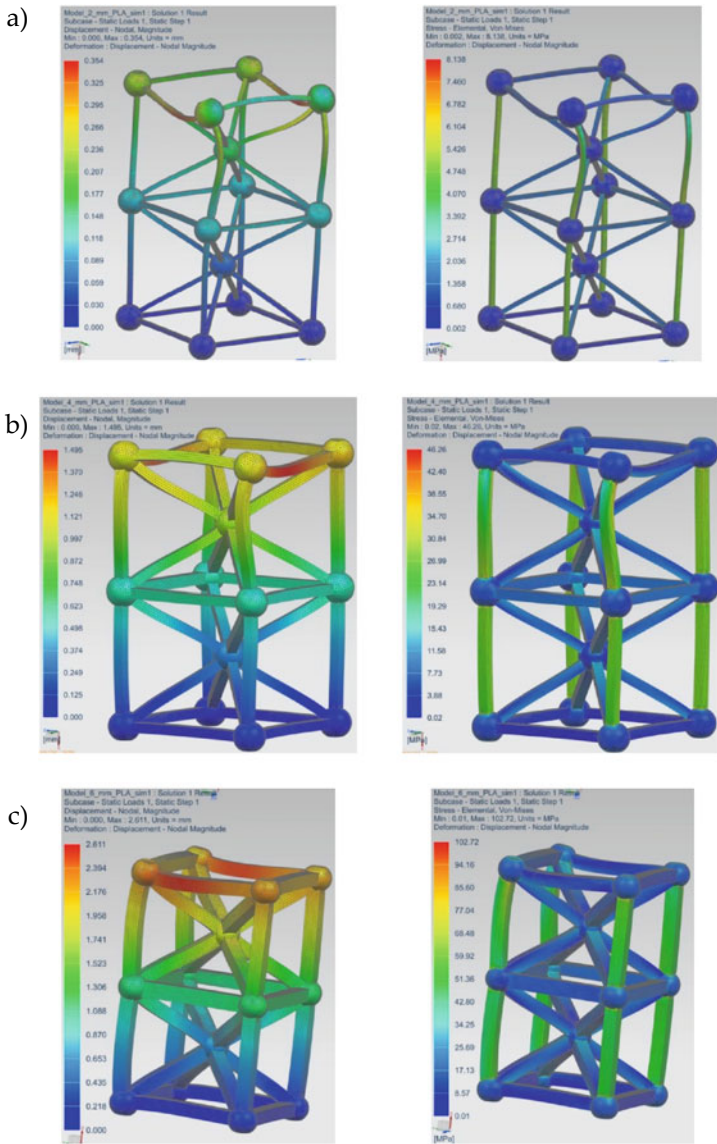
Fig. 14 Results of FEM analysis for **a** 2, **b** 4, and **c** 6 mm FDM samples

The conducted process of strength analysis of the designed elements using the finite element method showed very good compliance of the created models with real objects in the case of elements produced with the FDM technology and very significant discrepancies in the case of the MJP technology. This indicates the necessity

Fig. 15 Stress concentration points on the example of a 6 mm model
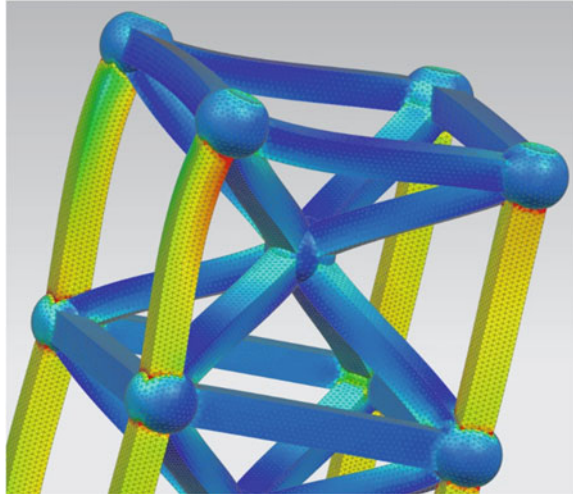
to conduct further tests of elements produced with the use of MJP in order to determine the plastic and strength properties of elements produced in this technology. The properties determined in this way should be used in further iterative processes of validation of computer models in order to obtain the compatibility of the results of the analyzes obtained with their application with the tests of real objects at a similarity level as good as in the case of the results obtained for FDM elements. In this case, the discrepancies between the obtained results were very small and only in one case slightly exceeded 10%. This means that the model developed and defined in this way can be successfully used in further research work aimed at designing a structure characterized by high compressive strength while maintaining a minimum weight. These issues will be the subject of further research and presented by the authors in subsequent publications.

References

1. Savolainen J, Collan M (2020) How additive manufacturing technology changes business models?−review of literature. Addit Manuf 32:101070
2. Gibson I, Rosen DW, Stucker B (2010) Introduction and basic principles. additive manufacturing technologies: rapid prototyping to direct digital manufacturing, Springer. US, Boston, MA, pp 20–35
3. Wong KV, Hernandez A (2012) A review of additive manufacturing. ISRN Mech Eng 2012:208760
4. Vyavahare S et al (2020) Fused deposition modelling: a review. Rapid Prot J 26(1):176–201
5. Ziaee M, Crane NB (2019) Binder jetting: a review of process, materials, and methods. Addit Manuf 28:781–801
6. Dilag J et al (2019) Design and direct additive manufacturing of three-dimensional surface micro-structures using material jetting technologies. Addit Manuf 27:167–174

7. Vock S et al (2019) Powders for powder bed fusion: a review. Prog Addit Manuf 4(4):383–397
8. Gibson I, Rosen DW, Stucker B (2010) sheet lamination processes, in additive manufacturing technologies: rapid prototyping to direct digital manufacturing. In: Gibson I, Rosen DW, Stucker B (eds). Springer US, Boston, MA, pp 223–252
9. Tang Z et al (2020) A review on in situ monitoring technology for directed energy deposition of metals. Int J Adv Manuf Technol 108(11):3437–3463
10. Ngo TD et al (2018) Additive manufacturing (3D printing): a review of materials, methods, applications and challenges. Compos Part B Eng 143:172–196
11. Gebhardt A, Hötter JS (2016) Rapid prototyping, in additive manufacturing. In: Gebhardt A, Hötter J-S (eds) Hanser, pp 291–352
12. Cuellar JS et al (2018) Additive manufacturing of non-assembly mechanisms. Addit Manuf 21:150–158
13. Ariffin MM et al (2018) Slicer method comparison using open-source 3d printer. In: IOP conference series: earth and environmental science. IOP Publishing.
14. Hernandez Korner ME et al (2020) Systematic literature review: integration of additive manufacturing and industry 4.0. Metals 10(8):1061
15. Yang H et al (2017) Performance evaluation of ProJet multi-material jetting 3D printer. Virtual Phys Prot 12(1):95–103
16. Calignano F et al (2017) Overview on additive manufacturing technologies. Proc IEEE 105(4):593–612
17. Kumbhar NN, Mulay AV (2018) Post processing methods used to improve surface finish of products which are manufactured by additive manufacturing technologies: a review. J Inst Eng (India) Series C 99(4):481–487
18. Bourell D et al (2017) Materials for additive manufacturing. CIRP Ann 66(2):659–681
19. Salcedo E et al (2018) Simulation and validation of three dimension functionally graded materials by material jetting. Addit Manuf 22:351–359
20. Bhattacharjee N et al (2016) The upcoming 3D-printing revolution in microfluidics. Lab Chip 16(10):1720–1742
21. Sochol RD et al (2016) 3D printed microfluidic circuitry via multijet-based additive manufacturing. Lab Chip 16(4):668–678
22. Gibson I, Rosen DW, Stucker B (2010) Photopolymerization processes, in additive manufacturing technologies: rapid prototyping to direct digital manufacturing. In: Gibson I, Rosen DW, Stucker B (eds), Springer US, Boston, MA, pp 78–119
23. Khoshkhoo A, Carrano AL, Blersch David M (2018) Effect of build orientation and part thickness on dimensional distortion in material jetting processes. Rapid Prot J 24(9):1563–1571
24. Guo Y et al (2018) Control-oriented models for ink-jet 3D printing. Mechatronics 56:211–219
25. Yuan J et al (2020) 3D printing of oil paintings based on material jetting and its reduction of staircase effect. Polymers 12(11):2536
26. Paterson Abby M et al (2015) Comparing additive manufacturing technologies for customised wrist splints. Rapid Prot J 21(3):230–243
27. Chen H, Zhao Yaoyao F (2016) Process parameters optimization for improving surface quality and manufacturing accuracy of binder jetting additive manufacturing process. Rapid Prot J 22(3):527–538
28. Udroiu R, Braga IC, Nedelcu A (2019) Evaluating the quality surface performance of additive manufacturing systems: methodology and a material jetting case study. Materials 12(6):995
29. Hafsa MN et al (2013) Evaluation of different internal structure and build orientation for multijet modeling process. Appl Mech Mater 315:587–591
30. Barclift M, Williams C (2012) Examining variability in the mechanical properties of parts manufactured via polyjet direct 3D printing, 23rd annual international solid freeform fabrication symposium—an additive manufacturing conference. SFF 2012:876–890
31. Khoshkhoo A, Carrano AL, Blersch DM (2018) Effect of surface slope and build orientation on surface finish and dimensional accuracy in material jetting processes. Proced Manuf 26:720–730

32. Kim H, Zhao Y, Zhao L (2016) Process-level modeling and simulation for HP's multi jet fusion 3D printing technology. In: 2016 1st international workshop on cyber-physical production systems (CPPS)
33. He Y et al (2016) An investigation of the behavior of solvent based polycaprolactone ink for material jetting. Scient Reports 6(1):20852
34. Moore Jacob P, Williams Christopher B (2015) Fatigue properties of parts printed by PolyJet material jetting. Rapid Prot J 21(6):675–685
35. Bass L, Meisel NA, Williams CB (2016) Exploring variability of orientation and aging effects in material properties of multi-material jetting parts. Rapid Prot J 22(5):826–834
36. Yap YL et al (2017) Material jetting additive manufacturing: An experimental study using designed metrological benchmarks. Prec Eng 50:275–285
37. Dhinakaran V et al (2020) A review on recent advancements in fused deposition modeling. Mater Today Proc 27:752–756
38. Mazzanti V, Malagutti L, Mollica F (2019) FDM 3D printing of polymers containing natural fillers: a review of their mechanical properties. Polymers 11(7):1094
39. Armillotta A et al (2018) Warpage of FDM parts: experimental tests and analytic model. Robot Comput Integr Manuf 50:140–152
40. Kuo CC et al (2019) Minimizing warpage of abs prototypes built with low-cost fused deposition modeling machine using developed closed-chamber and optimal process parameters. Int J Adv Manuf Technol 101(1–4):593–602
41. Popescu D et al (2018) FDM process parameters influence over the mechanical properties of polymer specimens: a review. Polym Testing 69:157–166
42. Chohan JS, Singh R (2017) Pre and post processing techniques to improve surface characteristics of FDM parts: a state of art review and future applications. Rapid Prot J 23(3):495–513
43. Lalegani Dezaki M, Mohd Ariffin MKA, Ismail MIS (2020) Effects of CNC machining on surface roughness in fused deposition modelling (FDM) products. Materials 13(11):2608
44. Galantucci LM, Lavecchia F, Percoco G (2009) Experimental study aiming to enhance the surface finish of fused deposition modeled parts. CIRP Ann 58(1):189–192
45. Jaisingh Sheoran A, Kumar H (2020) Fused Deposition modeling process parameters optimization and effect on mechanical properties and part quality: Review and reflection on present research. Mater Today Proc 21:1659–1672
46. Tlegenov Y et al (2018) Nozzle condition monitoring in 3D printing. Robot Comput Integr Manuf 54:45–55
47. Beran T et al (2018) Nozzle clogging factors during fused filament fabrication of spherical particle filled polymers. Addit Manuf 23:206–214
48. Matsuzaki R et al (2016) Three-dimensional printing of continuous-fiber composites by in-nozzle impregnation. Scient Reports 6:23058
49. Sukindar NA et al (2018) Analysis of mechanical properties of polylactic acid using a new 3D printer nozzle. J Comput Theor Nanosci 15(2):666–675
50. Taufik M, Jain PK (2016) A study of build edge profile for prediction of surface roughness in fused deposition modeling. J Manuf Sci Eng 138(6)
51. Samykano M et al (2019) Mechanical property of FDM printed ABS: influence of printing parameters. Int J Adv Manuf Technol 102(9):2779–2796
52. Wang J et al (2016) A novel approach to improve mechanical properties of parts fabricated by fused deposition modeling. Mater Design 105:152–159
53. Fernandez-Vicente M et al (2016) Effect of infill parameters on tensile mechanical behavior in desktop 3D printing. 3D Printing Addit Manuf 3(3):183–192
54. Dave H K et al. (2019) Effect of infill pattern and infill density at varying part orientation on tensile properties of fused deposition modeling-printed poly-lactic acid part, proceedings of the institution of mechanical engineers. Part C J Mech Eng Sc 0954406219856383
55. Masood SH, Mau K, Song WQ (2010) Tensile properties of processed fdm polycarbonate material. Mater Sci Forum 654–656:2556–2559

56. Pérez CJL (2002) Analysis of the surface roughness and dimensional accuracy capability of fused deposition modelling processes. Int J Prod Res 40(12):2865–2881
57. Ahn D et al (2009) Representation of surface roughness in fused deposition modeling. J Mater Process Technol 209(15–16):5593–5600
58. Salmi M et al (2017) Effect of build orientation in 3D printing production for material extrusion, material jetting, binder jetting, sheet object lamination, vat photopolymerisation, and powder bed fusion. Int J Collab Enterp 5:218
59. Di Angelo L, Di Stefano P, Marzola A (2017) Surface quality prediction in FDM additive manufacturing. Int J Adv Manuf Technol 93(9):3655–3662
60. Vayre B, Vignat F, Villeneuve F (2012) Designing for additive manufacturing. Proced CIRP 3:632–637
61. Karpus V et al (2018) Technological assurance of complex parts manufacturing. in design, simulation, manufacturing: the innovation exchange. Springer
62. Zhao J et al. (2018) A novel optimization design method of additive manufacturing oriented porous structures. In: ASME 2018 international mechanical engineering congress and exposition, american society of mechanical engineers
63. El-Reedy MA (2012) Chapter 3−offshore structure platform design. In: El-Reedy MA (ed) Offshore structures. Gulf Professional Publishing, Boston, pp 93–211
64. Ciocca L et al (2009) CAD/CAM and rapid prototyped scaffold construction for bone regenerative medicine and surgical transfer of virtual planning: a pilot study. Comput Med Imaging Graph 33(1):58–62
65. Bose S, Vahabzadeh S, Bandyopadhyay A (2013) Bone tissue engineering using 3D printing. Mater Today 16(12):496–504
66. An J et al (2015) Design and 3D printing of scaffolds and tissues. Engineering 1(2):261–268

Atomistic Modelling of Nanocutting Processes

**Francisco Rodriguez-Hernandez, Michail Papanikolaou,
and Konstantinos Salonitis**

Abstract   This chapter presents some of the state-of-the art investigations on Molecular Dynamics simulations of Nanocutting processes. The basic theory of Molecular Dynamics simulations has been presented to facilitate the understanding of the fundamental principles of this numerical modelling method and the techniques employed to extract meaningful macroscopic properties out of atomistic simulations. The advances of Molecular Dynamics simulations with respect to modelling nanocutting processes are at core of this chapter. More specifically, fundamental and pioneering MD studies of nanocutting processes are thoroughly discussed with special emphasis laid on phenomena taking place during material removal, such as thermal softening, dislocation generation and stress evolution. The nature of the Molecular Dynamics simulation method allows for capturing and monitoring the aforementioned phenomena; this cannot be easily achieved via experimental and other modelling techniques such as Finite Element Analysis and Discrete Element Modelling. It is expected that, over the years to come, Molecular Dynamics simulations will be increasingly employed for investigating material removal processes due to the rapid development of computational power.

1   Introduction

Owing to the vast increase of computational power over the past few decades, numerical simulation has been used as tool for investigating phenomena taking place during material removal and for optimising the process. Material removal has been numerically investigated in various scales ranging from continuum to atomistic using different numerical modelling techniques; a thorough review of the modelling techniques implemented and the advances in numerical simulation since the early 1990s has been provided by Brinksmeier et al. [1]. The authors identified 7 main modelling techniques of grinding processes, namely: (1) Rule Based, (2) Artificial

F. Rodriguez-Hernandez · M. Papanikolaou (✉) · K. Salonitis
Manufacturing Theme, Cranfield University, Cranfield MK43 0AL, UK
e-mail: m.papanikolaou@cranfield.ac.uk

Neural Networks, (3) Regression Models, (4) Finite Element Analysis (FEA), (5) Fundamental Analytical Approaches, (6) Kinematic-Geometrical models and (7) Molecular Dynamics (MD) simulations. Discrete Element Models (DEM) of material removal have also been developed over the last few years [2, 3] and could be added to the aforementioned categories.

Although Molecular Dynamics simulations are characterised by high computational cost and have temporal and spatial limitations have significant advantages over the aforementioned computational modelling techniques with regard to modelling material removal processes which are characterised by complex relationships between machining parameters and work results. More specifically, in contrast to other modelling techniques such as FEA and DEM, they do not rely on constitutive or empirical relationships. On the contrary, as it will be discussed in the following sections, the system's response is reproduced as a result of the evolution of the atoms' trajectories which are dictated by the Newton's laws of motion and a set of interaction potentials. The aforementioned features render MD unique as a computational technique with respect to capturing nanoscale phenomena as they take place with high resolution.

The present chapter focuses on the applications of MD simulations on nanocutting processes. Initially, the basic theory of MD simulations will be presented with respect to (a) the typical structure of a MD code, (b) the primary interaction potentials implemented in nanocutting simulations, (c) time integration and (d) calculation of macroscopic properties using statistical mechanics. Subsequently, the current state of the art in MD simulations of nanocutting processes will be presented. As it will be further elaborated, MD simulations are capable of capturing a variety of phenomena occurring during nanocutting, including thermal softening, dislocation generation and residual stresses' relaxation in polycrystalline materials. Finally, the effects of various process parameters including the cutting tool geometry, depth of cut, tool stiffness and surface roughness on the nanocutting behaviour will be discussed.

2 Basic Theory of Molecular Dynamics Simulations

Molecular Dynamics simulations is a numerical technique pioneered by Alder and Wainwright [4] and used to accurately reproduce physical phenomena in the atomic scale by monitoring the position and the interaction between a group of atoms enclosed in a computational domain. The atoms' trajectories are dictated by the Newton's laws of motion while the interatomic interactions are modelled using force fields and interatomic potentials. More specifically, the atoms' positions and momenta are time-integrated by solving the classical equations of motion in a step-by-step manner:

$$m_i \ddot{\boldsymbol{r}}_i = \boldsymbol{f}_i$$
$$\boldsymbol{f}_i = -\frac{\partial U}{\partial \mathbf{r}_i} \tag{1}$$

where m_i the mass, $\mathbf{r}_i$ the set of cartesian coordinates and $\mathbf{f}_i$ the force vector corresponding to an atom i. U is the potential energy function.

Molecular Dynamics simulations are characterised by very high resolution while their spatial and temporal limitations are continuously expanding owing to the rapid increase of the computational power. In the following subsections the basic theory of Molecular Dynamics simulations will be discussed with respect to the following subtopics: (a) typical structure of a MD code, (b) description of the main interaction potentials implemented in MD simulations of material removal processes, (c) time integration and (d) calculation of macroscopic properties.

2.1 Structure of a Molecular Dynamics Code

The typical structure of a MD simulation is represented in the flowchart of Fig. 1. The first step is to position the atoms within the simulation domain in such a way so as to avoid overlapping of atoms and effectively represent the material structure. In the case of liquids and gases, atoms can be placed randomly in the simulation domain. However, in the case of solids, atoms have to be positioned in a way mimicking the

Fig. 1 Flowchart of a typical MD simulation
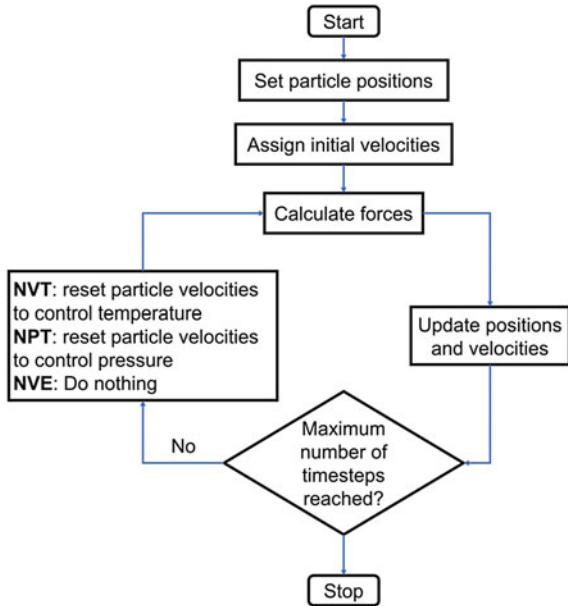
microstructure of the material; e.g. in the case of crystalline materials, atoms should be placed in the positions of a crystal lattice. It is of crucial importance to avoid overlapping of atoms as strong repulsive forces might lead to atoms escaping the simulation domain and additional computational hindrance. In order to facilitate and speed up the equilibration, energy minimisation [5] is often performed prior to the run in order to minimise the potential energy of the system by adjusting the atomic positions. Following minimisation, a set of velocities is assigned to the atoms; this is usually performed using a random number generator and the aim is to reach as close as possible to the desired temperature. Then the system of atoms is equilibrated by numerically solving the Newton's equations of motion in a step-by-step manner; the equilibration is usually terminated when the temperature and pressure of the system and its components have reached the desired levels and have been stabilised. During equilibration, atoms' trajectories are rescaled in order to satisfy the constraints of common statistical ensembles. Equilibration is then followed by the production runs during which thermodynamic/structural/physical properties of interest (pressure, stresses, temperature, Radial Distribution Function) are measured or monitored. The forces exerted on each one of the atoms are calculated in each timestep according to Eq. (1) and the positions of atoms are updated accordingly. Production runs are terminated when the required number of timesteps has been achieved.

2.2 Interatomic Potentials

In nature there are 3 primary types of bonds, i.e. (a) covalent, (b) metallic and (c) ionic bonds. Bonded atoms exhibit a common behaviour: they are repulsed when the interatomic distance falls below a threshold (equilibrium distance) and attracted when the interatomic distance is greater than this threshold. Over the years, several interatomic potentials have been developed for accurately describing the interaction between atoms of macromolecules [6–9], noble gases [10], fluids [11] and metals [12, 13] as well as the interactions between different materials. Moreover, reactive force fields have been developed for modelling chemical reactions which cannot be modelled using classical force fields [14–16]. Reactive force fields have been proven to be quite effective but the high amount and complexity of calculations performed per timestep significantly increases their computational cost which however is still maintained below the corresponding cost of quantum mechanical methods such as Density Functional Theory (DFT). In this section, the main interatomic potentials employed in Molecular Dynamics simulations of manufacturing processes will be described.

Interactions between the workpiece atoms

Molecular Dynamics simulations of nanocutting processes contain a metallic workpiece in the majority of cases is made of copper [17, 18], iron [19, 20], silicon [21, 22]

and aluminium [23, 24]. The interaction between the copper workpiece atoms (Cu-Cu) has been primarily modelled using the Embedded Atom Model (EAM) potential which falls under the category of many-body potentials. Many-body potentials can effectively differentiate the atoms lying at the surface from the ones at the bulk of a solid and capture the elastic behaviour of metals [25]. According to the EAM formulation, the potential energy of a single atom i (V_i) is dependent on its neighbours as follows:

$$V_i = \sum_{j=1}^{N_i} V(r_{ij}) + f(\rho_i) \tag{2}$$

where V_i the potential energy of atom i, $V(r_{ij})$ the interaction energy between atoms i and j, N_i the number of neighbouring atoms lying within the cutoff distance, ρ_i the local electron density and f an embedding function. Less commonly [26], the classical 12-6 Lennard–Jones (LJ) potential [27] has been used to describe the interactions between the copper atoms of the workpiece. The interaction energy V is given by:

$$V = 4\varepsilon \left[\left(\frac{\sigma}{r}\right)^{12} - \left(\frac{\sigma}{r}\right)^6 \right] \tag{3}$$

where ε the depth of the potential well which is indicative of the interaction strength, σ is the interatomic distance at which V is annihilated and r the interatomic distance. However, according to [28] the EAM potential should be favoured over the Lennard–Jones and Morse potentials to describe the Cu–Cu interactions of the workpiece due to its inherent capability to describe metallic bonds.

The Finnis–Sinclair potential [29] is similar to EAM and has been implemented to describe the interactions between Fe–Fe [20] and Al–Al [24] atoms of the workpiece. The potential energy (E_{tot}) of a group of N atoms is given by:

$$E_{tot} = \frac{1}{2} \sum_{j=1}^{N} \sum_{j=1}^{N} V_{ij}(r_{ij}) - A \sum_{i=1}^{N} \sqrt{\rho_i} \tag{4}$$

where A the binding energy while the local electron density ρ_i can be calculated as follows:

$$\rho_i = \sum_{j=1, i \neq j}^{N} \varphi_{ij}(r_{ij})$$

$$\varphi_{ij}(r_{ij}) = \begin{cases} (r_{ij} - d)^2 + \beta \frac{(r_{ij}-d)^3}{d} & if \ r_{ij} \leq d \\ 0 & if \ r_{ij} > d \end{cases} \tag{5}$$

where φ_{ij} the atomic charge density, r_{ij} the interatomic distance between atoms i and j, d the cutoff distance and β a constant used to tune the maximum value of φ_{ij}. Fe–Fe bonds have also been modelled using the Modified Embedded Atom Model (MEAM) proposed by Baskes et al. [30]. The main difference between the EAM and MEAM potentials is that the latter one accounts for angular contributions when calculating the electron density; this makes MEAM suitable for modelling materials characterised by directional bonding [31].

The interaction between Silicon atoms (Si–Si) has often been modelled [32, 33] using the Tersoff potential [34] which is given by:

$$
\begin{aligned}
E &= \frac{1}{2} \sum_i \sum_{i \neq j} V_{ij} \\
V_{ij} &= f_c(r_{ij})[f_R(r_{ij}) + b_{ij} f_A(r_{ij})]
\end{aligned}
\tag{6}
$$

where E and V_{ij} are the total and bond energy respectively, $f_c(r_{ij})$ a cutoff function, $f_R(r_{ij})$ and $f_A(r_{ij})$ correspond to the repulsive and attractive components respectively while b_{ij} is the bond order.

Interactions between the tool atoms

The vast majority of Molecular Dynamics simulations of nanocutting processes consider a cutting tool made of diamond. The interaction between the carbon atoms of the diamond tool has often been neglected due to the superior hardness exhibited by diamond while the atoms of the cutting tool have been placed on the sited of a diamons cubic lattice and considered to be rigid [23, 35]. However, in the majority of MD studies the interaction between the diamond atoms has been modelled using the Tersoff potential given by Eq. (6) [17, 24, 36]. The latter approach is more accurate compared to the simplified former one but more computationally expensive.

Interactions between the tool and workpiece atoms

The Morse potential [36–38] has been extensively used to model the interaction between the tool and workpiece atoms as it has led to good agreement between numerical and experimental results. According to the Morse formulation the pairwise interaction energy E is given by:

$$
E = D_0[e^{-2a(r-r_0)} - 2e^{-a(r-r_0)}]
\tag{7}
$$

where D_0 is the cohesion energy, α the elastic modulus, r_0 the equilibrium distance and r the distance between two atoms. The first term in the parenthesis corresponds to the repulsive force while the latter to the attracting one. Besides the Morse potential, the classical 12-6 Lennard–Jones potential given by Eq. (3) has been used to model the interaction between the workpiece (Fe) and tool (C) atoms [39], although this is not a common practice.

2.3 Time Integration

As mentioned in the beginning of this section, in Molecular Dynamics simulations the atoms' positions and momenta are time-integrated by solving the classical equations of motion in a step-by-step manner. The most common algorithm for performing time-integration is the Verlet algorithm which offers stability and time-reversibility [40]. The position of a particle is a function of time and can be calculated using the Taylor expansion as follows:

$$r(t + \Delta t) = r(t) + u(t)\Delta t + \frac{f(t)}{2m}\Delta t^2 + \frac{\Delta t^3}{3!}\dddot{r} + O(\Delta t^4) \qquad (8)$$

where $r(t)$, $u(t)$ and $f(t)$ the position, velocity and force respectively while m the particle mass and Δt the timestep. Similarly, it can be obtained:

$$r(t - \Delta t) = r(t) - u(t)\Delta t + \frac{f(t)}{2m}\Delta t^2 - \frac{\Delta t^3}{3!}\dddot{r} + O(\Delta t^4) \qquad (9)$$

The particle position at the following timestep can be calculated by adding Eqs. (8) and (9):

$$\overset{(1.8)+(1.9)}{\Rightarrow} r(t + \Delta t) + r(t - \Delta t) = 2r(t) + \frac{f(t)}{m}\Delta t^2 + O(\Delta t^4) \Leftrightarrow$$

$$\Leftrightarrow r(t + \Delta t) \cong 2r(t) - r(t - \Delta t) + \frac{f(t)}{m}\Delta t^2 \qquad (10)$$

The particle velocity at the current timesteps can be calculated using the mean value theorem:

$$\Leftrightarrow u(t) = \frac{r(t + \Delta t) - r(t - \Delta t)}{2\Delta t} + O(\Delta t^2) \qquad (11)$$

By observing Eq. (11) it can be concluded that the velocity at the current timestep cannot be calculated until the particle position at the following timestep $r(t + \Delta t)$ is known. Finally, it should be noted that the error in the velocity calculation is of the order of $O(\Delta t^2)$.

2.4 Calculation of Macroscopic Properties

Molecular Dynamics simulations are capable of monitoring the evolution of the dynamics of a system, such as the particles' positions and momenta. However, the extraction of meaningful macroscopic properties can be achieved with the help of

statistical mechanics. Let us consider a phase space $\boldsymbol{\Gamma(r, p)}$ with $\boldsymbol{r, p}$ being the positions and the momenta of the atoms respectively. In order to estimate a macroscopic property $A(\boldsymbol{\Gamma})$ being a function of the phase space (e.g. kinetic energy), the average of A over a long observation t_{obs} has to be calculated:

$$A_{obs} = \langle A \rangle_{time} = \langle A(\boldsymbol{\Gamma}(t)) \rangle_{time} = \lim_{t_{obs} \to \infty} \frac{1}{t_{obs}} \int_0^{t_{obs}} A(\boldsymbol{\Gamma}(t))dt \qquad (12)$$

However, the calculation of time averages of a system's property over long time intervals is very computationally expensive. This issue can be overcome with the help of the ergodic hypothesis which states that all the potential microstates of an equilibrated system are equally probable over a long time interval. In other words the average of a property over time is equal to the ensemble average; this hypothesis can significantly reduce the computational cost and can be expressed as follows:

$$\langle A \rangle_{time} = \langle A \rangle_{ensemble} \qquad (13)$$

A system that adheres to the aforementioned principle is also known as *ergodic*. Macroscopic properties of the system, such as pressure and temperature, can be calculated based on the aforementioned principles and can be linked to the particles' trajectories [41].

3   Atomistic Simulations of Nanocutting Processes

The main aim for the development of nanocutting technologies is the fabrication of ultra-precision and complex nanodevices or components. One of the main nanocutting processes is nanomechanical machining which is a process with high controllability [42]. For many decades, researchers focused on the development of interatomic potentials being capable of accurately describing the interaction between different atom types which were exploited for the development of numerical models of manufacturing processes in the atomic scale. Molecular Dynamics simulations have been the main computational technique among others, such as Finite Element Analysis and Discrete Element Models [43–48], implemented for the development of such models. Atomistic numerical models of nanocutting processes have evolved over the years and covered a variety of parameters affecting the process mechanics including material, tool geometry, cutting forces, friction factor, stress, dislocations, surface temperature, contact stiffness, surface roughness as it will be further discussed in the following subsections.

3.1 Workpiece Material and Tool Geometry

The basis of Molecular Dynamics simulations of nanocutting processes is modelling the interaction of a cutting tool and a workpiece. In order to effectively and realistically represent the material properties of the tool and workpiece there are many simulation parameters needed to be considered and tuned; these include the crystalline orientation, the interatomic potential between the various kinds of atoms and their capability to effectively capture phase transition and stacking fault energy. Both brittle and ductile materials have been used in Molecular Dynamic studies of nanocutting processes. More specifically, investigations have been focused on nanocutting of various materials, including copper [49], aluminium [23] and silicon [50] workpieces, with different cutting tool sizes and shapes as well as depths of cut.

In one of the earliest and pioneering studies, Inamura et al. [38] investigated the interaction between a workpiece and a cutting tool, made of copper and diamond respectively, via 2-dimensional Molecular Dynamics simulations. They found that plastic deformation occurred along grain boundaries and then propagated into each grain. They also investigated brittle/ductile transition phenomena in the machining of defect-free monocrystalline silicon [51]. Following a similar research line but considering a brittle workpiece made of single crystal silicon, Han et al. [52] showed that brittle fracture can be dominant during nanocutting processes. They advocated that brittle fracture leads to high removal rates and increases energy efficiency. By performing visual examination of their simulation results, they concluded that the dislocation density is dependent on both tool geometry and depth of cut. More specifically, the dislocation density appeared to increase with the depth of cut due to the higher cutting forces induced. Negative rake angles were found to promote dislocation formation due to the intensification of the rubbing and ploughing phenomena. On the other hand, positive rake angles favoured the cutting action instead and consequently led to increased chip thickness and decreased subsurface dislocations. Komanduri et al. [53] investigated the effects of the workpiece material ductility, the tool rake angle as well as the depth of cut on the burr formation and exit failure using MD simulations. It was shown that the failure mode is strongly dependent on the workpiece material (ductile or brittle). In the case of the more ductile workpiece material (copper) positive burr formation was observed while crack propagation was kept at a minimum. The authors also examined the case of a more brittle material by modifying the parameters of the Morse potential, initially used for describing the interactions between the copper atoms of the workpiece. In that case, negative burr formation and crack propagation were observed; this led to increased probability of tool fracture as expected. The burr dimensions were found to decrease with increasing rake angles for both ductile and brittle workpiece materials while the cutting forces followed a similar trend. The depth of cut was also proven to affect the failure mode at the exit; higher values of the depth of cut promoted crack initiation at the exit edge. The performed simulations were found to be in good agreement with experimental results with respect to the "foot" pattern observed at the exit of the workpiece [54].

Fig. 2 Schematic representation of cutting tool geometry
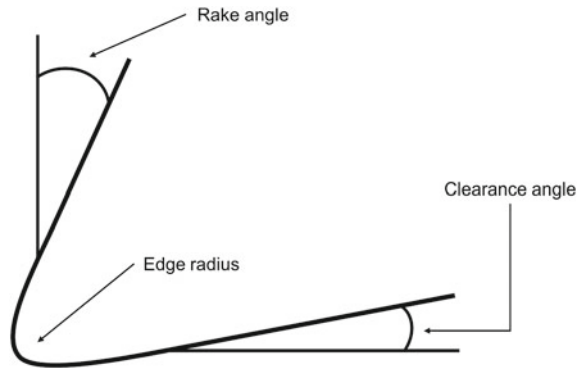
Theoretical and experimental investigations have shown that in brittle materials, ductile chip formation can be achieved when high compressive and shear stresses are present in the chip formation zone [55]. Two main conditions have to satisfied for this purpose: the undeformed chip thickness should be (a) quite small and (b) lower than the radius of the tool edge. When the aforementioned conditions are realised, the stress intensity factor is smaller than fracture toughness and consequently crack propagation is hindered in the cutting area. The aforementioned observations were later on verified via means of MD simulations [56]. In this study, Cai et al. investigated the nanocutting process of monocrystalline silicon and focused on the effects of the undeformed chip thickness on the magnitude of principal and shear stresses as well as the cutting forces. Their numerical results confirmed that the chip formation mode changes from ductile to brittle for high values of the tool cutting edge and lower shear stresses at the cutting region.

One of the most extensively investigated topics via MD simulations is the effect of the tool geometry on the nanocutting process characteristics with the rake angle (see Fig. 2) being one of the critical parameters affecting nanocutting mechanics. Komanduri et al. [57] performed MD simulations on copper nanocutting using cutting tools with rake angles ranging from $-75°$ to $40°$. They observed that both the cutting forces per unit width and specific energy decrease with the rake angle. Their results were also compared against experimental ones of conventional cutting [58]. Very good qualitative and quantitative agreement was observed with respect to the cutting forces. Similar trends between experimental and numerical results were identified for the specific energy, although the estimated MD values were found to be an order of magnitude higher compared to conventional cutting; this was attributed to size effects. In another study, Komanduri et al. [59] demonstrated the effects of the tool geometry and depth of cut on a variety of nanocutting process features including the cutting forces, friction coefficient, specific energy and subsurface damage. In their MD simulations they kept the ratio of the depth of cut to the tool edge radius (d/r) constant. Their results suggested that cutting forces tend to increase with the depth of cut regardless of the value of the d/r ratio while in contrast to preceding experimental and numerical investigations the specific energy was found to be insensitive

to d/r; this was attributed to the limited range of d/r ratios examined in the particular study. Finally, it was shown that extensive subsurface damage, expressed in terms of dislocation density, might occur for higher depths of cut; this was associated with the increase of cutting forces with the depth of cut. Subsurface damage was proven to be affected by the d/r ratio. More specifically, it was shown that subsurface deformation decreases with the d/r ratio; this is indicative of the dominance of the cutting over the ploughing/rubbing action for higher d/r values. For the identical reasons, chip formation was favoured for higher d/r ratios when the depth of cut was kept constant. In contrast to the aforementioned studies, which consider a tool having a cutting edge and consequently a rake and clearance angle, Li et al. [60] considered a spherical cutting tool; in this case the term "tool radius" is indicative not only of the curvature of the tool tip but also of the amount of material removed. The latter one is the reason why the authors observed increased subsurface temperature values and higher values of the cutting forces as the tool radius increased and depth of cut remained constant.

Molecular Dynamics simulations have also been performed to optimise precision and nano-manufacturing processes. Xie and Fang [61] carried out a MD investigation focused on the effects of the tool rake angle and edge radius on atomic and close-to-atomic scale (ACS) manufacturing processes. In such small scales the depth of cut could be down to a single atomic layer and the tool geometry should be very carefully selected. Their results suggested that the precision of the process is dependent on the tool rake angle, the effective rake angle and the tool edge radius; more specifically, it was shown that single atomic layer removal in a copper workpiece can be enabled for effective rake-angles between $-70°$ and $-65°$, tool rake angles between $-17°$ and $-14°$ and tool edge radii lower than 2 nm. In a similar study [62], the authors advocated that chip formation is driven by dislocation movement at the top layers of the workpiece and identified 3 main deformation zones at the cutting area, namely: (I) the dislocation slip zone, (II) chip formation zone and (III) the elastic deformation zone. The slip dislocation zone contains workpiece atoms at the front of the cutting tool located at the top layers of the workpiece. These atoms will either be transformed into chip (chip formation zone) or compressed into the elastic deformation zone as shown in Fig. 3.
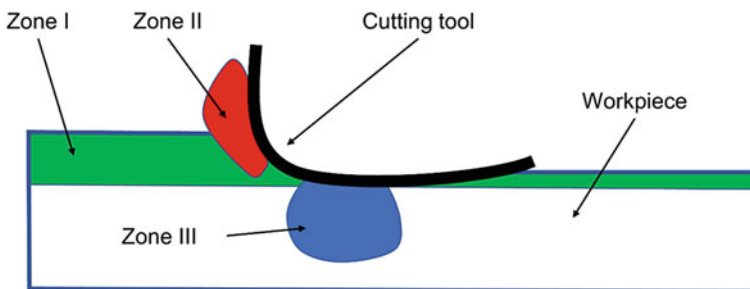
Fig. 3 Deformation zones in ACS nanocutting

Additional MD investigations supporting the fact that the workpiece material and tool geometry in combination with other process parameters, such as the depth of cut and the cutting speed, might significantly affect heat dissipation at the workpiece subsurface, chip formation, specific energy and tool wear can be found in literature [63–67].

3.2 Cutting Forces

One of the most common process features measured and monitored in Molecular Dynamics simulations of nanocutting processes is the evolution of the cutting forces as well as their average magnitude over the cutting duration. Cutting forces are usually categorised as (a) tangential (F_x), (b) normal (F_y) and transverse (F_z) as shown in Fig. 4. They are usually calculated by summing up the per atom forces exerted on the tool atoms while the force acting on an individual atom is obtained by summing the forces contributed by the surrounding atoms [68]. In the majority of MD investigations, the transverse force (F_z) fluctuates around zero due to symmetry and consequently the corresponding data are often not presented.

Proper selection of interatomic potentials is vital for the accurate estimation of the cutting forces. In a typical nanocutting MD simulation there are three types of atomic interactions, namely: (a) tool-tool, (b) tool-workpiece and (c) workpiece-workpiece [69]. Furthermore, a wide variety of potentials has been used to compute the interactions between atoms from the tool or the workpiece depending on the tool and workpiece materials chosen. The most common potentials used in such simulations are the Tersoff [70], Embedded Atom Method (EAM) [71] and Morse [72] potentials. In some early studies, Ikawa et al. [73] and Shimada et al. [74–76] investigated the nanocutting of a copper workpiece by a diamond tool. These studies demonstrated the effect of the edge radius and minimum depth of cut on
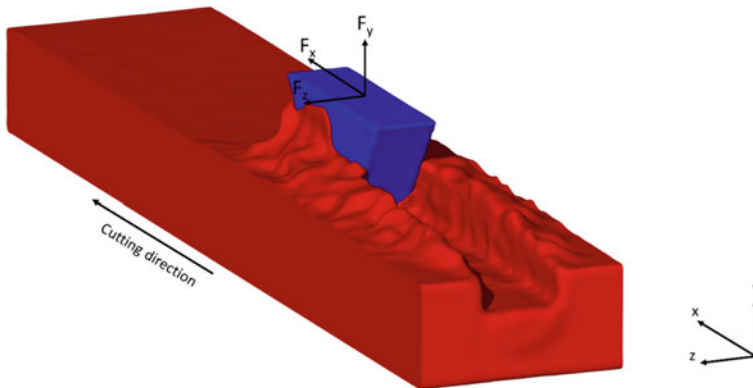
Fig. 4 Cutting forces

the chip formation process, subsurface deformation and specific cutting energy. The aforementioned features of the process were found to be inherently related to the cutting forces. Furthermore, according to Lin et al. [77], the large oscillations of cutting forces (tangential and normal) during nanocutting are related to the generation of dislocations. In a similar study, Zhu et al. [78] found that the cutting force variation follows a pattern similar to the number variation of elastic displaced atoms in the workpiece. Cutting forces have also been found to be affected by the grains' contact stiffness [79], the tool geometry [17, 80], the workpiece material and crystalline structure [81, 82], the depth of cut and cutting speed [68] as well as the crystal orientation of the workpiece material [83]. Finally, according to [79], the magnitude of the cutting forces can be indicative of the subsurface temperature; the higher the cutting forces the higher the subsurface temperature and the more dominant the thermal softening phenomenon at the cutting area.

3.3 Friction Coefficient

The friction force between the workpiece and cutting tool can significantly affect the magnitude of the cutting forces during nanocutting. The friction coefficient η is defined as the instantaneous ratio of the tangential to the normal forces ($\eta = F_x/F_y$) and its value is dependent on a number of process features including the depth of cut, the type of interface between the workpiece and the cutting tool and the cutting speed as it will be discussed in the following paragraphs. In contrast to experimental investigations of material removal, where the friction coefficient ranges between 0.4 and 0.7 [84, 85], much higher values have been reported in MD studies [17, 79, 86]. This is attributed to the material pile-up at the front of the cutting tool which plays an important role in atomistic simulations and induces an additional resistance in the motion of the tool, which in turn increases the value of the friction coefficient [87].

Pioneering Molecular Dynamics investigations [88–92] dealt with energy dissipation and atomic scale friction between hydrogen-terminated diamond surfaces sliding on top of each other. It has been observed that the friction coefficient is dependent on the normal load and crystallographic orientation whereas independent of the sliding velocity for the examined ranges (>0.5 Å/ps), which were much higher than experimental values; this result was in agreement with corresponding experimental results [93]. A Finite Element Modelling (FEM) investigation [94] has shown that in contrast to sliding, in the case of ploughing/cutting the friction coefficient appears to be dependent on the cutting speed and the depth of cut. Similar results have been obtained by MD simulations which have shown that the friction coefficient increases with the depth of cut [17]. However, according to another MD study focusing on indentation/sliding, it was observed that the friction coefficient appeared to be insensitive to the depth of cut but strongly dependent on the rake angle of the tool [95].

Another topic that has been investigated via means of MD simulations is the effect of lubricants on the cutting forces and the friction between the workpiece and the cutting tool. According to [96] although both of the cutting forces increase under

the presence of a lubricant, the friction coefficient decreases as the increase in the normal force is proportionally higher compared to the increment of the tangential component. Similar results have been obtained in [97]. The increase of the cutting forces under the presence of the lubricant has been attributed to the fact that a layer of lubricant atoms is accumulated on the surface of the cutting tool. Moreover, it has to be noted that according to [98] lubricants act as a heat sink while their presence does not favour heat dissipation in the workpiece; as a consequence, thermal softening is hindered and this might be another potential cause of the intensification of the cutting forces.

3.4 Contact Stiffness

One of the most important nanocutting parameters affecting the cutting forces and consequently the subsurface temperature and friction coefficient in nanocutting processes is the depth of cut. In reality, abrasive grains are not fixed in space but attached to their positions with the help of a binder (usually ceramic or resin) as illustrated in Fig. 5. Therefore, during grinding, the binder material might get deformed or even the wheel might exhibit some stiffness; consequently, the real depth of cut is always less than its programmed value [99].

Shimizu et al. [100, 101] performed 2-dimensional MD simulations to investigate the effects of the grinding wheel stiffness on the cutting forces, friction coefficient and depth of cut. They considered an abrasive grain moving with a constant speed and attached to springs in the cutting and normal directions. Their results revealed that the cutting forces as well as the depth of cut followed a specific pattern over time, i.e. gradual and approximately linear increase followed by a sharp decrease in value. This behaviour was indicative of the stick–slip phenomenon [102] and was more pronounced for low values of the spring constants. In a recent study, Papanikolaou et al. [79] performed 3-dimensional MD simulations to investigate contact stiffness effects on nanocutting. Since the grinding speeds in this study were set above 100 m/s

Fig. 5 Schematic illustration of grinding wheel composition
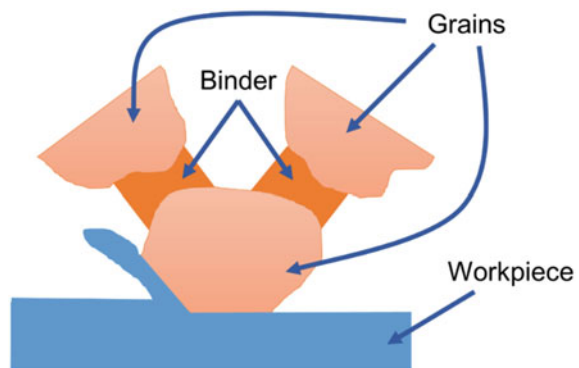
Fig. 6 Resultant spring
constant k_g

$$k_g = \sum_{i=1}^{N_s} k_i$$
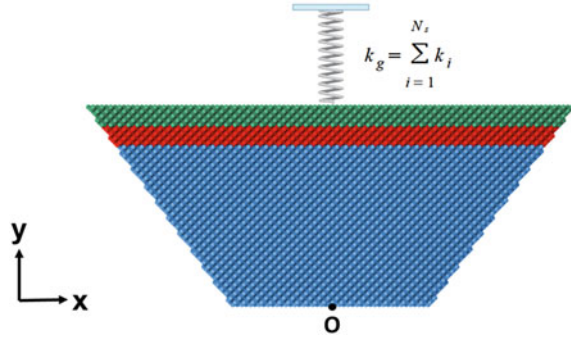
the stick slip phenomenon was not expected to be dominant and the top (N_s) abrasive atoms were attached to their initial positions using parallel springs, with an individual spring constant k_i, being applied only to the normal grinding direction as shown in Fig. 6. It was shown that the average depth of cut and consequently the cutting forces increase asymptotically with the resultant spring constant. The magnitude of the cutting forces is indicative of the workpiece subsurface temperature and vice versa; this interrelation leads to a non-monotonic behaviour of the cutting forces as a function of the spring constant for high grinding speeds ($v_g = 200, 300$ m/s). More specifically, this behaviour was attributed to the superposition of two contradicting phenomena, i.e. higher spring constants lead to (a) increased depths of cut and thus cutting forces and (b) local temperature rise at the cutting region which contributes to thermal softening and degradation of the mechanical properties of the workpiece material. For the exact same reasons, the vibrations transmitted to the abrasive grains (and consequently the ground surface roughness) were found to decrease for higher spring stiffness values and grinding speeds.

3.5 Surface Roughness

Surface roughness has been investigated both as an input and output of typical MD nanocutting models. More specifically, researchers have focused on the effects of various process parameters on the surface roughness of the ground workpiece and at the effects of rough tool-workpiece interfaces on the subsurface temperature, cutting forces and friction coefficient. Back in 1997, Isono and Tanaka [103] performed 3-dimensional MD simulations to examine the effects of the interaction potential (Morse) parameters and the temperature on the surface roughness of the ground workpiece which was quantified by the ratio of side flow to undeformed chip thickness (η):

$$\eta = \frac{\sum_{i=1}^{n} \frac{h_{max}}{\delta}}{n}, n = 10 \tag{14}$$

where h_{max} the maximum height of the side flow, δ the depth of cut and n the number of measurements. The authors advocated that surface roughness increases for higher values of the equilibrium distance between the workpiece and tool atoms and decreases with the adhesion energy and the parameter α, which is indicative of the potential width. Temperature appeared to have an adverse effect on surface roughness; the higher the temperature the higher the value of η. According to Li et al. [104], the crystal orientation of the workpiece as well as the rake angle of the cutting tool and the depth of cut play an important role in the surface roughness of the machined workpiece. More specifically, the smoothest machined surface could be obtained for a very low depth of cut, a rake angle of 30° and a crystal orientation of (100) for the cerium workpiece.

Molecular Dynamics simulations have also been performed to investigate the effects of rough tool-workpiece interfaces on the cutting process features, i.e. cutting forces, friction coefficient and subsurface temperature. Li et al. [105] considered a copper workpiece with a rough top surface. Surface roughness was modelled using orthogonal asperities whose morphology was dictated by the texture density $\rho = R_x/R_0$, with R_x being the width of a single asperity and R_0 the distance separating two subsequent asperities. Both cutting forces and friction coefficient exhibited an increasing trend with texture density. In another study, Dai et al. [80] employed a nanostructured diamond tool with grooves having various directions, depths, widths, factors and shapes to investigate their effects on nanocutting. They concluded that a groove orientation of 60° should minimise the cutting forces while grooves with small widths lead to enhanced removal rate but increased cutting forces and subsurface temperature, as expected. Finally, the number of chip atoms was found to be larger for V-shaped grooves, leading to enhanced removal rate. In contrast to the previous studies, where patterned geometries were used to model rough surfaces, Papanikolaou et al. [17] employed the multivariate Weierstrass-Mandelbrot function [106] to generate stochastically rough workpiece (top) and tool (bottom) surfaces. According to [107] the surface of the majority of materials can be modelled with fractal profiles having a fractal dimension in the range of $2 \leq D_s \leq 3$. The generated surfaces' irregularity was tuned by controlling the value of the fractal dimension as illustrated in Fig. 7. The obtained results indicated that the upper workpiece surface does not significantly affect the mechanics of the process in contrast to the lower tool surface which dictates the interface type between the two solid components (workpiece and abrasive grain). The cutting forces, friction coefficient and workpiece subsurface temperature increased with the depth of cut for both smooth and rough interface conditions. The rough interface between the workpiece and the abrasive also led to increased heat dissipation at the workpiece subsurface. Finally, it was proposed that the lower tool surface should have the lowest fractal dimension possible in order to decrease the cutting forces and the energy efficiency of the process.
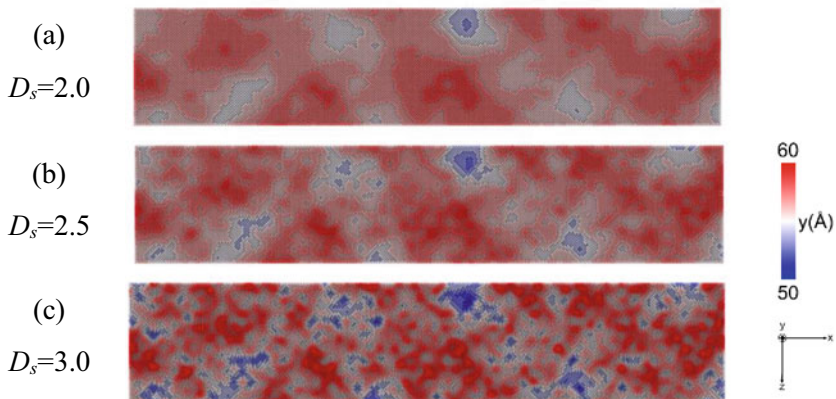
Fig. 7 Representation of the effect of fractal dimension D_s on atomic surface profiles

3.6 Subsurface Temperature

The workpiece subsurface temperature is a key parameter in nanocutting processes, influencing material removal rates, machined surface quality, nanocutting forces, chip formation and dislocations/stress [99]. In contrast to FEA models which employ thermal models in order to estimate the workpiece temperature [108, 109], MD simulations do not rely on constitutive relations while the temperature of a group of N atoms can be calculated using the virial theorem [110] as follows:

$$\left\langle \sum_{i=1}^{N} |\mathbf{p}_i|^2 / m_i \right\rangle = 2\langle K \rangle = 3Nk_BT \tag{15}$$

where $\boldsymbol{p}_i$ and m_i the momentum and mass of the atom i, k_B the Boltzmann's constant and T the temperature.

Fang et al. [111] performed 3-dimensional MD simulations to investigate, among other process parameters, the effects of the workpiece temperature on nano-scratching and nano-indentation of gold and platinum films. Their model consisted of a diamond indenter mounted on horizontal and vertical springs while the cutting speed was set to 250 m/s. Their results indicated that the film temperature significantly affects the wear depth which appeared to asymptotically increase with the film temperature as the applied loads were maintained constant. The authors attributed this behaviour to the increased kinetic energy of the film atoms. Cai et al. [112] developed a 3-dimensional MD model to study the temperature and stress distribution over the a silicon workpiece during nanocutting. They monitored principal and shear stresses as well as the temperature in three deformation zones lying at the vicinity of a cutting tool and observed that the evolution of temperature and stress over time follows similar patterns, i.e. stress and temperature reach their peak values

at identical timesteps. The authors also advocated that the high temperature observed at the cutting region may adversely affect the hardness of the diamond tool via the formation of carbon oxides and consequently reduce the tool life. Guo and Liang [113] focused on the temperature distribution during nanocutting of a monocrystalline copper workpiece. They found that the temperature distribution follows an approximately concentric profile while the higher temperature values were observed at the chip region; similar temperature profiles were obtained by Lin et al. [114]. In a recent study, Papanikolaou et al. [86] focused on the effects of the workpiece temperature on nanocutting. They concluded that the workpiece temperature significantly affects the cutting forces as well as stress distribution over the workpiece. More specifically, the steep reduction of the cutting forces for increased initial workpiece temperatures as well as the obtained Von-Mises stress profiles emphasised the effect of the thermal softening phenomenon. Subsurface temperature is inherently linked to the stress distribution at the workpiece as it will be further elaborated within the following section. Finally, it was also shown that the response of the workpiece material in temperature changes becomes slower for higher workpiece temperatures; this phenomenon was attributed to the drop of thermal conductivity with temperature and leads to slower heat dissipation.

3.7 Stresses and Dislocations

Stress profiles at the shear zone provide a great deal of information on the nanocutting mechanics. Among the various types of stresses, including principal, shear and hydrostatic, Von Mises stresses have been extensively used in MD simulations to describe the stress distribution in the shear zone. Experimental studies [115] have shown that compressive and tensile stresses arising during material removal are inherently linked to the nucleation and propagation of dislocations. In one of the early studies focused on dislocation propagation during nanocutting, Pei et al. [68] showed that the nucleation and propagation of dislocations is strongly dependent on a number of process parameters including the depth of cut, cutting speed and the lattice orientation of the workpiece. Wang et al. [116] performed 3-dimensional MD simulations on nanocutting and observed the stress and dislocation distribution across a copper workpiece during material removal. They advocated that the formation of Stacking Fault Tetrahedra (SFT) is stressed induced; tensile and compressive stresses were found to be responsible for the nucleation and propagation of stacking faults and screw dislocations respectively. In a recent study, Hao et al. [117] demonstrated that the heat generated in the workpiece during the nanocutting process affects the magnitude of principal, shear and Von Mises stresses and suggested that the higher the subsurface temperature the lower the stresses at the cutting region. These results are in agreement with [86] where the Von Mises stress distribution was found to be significantly affected by the workpiece temperature due to thermal softening of the workpiece material. As illustrated in Fig. 8 there is high stress concentration at the cutting region when the workpiece temperature T_w is relatively low (Fig. 8a)
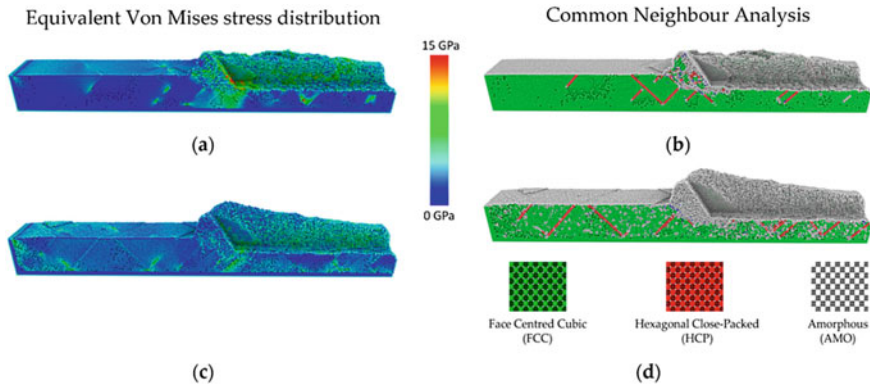
Fig. 8 Evolution of Von Mises distribution and common neighbour analysis for two workpiece temperature values: **a, b** $T_w = 300$ K and **c, d** $T_w = 900$ K [86]

whereas stress distribution is more uniform across the workpiece for higher workpiece temperatures (Fig. 8b). By comparing the results of the Common Neighbour Analysis (CNA) with the corresponding stress distribution profiles, it can be observed that there is high concentration at the vicinity of lattice dislocations as expected.

The aforementioned MD studies consider the case of a monocrystalline workpiece. However, this is an assumption that does not hold in reality; metals are polycrystalline. Contemporary MD studies have also focused on the stress distribution and dislocation propagation in polycrystalline materials as well. Shi et al. [81] considered the case of a polycrystalline workpiece made of copper; the polycrystalline workpiece structures were generated using the Voronoi site-rotation and cut package of the AtomEye software [118]. The obtained equivalent stress distribution profiles during nanocutting revealed that there is high stress concentration in the primary and secondary shear zones. Moreover, it was shown that equivalent stresses at the grain boundaries are 30–60% higher than at the core of the grains. In a similar study, Liu et al. [82] performed 3-dimensional MD simulations on the nanocutting of a polycrystalline silicon carbide workpiece. They advocated that tangential stresses exhibit a strong dependence on the grain structure; they obtain higher values when the subsurface structure is polycrystalline due to the fact that there is high stress concentration at the grain boundaries. On the contrary, normal forces were found to be insensitive to the workpiece grain structure. In a recent study, Papanikolaou and Salonitis [24] monitored stress distribution and dislocation evolution during nanocutting of monocrystalline and polycrystalline Aluminium workpieces with various average grain diameters (4.49, 2.58 and 1.98 nm); these were prepared by solidifying Aluminium melt under various cooling rates. The obtained equivalent stress distribution profiles revealed high stress concentration at the shear zone, the vicinity of the lattice dislocations and at the grain boundaries as shown in Fig. 9; this was in agreement with previous studies [81, 86]. The dislocation types distribution was evaluated before and after nanocutting at the uncut region of the workpiece and it was
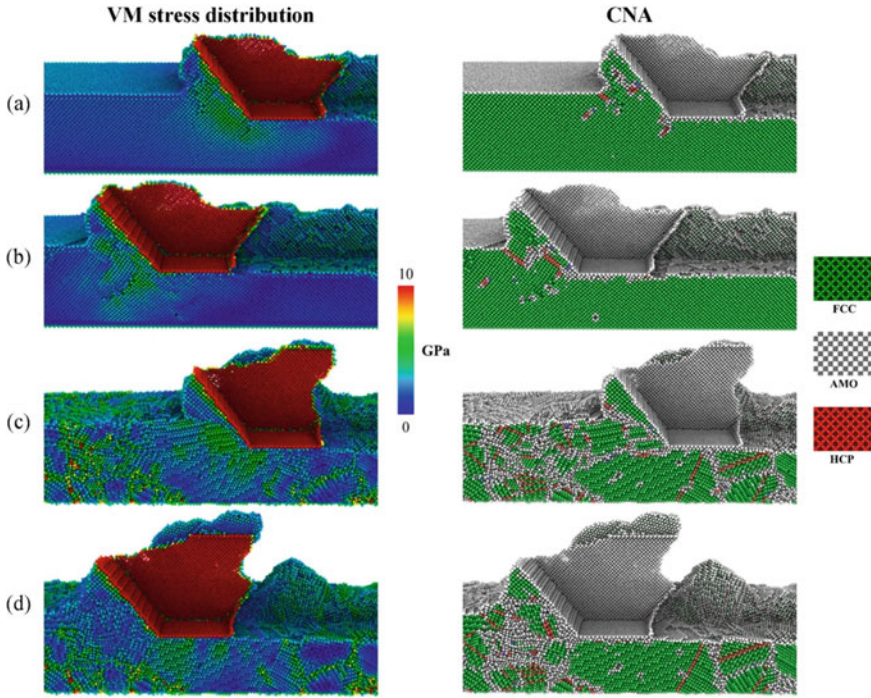
Fig. 9 Monocrystalline (**a** & **b**) and polycrystalline with dg,ave = 1.98 nm (**c** & **d**) workpiece VM stress profiles and CNA at t = 400 ps (**a** & **c**) and (**b**) 480 ps (**b** & **d**). [FCC: Face Centred Cubic, AMO: amorphous, HCP: Hexagonal Close Packed] [24]

suggested that Shockley dislocations are prevalent among the other types (Perfect, Stair-rod, Hirth and Frank). Finally, it was shown that the residual stresses at the grain boundaries, owing to solidification, can be partially relieved after the pass of the cutting tool due to the elevated temperature at the cutting region; this phenomenon resembles heat treatment.

4   Summary

The rapid evolution of the computational power over the past few decades has allowed for the numerical modelling of nanocutting processes using 3-dimensional Molecular Dynamics simulations. This atomistic computational technique has been proven to be effective for capturing nanoscale phenomena and features, such as dislocation generation, stress and temperature distribution in the subsurface and microstructure evolution occuring during material removal, which cannot be easily observed using experimental techniques. Although the results of Molecular Dynamics simulations are highly dependent on the accuracy of the selected interatomic potentials, they have

been found to be in good agreement in with experimental ones, with respect to the evaluation of cutting forces, friction factor and subsurface temperature. Molecular Dynamics simulations appear to be a very promising numerical modelling technique especially when considering that computational power will further increase in the future and more accurate interatomic potentials will be proposed. Finally, a significant challenge for the future will be the development of multiscale models of material removal processes being capable of feeding information from a Molecular Dynamics simulator to a FEM solver and vice versa.

References

1. Brinksmeier E, Aurich J, Govekar E et al (2006) Advances in modeling and simulation of grinding processes. CIRP Ann Technol 55:667–696
2. Li H, Yu T, Zhu L, Wang W (2015) Analysis of loads on grinding wheel binder in grinding process: insights from discontinuum-hypothesis-based grinding simulation. Int J Adv Manuf Technol 78:1943–1960. https://doi.org/10.1007/s00170-014-6767-6
3. Osa JL, Sánchez JA, Ortega N et al (2016) Discrete-element modelling of the grinding contact length combining the wheel-body structure and the surface-topography models. Int J Mach Tools Manuf 110:43–54. https://doi.org/10.1016/J.IJMACHTOOLS.2016.07.004
4. Alder B, Wainwright T (1959) Studies in molecular dynamics. I. General method. J Chem Phys 31:459
5. Payne MC, Teter MP, Allan DC et al (1992) Iterative minimization techniques for ab initio total-energy calculations: molecular dynamics and conjugate gradients. Rev Mod Phys 64:1045–1097. https://doi.org/10.1103/RevModPhys.64.1045
6. Brooks BR, Bruccoleri RE, Olafson BD, States DJ, Swaminathan SA, Karplus M (1983) CHARMM: a program for macromolecular energy, minimization, and dynamics calculations. J Comput Chem 4(2):187–217
7. Mayo SL, Olafson BD, Goddard WA (1990) DREIDING: a generic force field for molecular simulations. J Phys Chem 94(26):8897–8909
8. Wang J, Wolf R, Caldwell JW, Kollman PA, Case DA (2004) Development and testing of a general amber force field. J Comput Chem 25(9):1157–1174
9. Rappé AK, Casewit CJ, Colwell KS, Goddard III WA, Skiff WM (1992) UFF, a full periodic table force field for molecular mechanics and molecular dynamics simulations. J Am Chem Soc 114(25):10024–10035
10. Ashurst WT, Hoover WG (1973) Argon shear viscosity via a lennard-jones potential with equilibrium and nonequilibrium molecular dynamics. Phys Rev Lett 31:206–208. https://doi.org/10.1103/PhysRevLett.31.206
11. Mark P, Nilsson L (2001) Structure and dynamics of the TIP3P, SPC, and SPC/E water models at 298 K. J Phys Chem a 105:9954–9960. https://doi.org/10.1021/jp003020w
12. Daw MS, Baskes MI (1984) Embedded-atom method: derivation and application to impurities, surfaces, and other defects in metals. Phys Rev B 29:6443–6453. https://doi.org/10.1103/PhysRevB.29.6443
13. Angelo J, Baskes M (1997) Interfacial studies using the EAM and MEAM. Interface Sci 4. https://doi.org/10.1007/BF00200838
14. Brenner DW (1990) Empirical potential for hydrocarbons for use in simulating the chemical vapor deposition of diamond films. Phys Rev B 42:9458–9471. https://doi.org/10.1103/PhysRevB.42.9458
15. Root D, Landis C, Cleveland T (1993) Valence bond concepts applied to the molecular mechanics description of molecular shapes. 1. Application to nonhypervalent molecules of the P-block. J Am Chem Soc 115(10):4201–4209

16. Van Duin ACT, Dasgupta S, Lorant F, et al (2001) ReaxFF: a reactive force field for hydrocarbons. J Phys Chem 105:9396–9409
17. Papanikolaou M, Salonitis K (2019) Fractal roughness effects on nanoscale grinding. Appl Surf Sci 467–468:309–319. https://doi.org/10.1016/J.APSUSC.2018.10.144
18. Wang Q, Bai Q, Chen J et al (2015) Subsurface defects structural evolution in nano-cutting of single crystal copper. Appl Surf Sci 344:38–46. https://doi.org/10.1016/j.apsusc.2015.03.061
19. Narulkar R, Bukkapatnam S, Raff LM, Komanduri R (2009) Graphitization as a precursor to wear of diamond in machining pure iron: a molecular dynamics investigation. Comput Mater Sci 45:358–366. https://doi.org/10.1016/j.commatsci.2008.10.007
20. Eder S, Cihak-Bayr U, Pauschitz A (2015) Nanotribological simulations of multi-grit polishing and grinding. Wear 340–341:25–30. https://doi.org/10.1016/J.WEAR.2015.03.006
21. Guo X, Li Q, Liu T et al (2016) Molecular dynamics study on the thickness of damage layer in multiple grinding of monocrystalline silicon. Mater Sci Semicond Process 51:15–19. https://doi.org/10.1016/J.MSSP.2016.04.013
22. Li J, Fang Q, Zhang L, Liu Y (2015) Subsurface damage mechanism of high speed grinding process in single crystal silicon revealed by atomistic simulations. Appl Surf Sci 324:464–474
23. Xu F, Fang F, Zhu Y, Zhang X (2017) Study on crystallographic orientation effect on surface generation of aluminum in nano-cutting. Nanoscale Res Lett 12:289. https://doi.org/10.1186/s11671-017-1990-3
24. Papanikolaou M, Salonitis K (2020) Grain size effects on nanocutting behaviour modelling based on molecular dynamics simulations. Appl Surf Sci 148291. https://doi.org/10.1016/j.apsusc.2020.148291
25. Zhou L, Huang H (2004) Are surfaces elastically softer or stiffer? Appl Phys Lett
26. Markopoulos AP, Kalteremidou KAL (2014) Molecular dynamics modelling of nanometric cutting. In: Key engineering materials, pp 298–303. Trans Tech Publications Ltd
27. Lennard-Jones JE (1931) Cohesion. Proc Phys Soc 43:461
28. Oluwajobi A, Chen X (2011) The effect of interatomic potentials on the molecular dynamics simulation of nanometric machining. Int J Autom Comput 8:326–332. https://doi.org/10.1007/s11633-011-0588-y
29. Finnis MW, Sinclair JE (1984) A simple empirical N-body potential for transition metals. Philos Mag A 50:45–55
30. Baskes MI (1992) Modified embedded-atom potentials for cubic materials and impurities. Phys Rev B 46:2727–2742. https://doi.org/10.1103/PhysRevB.46.2727
31. Vella JR, Stillinger FH, Panagiotopoulos AZ, Debenedetti PG (2015) A comparison of the predictive capabilities of the embedded-atom method and modified embedded-atom method potentials for lithium. J Phys Chem B 119:8960–8968. https://doi.org/10.1021/jp5077752
32. Fang FZ, Wu H, Zhou W, Hu XT (2007) A study on mechanism of nano-cutting single crystal silicon. J Mater Process Technol 184:407–410. https://doi.org/10.1016/j.jmatprotec.2006.12.007
33. Zhang P, Zhao H, Zhang L et al (2014) A study on material removal caused by phase transformation of monocrystalline silicon during nanocutting process via molecular dynamics simulation. J Comput Theor Nanosci 11:291–296. https://doi.org/10.1166/jctn.2014.3350
34. Tersoff J (1989) Modeling solid-state chemistry: interatomic potentials for multicomponent systems. Phys Rev B 39:5566–5568. https://doi.org/10.1103/PhysRevB.39.5566
35. Alhafez IA, Urbassek HM (2020) Influence of the rake angle on nanocutting of Fe single crystals: a molecular-dynamics study. Crystals 10:516. https://doi.org/10.3390/cryst10060516
36. Zhao H, Shi C, Zhang P et al (2012) Research on the effects of machining-induced subsurface damages on mono-crystalline silicon via molecular dynamics simulation. Appl Surf Sci 259:66–71. https://doi.org/10.1016/j.apsusc.2012.06.087
37. Girifalco LA, Weizer VG (1959) Application of the morse potential function to cubic metals. Phys Rev 114:687–690. https://doi.org/10.1103/PhysRev.114.687
38. Inamura T, Takezawa N, Taniguchi N (1992) Atomic-scale cutting in a computer using crystal models of copper and diamond. CIRP Ann 41:121–124. https://doi.org/10.1016/S0007-8506(07)61166-4

39. Banerjee S, Naha S, Puri IK (2008) Molecular simulation of the carbon nanotube growth mode during catalytic synthesis. Appl Phys Lett 92:233121. https://doi.org/10.1063/1.2945798
40. Verlet L (1968) Computer "experiments" on classical fluids. II. equilibrium correlation functions. Phys Rev 165:201–214. https://doi.org/10.1103/PhysRev.165.201
41. Allen MP, Tildesley DJ (1989) Computer simulation of liquids. Clarendon Press
42. Karkalos E, Markopoulos NP (2017) A Modeling nano-metric manufacturing processes with molecular dynamics method: a review. Current Nanosci
43. Liu Q, Roy A, Tamura S et al (2016) Micro-cutting of single-crystal metal: finite-element analysis of deformation and material removal. Int J Mech Sci 118:135–143. https://doi.org/10.1016/j.ijmecsci.2016.09.021
44. Tajalli SA, Movahhedy MR, Akbari J (2014) Simulation of orthogonal micro-cutting of FCC materials based on rate-dependent crystal plasticity finite element model. Comput Mater Sci 86:79–87. https://doi.org/10.1016/j.commatsci.2014.01.016
45. Lee WB, Wang H, Chan CY, To S (2013) Finite element modelling of shear angle and cutting force variation induced by material anisotropy in ultra-precision diamond turning. Int J Mach Tools Manuf 75:82–86. https://doi.org/10.1016/j.ijmachtools.2013.09.007
46. Dong Y, Si F, Jin W et al (2020) A new mechanistic model for abrasive erosion using discrete element method. Powder Technol. https://doi.org/10.1016/j.powtec.2020.11.017
47. Zhao Y, Ma H, Xu L, Zheng J (2017) An erosion model for the discrete element method. Particuology 34:81–88. https://doi.org/10.1016/j.partic.2016.12.005
48. Peng R, Tong J, Tang X et al (2020) Crack propagation and wear estimation of ceramic tool in cutting inconel 718 based on discrete element method. Tribol Int 142:105998. https://doi.org/10.1016/j.triboint.2019.105998
49. Stowers FI (1991) Molecular dynamics simulation of the chip formation process in single crystal copper and comparison with experimental data. ASPE Annu Meet Oct 100
50. Fang FZ, Wu H, Liu YC (2005). Modelling and experimental investigation on nanometric cutting of monocrystalline silicon. https://doi.org/10.1016/j.ijmachtools.2005.03.010
51. Inamura T, Shimada S, Takezawa N, Nakahara N (1997) Brittle/ductile transition phenomena observed in computer simulations of machining defect-free monocrystalline silicon. CIRP Ann Manuf Technol 46:31–34. https://doi.org/10.1016/s0007-8506(07)60769-0
52. Han XS, Lin B, Yu SY, Wang SX (2002) Investigation of tool geometry in nanometric cutting by molecular dynamics simulation. J Mater Process Technol 129:105–108
53. Komanduri R, Chandrasekaran N, Raff LM (2001) MD simulation of exit failure in nanometric cutting. Mater Sci Eng A 311:1–12. https://doi.org/10.1016/S0921-5093(01)00960-1
54. Pekelharing AJ (1984) The exit failure of cemented carbide face milling cutters part I—fundamentals and phenomenae. CIRP Ann 33:47–50
55. Liu K, Li XP, Liang SY (2007) The mechanism of ductile chip formation in cutting of brittle materials. Int J Adv Manuf Technol 33:875–884
56. Cai MB, Li XP, Rahman M (2007) Study of the mechanism of nanoscale ductile mode cutting of silicon using molecular dynamics simulation. Int J Mach Tools Manuf 47:75–80. https://doi.org/10.1016/j.ijmachtools.2006.02.016
57. Komanduri R, Chandrasekaran N, Raff LM (1999) Some aspects of machining with negative-rake tools simulating grinding: a molecular dynamics simulation approach. Philos Mag B Phys Condens Matter Stat Mech Electr Opt Magn Prop 79:955–968. https://doi.org/10.1080/13642819908214852
58. Crawford JH, Merchant ME (1953) The influence of higher rake angles on performance in milling. Trans ASME 75:561–566
59. Komanduri R, Chandrasekaran N, Raff LM (1998) Effect of tool geometry in nanometric cutting: a molecular dynamics simulation approach. Wear 219:84–97. https://doi.org/10.1016/S0043-1648(98)00229-4
60. Li J, Fang Q, Liu Y, Zhang L (2014) A molecular dynamics investigation into the mechanisms of subsurface damage and material removal of monocrystalline copper subjected to nanoscale high speed grinding. Appl Surf Sci 303:331–343. https://doi.org/10.1016/j.apsusc.2014.02.178

61. Xie W, Fang F (2020) Mechanism of atomic and close-to-atomic scale cutting of monocrystalline copper. Appl Surf Sci 503:144239. https://doi.org/10.1016/j.apsusc.2019.144239

62. Xie W, Fang F (2020) Rake angle effect in cutting-based single atomic layer removal. J Manuf Process 56:280–294. https://doi.org/10.1016/j.jmapro.2020.04.068

63. Komanduri R, Lee M, Raff LM (2004) The significance of normal rake in oblique machining. Int J Mach Tools Manuf 44:1115–1124. https://doi.org/10.1016/j.ijmachtools.2004.02.015

64. Biddut AQ, Rahman M, Neo KS et al (2007) Performance of single crystal diamond tools with different rake angles during micro-grooving on electroless nickel plated die materials. Int J Adv Manuf Technol 33:891–899. https://doi.org/10.1007/s00170-006-0535-1

65. Karkalos NE, Markopoulos AP, Kundrák J (2017) Molecular dynamics model of nano-metric peripheral grinding. In: Procedia CIRP

66. Fang TH, Weng CI (2000) Three-dimensional molecular dynamics analysis of processing using a pin tool on the atomic scale. Nanotechnology 11:148–153. https://doi.org/10.1088/0957-4484/11/3/302

67. Avila KE, Vardanyan VH, Alabd Alhafez I et al (2020) Applicability of cutting theory to nanocutting of metallic glasses: atomistic simulation. J Non Cryst Solids 550:120363. https://doi.org/10.1016/j.jnoncrysol.2020.120363

68. Pei QX, Lu C, Lee HP (2007) Large scale molecular dynamics study of nanometric machining of copper. Comput Mater Sci 41:177–185. https://doi.org/10.1016/J.COMMATSCI.2007.04.008

69. Goel S, Luo X, Agrawal A, Reuben RL (2015) Diamond machining of silicon: a review of advances in molecular dynamics simulation. Int J Mach Tools Manuf 88:131–164. https://doi.org/10.1016/J.IJMACHTOOLS.2014.09.013

70. Wang J, Zhang X, Fang F (2016) Molecular dynamics study on nanometric cutting of ion implanted silicon. Comput Mater Sci 117:240–250. https://doi.org/10.1016/j.commatsci.2016.01.040

71. Ren J, Hao M, Lv M et al (2018) Molecular dynamics research on ultra-high-speed grinding mechanism of monocrystalline nickel. Appl Surf Sci 455:629–634. https://doi.org/10.1016/j.apsusc.2018.06.042

72. He Y, Lai M, Fang F (2019) A numerical study on nanometric cutting mechanism of lutetium oxide single crystal. Appl Surf Sci 496:143715. https://doi.org/10.1016/j.apsusc.2019.143715

73. Ikawa N, Donaldson RR, Komanduri R et al (1991) Ultraprecision metal cutting—the past, the present and the future. CIRP Ann Manuf Technol. https://doi.org/10.1016/S0007-8506(07)61134-2

74. Shimada S, Ikawa N (1992) Molecular dynamics analysis as compared with experimental results of micromachining. CIRP Ann Manuf Technol 41:117–120. https://doi.org/10.1016/S0007-8506(07)61165-2

75. Shimada S, Ikawa N, Tanaka H et al (1993) Feasibility study on ultimate accuracy in micro-cutting using molecular dynamics simulation. CIRP Ann Manuf Technol 42:91–94. https://doi.org/10.1016/S0007-8506(07)62399-3

76. Shimada S, Ikawa N, Tanaka H, Uchikoshi J (1994) Structure of micromachined surface simulated by molecular dynamics analysis. CIRP Ann Manuf Technol 43:51–54. https://doi.org/10.1016/S0007-8506(07)62162-3

77. Lin B, Yu SY, Wang SX (2003) An experimental study on molecular dynamics simulation in nanometer grinding. J Mater Process Technol 138:484–488. https://doi.org/10.1016/S0924-0136(03)00124-9

78. Zhu ZX, Gong YD, Zhou YG, Gao Q (2016) Molecular dynamics simulation of single crystal Nickel nanometric machining. Sci China Technol Sci 59:867–875. https://doi.org/10.1007/s11431-016-6061-y

79. Papanikolaou M, Salonitis K (2019) Contact stiffness effects on nanoscale high-speed grinding: a molecular dynamics approach. Appl Surf Sci 493:212–224

80. Dai H, Chen G, Li S et al (2017) Influence of laser nanostructured diamond tools on the cutting behavior of silicon by molecular dynamics simulation. RSC Adv 7:15596–15612. https://doi.org/10.1039/C6RA27070K

81. Shi J, Wang Y, Yang X (2013) Nano-scale machining of polycrystalline coppers—effects of grain size and machining parameters. Nanoscale Res Lett 8:1–18. https://doi.org/10.1186/1556-276X-8-500

82. Liu Y, Li B, Kong L (2018) A molecular dynamics investigation into nanoscale scratching mechanism of polycrystalline silicon carbide. Comput Mater Sci 148:76–86. https://doi.org/10.1016/j.commatsci.2018.02.038

83. Sharma A, Datta D, Balasubramaniam R (2018) Molecular dynamics simulation to investigate the orientation effects on nanoscale cutting of single crystal copper. Comput Mater Sci 153:241–250. https://doi.org/10.1016/j.commatsci.2018.07.002

84. Pan R, Zhong B, Chen D et al (2018) Modification of tool influence function of bonnet polishing based on interfacial friction coefficient. Int J Mach Tools Manuf 124:43–52. https://doi.org/10.1016/j.ijmachtools.2017.09.003

85. Zhang Y, Li C, Ji H et al (2017) Analysis of grinding mechanics and improved predictive force model based on material-removal and plastic-stacking mechanisms. Int J Mach Tools Manuf 122:81–97. https://doi.org/10.1016/j.ijmachtools.2017.06.002

86. Papanikolaou M, Hernandez FR, Salonitis K (2020) Investigation of the subsurface temperature effects on nanocutting processes via molecular dynamics simulations. Metals (Basel) 10:1220. https://doi.org/10.3390/met10091220

87. Zhu PZ, Hu YZ, Ma TB, Wang H (2010) Study of AFM-based nanometric cutting process using molecular dynamics. Appl Surf Sci 256:7160–7165. https://doi.org/10.1016/j.apsusc.2010.05.044

88. Harrison JA, White CT, Colton RJ, Brenner DW (1992) Molecular-dynamics simulations of atomic-scale friction of diamond surfaces. Phys Rev B 46:9700–9708. https://doi.org/10.1103/PhysRevB.46.9700

89. Harrison JA, Colton RJ, White CT, Brenner DW (1993) Effect of atomic-scale surface roughness on friction: a molecular dynamics study of diamond surfaces. Wear 168:127–133. https://doi.org/10.1016/0043-1648(93)90208-4

90. Harrison JA, White CT, Colton RJ, Brenner DW (1993) Atomistic simulations of friction at sliding diamond interfaces. MRS Bull 18:50–53. https://doi.org/10.1557/S0883769400047138

91. Harrison JA, White CT, Colton RJ, Brenner DW (1993) Effects of chemically-bound, flexible hydrocarbon species on the frictional properties of diamond surfaces. J Phys Chem 97:6573–6576. https://doi.org/10.1021/j100127a001

92. Harrison JA, White CT, Colton RJ, Brenner DW (1995) Investigation of the atomic-scale friction and energy dissipation in diamond using molecular dynamics. Thin Solid Films 260:205–211. https://doi.org/10.1016/0040-6090(94)06511-X

93. Johnson R, Swikert M, Bisson E (1947) Friction at high sliding velocities. Cleveland, Ohio

94. Anderson D, Warkentin A, Bauer R (2011) Experimental and numerical investigations of single abrasive-grain cutting. Int J Mach Tools Manuf 51:898–910

95. Komanduri R, Chandrasekaran N, Raff L (2000) Molecular dynamics simulation of atomic-scale friction. Phys Rev B Condens Matter Mater Phys 61:14007–14019. https://doi.org/10.1103/PhysRevB.61.14007

96. Lautenschlaeger MP, Stephan S, Urbassek HM et al (2017) Effects of lubrication on the friction in nanometric machining processes: a molecular dynamics approach. Appl Mech Mater 869:85–93. https://doi.org/10.4028/www.scientific.net/amm.869.85

97. Chen Y, Han H, Fang F, Hu X (2014) MD simulation of nanometric cutting of copper with and without water lubrication. Sci China Technol Sci 57:1154–1159. https://doi.org/10.1007/s11431-014-5519-z

98. Rentsch R, Inasaki I (2006) Effects of fluids on the surface generation in material removal processes—molecular dynamics simulation. CIRP Ann Manuf Technol 55:601–604. https://doi.org/10.1016/S0007-8506(07)60492-2

99. Rowe WB (2013) Principles of modern grinding technology. Elsevier Inc.

100. Shimizu J (2007) Molecular dynamics simulation of nano grinding-influence of tool stiffness. Int J Manuf Sci Technol 9:69

101. Shimizu J, Zhou L, Eda H (2008) Molecular dynamics simulation of effect of grinding wheel stiffness on nanogrinding process. Int J Abras Technol 1:316–326
102. Mate CM, McClelland GM, Erlandsson R, Chiang S (1987) Atomic-scale friction of a tungsten tip on a graphite surface. Springer, Dordrecht, pp 226–229
103. Isono Y, Tanaka T (1997) Three-dimensional molecular dynamics simulation of atomic scale precision processing using a pin tool. JSME Int J Ser a 40:211–218. https://doi.org/10.1299/jsmea.40.211
104. Li Y, Shuai M, Zhang J et al (2018) Molecular dynamics investigation of residual stress and surface roughness of cerium under diamond cutting. Micromachines 9:386. https://doi.org/10.3390/mi9080386
105. Li J, Fang Q, Zhang L, Liu Y (2015) The effect of rough surface on nanoscale high speed grinding by a molecular dynamics simulation. Comput Mater Sci 98:252–262. https://doi.org/10.1016/J.COMMATSCI.2014.10.069
106. Ausloos M, Berman DH (1985) A multivariate Weierstrass-Mandelbrot function. Proc R Soc London A Math Phys Sci 400:331–350
107. Avnir D, Farin D, Pfeifer P (1984) Molecular fractal surfaces. Nature 308:261–263. https://doi.org/10.1038/308261a0
108. Jaeger CJ (1942) Moving sources of heat and the temperature of sliding contacts. J Proc Roy Soc New South Wales 76:202
109. Outwater JO, Shaw CS (1952) Surface temperatures in grinding pdf. Trans ASME 74:73–86
110. Munster A (1974) Statistical thermodynamics. Springer-Verlag
111. Fang TH, Chang WJ, Weng CI (2006) Nanoindentation and nanomachining characteristics of gold and platinum thin films. Mater Sci Eng A 430:332–340. https://doi.org/10.1016/j.msea.2006.05.106
112. Cai MB, Li XP, Rahman M (2007) Study of the temperature and stress in nanoscale ductile mode cutting of silicon using molecular dynamics simulation. J Mater Process Technol 192–193:607–612. https://doi.org/10.1016/j.jmatprotec.2007.04.028
113. Guo YB, Liang YC (2012) Atomistic simulation of thermal effects and defect structures during nanomachining of copper. Trans Nonferrous Met Soc China English Ed 22:2762–2770. https://doi.org/10.1016/S1003-6326(11)61530-6
114. Lin ZC, Lin MH, Hsu YC (2014) Simulation of temperature field during nanoscale orthogonal cutting of single-crystal silicon by molecular statics method. Comput Mater Sci 81:58–67. https://doi.org/10.1016/j.commatsci.2013.07.018
115. Zhao X, Bhushan B (1998) Material removal mechanisms of single-crystal silicon on nanoscale and at ultralow loads. Wear 223:66–78. https://doi.org/10.1016/S0043-1648(98)00302-0
116. Wang Q, Bai Q, Chen J et al (2015) Stress-induced formation mechanism of stacking fault tetrahedra in nano-cutting of single crystal copper. Appl Surf Sci 355:1153–1160. https://doi.org/10.1016/j.apsusc.2015.06.176
117. Hao ZP, Cui RR, Fan YH, Lin JQ (2019) Diffusion mechanism of tools and simulation in nanoscale cutting the Ni–Fe–Cr series of Nickel-based superalloy. Int J Mech Sci 150:625–636. https://doi.org/10.1016/j.ijmecsci.2018.10.058
118. Li J (2003) AtomEye: an efficient atomistic configuration viewer. Model Simul Mater Sci Eng 11:173. https://doi.org/10.1088/0965-0393/11/2/305

Advanced Manufacturing of the Holes by Controlled Texture

Check for updates

Daniel Chiriţa and Dumitru Nedelcu

The chapter aims to establish the optimal texture area, which is why four areas were analyzed depending on the stroke of the lubrication segment, as follows: total texture, between upper and lower dead center; in the area of the upper dead center; in the middle area, between the upper dead center and the lower dead center; lower dead center area. The optimal location of the textured area must be in the area of the outer dead center (PME) of the "fire" segment. Following the simulation, a device was conceived, designed and executed that can achieve this texturing and then SEM and AFM analyzes of the material used showed the tendency of the material to deform depending on the rotational speed and the impact distance, at a constant force. With the increase of the speed of the percussion head, an elongation of the cavities created in the rotation direction, which led to the discharge of the material in the same direction. The SEM and AFM analyzes also showed the lack of cracks or fractures in the percussion area for the chosen material. Also, the same textures were analyzed from the point of view of the uniformity of the shapes and depths of the cavities by drawing the profile diagrams resulting in almost identical shapes on the analyzed surfaces.

D. Chiriţa · D. Nedelcu (✉)
Gheorghe Asachi Technical University of Iasi, Blvd. Mangeron no. 59A, 700050 Iasi, Romania
e-mail: dnedelcu@tuiasi.ro

D. Chiriţa
e-mail: daniel.chirita@tuiasi.ro

1 Introduction

Various processing methods are currently used to create micro-cavities on the surface of different materials, which can be grouped into three groups, as follows:

(I)   Chemical texturing processes:

 – Chemical etching for the creation of modulated or curved cavities that act as traps for oxide wear residues, the method developed by Suh [1];
 – Photolithography consisting in the use of a hydroxide to create cavities and depressions of different shapes, developed by Pattersson and Jacobson [2].

(II)   Mechanical processes:

 – Vibro-lamination, to create superficial channels using a hard indenter that vibrates on the workpiece, the method developed by Schneider [3];
 – Honing, to generate micro-grooves on the cylinder holes of internal combustion engines, developed by Willis [4];
 – Abrasive jet processing (AJM), where the surface is bombarded with fine abrasive particles at high speed that causes the removal of portions of the surface layer of the material, developed by Wukada [5];
 – Ultrasonic engraving, for the realization of shallow cavities on the surface of the semi-finished product.

(III)   Laser texturing refers to Excimer laser beam processing (LBM).

Pattersson and Jacobson [2] used standard photolithography, using the anisotropic etching technique with potassium hydroxide, to create cavities and square depressions 5 μm deep on silicon plates. The standard steps for anisotropic etching of silicon wafers.

Wukada et al. [5] used abrasive jet processing (AJM), where the surface is bombarded with fine abrasive particles at high speed which causes the removing material. These two manufacturing methods allow different profiles to be obtained, even the effect of the shape of the texture is considered insignificant.

Dumitru and collaborators [6] investigated the effects of micro-cavities on steel discs under mixed lubrication conditions. The texture surfaces were in square-shaped patterns. Diameters ranged from (50–100) μm, depths ranged from (5–8) μm, and distance between holes ranged from (30–60) μm. The study showed an eight-fold improvement in the lifespan of the samples.

Surface texture is used to increase tribological performance that includes decreased wear and friction, especially in the manufacture of automotive components, tools, and microelectric circuits [7] (MEMS).

In the automotive industry, research has shown that one of the major factors influencing wear in the segment-cylinder torque is the presence of mutual friction [8–10]. The inner surface of the cylinders is usually worn in the shape of a bell, barrel or cylinder [10], and may also show traces of abrasion and gripping or corrosion stains.

Based on the above, the texture of metal surfaces proves to be an effective means of increasing tribological performance. Most studies have investigated the effects of texturing surfaces under lubrication conditions and a very limited number of studies have addressed the state of dry slip for textured surfaces.

In this chapter, the control of the contact area of the hole surface in the segment-cylinder coupling by using textured surfaces using a new method of mechanical texturing, roto-percussion, is the main objective of the research. Finally, the area and the optimal degree of texture of the hole will be determined by the proposed method, taking into account the significant parameters that minimize friction.

2   Material and Method

In order to obtain the texture to be analyzed, gray cast iron cylinder holes with lamellar graphite SR EN 1561: 1999 EN-GJL-BH 175 detachable by the spark-ignition heat engine have been prepared, on which sections of the cylindrical jacket will be mounted/disassembled and will constitute as test specimens (Fig. 1).

In order to create a micro-cavities texture on the inner surface of the holes, a new method has been designed, namely rotary-percussion, which derives from the repetitive hitting (percussion) of the surface to be processed with a mechanical pulse generator that also performs rotational movements around the axis of the hole being machined, simultaneously with the feed motion. According to the diagram in Fig. 2, the X and Y axes are used in the centering with respect to the axis of the hole to be processed and along the Z axis the operation of lowering-raising the mechanical pulse generator is performed. Arriving in the processing area, the generator must receive from the fourth axis, derived from the Z axis, the rotation of the impact pulse generator on the area chosen for texture.

Starting from the principle diagram of the actuation of the rotary-percussion device (Fig. 2) with electromagnetic pulse generator for the pointed conical mandrel, the device from Fig. 3 was designed, where the percussion head was constructed of

Fig. 1 Cylinder hole
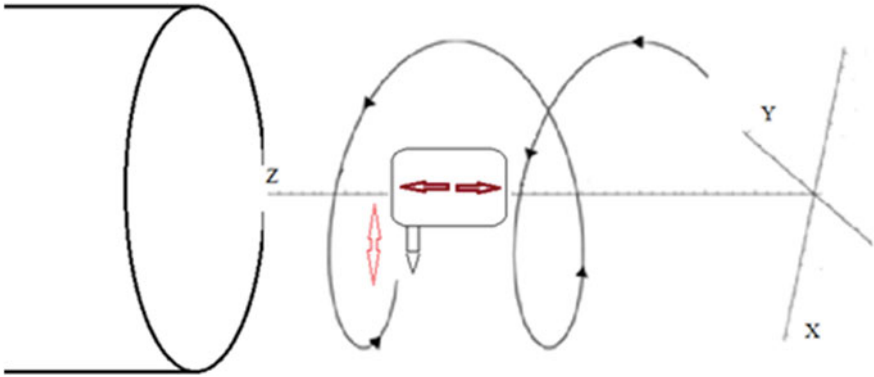
Fig. 2 Schematic diagram of the rotary-percussion device
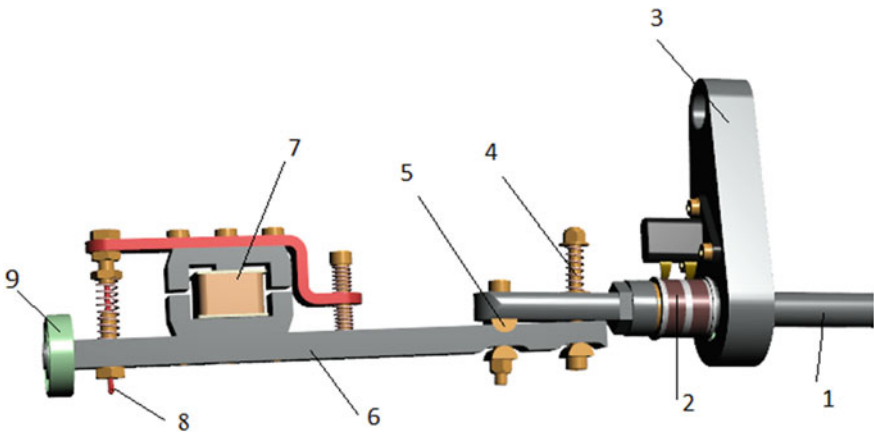
Fig. 3 General scheme of the rotary percussion head

an electromagnet (6) which uses an electromagnetic core that acts on a pointing mandrel (8) that strikes the cylindrical surface to be processed. The striker head was attached to a rod (6) on which a spring-type tensometer (4) was mounted to adjust the percussion force. The rod (6) is fixed to the central shaft (1) by a rocker type system (5) for adjusting the actuating position, depending on the diameter of the processing cylinder. An electric collector (2) mounted to the system to supply the electromagnet was mounted on the central shaft. The collector is fed by two brushes which are fastened in a support (3) which does not rotate with the striker head, remaining fixed in a certain position, while the central shaft, by which all the elements are fastened, will perform the movement of rotation and advance controlled simultaneously with the supply of the coil. In order to have the same impact distance at the end of the rod (6) a bearing (9) was mounted, which keeps the device constant at the same impact distance from the bore surface.
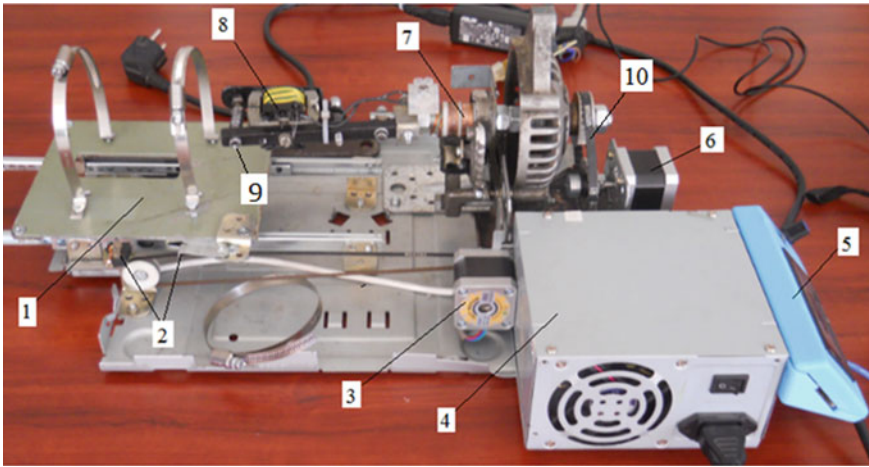
Fig. 4 Numerical control rotary-percussion equipment details

In the laboratory of Fine Mechanics and Nanotechnologies, Department of Machine Manufacturing Technology, "Gheorghe Asachi" Technical University of Iasi, was built the numerically controlled equipment (Fig. 4) to which was attached the striker head (9) acting on the cylinder fixed on the moving table (1). The moving table has been connected to the stepper motor (3) which together with the position sensor (2) determines the zero point of the equipment and the texture area. The Arduino shield together with the power supply is embedded in the metal box (4) to which the LCD is attached to visualize the work process and determine the zero point of the bore to be textured. In order to have the most efficient control of the rotational speed of the device to be rewound with the stepper motor (6), it was connected to the device (9), by a system of gears with a timing belt to a ratio from 1 to 1, (10). The electromagnet (8) is supplied by the collector (7).

3 Results and Discussion

The frequency of the single-phase alternating electric current used in the research is 50 Hz, which when applied to the percussion equipment solenoid will generate a precautionary impact with a frequency of 50 beats per second.

To obtain a cavity (Fig. 5) with a maximum depth h, the working stroke C of the electromagnet, the impact distance Hp and the hardness of the material must be taken into account. The percussion mandrel performs I movement.

In the situation without impact distance ($H_p = 0$ mm), the maximum depth of the cavities h will be given by the working stroke C of the electromagnet and the hardness of the material.
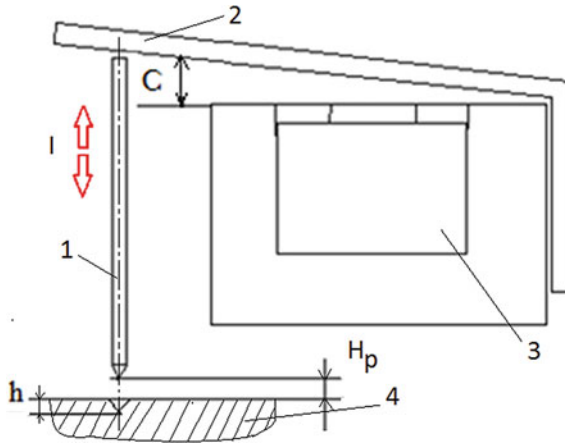
Fig. 5 Depth of cavity h depending on the stroke of the electromagnet C and hitting distance H_p: 1-percussion mandrel; 2-electromagnet moving part; 3-electromagnet; 4-hole material

In order to have a uniform deformation process the force of the electromagnet during the experiment must be constant.

The impact force of the pointing mandrel will be given by the variation of the impact distance H and will determine the created cavity and the volume of deformed material in the vicinity of the cavity.

According to Fig. 6a, after hitting the bore with the pointing mandrel, a cavity and an area around the cavity are obtained, with functionally unsuitable tips of material that require additional finishing honing operations.

In order not to break the material in the cavity area (Fig. 6b), the distance between the percussions must be controlled on the spiral as well as between the spirals of the cavities.

Taking into account the frequency of the current used, the following fact is found: the attraction and relaxation time of the electromagnet is 0.01 s (Fig. 7). From this it follows that the intensity of the blow depends on the force of attraction of the electromagnet and the distance of impact, and the distance between the percussions depends on the speed of return from the electromagnetic torque at rest in conjunction with the rotational speed of the percussion head.

Fig. 6 The distance between the cavities depends on the hardness of the material
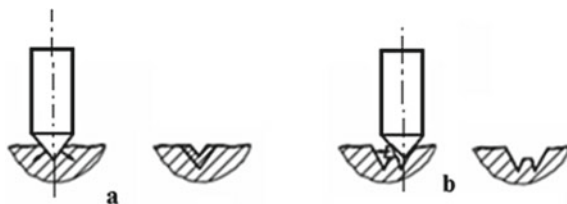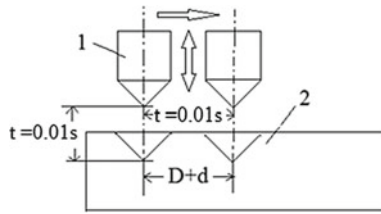
Fig. 7 Percussion distribution as a function of time: 1-mandrel percussion; 2-rototextured material

Fig. 8 Percussion dispersion depending on the speed and advance of the device

Increasing the rotation speed of the impactor head (Fig. 8, $V_1 < V_2 < V_3$) will result an elongation of the cavities created in the direction of rotation which leads to the discharge of the material in the same direction. Thus, it is not possible to approach the impactor head in the retracted position in relation to the surface to be processed without taking into account the discharge of the material.

3.1 Analysis of the Dependence Between the Parameters of the Textured Surface and the Tribological Behavior of the Segment-Cylinder Coupling

According to Fig. 9, the oil in the area of the lubrication segment "does not reach the area of the fire segment", for two reasons:

intake   compression   combustion   evacuation
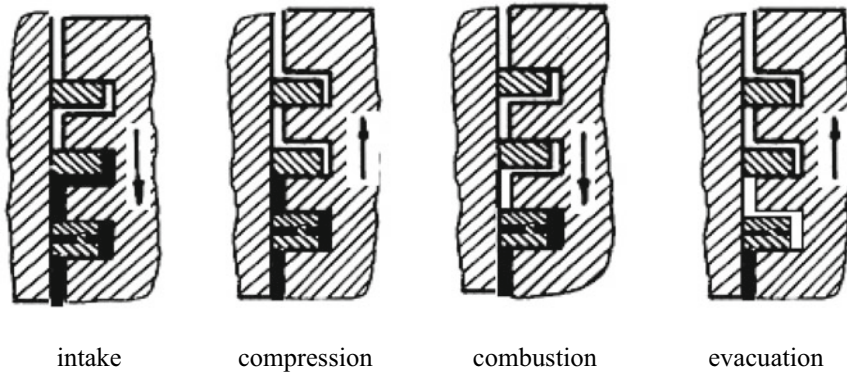
Fig. 9 Displacement of oil between segments

– The segments, through the function of sealing the combustion chamber to the crankcase, also have the function of scraping/cleaning the work surface of oil and abrasive impurities;
– Compression and expansion of the gases in the combustion chamber push the oil from the segment-cylinder coupling (Fig. 10).

Analyzing the way, the oil reaches the surface of the cylinder, using a straight profile segment, it was found that the amount of oil in the PMI area is deficient, leading to a mixed working regime of the segment-cylinder coupling at dry regime, and the first compression segment comes into contact with oil in the PME area at the beginning of the compression stroke and the exhaust stroke and the end of the intake and combustion or expansion strokes (Fig. 9).

Analyzing the surface of the cylinder traversed by the lubrication segment (Fig. 11) it is observed that it is not total. In the PMI area there is an S_1 surface that is not traversed by the lubrication segment but is touched by the compression (fire) segment.

Starting from the idea of applying an additional lubrication regime in the cylinder-segment coupling, an additional texture was created, by roto-percussion, on the cylindrical surface. To this by adding the compression segment, with spherical working surface (Fig. 12), in the oil film (3), developed between the piston (1) and the cylinder (2), a cavitation force (F_{cav}) is developed given by the force of compression and expansion (4), which push the oil film on the surface of the segment.

In order to have a hydrodynamic lubrication regime, it follows that the texturing must be done from the SME area of the lubrication segment to the PMI and must be calculated taking into account: toggle area of SMEs and PMIs; the distance between the fire segment and the lubrication segment; gas pressure during expansion; tilting area in PMI.

These textures will lead to a hydrodynamic regime of fluid lift due to the formation of a "squeeze" regime. The lubricant being incompressible and having no place to
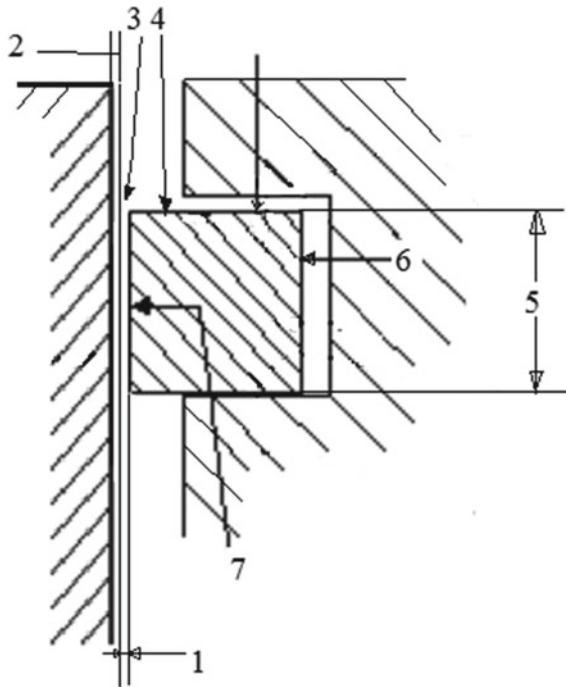
Fig. 10 Honing channel represented longitudinally: 1-oil film thickness; 2-honing chanal; 3-compression force; 4-relaxation force; 5-segment width; 6-elastic force segment; 7-segment mirror

discharge and combined with the effect of the compressive and relaxation forces ($_{Fc/d}$), will push in the segment (Fig. 13).

In order to increase the tightness of the combustion chamber with respect to the crankcase in the conditions of a hydrodynamic lubrication regime, the creation of a minimum texturing area by rotopercussion was analyzed starting from several scenarios.

These scenarios were analyzed from the perspective of the amount of oil that reached the combustion chamber during intake and combustion, depending on the number of cavities created by rotopercussion. The oil reaches above the compression segment through the cavities created only at times when the piston performs the downward movement from PMI to PME.

Performing an analysis of the volume of a cavity and the number of cavities exposed to the gases in the combustion chamber, a scenario was constructed on different positioning's of textured surfaces on the bore surface.

In order to perform an easy analysis, we started from the calculation of the volume of a cavity processed by rotopercussion as, being spherical in shape with an average diameter of 230 µm. The textured cavities made are not completely spherical so that they were approximated to half a sphere, the volume being given by the relation (1).
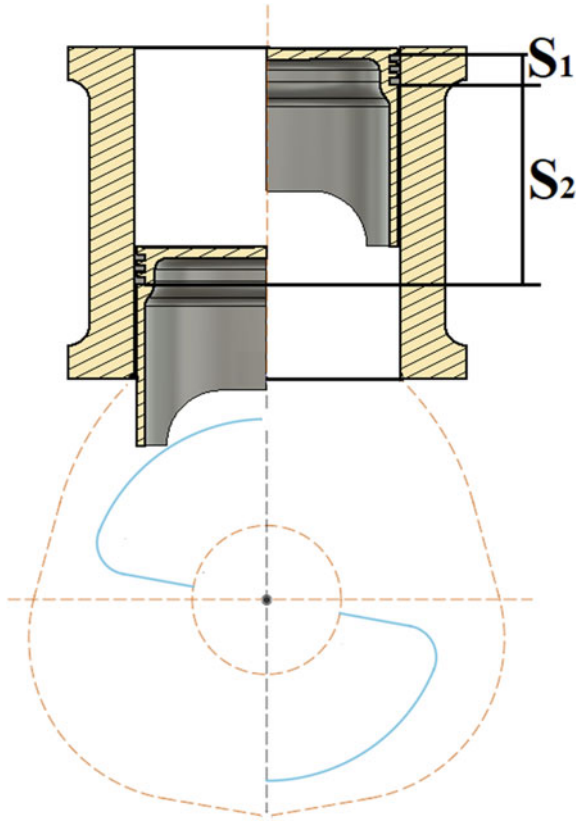
Fig. 11 Cylinder wear depending on the lubrication segment: S_1-cylinder surface not touched by the lubrication segment; S_2-the surface of the cylinder touched by the lubrication segment; b-graphical cylinder liner wear depending on the fire segment

Fig. 12 Pushing the oil film on the surface of the segment
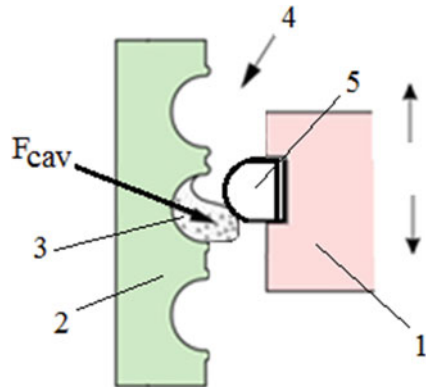
Fig. 13 Compression force /expansion gas ($F_{c/d}$) in the combustion chamber on the oil in the cavities
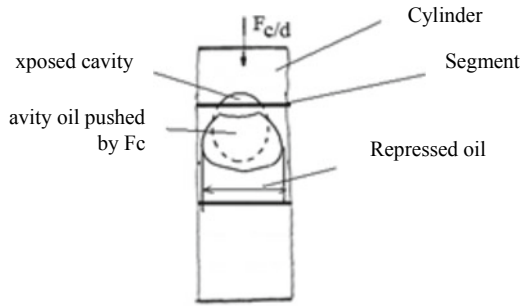
$$\frac{V}{2} = \frac{\pi^3}{2} = 20 \ \mu m^3 \tag{1}$$

From the calculated cavity volume, 7/8 of the volume was subtracted in the hypothesis of exemplifying the scenario in which the oil does not remain entirely on the walls of the textured bore, but part is pushed back by the segment passing through the cavity, and another part is pushed by gases from combustion chamber. In this case, it was assumed that the amount of oil remaining for exposure in the combustion chamber is the one that adhered to the cavity walls.

To define the minimum texturing area by rotopercussion, 4 scenarios were created taking into account the area reached by the lubrication segment to see after 3000 rotations, what volume of oil reaches the combustion chamber and what regime operation will exist.

Starting from this presentation of the surface covered by the lubrication segment, it must be identified which would be the minimum area required for texturing in the bore surface to obtain a better lubrication regime of the "fire" compression segment from the PME zone to the PMI zone.

3.2 Total Textured Surface Analysis

In the first case, the total texture of only the surface S_2 was considered, not the surface S_1, because it is not supplied with oil by the lubrication segment (Fig. 14) and the below analysis was made.

As previously presented, on a texture spiral can be a number N of cavities that can be calculated with the relation (2):

$$N = \frac{L}{D + d} = 471 \ \text{cavities} \tag{2}$$

where: L is the length of a spiral to be calculated according to the relation $L = 2\pi R + (D + d)/2$; D is the diameter of a cavity with an average value of 235.75 μm and d is the distance between the edges of two percussions with the value of 264.25 μm.

Fig. 14 Fully textured S_2
surface
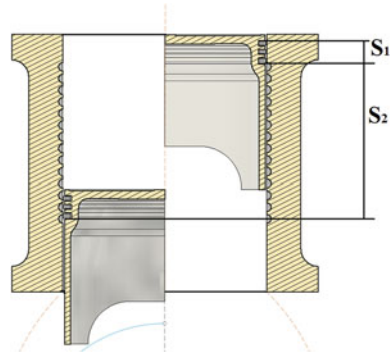
Making the product between the number of cavities per row and the number of springs according to relation (2) we have on the surface S_2 a total number (N_t) of cavities (relation 3):

$$N_t = N \times N_s = 471 \times 234 = 109898.43 \ \text{cavities} \tag{3}$$

Continuing the analysis, it is found that 1/8 of the volume of a cavity multiplied by the number of cavities on the surface S_2 will generate the volume V_{S2} of oil that reaches additionally in the combustion chamber, calculated with relation (4):

$$V_{S2} = \frac{V}{2} \times \frac{1}{8} \times N_t = 20 \times \frac{109898,43}{8} = 274746.07 \ \mu m^3 \tag{4}$$

Furthermore, considering that at a complete 4-stroke cycle we have two volume loads of V_{S2} oil, it will result that, in one minute, at a constant operating speed of 3000 rpm we will bring a calculated amount of oil into the combustion chamber with relation (5):

$$V_{S2} \times 3000 \ \text{rpm} \ = 824238210 \ \mu m^3 = 0.0008 \ cm^3 \ \text{oil} \tag{5}$$

From this calculation it resulted that the rototexturing process is not applicable for the entire surface S_2 because a quantity of oil is introduced which is not completely burned and is removed during the discharge, thus increasing the pollution regardless of the fuel used.

At the same time, the calculation was performed for a minute, which shows that the engine cannot run with a constant level of oil in the bath in the designed parameters, the oil consumption leading to the need for regular supply.

In this case an additional analysis is no longer necessary because the introduction of additional oil in the combustion chamber changes the engine operating mode leading to incomplete combustion, tar formation and the release into the atmosphere of a quantity of hydrocarbons that contravene the pollution rules imposed on heat engines any kind.

3.3 Textured Surface Analysis in the PMI Area of the Lubrication Segment

In this scenario (Fig. 15) a textured area consisting of three rows was schematically represented but the analysis will be performed only for a row of textured cavities to highlight the advantages or disadvantages of texturing in the maximum PMI ascent area of the lubrication segment.

The compression segment during the downward movement towards the SME will be fed with the oil from the texture performing the movement, further, in a mixed regime.

As in the previous case, the amount of oil reaching the combustion chamber was calculated for a single row of cavities and the volume V_{S1} given by the relation (6) resulted:

$$V_{S1} = \frac{V}{2} \times \frac{1}{8} \times N = 20 \times = 1177.5 \ \mu m^3 \tag{6}$$

The volume of oil brought into the combustion chamber after 3000 rpm will be according to relation (7):

$$V_{S1} \times 3000 \ rpm = 3.532.500.00 \ \mu m^3 = 3 \times 10^{-6} \ cm^3 \tag{7}$$

The volume of oil consumed being much smaller than in the situation of the total textured surface S_2 results, implicitly, also an increase of the operating time, up to the minimum level allowed by the manufacturer.

In this case, the temperature to which the oil remaining during the lowering of the piston is subjected must also be discussed, resulting in amounts of tar remaining in the cavities which will lead to malfunctions in the optimal operation of the engine, as follows:

Fig. 15 Textured surface in the PMI area of the lubrication segment
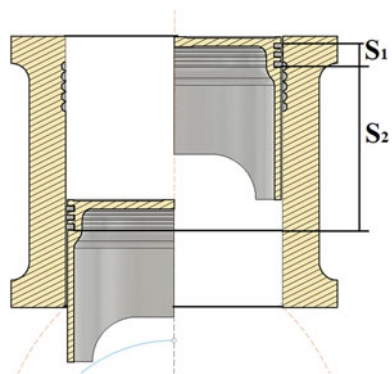
– The tar created will fill the rototextured cavities over time and will be an additional source of heat retention in the combustion chamber, being of a different nature than that of the material from which the cylinder is made;
– The compression segment will meet an additional source of heat that will be added to the heat during combustion;
– The cavities filling with tar will not lead to the decrease of the contact surface from the segment-cylinder coupling, but will increase it, the tar deposited in the cavities becoming abrasive after the complete burning of the oil;
– The additional heat source introduced into the combustion chamber during intake and compression will generate uncontrolled combustion.

And in this case, additional analysis is no longer necessary because the additional introduction of oil into the combustion chamber, changes the engine operating mode, producing instability and an operating environment at temperatures above the permissible limit, leads to the conclusion that the bore texture in the PMI area it is not beneficial to the operating mode of the heat engine.

3.4 Textured Surface Analysis Between PMI and SME Area, in the Middle

In this case, the analysis was also performed on a single row of cavities, on the surface between PMI and PME, i.e. in the area $S_2/2$ (Fig. 16).

Compared to the previous case, taking into account only one spiral, the same amount of oil will be brought into the combustion chamber of $3 \times 10^{-6} \mathrm{cm}^3$ but the following aspects are possible:

– The tar will form in a longer period of time because the exposed oil will not have a complete combustion and will be able to be partially washed by the lubrication segment;

Fig. 16 Textured surface in the middle area of the surface S_2
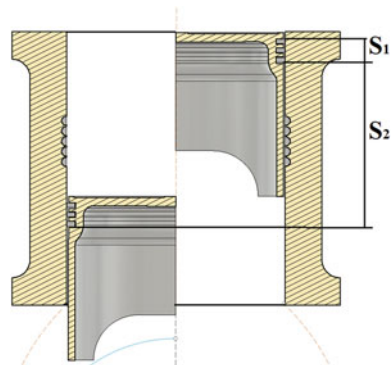
- A quantity of oil, partially burned, will reach the oil bath, changing, in a relatively short time, the properties of the oil necessary for the proper functioning of the friction torques in the entire engine;
- The additional heat source introduced into the combustion chamber during intake will not cause uncontrolled combustion, but will be an additional source of heat retention on the surface of the fire segment.

In this case, a further analysis shows the disadvantages previously shown that could occur in the operation of the engine with textured cylinders in this area. The additional introduction of oil into the area of the fire segment is only beneficial on the second part of its lowering during the expansion. A quantity of oil reaches the combustion chamber, which modifies the operating regime of the engine, producing hydrocarbons that contravene the pollution norms and an operating environment of the engine at higher temperatures for this texturing zone.

This analysis leads to the conclusion that the bore texture in the $S_2/2$ area is not beneficial to the operating mode of the heat engine.

3.5 Textured Surface Analysis in the SME Area of the Fire Segment

In this case, to exemplify the texture in the PME area, the textured area was also analyzed from a single row of cavities only in the area of the first compression segment from the PME point (Fig. 17).

In this case there may be the following scenario when using a single textured spiral:

- The cavities are fed directly by the bubbling of the oil in the bath and scraped by the lubrication segment;
- When the compression segment reaches the texture, the combustion process is completed;

Fig. 17 Textured surface in the SME area of the "Fire" segment
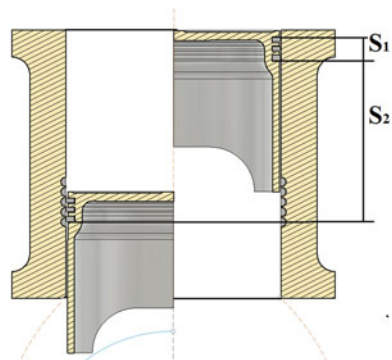
– The compression segment is additionally supplied with oil for the lifting movement from PME to PMI;
– During the supply of oil from the cavities of the textured row, the compression segment is discharged from the temperature accumulated during combustion by transferring it to the oil in the cavities and transmitting it to the bore surface in the PME;
– The tips of the roughness, detached during work, are deposited in the cavities after which they are washed by oil by bubbling;
– There is no tar formed by the combustion of waste gases at the end of combustion;
– The movement of the coupling elements will depend on the fluid regime, in the SME zone, towards the semi-dry mix, in the SME zone.

Examining the textured area with the Kestrel System K and Quadra-Chek 200 microscope, it was found that the cavities created on the surface of the bore do not have an elongated round shape, but have the shape of a falling water drop (Fig. 18).

In order to more clearly define the shape of the cavities, several rototextured surfaces were made, on the same hole, with different rotation and feed rates in order to analyze their shape at different texture densities, according to Fig. 19.
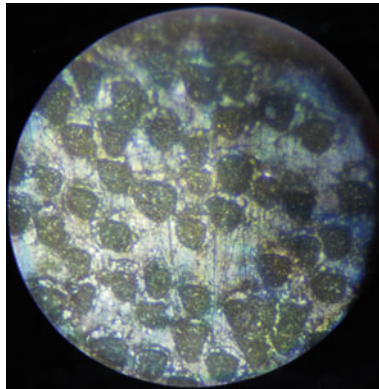
Fig. 18 Cavities image
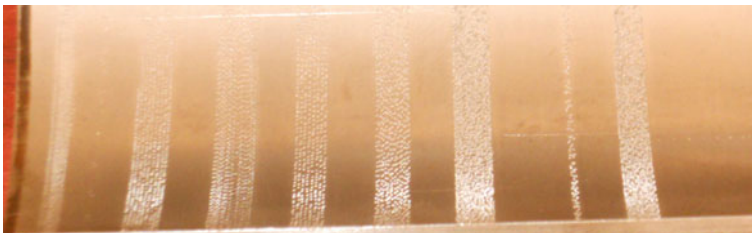
Fig. 19 Different textures depending on the rotational speed
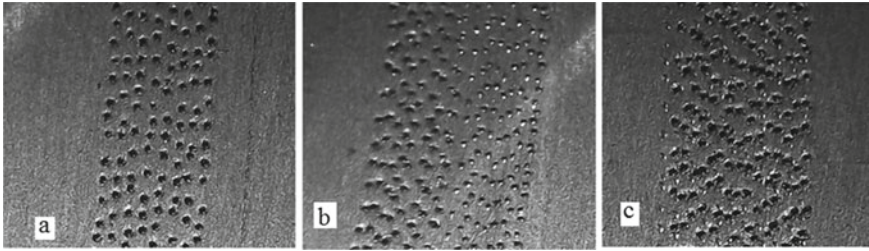
Fig. 20 Different cavity densities depending on rotational speed and feed rate

Fig. 21 Traces of support device blows
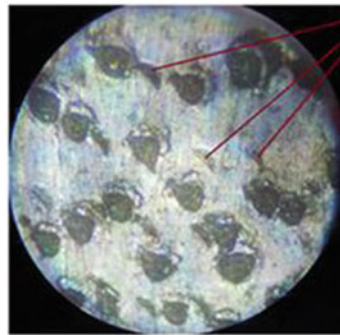
Blows to the support device

At the same impact force, given by the striker head, adjusting the rotation and feed rate, the degree of texture of the bore surface is higher the lower the rotation and feed speeds of the equipment (Fig. 20c).

Analyzing the textured areas under the microscope, traces of blows were visualized, which, apparently, are not formed due to the action of the percussion mandrel (Fig. 21). These marks are considered to be left by the bearing mounted on the head of the equipment shaft.

Analyzing the textured surfaces in detail, the following were found:

– The material is discharged from the cavities in the direction of rotation of the equipment;
– If the mandrel does not strike perpendicularly, the discharge of the material may be even at an angle greater than 900;
– An apparent bump appears on the surface of the bore (Fig. 20) which is not performed by the mandrel of the rototexturing device;
– The support for ensuring the constant impact distance performs a second impact during the withdrawal of the mandrel from the created cavity.

These traces of strokes, given by the bearing, could be seen under a microscope because several textures were performed on the same sample according to Fig. 19. The traces of strokes do not appear in the first texturing area but, due to the fact that

10 mm between textures, the following textures being performed on the impact area of the equipment support on the first texturing.

In order to avoid the traces due to the support bearing, the bearing was removed and a device with three support rollers (1) (Fig. 22) was designed with the outer surface of non-metallic material, placed at equal distances from each other.

Analyzing the cavities made during the research, it was observed that the shape of the graphite is the one that influences, most, the mechanical properties, but the quantity, the distribution and the size of the graphite separations in the composition should not be neglected. Figure 23 shows the influence of graphite in the cast iron structure of the cylinder liners on the discharge of the material. Graphite in the structure is in the form of material gaps, which causes the material or mandrel to be pushed back when it hits.
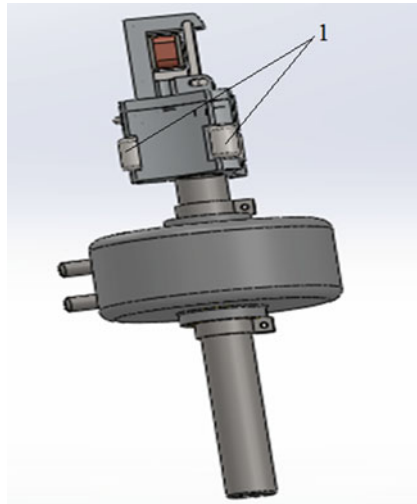
Fig. 22 Sketch device with three support rollers
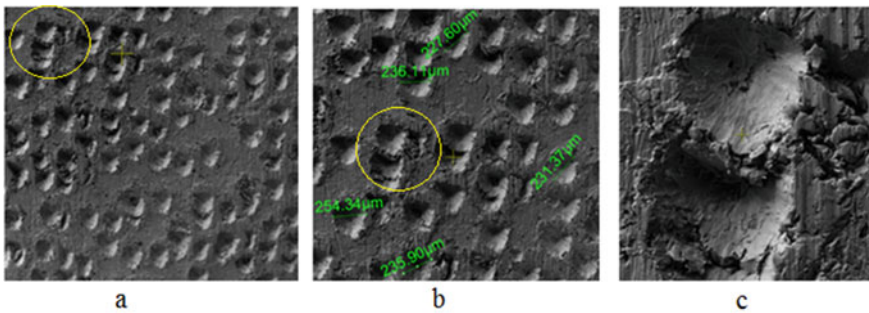
Fig. 23 Unevenly textured surface: **a**-magnitude 500X; **b**-magnitude 100X; **c**-magnitude 500X

The degree of repulsion of the material in the cavities is proportional to the impact force. From this visual finding it emerged that the distance between the percussions should be calculated not from the inside diameter of the cavity but from the maximum diameter of the material discharge (Fig. 24a, b).

In order not to have material interpenetrations with the adjacent cavities, it is considered that the following parameters should be taken into account when calculating the rotation speed and feed rate: impact distance; rotational speed of the impactor head; advance speed; material structure; games on the device; material stresses. Obtaining cavities can be compared to a cutting process.

In Fig. 25, using the Quanta 200 3D microscope, several diameters of the formed cavities were randomly measured.
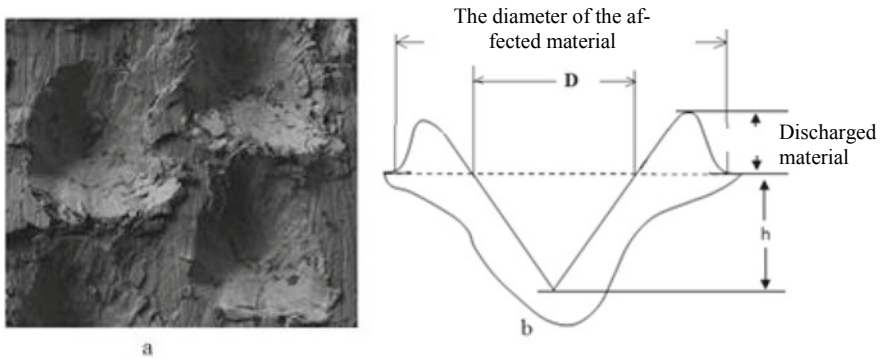
Fig. 24 Material removal: **a**-image of neighboring cavities, 5000X; **b**-schematic view of the uniformly discharged material

Fig. 25 The average diameter of the percussion textured surface
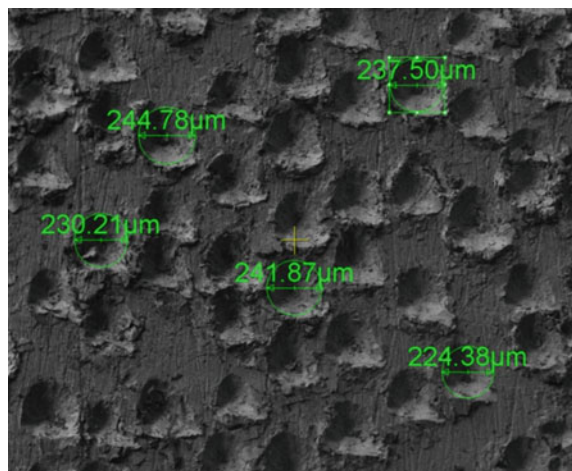
In calculating the number of cavities per coil (relation 2) the average value of 235.5 μm for the diameter of a cavity was taken into account.

Visualizing the cavities created by the rotary percussion device, with the help of the electron microscope for SEM QUANTA 200 3D analysis, the discharges resulting from the rotational percussion processing were analyzed for several samples with different rotation and feed speeds (Fig. 26I), made at 50X magnification and (Fig. 26II), performed at 100X magnification power.

Due to the discharged material from the cavity area in the direction of movement of the equipment, it was decided, following surface analysis, that the finishing honing
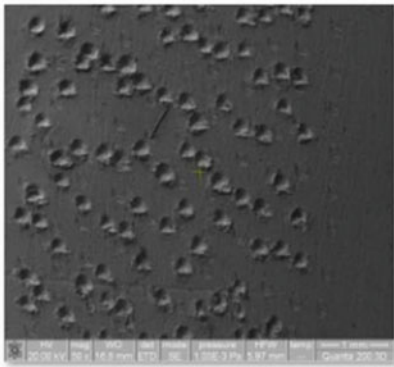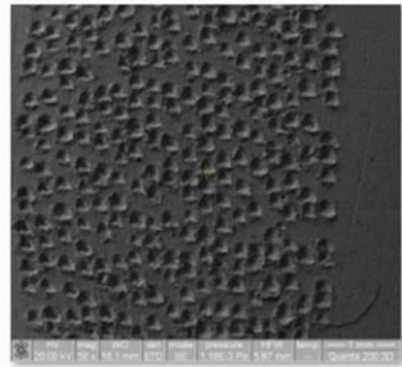
a) rotational speed of 10mm/s   b) rotational speed of 9mm/s

I)

II)
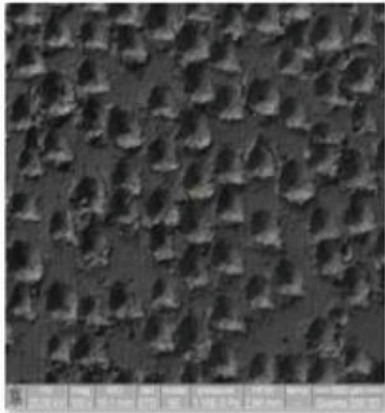
a) rotational speed of 10mm/s   b) rotational speed of 9mm/s
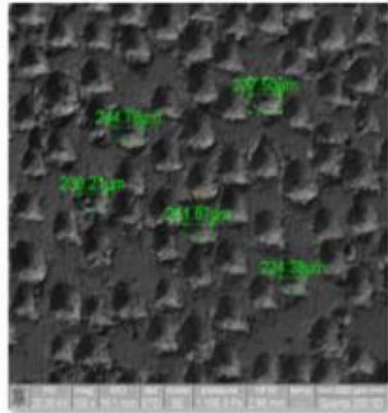
Fig. 26 Discharges of cavity material at different rotational speeds of the rotary head: **I**-50X; **II**-100X
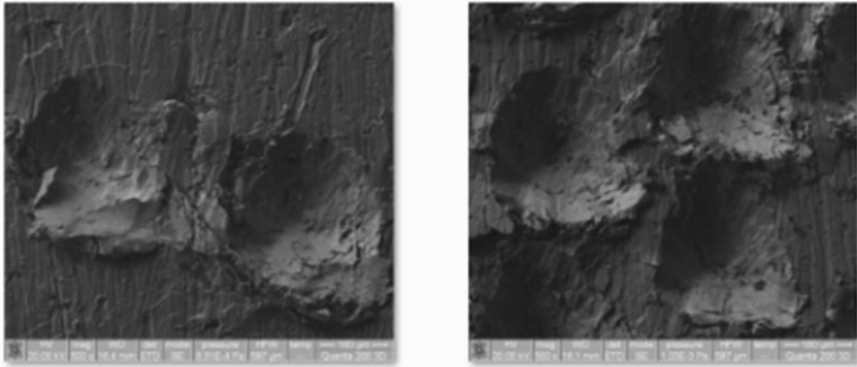
Fig. 27 Image of material discharges from the impact area, 500X

operation must be performed once again to remove the discharged material from the cavities by rotopercussion (Fig. 27).

4   AFM Analysis on Sections of Cavities Created by Rotopercussion

In order not to be influenced by surface analyzes, the samples (Fig. 28) were cut with a high-pressure water jet device with abrasive, making cuts that did not change the structure of the material, after which they were polished with diamond paste for to be able to analyze the material in section, more precisely, in the middle area of the back of a rotated percussion cavity.

Using the Park NX10 Atomic Force Microscope (AFM), which can provide the highest resolution data at the nano scale, research was conducted on the area behind the cavities. With this Park NX10 microscope due to the very high working resolution

Fig. 28 Cavity section prepared for AFM analysis
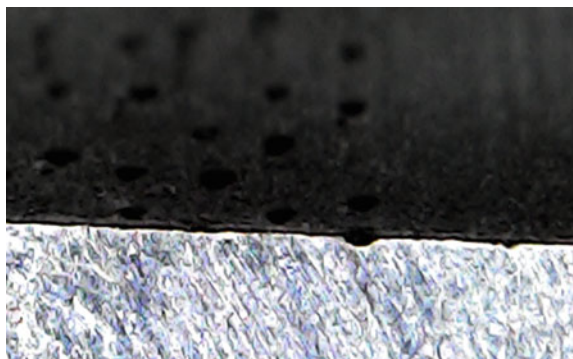
Fig. 29 The areas behind the cavity
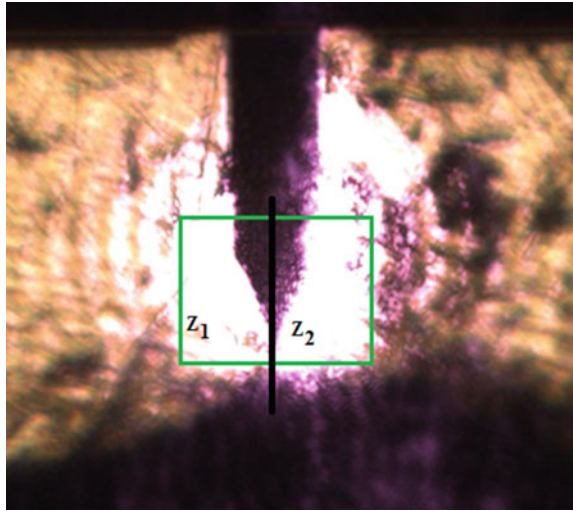
and using a nano profilometer, two areas, Z_1 and Z_2, (Fig. 29) from the wall of a cavity were analyzed.

After palpating the sample in the direction of the X and Y axes of the AFM, the polished surface was analyzed atomically and the only surface anomalies detected are those generated by the grains in the polishing paste.

The gap highlighted in Figs. 30 and 31 is given by the lamellar graphite ejected during the sample preparation polish.

The AFM software package also generated the values of the roughness components R_{pv}, R_q, R_a, R_z, R_{sk} and R_{ku} shown in the same Fig. 30.

For a clearer view of the existence of crack primers, the 3D image presented in Fig. 31 was also made.

Performing the same AFM analyzes on the Z_2 area (Fig. 32) no changes or non-conformities other than those in the Z_1 area were highlighted. AFM analysis of the polished surface in the cavity section in the Z_2 area (Figs. 32 and 33) showed a continuity of the analyzed material, which is not affected unless the abrasive particles in the polishing paste used to prepare the sample for analysis.

5 SEM Analysis in the Section of Cavities Created by Rotopercussion

Through the SEM analysis, performed by the QUANTA 200 3D electron microscope, it was possible to demonstrate the technological efficiency of the roto-percussion process applied to the bores in the thermal motors built from industrial cast iron with lamellar graphite.
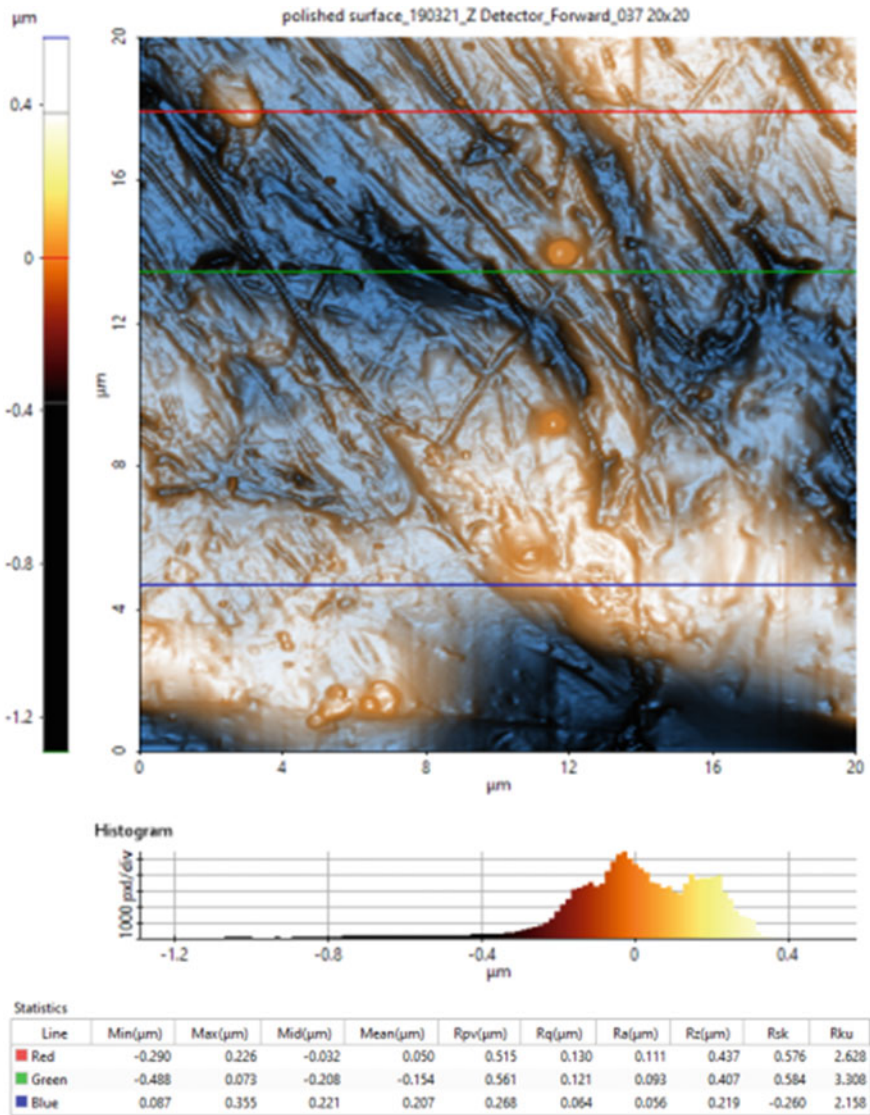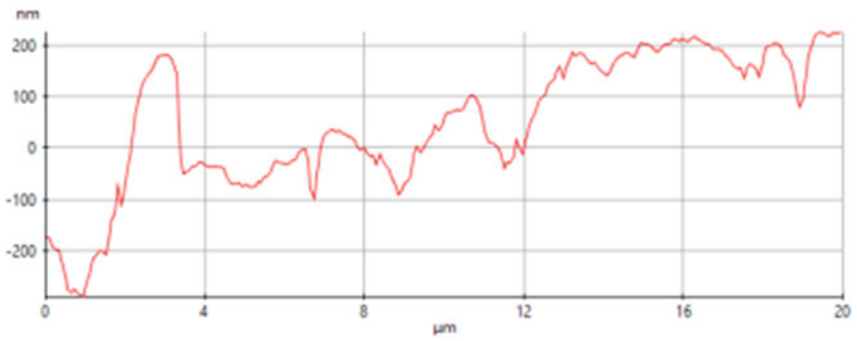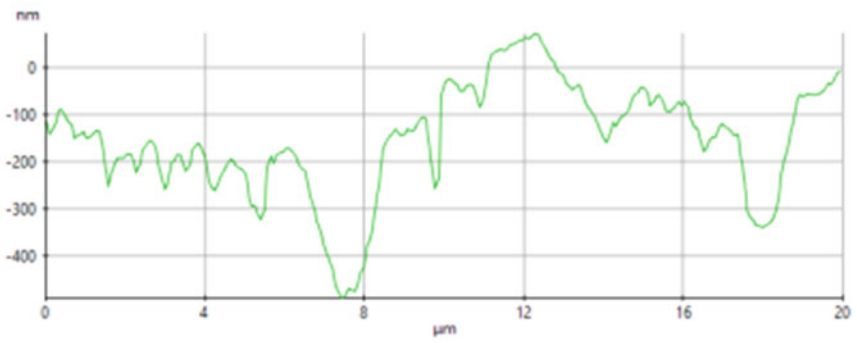
Fig. 30 Top view−AFM analysis of Z_1 area

The images presented in the SEM analysis, at different visual magnitudes according to Fig. 34, showed an unmodified structure of the material following the rotexturing.

The graphite in the structure of the material was not affected by the rotopercussion process and at the same time, following the analyzes, no cracks or unstable structures appeared in the material.
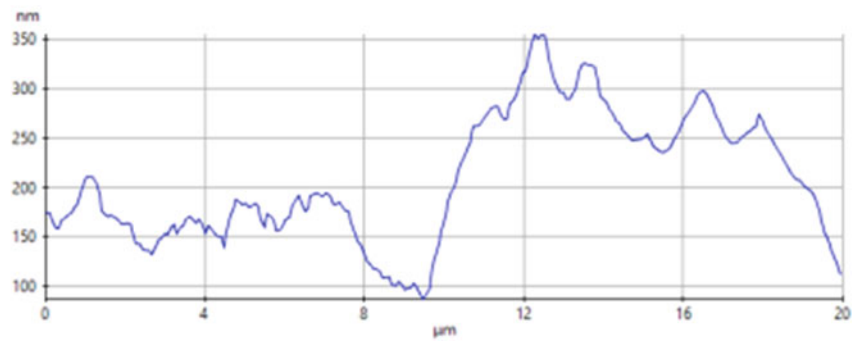
Line Profile: Red - 460

Line Profile: Green - 345

Line Profile: Blue - 121

Fig. 30   (continued)

File Name	polished surfa...Forward_037 20x20 copy
Comments	
Head Mode	NCM
Source	Z Detector
Data Width	256 (pxl)
Data Height	512 (pxl)
X Scan Size	20 (μm)
Y Scan Size	20 (μm)
Scan Rate	0.5 (Hz)
Z Servo Gain	1
Set Point	13.5E3 (nm)
Amplitude	19.672E3 (nm)
Sel. Frequency	260.77E3 (Hz)
Drive	2.47 (%)

File Name	polished surfa...Forward_037 20x20 copy
Comments	
Head Mode	NCM
Source	Z Detector
Data Width	256 (pxl)
Data Height	512 (pxl)
X Scan Size	20 (μm)
Y Scan Size	20 (μm)
Scan Rate	0.5 (Hz)
Z Servo Gain	1
Set Point	13.5E3 (nm)
Amplitude	19.672E3 (nm)
Sel. Frequency	260.77E3 (Hz)
Drive	2.47 (%)

Fig. 31 3D view of the Z_1 area

polished surface_190321_Z Detector_Forward_036 20x20 copy

Histogram

Statistics

Line	Min(nm)	Max(nm)	Mid(nm)	Mean(nm)	Rpv(nm)	Rq(nm)	Ra(nm)	Rz(nm)	Rsk	Rku
■ Red	−267.838	133.086	−67.376	−14.956	400.925	62.135	44.595	265.040	1.503	5.505
■ Green	−235.620	42.596	−96.512	−72.577	278.216	55.586	44.876	217.004	0.587	2.852
■ Blue	−561.562	95.852	−232.855	17.315	657.414	100.901	57.019	316.651	3.704	17.891
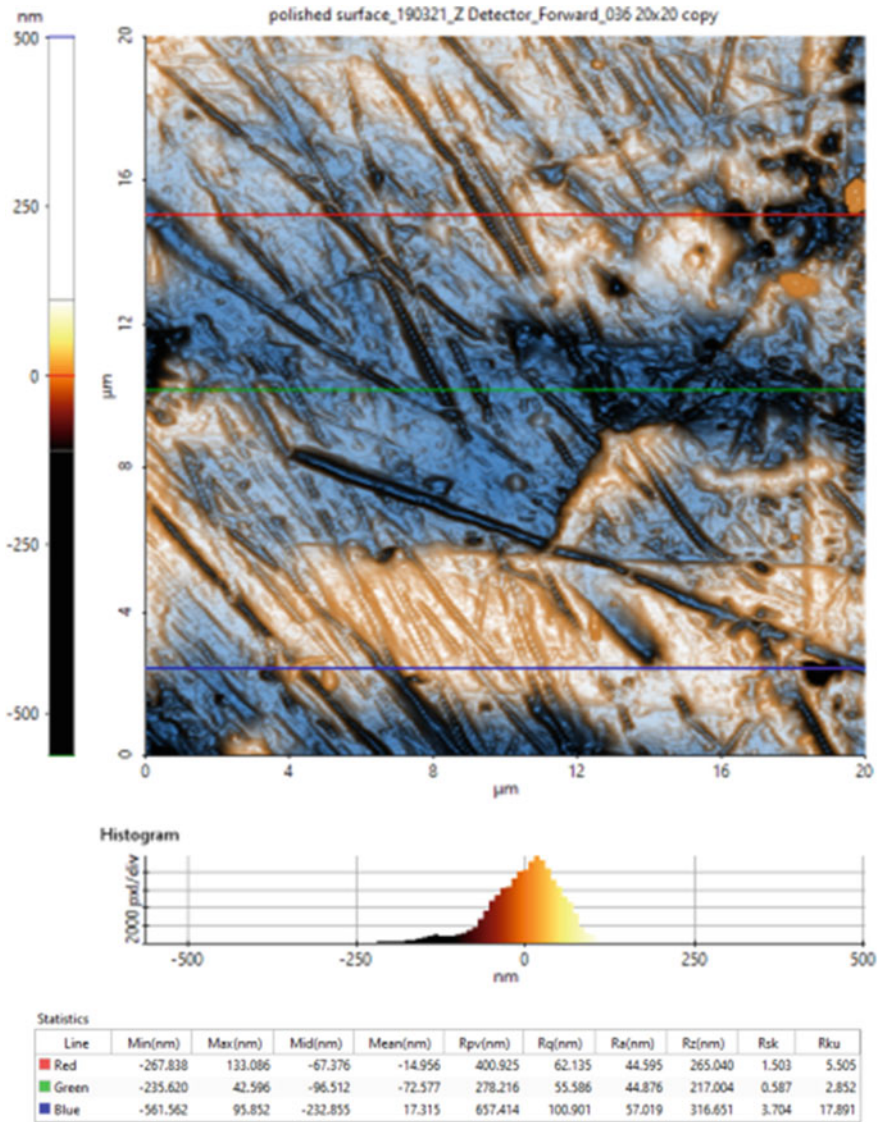
Fig. 32 Top view−AFM analysis of Z_2 area

6 Analysis of Rototextured Cavities with the Form Talysurf I 50 Profilometer

The measurements with the Form Talysurf I50 profilometer produced by Taylor Hobson, on several types of texture densities, from the same sample, aim to highlight the way the cavities look inside for different texturing speeds and to determine the shape parameters of the percussed cavities (Fig. 35).

Fig. 32 (continued)

File Name	polished surfa...Forward_036 20x20 copy
Comments	N/A
Head Mode	NCM
Source	Z Detector
Data Width	256 (pxl)
Data Height	512 (pxl)
X Scan Size	20 (µm)
Y Scan Size	20 (µm)
Scan Rate	0.4 (Hz)
Z Servo Gain	1
Set Point	14E3 (nm)
Amplitude	19.672E3 (nm)
Sel. Frequency	260.77E3 (Hz)
Drive	2.47 (%)

File Name	polished surfa...Forward_036 20x20 copy
Comments	N/A
Head Mode	NCM
Source	Z Detector
Data Width	256 (pxl)
Data Height	512 (pxl)
X Scan Size	20 (µm)
Y Scan Size	20 (µm)
Scan Rate	0.4 (Hz)
Z Servo Gain	1
Set Point	14E3 (nm)
Amplitude	19.672E3 (nm)
Sel. Frequency	260.77E3 (Hz)
Drive	2.47 (%)

Fig. 33 3D view of the Z_2 area
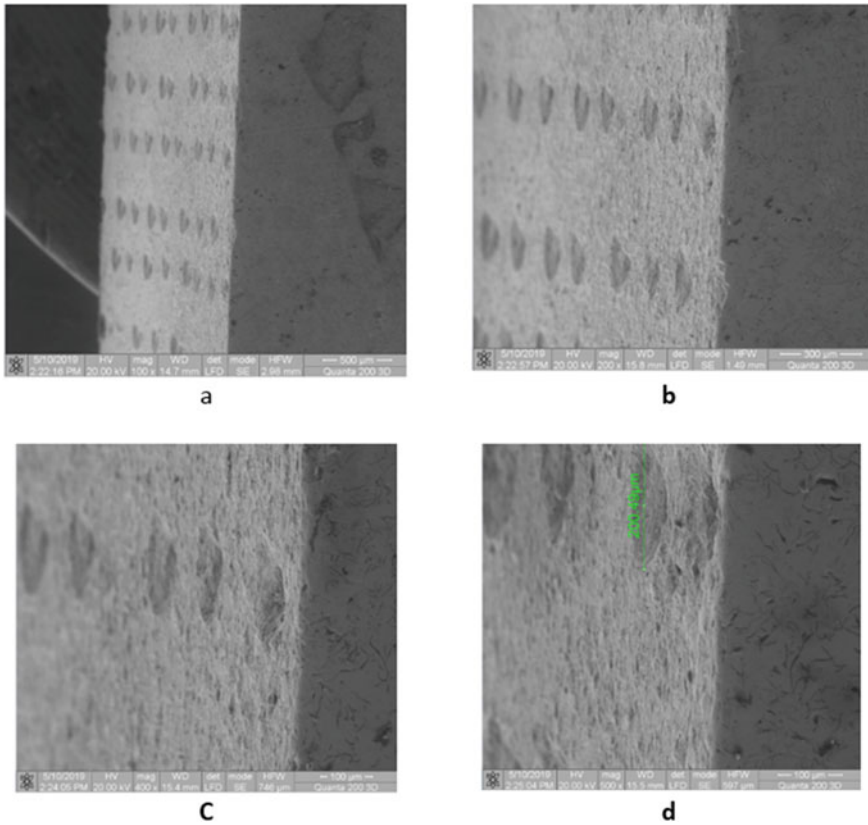
Fig. 34 Image section of material processed by rotopercussion, **a** 100X; **b** 200X; **c** 400X; **d** 500X

According to Fig. 35, the densities between the cavities belonging to the different rows and corresponding depths of the cavities can be seen. For the analysis, an area with as many cavities on the same vertical line was sought. In Fig. 36, among the cavities encountered in the path of the probe, the profile of an enlarged cavity was analyzed.

According to the graph of the analyzed cavity, Fig. 36, the shape of the analyzed cavity after performing the additional honing operation, has a depth of 0.05 mm, a diameter of 0.22 mm, which led to the previous theoretical calculation performed.

7 Conclusions

Following studies conducted by various researchers in the field of cold surface plastic deformations, it was found that most machine parts are destroyed due to mechanical and thermal stress, as well as due to the process of abrasive wear. This is primarily
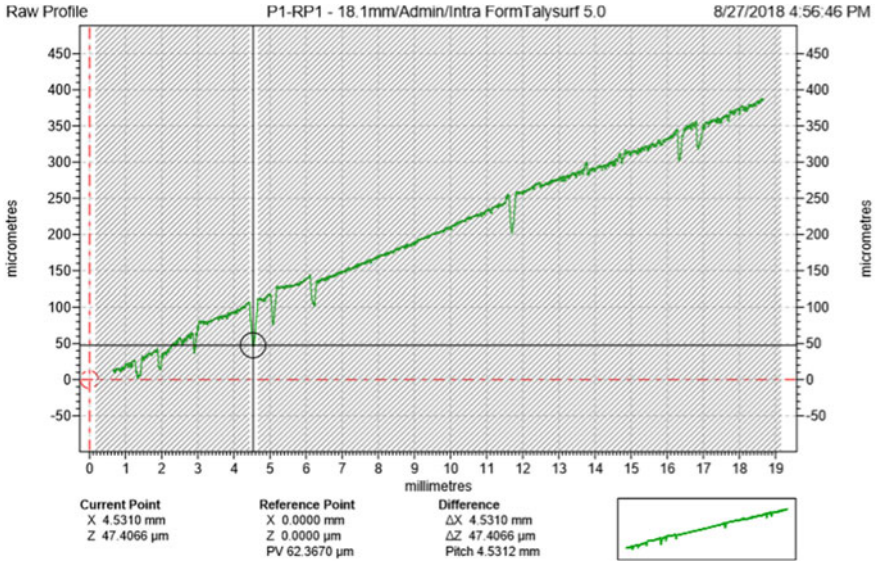
Fig. 35 Unfolded image of the measuring length at 10 mm/s of the cavities at different working speeds
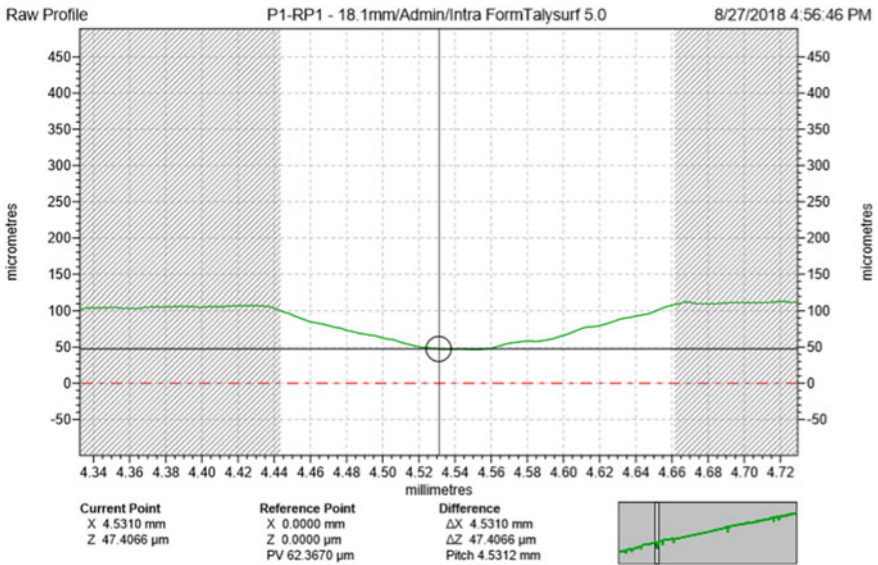
Fig. 36 Detail A for the cavity chosen in Fig. 35

due to uncontrolled (random) friction, as well as improper lubrication or even its absence.

In order to establish the optimal texturing area, four scenarios were analyzed. Following the presentation of the advantages /disadvantages for each scenario, it was concluded that the optimal location of the textured area must be in the area of the outer dead center (SME) of the "fire" segment. Before the SEM and AFM studies and following the simulation was conceived and executed a device in order to get this texturing. The SEM and AFM analyzes on the three dimensions of the space generated by the cavities created by rotopercussion showed the way and the way the material is deformed and why it must be taken into account in determining the maximum density of cavities on the chosen work surface. In the conditions of the variation of the rotation speed and advance, as input parameters, the increase of the speed of the percussion head resulted in an elongation of the cavities created in the direction of the rotation direction which led to the discharge of the material in the same direction. According to the SEM and AFM analyzes, the surface of the textured material at the achieved densities does not show cracks and fractures in the percussion area. The same textures which were used before analysis were under testing of shapes and depths uniformity of the cavities through the profiles diagrams which shows almost identical shapes of studied surfaces.

References

1. Suh NP, Mosleh M, Howard PS (1994) Control of friction. Wear 175(1–2):151–158
2. Pettersson U, Jacobson S (2003) Influence of surface texture on boundary lubricated sliding contacts. Stockholm, Sweden: Elsevier Ltd
3. Schneider YG (1984) Formation of surfaces with uniform micropatterns on precision machine and instrument parts. Prec Eng 6(4):219–225
4. Willis E (1985) Surface finish in relation to cylinder liners. Wear 109(1–4):351–366
5. Wakuda M, Yamauchi Y, Kanzaki S, Yasuda Y (2003) Effect of surface texturing on friction reduction between ceramic and steel materials under lubricated sliding contact. Wear 254(3–4):356–363
6. Dumitru G, Romano V, Weber HP, Haefke H, Gerbig Y, Pfluger E (2000) Laser microstructuring of steel surfaces for tribological applications. Appl Phys A Mater Sci Proc A70(4):485–7
7. Sugihara T, Enomoto T (2012) Improving anti-adhesion in aluminum alloy cutting by micro stripe texture. Prec Eng 36(2):229–237
8. Grunwald B (1980) Teoria, calculul si constructia motoarelor pentru autovehicule rutiere. Editura Didactica si Pedagogica, Bucuresti
9. Kragelsky V, Alisin VV (1982) Friction wear lubrication. Mir Publishers, Moscow
10. Popa B, Silasi C, Bataga N (1967) Rodarea si uzura motoarelor cu ardere interna. Editura Tehnica, Bucuresti

Parametric Study of Electro Discharge Boring of Inconel 718 with Radial Tool Movement Using Taguchi Method

Sudhanshu Kumar, Harshit K. Dave, and Keyur P. Desai

Abstract Electro discharge machining is an unconventional machining process in which material is removed by spark erosion. In the present research work, EDM process has been used for carrying out boring operation of Ni based superalloy (Inconel 718). Boring operation has been performed by guiding and controlling the movement of tool electrode on radial orbital tool path. Experiments have been conducted using Taguchi's method to obtain the influence of orbital and non-orbital parameters on material removal rate (MRR), tool wear rate (TWR) and surface roughness (Ra). ANOVA has been performed to identify the statistically significant parameters. It has been observed that all selected parameters are statistically significant in which peak current contributes 52.26% followed by flushing time i.e. 17.27% in determining the MRR. The peak current, pulse on time and orbital speed has been identified as significant parameters for TWR. The percentage contribution of peak current has been obtained maximum as 42.80% followed by pulse on time (38.48%) for TWR. The variation of surface roughness has been significantly affected by peak current, pulse on time, pulse off time and orbital speed. The peak current contributed about 80.21% followed by pulse on time about 15.03% for determining surface roughness. Estimation and confirmation experiments have been performed to verify the optimal combination of parameters.

S. Kumar (✉)
Department of Mechanical Engineering, M. A. National Institute of Technology, Bhopal,
Madhya Pradesh 462003, India
e-mail: sudhanshuk27@gmail.com

H. K. Dave · K. P. Desai
Department of Mechanical Engineering, S. V. National Institute of Technology, Surat,
Gujarat 395007, India
e-mail: harshitkumar@yahoo.com

K. P. Desai
e-mail: kpd@med.svnit.ac.in

1 Introduction

Electro-Discharge machining (EDM) process is one of the most widely used non-conventional machining process for machining of newly developed high strength alloys with high degree of dimensional accuracy. Machining of electrically conductive material irrespective of its hardness, by the application of thermal energy, is one of the prime advantages of this process [1]. Thus this process finds a suitable application in machining of Ni based superalloy i.e. Inconel 718 that is difficult to machine conventionally because of high hot hardness, high strength and poor thermal conductivity. Due to retention of hardness at higher temperature, Ni alloys are mostly used in aerospace vehicles [2].

Basically, in die-sinking EDM process, tool electrode has only vertical (jumping) movement. Therefore, it creates cavity that is mirror image of the shape of the tool electrode. However, if tool electrode is provided some orbital movement around its axis then a larger size of cavity is possible with smaller diameter of tool electrode. In orbital EDM, tool electrode continuously orbits while machining [3]. When the movement of tool electrode is controlled on circular path with continuously increasing in vertical axis (movement in X, Y, Z axis simultaneously) then this is termed as helical orbital EDM [4]. If tool electrode is allowed to move on circular path with continuously increasing radius (X, Y axis) then this machining is named as spiral orbital machining [5]. If the movement of tool electrode is controlled in such a way that it removes the material by slicing into cylinder with different radii, this cutting process is named as cylindrical orbital machining in EDM [6]. There is another possibility of tool path in orbital EDM i.e. radial tool path. In radial tool movement, tool electrode removes the material while actuating on the locus of radius of a circle. This movement of tool electrode can be applied for enlargement of a predrilled circular cavity that is boring operation. In the present investigation, boring of predrilled hole has been performed with radial tool movement in EDM process. Being EDM as a thermoelectric process [7], several electrical parameters are involved during machining such as peak current, pulse on time, pulse off time, gap voltage etc. If tool electrode is given some movement then some non-electrical parameters (orbital parameters) like orbital radius, orbital speed, flushing time etc. come into picture. Involvement of large number of parameters makes the EDM process more complex. Therefore it is important to identify the various factors influencing the response characteristics in order to understand the trend of process variable.

Literature indicates that several researchers have studied the influence of process parameters in EDM process. Belgassim and Abusaada [8] investigated the effect of electro discharge machining parameters on overcut for AISI D3 tool steel. Authors observed that overcut is significantly affected by peak current and pulse on time. Sing et al. [9] observed that the spark contact area of the tool electrode and workpiece plays critical role in material removal rate in EDM process. Effect of EDM parameters like peak current, pulse on time, pulse off time, gap voltage on performance measures like material removal rate, tool wear rate, surface roughness etc. in die-sinking EDM process is well explained in literature [10–13]. However, most of

the work is concentrated on die-sinking EDM process and little research works have been reported on orbital movement of tool electrode in EDM process. Rajurkar and Royo [14] used orbital tool movement with RF (Radio Frequency) control circuit in EDM process and observed improvement in surface integrity of machined surface. Yu et al. [15] used orbital tool movement for drilling of complex shape blind micro holes in EDM and observed that MRR increases and TWR decreases. Bamberg et al. [16] obtained an encouraging result with orbital tool movement in EDM process, due to improvement in dielectric flushing the material removal rate in micro hole drilling enhanced. The effect of other orbital parameter like orbital speed has not been discussed. Further, Bamberg and Heamawatanachai [6] investigated the orbital electrode actuation to improve efficiency of micro-holes varying orbital radius from 0 to 20 µm. It was reported that machining time and hole diameter has increased with the orbit radius. While radial overcut has decreased for higher orbital radius. The paper does not provide the details of orbital speed of tool electrode. El-Taweel et al. [5] conducted an investigation with spiral and helical modes of tool actuation in EDM process. It was reported that machining time has significantly reduced during orbital EDM. An incensement about 34% in MRR reported during the helical mode of tool actuation. Further, Dave et al. [4] performed the detailed study about the effect of electrical and orbital parameters on MRR and TWR using helical orbital strategy in EDM process. It was observed that orbital radius has significant effect on MRR but has insignificant effect in case of TWR .

The cutting ability and surface quality of machined surface of orbital tool movement over die sinking EDM process are reported. Most of the works are reported for drilling of circular holes with the help of EDM process. However, to the best of author's knowledge, published research on orbital tool movement in EDM process at radial path are very limited so far. The present work discusses the novel application of orbital tool movement at radial tool path in EDM process for boring operation of pre-drilled cavity, named as electro discharge boring. Therefore, in present study it is aimed to investigate the effect of process parameters during tool movement on radial path. Attempt is made to find parametric conditions for highest MRR with least TWR and surface roughness for electro discharge boring of existing hole.

2 Experimental Details

2.1 Experimental Setup

The experiments are performed on a Joemars, Taiwan make ZNC EDM machine, model JM 322, as shown in Fig. 1a. A special orbital head is attached to the quill of the EDM machine to provide orbit movement to the tool electrode as shown in Fig. 1b. Orbital unit consists of two stepped motors, each for guiding the tool electrode in X and Y direction during machining. Dial gauges are attached for monitoring the movement of the tool electrode; it indicates one revolution is equal to 1 mm tool
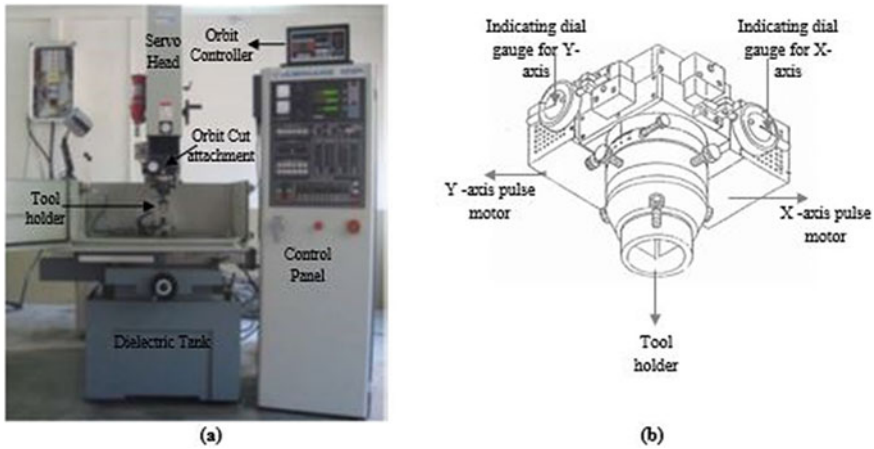
Fig. 1 Experimental set-up. **a** Electrical discharge machine. **b** Orbit cut attachment

travel. The movement of tool electrode as well as other necessary orbit parameters like radius, speed, flushing time, machining time etc. is controlled by an orbit cut controller. The maximum displacement of tool under orbiting condition is 4.999 mm from its centre. Thus, it can machine up-to the 9.999 mm diameter. The orbital cut controller can control X, Y and Z axis movement independently with 1 μm precision.

2.2 Concept of Radial Tool Movement

The tool movement under radial orbital strategy is confined to two dimensional planes only; its vertical (Z axis) movement is restricted. Tool electrode is guided to move on the locus of radius of a circular profile. In this strategy, material is removed by the side sparking on the tool electrode. First, tool electrode moves to the desired depth into the predrilled cavity on path 1 as depicted in Fig. 2a. After achieving required position in Z axis, its vertical movement is locked and is allowed to move on path 2. Tool electrode moves radially outward to the cavity wall where sparking occurs and erosion of work material takes place. Tool electrode returns back to its initial position at centre of cavity after cutting specified dimension of cut. The next movement of tool electrode is guided at 5° of angular increment from the previous tool path. In similar manner tool electrode moves on 72 paths, resulting into a circular cavity.

In radial tool movement, tool electrode advances towards the machining zone in fluctuating manner i.e. to and fro motion on straight line as illustrated in Fig. 3. The machining time decides the forward motion, depicted with F (0–1), F (2–3) in Fig. 3, of tool electrode and flushing time decides the backward motion, indicated with B (1–2), B (3–4) in Fig. 3, of tool electrode during radial tool movement in EDM.
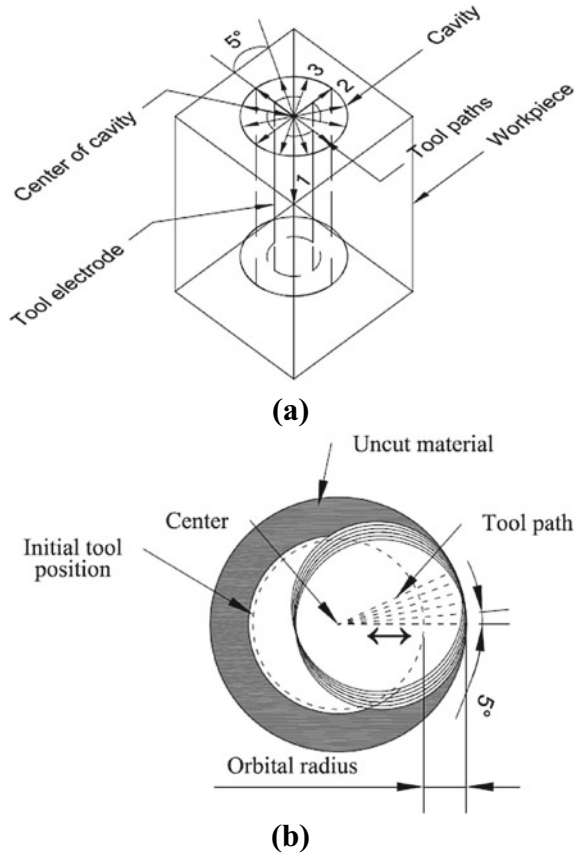
(a)

(b)

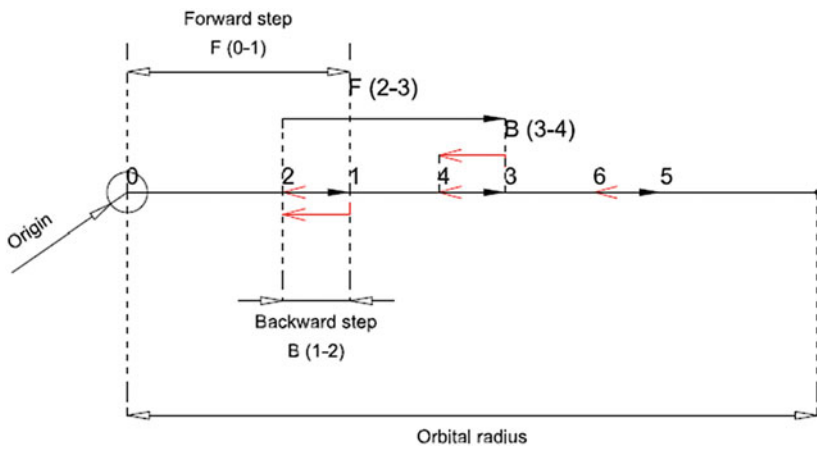**Fig. 2** Radial orbital strategy. **a** Isometric view. **b** Top view

Fig. 3 To and Fro movement of tool electrode in radial orbital EDM

Table 1 Chemical composition of Inconel 718 (Wt.%)

Ni	Mo	Ti	C	Si	Cu	Cr	Co	Nb	Al	Mn	B
50–55	2.8–3.3	0.65–1.15	0.08	0.35	0.3	17–21	1	4.75–5.5	0.2–0.8	0.35	0.006

2.3 Tool and Workpiece

Inconel 718 and pure electrolytic copper (99.9% Cu) are used as workpiece material and tool material for the experiments. Inconel 718 is Ni based superalloy that exhibit excellent mechanical strength and creep resistance at high temperature. The chemical composition of Inconel 718 is shown in Table 1. Split workpiece has been used and initial cavity having 8.0 mm diameter is generated in a way that cavity is generated equally on both parts thereby providing a scope of studying the surface characteristics of cavity. A block of 10 mm × 15 mm × 15 mm dimension was cut from Inconel 718 bar using WEDM process. Each surface of block was highly polished and made parallel to respective side. Cylindrical tool electrode was fabricated into stepped shape having body and shank of 8 mm and 10 mm diameter respectively.

2.4 Experimental Procedure

Before experimentation, initial weight of workpiece and tool electrode is measured using digital weighing machine (having accuracy of 0.1 mg). Two blocks of workpiece are held on the machine table using clamping vice in such a way that edges of predrilled cavity match with each other. Tool electrode is fixed into the chuck attached with the EDM head. The workpiece and tool electrode are connected to negative and positive polarity respectively. Dielectric fluid is flushed through an external nozzle at machining zone. The depth of predrilled cavity is fixed to 10 mm. Machining duration is noted using stop watch. Figure 4 shows the tool positions in EDM set up for boring operation.
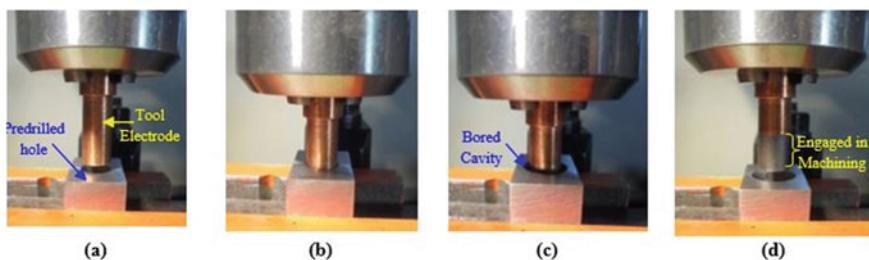

Fig. 4 Experimental procedure. **a** Predrilled cavity and tool electrode. **b** Tool electrode at full depth. **c** At the end of boring operation. **d** Bored cavity and tool wear

2.5 Input Parameters and Responses

EDM process uses spark energy to cut work metals therefore electrical parameters like peak current (I_p), pulse on time (t_{on}) and pulse off time (t_{off}) are considered for experimentations. Input parameters selected in present study with their range are listed in Table 2. Material Removal Rate (MRR), Tool Wear Rate (TWR) and Surface roughness (Ra) are selected as responses. MRR and TWR are expressed in mm3/min and calculated using following formula:

$$\text{MRR} = \frac{\text{Initial weight of workpiece} - \text{Final weight of workpiece}}{\text{Machining time} \times \text{Density of Inconel 718}} \quad (1)$$

$$\text{TWR} = \frac{\text{Initial weight of tool electrode} - \text{Final weight of tool electrode}}{\text{Machining time} \times \text{Density of Copper}} \quad (2)$$

Table 2 Input parameters and their values

S. no	Parameters	Values	Justification
1	A: Peak current (I_p)	6, 13, 21 A	Higher I_p values are omitted as they result into high tool wear and poor surface finish
2	B: Pulse on time (t_{on})	75, 195, 315 μs	Longer t_{on} improves the *MRR* but extra long t_{on} reduces the performance. Three levels of t_{on} are selected in lower to higher range available with the set up
3	C: Pulse off time (t_{off})	32, 82, 135 μs	t_{off} are selected in such a way that it should not be too short and too high
4	D: Orbital speed (S_o)	0.05, 0.09, 0.13 mm/s	Based on the similar study [4], S_o are selected from lower to higher values
5	E: Orbital radius (S_r)	0.50, 1.00, 1.50 mm	Higher setting of S_r increases tool travel time and reduces the *MRR*, therefore here S_r is varied from 0.50 to 1.50 mm
6	F: Machining time (t_m)	0.667, 1.034, 1.401 s	t_m should be sufficient to remove material. It is selected based on the tool movement capacity in existing set up to cover full available range
7	G: Flushing time (t_f)	0.067, 0.267, 0.467 s	Adequate flushing time is needed for effective and stable machining, higher t_f increases the total time that affects the *MRR*. Here, t_f is selected to cover full available range

Surface roughness of the machined cavities, expressed in micron, is measured in terms of arithmetic mean (Ra) using Mitutoyo surftest SJ 400 using a 90° diamond conical stylus with 5 μm tip radius. All the roughness measurements are carried out with the measuring length of 4 mm. The roughness parameter Ra is defined according to ISO 4287:1997 standard. Ra value is measured at six different locations (60° from each location) on the wall of cavity and average of all six values is taken as the surface roughness of cavity.

Taguchi technique is one of the most suitable methods for experimental study that reduce the number of experiments required to identify the optimal combination of parameters. The following steps are involved in Taguchi method:

1. Identification of process parameters and responses to be evaluated.
2. Selection of Orthogonal array as per number of parameters and their levels.
3. Allocation of process parameters to the orthogonal array and conduction of the experiment accordingly.
4. Calculation of signal-to-noise ratio (S/N ratio) according to quality characteristics of respective responses.
5. Analysis of results and identification of optimal combination of process parameters.
6. Verification of optimal parameters by conducting confirmation tests.

Taguchi method uses a set of orthogonal array for number of different experimental situations. Orthogonal array (OA) is designed in such a way that each level of a factor comes to equal number of times with all levels of other factors. Selection of suitable orthogonal array (from Taguchi's standard orthogonal array) is based on the total number of degree of freedom of experiments. Number of degree of freedom associated with a factor is one less than its total number of levels. In present case the degree of freedom for seven factors at 3 levels is 14 and for overall mean, degree of freedom is 1. Therefore, total degree of freedom is 15. The selected orthogonal array must have equal to or more experimental runs than the total number of degree of freedom required to study the responses. Thus the orthogonal array suitable for the study of seven parameters at three levels is L27 [17, 18], which implies 27 number of experiments should be performed. The layout of the experimental design is shown in Table 3. Each experiment is replicated twice. In Taguchi method, the calculated responses are converted into a variance index called Signal to Noise ratio (S/N ratio). The higher S/N ratio is always desirable in an experiment irrespective to quality characteristics. Higher value of S/N ratio indicates the more desirable condition. S/N ratio is categorized into three characteristics viz. lower the better (LB), nominal the better (NB), or higher the better (HB). MRR is HB characteristics while TWR and Surface roughness are LB characteristics. These are calculated using following formulae.

$$\eta_{HB} = -10 \log_{10} \left(\frac{1}{n} \sum_{j=1}^{n} \frac{1}{y_{ij}^2} \right) \tag{3}$$

Table 3 Experimental design and S/N ratios of responses

| Experimental design | | | | | | | | Responses | | |
| Exp. | A | B | C | D | E | F | G | S/N ratio | | |
No.	I_p	t_{on}	t_{off}	S_o	S_r	t_m	t_f	η_{MRR}	η_{TWR}	η_{Ra}
1	6	75	32	0.05	0.50	0.667	0.067	8.3455	43.9367	−14.372
2	6	75	32	0.05	1.00	1.034	0.267	6.6694	47.6747	−13.931
3	6	75	32	0.05	1.50	1.401	0.467	6.6113	38.9468	−14.1494
4	6	195	82	0.09	0.50	0.667	0.067	11.9613	49.3940	−14.8742
5	6	195	82	0.09	1.00	1.034	0.267	11.1146	51.3478	−15.5642
6	6	195	82	0.09	1.50	1.401	0.467	10.6038	51.8306	−15.1476
7	6	315	135	0.13	0.50	0.667	0.067	12.4233	46.2204	−15.2207
8	6	315	135	0.13	1.00	1.034	0.267	12.0360	55.7311	−14.959
9	6	315	135	0.13	1.50	1.401	0.467	11.0092	60.0234	−14.5716
10	13	75	82	0.13	0.50	1.034	0.467	16.3828	12.2230	−16.4324
11	13	75	82	0.13	1.00	1.401	0.067	17.8716	12.9044	−17.3137
12	13	75	82	0.13	1.50	0.667	0.267	15.4827	14.3635	−16.8199
13	13	195	135	0.05	0.50	1.034	0.467	13.4423	50.5230	−18.2009
14	13	195	135	0.05	1.00	1.401	0.067	19.1462	34.9149	−19.5407
15	13	195	135	0.05	1.50	0.667	0.267	15.1009	36.7834	−18.6019
16	13	315	32	0.09	0.50	1.034	0.467	17.5429	46.9172	−19.6807
17	13	315	32	0.09	1.00	1.401	0.067	23.3368	41.2279	−19.3333
18	13	315	32	0.09	1.50	0.667	0.267	19.0122	60.5943	−18.6991
19	21	75	135	0.09	0.50	1.401	0.267	19.2708	0.0284	−18.0335
20	21	75	135	0.09	1.00	0.667	0.467	11.1047	8.4967	−17.9171
21	21	75	135	0.09	1.50	1.034	0.067	20.4063	8.1500	−18.1907
22	21	195	32	0.13	0.50	1.401	0.267	23.9444	11.9592	−20.6707
23	21	195	32	0.13	1.00	0.667	0.467	16.0962	25.0513	−20.0656
24	21	195	32	0.13	1.50	1.034	0.067	25.9092	16.7359	−20.8634
25	21	315	82	0.05	0.50	1.401	0.267	17.8311	33.8323	−21.1666
26	21	315	82	0.05	1.00	0.667	0.467	9.8914	50.0871	−21.5996
27	21	315	82	0.05	1.50	1.034	0.067	19.5090	34.2391	−20.9621

$$\eta_{LB} = -10 \log_{10} \left(\frac{1}{n} \sum_{j=1}^{n} y_{ij}^2 \right) \tag{4}$$

where, y_{ij} is the response of ith quality characteristics at jth experimental run and n is the total number of repetition of a run.

3 Results and Discussion

3.1 Analysis of Material Removal Rate (MRR)

To analyze the effect of input parameters main effect plots are plotted using average values of S/N ratio at each level and shown in Fig. 5. Analysis based on S/N ratio indicates that optimal conditions for higher MRR are peak current (I_p) 21A (Level 3), pulse on time (t_{on}) 195 µs (Level 2), pulse off time (t_{off}) 32 µs (Level 1), orbital speed (S_o) 0.13 mm/s (Level 3), orbital radius (S_r) 1.5 mm (Level 3), machining time (t_m) 1.401 s (Level 3) and flushing time (t_f) 0.067 s (Level 1). Table 4 shows the results of analysis of variance for MRR. It is observed that all parameters are statistically significant however, peak current (I_p) is most contributing parameter followed by flushing time (t_f) and orbital speed (S_o) in determining the MRR.

From Fig. 5a, it can be observed that MRR increases with increase in peak current. Higher peak current leads to higher discharge energy between the electrodes. Higher discharge energy increases the removal of material per unit time. Similar observation has been reported by Sundaram et al. [19] and Kuppan et al. [20]. Plot of peak current (I_p) in Fig. 5a, reveals that the change in average response between lower and middle value (6 and 13A) is more than that of between middle and higher level of peak current (13 and 21A). It means increment in peak current from 6 to 13A has resulted higher MRR than that of from 13 to 21A peak current. At higher amperage of peak current, possibility of arcing increases in the working gap because higher peak current removes the material at higher rate. These eroded materials (large volume) accumulate and decrease the gap between tool electrode and work surface resulting
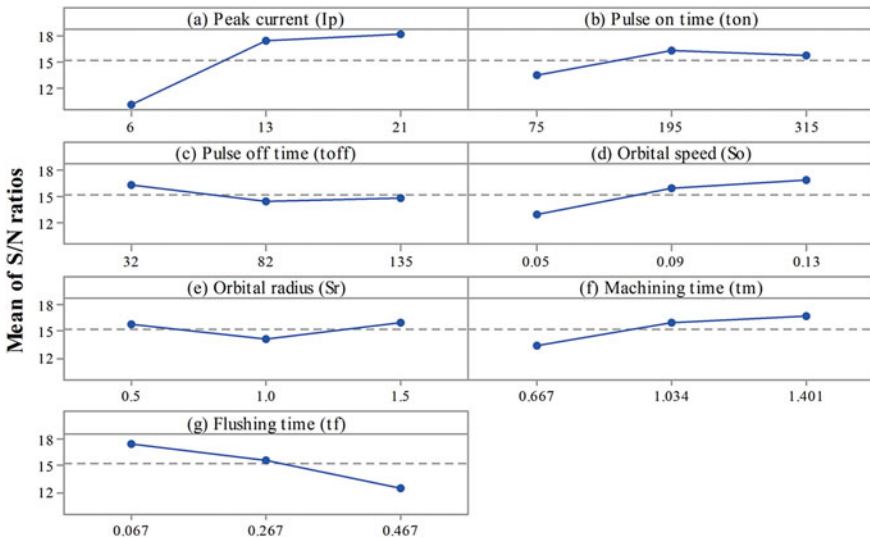
Fig. 5 Main effect plots for MRR

Table 4 ANOVA of S/N ratio for MRR

Source	DF	Sum of square	Mean square	F-Value	P-Value	% Contribution
A: Peak current (I_p)	2	364.033	182.016	322.71	0.00	52.26
B: Pulse on time (t_{on})	2	39.783	19.891	35.27	0.00	5.71
C: Pulse off time (t_{off})	2	17.657	8.828	15.65	0.00	2.53
D: Orbital speed (S_o)	2	74.711	37.355	66.23	0.00	10.73
E: Orbital radius (S_r)	2	17.299	8.649	15.33	0.00	2.48
F: Machining time (t_m)	2	56.031	28.015	49.67	0.00	8.04
G: Flushing time (t_f)	2	120.318	60.159	106.66	0.00	17.27
Error	12	6.768	0.564			0.97
Total	26	696.6				

into arcing. In case of radial orbital EDM, tool electrode retracts back to avoid such arcing and the repetitive retraction of tool electrode adds extra time to the total machining time. Therefore, increment in MRR at higher level of peak current is smaller than that of lower peak current. Further, Analysis of Variance (ANOVA) is performed to obtain the percentage contribution and significance of factors. The calculations for variance (ANOVA) are performed following the procedure explained by Montgomery and Runger [21] and the same is verified with the help of trial version statistical software MINITAB. ANOVA for MRR is shown in Table 4. Table 4 infers that peak current (I_p) represents a major portion of total variation of the observed result. It contributes 52.26% in order to control the total variability. Since its P value is <0.05 (95% confidence interval) therefore peak current (I_p) is statically significant in analyzing MRR.

The effect of Pulse on time (t_{on}) on MRR is illustrated in Fig. 5b. MRR first increases then marginally decreases in radial orbital EDM process. At the middle level of t_{on} (195 μs) the highest MRR is observed. These results are in agreement with the researchers Sohani et al. [22] in die-sinking EDM process. The reason behind such observation may be attributed to the available energy during pulse duration. When pulse on time is short then the energy produced at the point of spark is less which in turn removes lesser material. The spark energy increases with the increase in pulse duration which removes relatively larger material from the workpiece. However, extra long pulse on time distributes the heat energy over larger area through conduction, due to which lesser material is removed from the workpiece. Further, form ANOVA shown in Table 4, it can be observed that its percentage contribution is relatively smaller (5.71%), implying that MRR does not vary substantially on varying pulse on time in selected range.

Effect of pulse off time (t_{off}) on MRR in radial orbital EDM is shown in Fig. 5c. It can be observed that MRR decreases with increase in pulse off time (t_{off}). Lower value of pulse off time offers higher MRR. Higher pulse off time (t_{off}) causes longer machining time for removal of same material and hence it decreases the MRR. Similar findings are reported by researchers [23, 24]. The percentage contribution of pulse off time (t_{off}) indicates that it has very low contribution (2.53%) in affecting the MRR in radial orbital EDM process.

As discussed earlier, radial orbital EDM machining involves to and fro movement of tool electrode during the process therefore it is expected to have some effect of orbital parameters on MRR. Effect of orbital speed (S_o) on MRR is plotted in Fig. 5d. MRR is observed increasing with increase in speed of tool electrode (mm/s) during machining. An increase of about 30% in MRR (mm3/min) is observed at highest orbital speed (0.13 mm/s) relative to lower speed of tool electrode during the process. The increasing trend of MRR is due to the increase in speed of tool electrode during radial orbit EDM machining. With increase in speed of tool movement, time consumed in travelling of tool from centre to the machining area decreases and reduces the total machining time that has improved the material removal rate.

Effect of orbital radius (S_r) on MRR is depicted in Fig. 5e. With increase in orbital radius from 0.5 to 1.0 mm MRR is found reducing and during further increment in orbital radius from 1.0 to 1.5 mm MRR increased marginally. This may be a notable observation in radial orbital EDM process, because it allows to generate larger size of hole with using smaller size of tool electrode without sacrificing material removal rate. However, orbital radius (S_r) is found least contributing factor. The same can be observed from the main effect plot in Fig. 5e as its average S/N ratios do not vary much from the mean line.

Plot of machining time in Fig. 5f depicts the variation in MRR with machining time (t_m) in radial orbital EDM process. The mean S/N ratios calculated for MRR is increasing with increase in machining time (t_m). As machining time increases from lower to higher values, an increment about 25% in MRR is observed. Increment in MRR with machining time is due to longer forward step of tool electrode in radial orbital EDM process. As illustrated in Fig. 3, the movement of tool electrode in radial orbital machining is to and fro nature. The length of forward step travelled by tool electrode is decided by machining time in seconds. Larger setting of machining time implies longer step of tool travel during process. Therefore, higher machining time (t_m) reduces the time consumed during tool travelling and hence MRR is improved. The backward movement of tool electrode is controlled by flushing time. Higher the flushing time, longer will be the backward step. Longer flushing time (t_f) duration increases the tool retraction time that is non-cutting time (non productive time). Therefore, MRR is found reducing with increase in flushing time (t_f). The same can be observed from Fig. 5g. However, the percentage contribution of flushing time (t_f) is higher than that of machining time (t_m).

3.2 Analysis of Tool Wear Rate (TWR)

Tool wear is mostly observed on cylindrical surface of tool electrode during radial orbital EDM process. TWR is calculated using Eq. (3). The calculated TWR for each experiment is converted into the S/N ratio. Since TWR is lower the better quality characteristic, hence S/N ratio is calculated using Eq. (4) and shown in Table 3.

Figure 6 shows the main effect plots for TWR. The optimal combination of factors for lower TWR are 6A (Level 1) of peak current (I_p), 315 µs (Level 3) of pulse on time (t_{on}), 32 µs (Level 1) of pulse off time (t_{off}), 0.05 mm/s (Level 1) of orbital speed (S_o), 1.0 mm (Level 2) of orbital radius (S_r), 0.667 s (Level 1) of machining time (t_m) and 0.467 s (Level 3) of flushing time (t_f). Table 5 represents the results of analysis of variance of TWR. It shows that peak current (I_p) and pulse on time (t_{on}) are statistically significant parameters and have major effect over TWR as they collectively share approximately 81% of total sum of square. However, orbital speed (S_o) has relatively less contribution (8.73%) but is statistically significant. Remaining parameters viz., pulse off time (t_{off}), orbital radius (S_r), machining time (t_m) and flushing time (t_f) are observed as insignificant for TWR.

From Fig. 6a, it can be observed that the mean S/N ratio for TWR is maximum at 6A peak current (I_p) and decreases with increase in peak current. This implies that TWR is less at lower current setting. The obtained results are in good agreement with results reported by Lee and Li [24] Heat energy generated between workpiece and tool electrode interface increases with increase in peak current (I_p) that leads to the melting and vaporization of tool material resulting into higher TWR. Wear on tool surface can be clearly observed in the form of craters, as shown in Fig. 7. The size
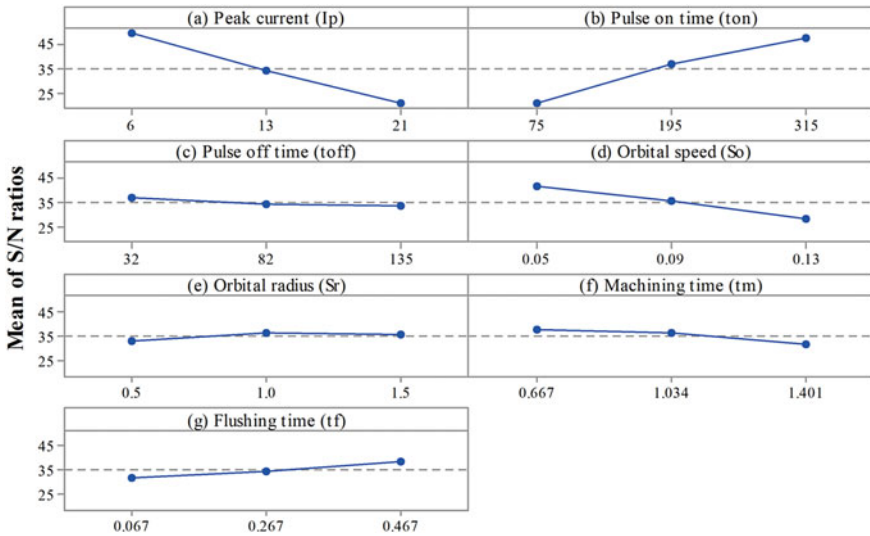
Fig. 6 Main effect plots for TWR

Table 5 ANOVA of S/N ratio for TWR

Source	DF	Sum of square	Mean square	F-Value	P-Value	% Contribution
A: Peak current (I_p)	2	3658.87	1829.43	54.72	0.000	42.80
B: Pulse on time (t_{on})	2	3289.42	1644.71	49.20	0.000	38.48
C: Pulse off time (t_{off})	2	60.87	30.43	0.91	0.428	0.71
D: Orbital speed (S_o)	2	745.81	372.91	11.15	0.002	8.73
E: Orbital radius (S_r)	2	66.39	33.19	0.99	0.399	0.78
F: Machining time (t_m)	2	147.8	73.9	2.21	0.152	1.73
G: Flushing time (t_f)	2	177.53	88.76	2.66	0.111	2.08
Error	12	401.18	33.43			4.69
Total	26	8547.86				

of these micro craters increases with increase in peak current. From ANOVA shown in Table 5, peak current (I_p) is the highest contributing (42.8%) factor amongst all selected factors.

Figure 6b shows the relationship between TWR and pulse on time (t_{on}) during boring operation in radial orbital EDM process. It can be seen that S/N ratio of TWR is higher at higher pulse on time (315 µs) and lower at lower pulse on time (75 µs) which implies that TWR decreases with the increase in pulse on time (t_{on}). Similar results are reported by Zarepour et al. [25] and Barenji et al. [26]. Increment in pulse on time (t_{on}) decreases the spatial current density and also increases the carbon deposition on tool surface that protects the tool electrode from wear [22]. Analysis of variance shown in Table 5 indicates that pulse on time (t_{on}) is statistically significant factor (P value < 0.05) and its percentage contribution is 38.48%.

The relationship between pulse off time (t_{off}) and mean S/N ratios of TWR is shown in Fig. 6c. As evident from Table 5, pulse off time (t_{off}) has insignificant effect on TWR; it shares only 0.71% contribution in controlling the variance of TWR. Figure 6c reveals that there is marginal change in S/N ratio of TWR on changing pulse off time (t_{off}) from lower to higher setting values. However, at lower pulse off time (t_{off}), minimum TWR is obtained.

The effect of orbital speed (S_o) on TWR is depicted in Fig. 6d. Change in orbital speed (S_o) has significantly affected the TWR during radial orbital EDM process. The mean S/N ratio for TWR has reduced to approx. 31% on changing orbital speed (S_o) from lower to higher (0.05 and 0.13mm/s) setting. Least TWR is observed at lowest orbital speed. The reason for higher TWR at higher orbital speed of tool electrode is the frequent sparking. Increment in orbital speed reduces the tool travelling time inside the cavity during radial orbital machining. This means tool electrode
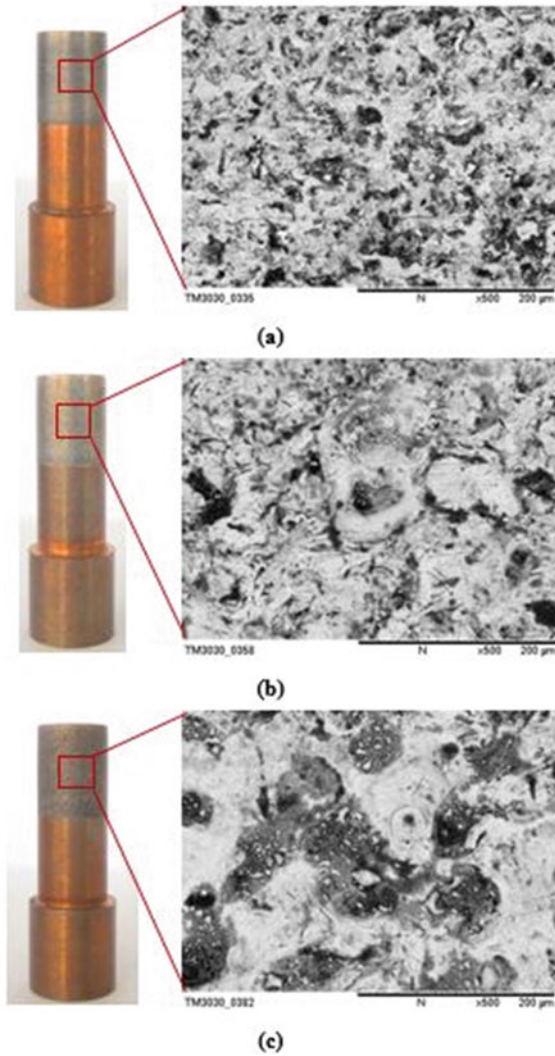
Fig. 7 Micrograph of tool surface at **a** $I_p = 6$A, $t_{on} = 75$ μs, **b** $I_p = 13$A, $t_{on} = 75$ μs, **c** $I_p = 21$A, t_{on} 75 μs

will complete the to and fro movement on radial distance quickly and tool electrode remains in contact with spark frequently that reduces the cooling as well as conduction time in turn increasing the erosion rate of tool electrode. On other hand, at lower orbital speed, tool electrode provides sufficient time for cooling and conducting heat that resulting into lower TWR in radial orbital EDM process. Analysis of variance for TWR shown in Table 5 indicates that orbital speed (S_o) has only 8.73% of contribution amongst others selected factors.

Effect of remaining factors such as orbital radius (S_r), machining time (t_m) and flushing time (t_f) has minimal effect on TWR as shown in Fig. 6e–g respectively. The insignificance of these factors can also be observed from Table 5; these factors collectively contribute about 4.5% in reducing the variance of TWR. However, maximum TWR is observed at lowest orbital radius (0.5 mm) and further increment in orbital radius from 1.0 to 1.5 mm caused little change in S/N ratios of TWR. It is worth noting that TWR is not significantly affected by orbital radius (S_r) and therefore any size of tool electrode can be used to enlarge cavity.

The effect of flushing time (t_f) for TWR in radial orbital EDM process is illustrated in Fig. 6g. The result shows that in radial orbital EDM, TWR is decreasing with increase in flushing time (t_f). Higher flushing time has resulted into minimum TWR. Flushing time implies the time duration of tool retracting during radial orbital EDM process. Higher the flushing time, larger will be the retracting distance of tool electrode from the machining zone. Higher flushing time provides sufficient time to tool electrode during radial orbital machining due to which TWR is observed decreasing with flushing time.

TWR does not conclude the nature of tool wear, it only gives the quantitative idea of wear. Therefore, in order to observe the wear on tool electrode, the cylindrical surface as well as bottom surface is considered for the investigation. Figures 7 and 8 show the side wear on cylindrical and bottom surfaces respectively of tool electrode used for boring operation at different peak current. It is observed that wear is mainly concentrated on cylindrical surfaces than that of bottom surfaces. This is due to the nature of tool movement during radial orbital machining process. As illustrated in Fig. 2b the tool electrode moves only in lateral direction and therefore major portion of cutting of material during this process takes place only through the cylindrical surface of tool electrode. Relatively lesser wear is observed on bottom surface of tool electrode is observed, this is because the tool electrode. Figure 8 shows the bottom end of tool electrode (taken at × 35 magnification using VMS) used for boring operation at different peak currents using radial tool movement in EDM process. Wear on bottom surface of tool electrode can be observed in the form of
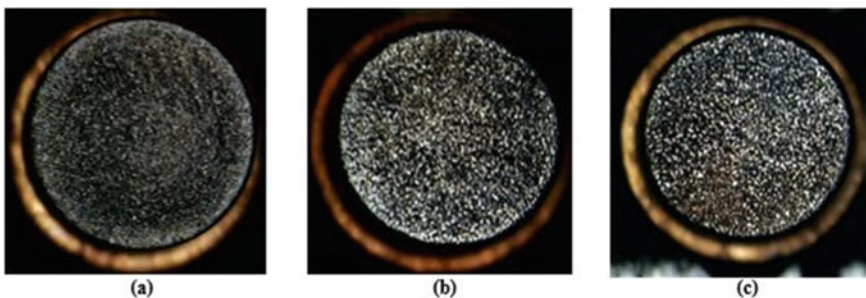
Fig. 8 Image of bottom surface of tool electrode at **a** $I_p = 6A$, $t_{on} = 75\,\mu s$ **b** $I_p = 13A$, $t_{on} = 75\,\mu s$ **c** $I_p = 21A$, $t_{on} = 75\,\mu s$
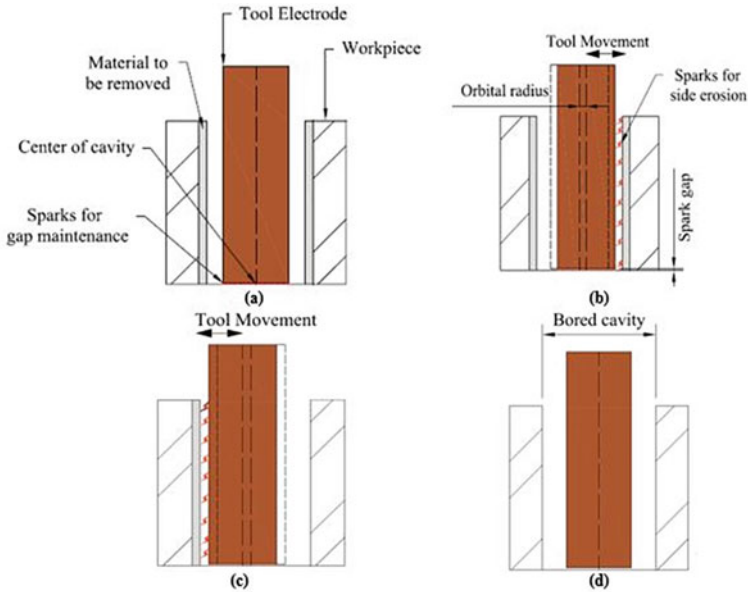
Fig. 9 Sparking phenomenon during radial EDM process. **a** Start of the process. **b** Removal of material in positive X direction. **c** Removal of material in negative X direction. **d** End of process

tiny crates which occurs due to few sparks that occur between bottom surfaces of tool electrode and cavity to maintain the spark gap.

From schematic representations of boring operation shown in Fig. 9, it can be observed that size of the cavity is being increased with sparks generated at side surface of tool electrode and the bottom end of tool electrode is engaged only for spark gap maintenance. Thus it can be understood that major portion of material is worn out from the cylindrical side surface of the tool electrode unlike the usual die sinking EDM process where tool wear occurs mainly on the bottom end surface.

3.3 Analysis of Surface Roughness (Ra)

As discussed in Sect. 3.2, the size of the cavity is enlarged mainly by cutting the materials from side walls of cavity and removal of materials from the bottom end of cavity is negligible during radial tool movement in EDM process. Therefore, in the present work surface roughness is measured on the side surface of cavity that is generated by radial movement of the tool electrode.

Main effect plots of Ra are plotted using mean of S/N ratios at each level for each factor and shown in Fig. 10. Analysis of S/N ratio reveals that the optimal parametric combination for lower surface roughness value (Ra) during radial orbital
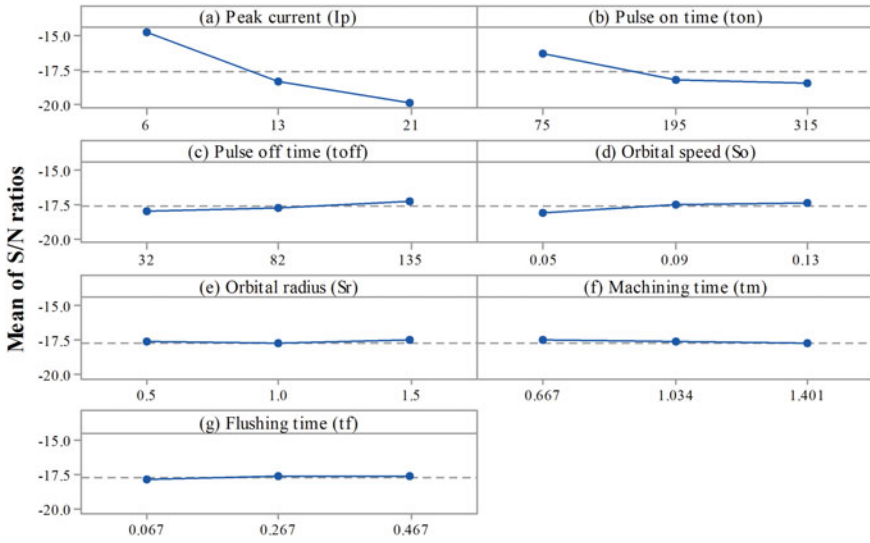
Fig. 10 Main effect plots for Ra

EDM process is 6A (Level 1) peak current (I_p), 75 µs (Level 1) pulse on time (t_{on}), 135 µs (Level 3) pulse off time (t_{off}), 0.13 mm/s (Level 3) orbital speed (S_o), 1.5 mm (Level 3) orbital radius (S_r), 0.667 s (Level 1) machining time (t_m) and 0.467 s (Level 3) flushing time (t_f). Table 6 contains the results of ANOVA for surface roughness.

Table 6 ANOVA of S/N ratio for Ra

Source	DF	Sum of square	Mean square	F-Value	P-Value	% Contribution
A: Peak current (I_p)	2	126.717	63.3585	383.023	0.000	80.21
B: Pulse on time (t_{on})	2	23.748	11.874	71.782	0.000	15.03
C: Pulse off time (t_{off})	2	2.475	1.2375	7.481	0.008	1.57
D: Orbital speed (S_o)	2	2.089	1.0445	6.314	0.013	1.32
E: Orbital radius (S_r)	2	0.293	0.1465	0.885	0.427	0.19
F: Machining time (t_m)	2	0.187	0.0935	0.565	0.583	0.12
G: Flushing time (t_f)	2	0.493	0.2465	1.490	0.264	0.31
Error	12	1.985	0.165417			1.26
Total	26	157.987				

Peak current (I_p) and pulse on time (t_{on}) are the major contributing parameters followed by pulse off time (t_{off}). Peak current (I_p), pulse on time (t_{on}), pulse off time (t_{off}) and orbital speed (S_o) are statistically significant parameters whereas orbital radius (S_r), machining time (t_m) and flushing time (t_f) are statistically insignificant parameters.

Figure 10a shows the effect of peak current (I_p) on surface roughness value (Ra). It can be observed that mean value of S/N ratio for Ra decreases with increase in peak current. It implies that surface roughness value (Ra) increases with increase in peak current. The obtained results are in good agreement with the results reported by Gostimirovic et al. [27]. Increase in peak current (I_p) increases the discharge energy between the tool electrode and the workpiece in EDM process. Removal of material takes place from workpiece at the end of spark leaving behind tiny craters in EDM process. The size of crater depends upon the discharge energy. Typical images of workpiece surfaces are shown in Fig. 11a–b. At lower peak current i.e. at 6A, the crater sizes are relatively smaller than that observed at highest peak current of 21A. High peak current has generated deeper and more irregular craters that have resulted higher surface roughness. The percentage contribution calculated in Table 6 represents the relative power of peak current (I_p) (80.21%) to reduce the variation.

The effect of pulse on time (t_{on}) on Ra value is shown in Fig. 10b. The S/N ratio of average surface roughness value (Ra) at lower pulse on time (t_{on}) is higher and is found minimum at longer pulse on time (t_{on}). This means lower pulse on time has resulted smother surface than higher pulse on time. From Fig. 12a–b it can be clearly observed that the size of craters are smaller as well as outer rings of these craters are relatively thin than that of craters generated at higher pulse on
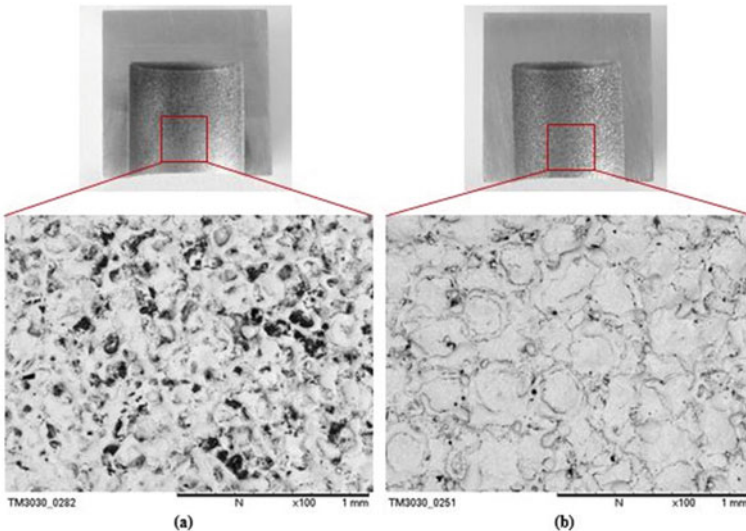
Fig. 11 Micrographs of machined surface generated at **a** lowest $I_p = 6A$ **b** highest $I_p = 21A$
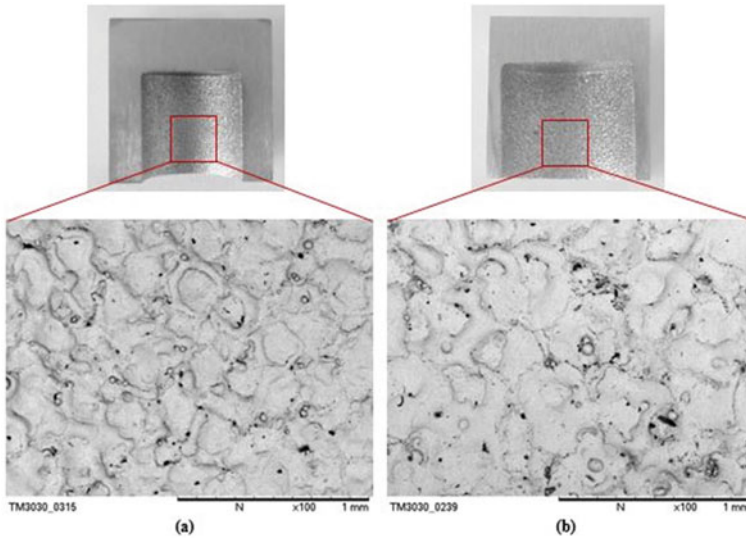
Fig. 12 Micrographs of machined surface generated at **a** lowest $t_{on} = 75\,\mu s$ **b** highest $t_{on} = 315\,\mu s$

time. Similar results are reported by Kiyak and Cakır [28]. Pulse on time (t_{on}) is the second most significant factor, as shown in Table 6; it shares 15.03% of contribution in controlling the variance of surface roughness value (Ra) during boring operation with radial orbital EDM process.

The effect of remaining parameters like, pulse off time (t_{off}), orbital speed (S_o), orbital radius (S_r), machining time (t_m) and flushing time (t_f) are marginal. This can be clearly observed from Fig. 10c–f, as the variation in S/N ratios between lower level and higher level are minimum or negligible. Their effect on surface roughness value (Ra) can also be statistically quantified using ANOVA shown in Table 6, their collectively percentage of contribution is only 3.5%.

4 Confirmation Tests

Confirmation experiments are important to verify the results as well as to confirm the reproducibility of experiments. A confirmation experiment is performed by conducting a test using a specific combination of the factors and levels previously evaluated. The following steps are involved in conducting a confirmation experiments:

1. Determination of the preferred combination of the levels of the process parameters by the analysis.
2. Calculation of estimated mean for preferred combination of the levels.
3. Calculation of the confidence interval value.

Table 7 Confirmation test results

Responses	Optimum level	Predicted S/N ratio (η_P) (db)	Experimental S/N ratio (η_E) (db)	% Prediction error $\left\| \frac{\eta_E - \eta_P}{\eta_E} \times 100 \right\|$
MRR	$A_3B_2C_1D_3E_3F_3G_1$	26.4416	26.2728	0.64
TWR	$A_1B_3C_1D_1E_2F_1G_3$	68.3879	64.2931	6.36
R_a	$A_1B_1C_3D_3E_3F_1G_3$	−12.7964	−13.3037	3.81

4. Calculation of the confidence interval for the true mean around estimated mean.
5. Conduction of tests under preferred combination of process parameters.
6. Comparison of the confirmation test average result to the confidence interval for true mean.

Taguchi recommends the prediction of responses at optimum setting of parameters [29]. Optimum combination of process parameters as stated in step 1 has been obtained by the analysis of MRR, TWR and surface roughness in Sects. 3.1, 3.2 and 3.3 respectively.

4.1 Estimation of Predicted Means

The estimated mean of MRR, TWR and Ra are calculated using following Eq. (5) [17].

$$\eta_P = T + \sum (\eta_i - T) \qquad (5)$$

where, T is overall mean of response parameter, η is average value of significant parameters.

The confirmation tests are performed on the optimal setting of parameters. The S/N ratios of obtained at the optimum combination of parameters and the predicted results are shown in Table 7. This shows that the optimum factors level combination for these experiments are very close to the predicted S/N ratio.

5 Conclusions

This study employs radial tool movement in EDM process for boring operation on Inconel 718 material. Experiments are performed using Taguchi method and the observed results are analysed using ANOVA. Following important conclusions can be drawn from this study:

1. Boring of predrilled cavity can be successfully achieved in EDM process using radial tool movement.
2. Boring operation in EDM process is not affected by bore size because tool wear rate and surface roughness is not significantly affected by orbital radius.
3. Peak current is found to be the most influencing parameter in boring operation in edm process.
4. Speed of the tool electrode during boring operation significantly affects the material removal rate, tool wear rate and surface roughness. With increase in speed, MRR increases but TWR and surface roughness (Ra) decreases.
5. Surface quality and tool wear rate does not depend on to and fro movement of tool electrode on radial path because machining time and flushing time has negligible effect on responses.

This study introduces the possibility of boring operation in electro discharge machining process. Several factors involved during machining have been analyzed, however in future one can study the dimensional accuracy of bored cavity that can be achieved in radial orbital EDM process.

References

1. Jahan MP, Rahman M, Wong YS (2011) A review on the conventional and micro-electrodischarge machining of tungsten carbide. Int J Mach Tools Manuf 51:837–858
2. Yadav US, Yadava V (2015) Experimental modeling and multiobjective optimization of electrical discharge drilling of aerospace superalloy material. Proc IMechE, Part B: J Eng Manuf 229:1764–1780
3. Lascoe OD (1988) Handbook of fabrication processes. ASM Int, Metal Park, Ohio
4. Dave HK, Desai KP, Raval HK (2013) A Taguchi approach-based study on effect of process parameters in electro discharge machining using orbital tool movement. Int J Mach Mach Mater 13:52–66
5. El-Taweel T, Hewidy M (2009) Enhancing the performance of electrical-discharge machining via various planetary modes. Int J Mach Mach Mater 5:308–320
6. Bamberg E, Heamawatanachai S (2009) Orbital electrode actuation to improve efficiency of drilling micro-holes by micro-EDM. J Mater Process Technol 209:1826–1834
7. Jain VK (2012) Advance machining processes. Allied Publishers Pvt, Ltd., New Delhi
8. Belgassim O, Abusaada A (2011) Investigation of the influence of EDM parameters on the overcut for AISI D3 tool steel Proc IMechE, Part B: J Eng Manuf. https://doi.org/10.1177/0954405411400498
9. Singh A, Kumar P, Singh I (2013) Electric discharge drilling of metal matrix composites with different tool geometries. Proc IMechE, Part B: J En Manuf 227:1245–1249
10. Jabbaripour B, Sadeghi M, Faridvand S, Shabgard M (2012) Investigating the effects of EDM parameters on surface integrity, MRR and TWR in machining of Ti–6Al–4V. Mach Sci Technol 16:419–444
11. Muthuramalingam T, Mohan B (2013) Influence of discharge current pulse on machinability in electrical discharge machining. Mater Manuf Process 28:375–380
12. Sivam SP, Michaelraj AL, Kumar SS, Prabhakaran G, Dinakaran D, Ilankumaran V (2014) Statistical multi-objective optimization of electrical discharge machining parameters XE "Machining parameters" in machining titanium grade 5 alloy using graphite electrode. Proc IMechE, Part B: J Eng Manuf 228:736–743

13. Kolli M, Kumar A (2015) Effect of dielectric fluid with surfactant and graphite powder on Electrical Discharge Machining of titanium alloy using Taguchi method. Eng Sci Technol, Int J 18:524–535
14. Rajurkar K, Royo G (1989) Effect of RF control and orbital motion on surface integrity of EDM components. J Mech Work Technol 20:341–352
15. Yu ZY, Rajurkar KP, Shen H (2002) High aspect ratio and complex shaped blind micro holes by micro EDM. CIRP Ann Manuf Technol 51:359–362
16. Bamberg E, Heamawatanachai S, Jorgensen JD (2005) Flexural micro-EDM head for increased productivity of micro-holes. ASPE Conf Norfolk 82–85
17. Ross PJ (2005) Taguchi techniques for quality engineering: loss function, orthogonal experiments, parameter and tolerance design. McGraw Hill Education, New Delhi
18. Phadke MS (1995) Quality engineering using robust design. Prentice Hall PTR, New Jersey
19. Sundaram MM, Pavalarajan GB, Rajurkar KP (2008) A study on process parameters of ultrasonic assisted micro EDM based on Taguchi method. J Mater Eng Perform 17:210–215
20. Kuppan P, Rajadurai A, Narayanan S (2008) Influence of EDM process parameters in deep hole drilling of Inconel 718. Int J Adv Manuf Technol 38:74–84
21. Montgomery DC, Runger GC (2010) Applied statistics and probability for engineers. Wiley, New York
22. Sohani MS, Gaitonde VN, Siddeswarappa B, Deshpande AS (2009) Investigations into the effect of tool shapes with size factor consideration in sink electrical discharge machining (EDM) process. Int J Adv Manuf Technol 45:1131–1145
23. Eyercioglu O, Cakir MV and Kursad G (2013) Influence of machining parameters on the surface integrity in small-hole electrical discharge machining. Proc IMechE, Part B: J Eng Manuf. https://doi.org/10.1177/0954405413498730
24. Lee S, Li X (2001) Study of the effect of machining parameters on the machining characteristics in electrical discharge machining of tungsten carbide. J Mater Process Technol 115:344–358
25. Zarepour H, Tehrani AF, Karimi D, Amini S (2007) Statistical analysis on electrode wear in EDM of tool steel DIN 1.2714 used in forging dies. J Mater Process Technol 187:711–714
26. Barenji RV, Pourasl HH, Khojastehnezhad VM (2016) Electrical discharge machining of the AISI D6 tool steel: prediction and modeling of the material removal rate and tool wear ratio. Precis Eng 45:435–444
27. Gostimirovic M, Kovac P, Sekulic M, Skoric B (2012) Influence of discharge energy on machining characteristics in EDM. J Mech Sci Technol 26:173–179
28. Kiyak M, Cakır O (2007) Examination of machining parameters on surface roughness in EDM of tool steel. J Mater Process Technol 191:141–144
29. Taguchi G, Chowdhury S, Wu Y (2005) Taguchi's quality engineering handbook. Wiley, New Jersey

Index